Ultrafast dynamics in hybrid perovskites

Marie Cherasse

INSTITUT POLYTECHNIQUE DE PARIS

NNT : 2022IPPAX127

Thèse de doctorat

Ultrafast dynamics in hybrid perovskites

Thèse de doctorat de l'Institut Polytechnique de Paris
préparée à l'École polytechnique

École doctorale n°626 École doctorale de l'Institut Polytechnique de Paris (EDIPP)
Spécialité de doctorat : Physique de la matière condensée

Thèse présentée et soutenue à Palaiseau, le jeudi 8 décembre 2022, par

Marie Cherasse

Composition du Jury :

Pere Roca i Cabarrocas Directeur de recherche CNRS, École polytechnique (LPICM), France	Président
Majed Chergui Professeur, École Polytechnique Fédérale de Lausanne (LUS), Suisse	Rapporteur
Maciej Lorenc Directeur de recherche CNRS, Université de Rennes 1 (IPR), France	Rapporteur
Paulina Plochocka Directrice de recherche CNRS, Université Toulouse III Paul Sabatier (LNCMI), France	Examinatrice
Jelena Sjakste Chargée de recherche CNRS, École polytechnique (LSI), France	Examinatrice
Luca Perfetti Professeur, École polytechnique (LSI), France	Directeur de thèse
Sebastian Maehrlein Maître de conférence, Fritz Haber Institute of the Max Planck Society (PC), Allemagne	Invité

Philosophes, écoutez cette phrase est pour vous
Le bonheur est un astre volage
Qui s'enfuit à l'appel de bien des rendez-vous
Il s'efface, il se meurt devant nous
Quand on croit qu'il est loin, il est là tout près de vous
Il voyage, il voyage, il voyage
Puis il part, il revient, il s'en va n'importe où
Cherchez-le, il est un peu partout

— *Le soleil et la lune*, Charles Trenet

La mer, c'est elle qui m'a guérie.
Sa grande main humide en travers de mon front.
Sa vapeur dans mes narines.
Sa potion amère sur mes lèvres.

— *Moi, Tituba sorcière*, Maryse Condé

Da gibt es kein Messen mit der Zeit, da gilt kein Jahr, und zehn Jahre sind nichts, Künstler sein heißt: nicht rechnen und zählen; reifen wie der Baum, der sein Säfter nicht drängt und getrost in den Stürmen des Frühlings steht ohne die Angst, daß dahinter kein Sommer kommen könnte. Er kommt doch. Aber er kommt nur zu Geduldigen, die da sind, als ob die Ewigkeit vor ihnen läge, so sorglos still und weit.

— *Briefe an einen jungen Dichter*, Rainer Maria Rilke

She rose, but without precipitation, called her dogs, and went firmly but with great alertness of movement down the staircase and out into the garden. Here the shadows of the plants were miraculously distinct.

— *Orlando: A Biography*, Virginia Woolf

Mentivano molte parole, mentivano quasi tutte. Ecco che cosa dovevo fare: studiare le parole esattamente come si studiano le piante, gli animali… E poi, ripulirle dalla muffa, liberarle dalle incrostazioni di secoli di tradizione, inventarne delle nuove [...].

— *L'arte della gioia*, Goliarda Sapienza

À Grand-père, Grand-mère, Maman, Quinquin
..et à un bel avenir !

Acknowledgements

I am extremely grateful to have had the opportunity to do an international PhD thesis between two excellent laboratories, in two great cities, surrounded by many great people. It was a unique opportunity for me to discover different techniques, far away from my knowledge at the time, while learning about condensed matter physics and being a researcher. I hope this modest work will be able to contribute to the understanding of the physical properties of the surprising lead halide perovskites and to the development of this technology to reinforce the use of renewable energies (or at least to enlighten a PhD student in distress). A PhD thesis is far from being a single work person. This chapter dedicated to acknowledgments would actually have to be much longer than my thesis if I were to take the time to thank all the people who helped and accompanied me during these three years. However, I doubt that the jury and my supervisors would appreciate this very much, so I will limit myself to these few pages.

I would like to thank the members of the jury for giving me the opportunity to discuss and demonstrate my research work to peers. I am very grateful to all the members of the jury, particularly to the referees, for taking the time to read this manuscript and to generate various discussions on the results of my work.

I also have many colleagues to thank from the different institutes that have hosted me during these three years. I will start by thanking my colleagues at the École polytechnique, which happens to be my main institute. First of all, I would like to thank my thesis director Luca Perfetti for allowing me to do this thesis with him. I have been extremely lucky to learn from a supervisor who is as warm as he is understanding, caring, funny and demanding. Thank you for all the opportunities you gave me, for your support and your unparalleled laughter. Then I would like to thank Evangelos Papalazarou, who told me about this thesis topic and gave me a lot of support. Thank you for your patience, our discussions, your humour and all your explanations about physics. I would also like to thank Michèle Raynaud, director of the laboratory, for her listening and her support, as well as the administrative team who helped me a lot during all my travels, like Elodie Dubois, Marylène Raclot, Bénédicte Guichard. I would like to sincerely thank all the members of my research group and of the LPS who were at the Synchrotron Soleil during my experiments. I was lucky enough to be part of an

extremely friendly group with people who were always available to answer my questions or have interesting conversations. I would like to particularly thank Yannis Laplace, Nadège Ollier, Romain Grasset, Zhescheng Chen, Weiyan Qi, Niloufar Nilforoushan, Jingwei Dong. I would like to warmly thank Paula Kleij, my partner in crime of laughter and office. Thanks to all the members of the laboratory who did not work directly with me but whom I had the chance to meet, notably Georg Michelitsch, Mariusz Drong, Ozlem Oral, Travis Wade, Lucia Reinig, Andrea Cucca, Francesco Sottile and many others. More at LSI but never far away when there is an aperitif, I would like to thank all the members of the QCMX lab for all our lively discussions and good times, and in particular Landry Bretheau and Jean-Damien Pillet. I promise one day I will come to the volleyball! I would like also to warmly thanks Carolina Garcia Soto from LPP.

I met or met again many people on the *plateau* and belonging to various IPP institutions whom I would also like to thank. I would like to deeply thanks Davide Boschetto for his support, patience and all the good moment we had discussing physics (and many other things!) together. I also would like to sincerely thanks Antigoni Alexandrou for her great advise as well as for her incommensurable and deeply needful involvement for women in science. I would also like to thank Manuel Joffre for his friendly advise and discussion about physical concepts I had pain to master. I would like to sincerely thank Jean Eric Bourré for his enthusiasm for life and for science, as well as his unconditional support for new generations of researchers. It is always a pleasure to meet you at the conferences! I would like to thank the teaching staff of the École polytechnique who contributed to the extremely high quality teaching that I was lucky enough to receive as a PhD student, such as the teaching from Pere Roca i Cabarrocas and Enric Garcia-Caurel from LPICM. I would also like to thank the different associations that welcomed me. It was a pleasure to be part of the viola team of the Paris-Saclay Symphony Orchestra (OPS), thank you for letting me play Saint-Saëns with you at Saint-Eustache! Thank you very much to the members of the Sustainable Student Association (DDX), it was a pleasure to garden with you and to look after the most beautiful chickens in the world. I would like to thank Sylvie Coussot very warmly for her listening and her positivism. A big thank you for what you do for the students of the IPP and for the well-being of the PhD students!

My co-supervision thesis was made possible by the relationships created during my time at Columbia University. Thus, I would first like to thank Xiaoyang Zhu for hosting me in NYC and for his support. I would like to thank Sebastian Maehrlein, who I first met as a PostDoc at the time and for introducing me to the Kerr effect during this short stay. I would like to thank the great team around me that made this stay exciting, especially Feifan (king of the FROG), Prakritri, Mark, Nick, and Mary. I warmly thank my amazing neighborhood from the 119th street and the Brooklyn crew as well as Lyonel.

This stay has led me to collaborate with the FHI. I would first like to thank Martin Wolf for giving me the opportunity to co-supervise my thesis at his prestigious institute (and for proudly winning the petanque tournament with me). I would then like to thank my supervisor Sebas-

tian Maehrlein, who allowed me to discover techniques that were still totally unknown to me, to acquire a solid experience of the phenomena studied and a rigorous vision of physics. I would also like to thank the members of the Terahertz Structural Dynamics group (and VIP members of the pizza Friday), notably Maximilian Frenzel, Leona Nest, Dorothy Mader. I would like to particularly thanks Michael (aka *djjjjj wo ist der EOS ?*) and Joanna for their humour, kindness and our greats discussions. Thanks again for making me become a Blender addict. I would also like to warmly thank the FHI members who shared the laser lab with me day and night, especially Tobias Kamprath's team. I would like to thank Alexander Chekhov, Yannic Behovits, Bruno Rosinus Serrano, Oliver Gueckstock, Reza Rouzegar for the great moments, the "not so good" ones (*Achhhh* the ice in the cavity..) and all the precious information they gave me to better understand the setup.

Apart from the research, I had the chance to meet some wonderful people at the FHI. I would light to infinitely thanks the FHI cool kids. Thank you again Reza Rouzegar, Ivana Lapsanska, Alexander Neef, Stefano Calati for his cardamom chocolate coffee breaks and Berlin adventures. Thank you for your zest for life, It was delightful to spend all these crazy moments with you by my side! I would also like to thank Boubacar Tanda Bonkano warmly, for his kindness, his incredible wisdom and his friendship. I also thank Fabian Schulz for our nice discussions and our (unsuccessful) attempt at Berlin parties. I thank all the other members of the laboratory with whom I had the chance to meet and discuss, particularly Martin Thaemer. I would also like to thank the technical and administrative staff of the FHI, who are an undeniable pillar to facilitate our research and keep our spirits up when the laser is acting up. In particular, I would like to warmly thank Manuel Krueger for our discussions and his enthusiasm, as well as Daria Haberland, Marcel Krenz, Martin Schmidt, Albrecht Ropers and Reinhardt Franke. I would like to warmly thank all the collaborators of the different universities who made my work possible. I would especially like to thank Niusha Heshmati and Feray Unlu from Cologne University, it was a pleasure to work with you.

Away from Dahlem and in the Ring, I got to meet a lot of great people who made me love my stay in Berlin. I would like to thank the more or less temporary inhabitants of the Graefeklub, the amazing inhabitants of Graefekiez (big up to Ali, Ibo, Mehmet, Joe, Plan Cafe and Albatross team) as well as my fellow rail adventurers and the great people I met via Hans Eissler/Edeka (big up to Pierre, Leon and Silvia!).

I am still trying to figure out how it is possible to still have problem in humankind with a group as benevolent as the Berlineuses. Without you, I would never have been able to join the fabulous litterature club *Les Elephantes*. I would like to thank all the fantastic women I met during our literary discussions: Lisa, Emeline, Essia, Joanna, Clémence, Claire, Ozi, Gabrielle, Alexe, Anne-Lise, Judith, Maryse and so many others! Thank you for embellishing my stay with magic and beautiful literature.

I would like to thank the members of the French PhD Discord for being my faithful daily

partners, especially my Rush comrades. Thank you for your hilarious memes and kitschy GIFS. Thank you for your support, your good mood and your benevolence during this long way that is the thesis!

Thank you for the GDR HPero summer school. This week was a breath of fresh air in my thesis and I keep excellent memories, studious and full of sand. A big thank you to Claudine Katan, Constantinos Stoumpos and all the great PhD students I met there, especially Bruno Cucco, Hindia Nahdi, Joanna Urban and Javid Hajhemati!

I was lucky enough to receive two grants during this thesis. Thanks to DAAD for offering me this fellowship and for facilitating my stay in Berlin. I also would like to thank a lot the L'Oreal foundation for giving me the L'Oreal-UNESCO for Women in Science award. This award will help me enormously to continue my academic research and scientific outreach to young audiences. I would like to thank the staff and the 34 other laureates for their kindness, their advices and the great time I had with them.

I would like to thank the Soapbox Science Berlin organizing team for allowing me to discover the incredible feeling of doing scientific outreach in the street while promoting women and non-binary people in science. Thank you for this great event!

I would like to thank all my long-time friends from Dunkerque, especially Felicia, Celine and the whole Ducroc family. I have had the pleasure of being with you for many years in this great city, which has given me the love of wind and cold (which is not insignificant when you have to spend two winters in Berlin). Only *carnavaleux* people can keep up with this weather and be so happy!

I thank my friends from Palaiseau and elsewhere. Thank you for always being there and accompanying me step by step before and during this thesis. In particular, I would like to sincerely thank Salome, Lauren, Charlotte, Elisa, Azza, Narjiss, Adele, Alice, Tessa, Antoine, Eric, Adil, Irene, Elise, Vita, Simona, Weye, Lise, Enzo, Hugo, Lorena, Nisrine, Amina, Inès, Timothée, Noel, Joseph, Pierre, Clement, Mumu, Kévin, Chloé, Roman and many others.

Thanks to my wonderful neighbors and the members of the Jesse's Gardens association for creating such a special atmosphere in the neighborhood! Special thanks to the Radovic family for their unconditional kindness.

I would like to thank Martin, his family and his flatmates (Auguste, Pierre and of course Jordy), for having in some way lived this thesis by my side. Martin, it is fair to say that an *aligot-saucisse* dinner has never been more worthwhile, as a woman with *auvergnate* origin can tell you. Thank you for being so patient and lovely during this mental *yo-yo* that is the thesis. Thank you for all your love and support. But frankly, what a crazy idea to date a PhD student?!

Finally, I would like to extend my heartfelt thanks to my family, to whom I dedicate this work. I am very lucky to have been born into the Martin family. Thank you for helping me as much as you could during this thesis. Thank you Grand-père, for your kindness and for awakening me to science. Thank you Grand-mère, for your love, all our laughs and exciting discussions. Thank you Eric, for being the warmest and funniest uncle. Thank you Maman, for your unconditional support and for all our good times. Orion, you don't like long speeches and you prefer walks in the forest. So I will finish writing and go for a walk with you.

Thank you very much to all of you and *merci*! I'm super excited about what is coming for the next few years. There are still so many great things to learn and discover!

Marie

Abstract

Key words: *Condensed matter physics, THz spectroscopy, Photoemission, Lattice dynamics, Lead halide perovskites*

Metal halide perovskites have emerged as a fascinating class of semiconductors in the last decade. Exhibiting excellent optoelectronic properties, they are promising in the field of solar energy. Indeed, the use of perovskites in the manufacture of new generations of photovoltaic cells would allow the design of high-efficiency, flexible and printable solar panels at low cost. Their structure, complex and disordered at room temperature compared to other semiconductors, has many defects. However, lead halide perovskites unveiled for a long electron diffusion length and a low charge recombination rate, which are key parameters for photovoltaic applications. A fundamental understanding of the dynamics of these materials is thus necessary, particularly those of the charge carriers (electrons) and the vibrations of the crystal lattice (phonons) governing their optoelectronic properties. This research work presents state-of-the-art time-resolved techniques to observe these dynamics during their very short characteristic time scales, in the femtosecond to picosecond range (10^{-15}s to 10^{-12}s).

The first phase of this research consisted in studying the relaxation of electrons in the conduction band. A thorough characterisation of the dynamics of electrons in the conduction band after being excited beyond the band gap by a laser pulse, using a time-resolved photoemission spectroscopy (2PPE) technique on the FemtoARPES setup at Ecole Polytechnique was used to measure the evolution of the electron population of the perovskite band structure. This technique made it possible to study the influence of the orientation of the A-site cations and the crystallographic structure on (slow) defect screening and thus to explain the high tolerance to electron trapping on the surface of $MAPbI_3$ crystals. Time- and angle-resolved photoemission spectroscopy was then performed on 2D lead halide perovskites to observe potential Rashba splitting in the conduction band of the material and a a promising proof of concept has been obtained.

The second phase of the research project aimed to understand the role of phonons and their influence on charge carrier dynamics. Although the inorganic octahedral structure BX_3 is in

a state of high dynamic disorder, the charge carriers have a relatively long diffusion length. This mechanism, which was previously likened to carrier screening, can be explained by an ultrafast polarisation of the octahedral structure during charge carrier generation, thus shielding the charge carriers. In order to address this research question in co-direction with the Fritz Haber Institute of the Max Planck Society (Berlin, Germany), an innovative Terahertz-pumped time-resolved Kerr spectroscopy (TKE) technique was used. In the experiments, $MAPbBr_3$ bulk single crystals and thin films were excited by an intense Terahertz pump, a wavelength exciting in particular the collective phonon modes of the inorganic structure. It is possible to characterise their dynamics by following the Kerr-induced birefringence change of the sample. Important results have been obtained for the community, in particular the detection of the most polarizable Raman-active phonon mode governing the dynamic lattice response to a sub-picosecond transient electric field. Optical Kerr (OKE) experiments and simulation carried out in collaboration with Columbia University (USA) have allowed to theoretically confirm these experimental results. With samples and characterization from the University of Cologne (Germany), an equivalent study was carried out on a new material comprising a several complex A-site cation with high potential for industrial applications. Here, a phonon mode similar to $MAPbBr_3$ was observed, with a potential doubling of the lifetime and improved electronic properties. This work enables a better understanding of slow static screening as well as dynamic screening in lead halide perovskites and paves the way for further study of 2D perovskites.

Résumé

Mots-clefs : *Matière condensée, Spectroscopie THz, Photoémission, Dynamique de réseaux, Pérovskites*

Les pérovskites à halogénures métalliques sont apparues comme une classe fascinante de semi-conducteurs au cours de la dernière décennie. Présentant d'excellentes propriétés optoélectroniques, elles s'avèrent être particulièrement prometteuses dans le domaine de l'énergie solaire. L'utilisation des pérovskites dans la fabrication de nouvelles générations de cellules photovoltaïques permettrait de concevoir des panneaux solaires à haut rendement, flexibles et imprimables à faible coût. Leur structure, complexe et désordonnée à température ambiante par rapport aux autres semi-conducteurs, présente de nombreux défauts. Cependant, elle permet une grande longueur de diffusion des électrons et un faible taux de recombinaison des charges, qui sont des paramètres clés pour les applications photovoltaïques. Une compréhension fondamentale des dynamiques intrinsèques de ces matériaux est ainsi nécessaire, en particulier celle des porteurs de charge (électrons) et des vibrations du réseau cristallin (phonons) qui régissent leurs propriétés électroniques. Les travaux de recherche présentés jusqu'à présent ont consisté à développer et à utiliser des techniques de pointe à résolution temporelle pour observer ces dynamiques pendant leurs périodes caractéristiques très courtes, de l'ordre de la femtoseconde à la picoseconde (10^{-15}s à 10^{-12}s).

La première phase de ces travaux a consisté à étudier la relaxation des électrons dans la bande de conduction. Une caractérisation approfondie de la dynamique des électrons dans la bande de conduction après avoir été excités au-delà de la bande interdite par une impulsion laser a été utilisée pour mesurer l'évolution de la population électronique de la structure de bande de la pérovskite. Pour ce faire, une technique de spectroscopie de photoémission résolue en temps (2PPE) sur le dispositif FemtoARPES de l'Ecole polytechnique a été utilisée. Cette technique a permis d'étudier l'influence de l'orientation des cations A et de la structure cristallographique sur le écrantage des charges et ainsi d'expliquer la haute tolérance au piégeage des électrons à la surface des cristaux de $MAPbI_3$. La spectroscopie de photoémission à résolution temporelle et angulaire (tr-ARPES) a ensuite été réalisée sur des pérovskites d'halogénure de plomb 2D afin d'observer le dédoublement Rashba dans la bande de conduction du matériau

et une preuve de concept prometteuse a été obtenue.

La deuxième phase du projet de recherche visait à comprendre le rôle des phonons et leur influence en terme d'écrantage sur les électrons. Bien que la structure octaédrique inorganique BX_3 soit dans un état de désordre dynamique élevé, les porteurs de charge ont une longueur de diffusion relativement longue. Ce mécanisme, qui peut être assimilé à un écrantage de charge, peut s'expliquer par une polarisation ultrarapide de la structure octaédrique lors de la génération des porteurs de charge, faisant ainsi écran à ces derniers. Afin de confirmer cette hypothèse et en co-direction avec l'Institut Fritz Haber de la Société Max Planck (Allemagne), une technique innovante de spectroscopie Kerr à résolution temporelle (TKE) pompée aux Terahertz a été utilisée. Dans les expériences, des films minces de $MAPbBr_3$ ont été excités par une pompe Terahertz intense, une longueur d'onde excitant en particulier les modes phonon collectifs de la structure inorganique. Il est possible de caractériser leur dynamique en suivant le changement de biréfringence de l'échantillon induit par effect Kerr. Des résultats importants ont été obtenus pour la communauté, en particulier la détection du mode de phonon Raman le plus polarisable dans les $MAPbBr_3$ et $CsPbBr_3$. Des expériences et simulations d'effet Kerr optique (OKE) réalisées en collaboration avec l'Université de Columbia (USA) ont permis de confirmer théoriquement ces résultats expérimentaux. En partenariat avec l'Université de Cologne (Allemagne), une étude équivalente a été réalisée sur un nouveau matériau comprenant un quadruple cation A à fort potentiel pour les applications industrielles. Un mode phonon similaire à $MAPbBr_3$ est observable, avec un doublement de la durée de vie du phonon et des propriétés électroniques améliorées.

List of abreviations

LHPs : Lead halide perovskites
CB : Conduction band
VB : Valence band
TKE : Terahertz-induced Kerr effect
OKE : Optical Kerr effect
ARPES : Angle-resolved photoemission spectroscopy
THz : Terahertz
LO : Longitudinal optical (phonons)
TO : Transversal optical (phonons)
PL : Photoluminescence
XRD : X-ray diffraction

Contents

1 Introduction

Studies conducted in recent years have shown that humankind is facing an era of climate change, consequence of human activity, and that the contemporary way of life is not sustainable for our society [1, 2, 3, 4]. This climate change implies an overhaul and a rethinking of our lifestyles, especially in terms of energy consumption and production. The political choices intrinsic to each country concerning their choice of energy mix have an extremely important part in the current public debates [5]. In order to best face this problem that concerns the whole of humankind as well as biodiversity [6], a precise understanding of the different types of energy that can be envisaged is necessary. This thesis focuses on photovoltaic renewable energy, generated from solar panels and particularly on the interaction between solar radiation and the semiconductor materials used for these panels. In this work, we deal with a new class of innovative material for photovoltaics, called lead halide perovskites (LHPs). We focus on the understanding and control of some fundamental properties, such as light propagation, coherent phonons excitations, charge carriers dynamics (electrons and holes). This chapter serves as a brief introduction to the understanding of the current global energy mix. Solar photovoltaic energy and the main devices currently on the market are then presented. Later, a general description of perovskites allows the reader to understand the structure of this material as well as the main scientific questions it raises. Finally, we define the motivations of this thesis and the scientific approach chosen for its implementation.

1.0.1 Climate change and energy transition: towards solar energy?

The awareness of global warming and its human origin appeared at the end of the 20th century, in particular with the Meadows report [1] and the first Intergovernmental Panel on Climate Change (IPCC) report [7], which proved that the increase of greenhouse gases concentration in the atmosphere originates for a significant part from emissions related to human activities as well as the importance of public policies to limit the increase in the Earth's temperature.

Indeed, states can choose the energy orientation of their country, via lowering the rate of energy consumption [8] but also the choice of the energy mix, i.e. the distribution of the various

primary energies (nuclear, gas, coal, solar, wind, hydraulic, biomass...) in the production of directly usable energy such as electricity or heat. Fig. 1.1.a shows the evolution of the global primary energy consumption by energy source, from 1800 to 2018 [9]. The graph shows the drastic evolution of worldwide energy consumption in less than two centuries, following the industrial revolution. It also highlights the importance of energy consumption from fossil sources, such as coal, oil and gas, which are non-renewable energy on a human scale and above all very emitting of green house gases (carbon dioxide CO_2, methane CH_4 and others) [10]. If we focus only on the carbon footprint, it is obvious that fossil fuels have a much higher emission impact than renewable and hydroelectric energies, as shown on Fig. 1.1.b. Among them, solar energy has a relatively low carbon footprint and therefore could be considered as an interesting energy source for energy transition, although it should also consider the pollution generated by the extraction of metals [11], the recycling [12, 13] and the geopolitical interests involved [11, 14]. The decrease in the price per Watt associated with photovoltaics also makes it an increasingly affordable energy source, going from \$76/Watt to \$0.36/Watt from 1977 to 2014 in the case of silicon photovoltaic cells [15]. But its greatest advantage is probably that it relies on an infinite source of energy on a human scale, the sun.

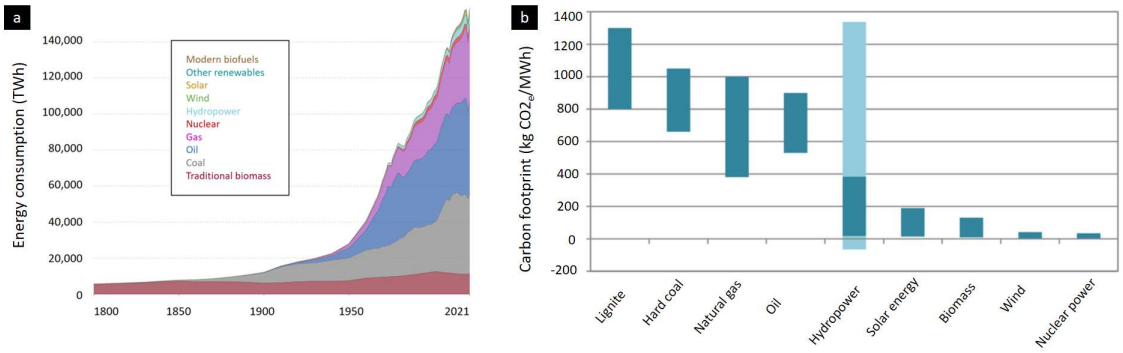

Figure 1.1: (a) Worldwide evolution of the global primary energy consumption by energy source, from 1800 to 2018. Nowadays, gas, oil and coal, are the main sources of energy used. Extracted from [9]. (b) Estimation of carbon foot print emission in fonction of the energy sources and error bar on the hydroprower energy source, extracted from [16].

Estimation of finite and renewable planetary energy ressources in Terawatt/years in 2009 are represented on Fig. 1.2, where solar remains the largest resource by far. Even when pushing economically acceptable fossil sources to their current limit, the global picture is basically unchanged, especially by considering that the threshold for economic viability will be lowered by environmental pressure. Thus, solar energy and in particular the energy produced through photovoltaic panels seems to be one of the most interesting alternatives in terms of sustainability ratio, price and environmental impact.

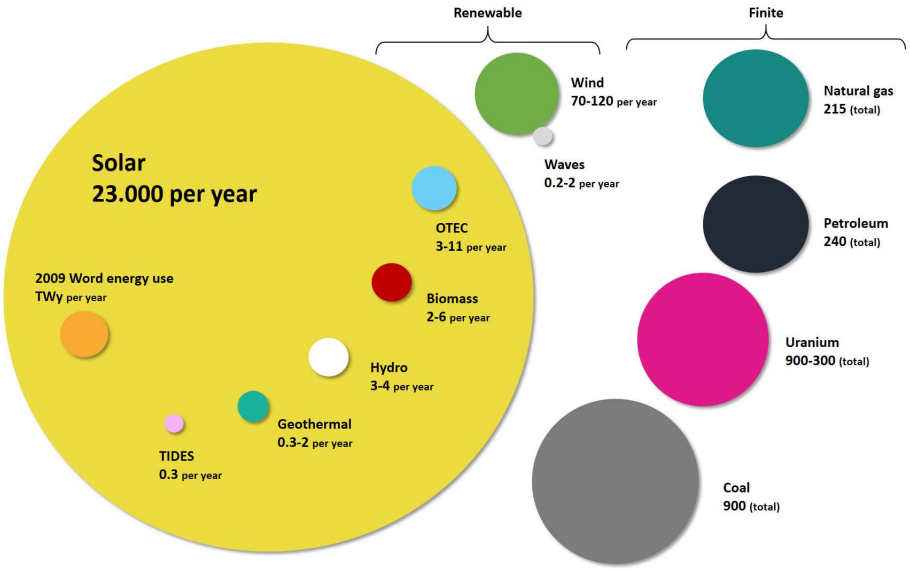

Figure 1.2: Estimation of finite and renewable planetary energy reserves in Terawatt/year, in 2009. Total recoverable reserves are shown for the finite resources, while yearly potential is shown for the renewables. Adapted from [17].

1.0.2 Photovoltaic solar cells

Physical principles of a solar Cell

The goal of photovoltaic is to generate electric power by using solar cells, composed of at least one semiconductor active layer, to convert energy from the sun light into a flow of electrons (electric current) by the photovoltaic effect [18]. The later is really closed to the photoelectric effect as for both, light is absorbed by the semiconductor active layer, causing excitation of an electron above the bandgap E_g of the semiconductor. The photovoltaic effect differs from the photoelectric effect in the sense that the electron is not ejected out of the material but is contained within.

When designing a solar cell, it is important to do everything to hinder as much as possible the charges (electrons and holes) recombination in the semiconductor active layer in order to extract the maximum of current and improve the solar cell performance. To fulfill this charge separation, the active layer is surrounded by several diverse material with different energy potential. Knowing that the electrons tend to go where the potential energy is lowest, a material with an active layer is used to capture the electrons: it is the electron transport material (ETM). The opposite principle will take place for the holes, which will be attracted to the hole transport material (HTM) having a valence band higher in energy than the one of the active layer, as shown on Fig. 1.3.

In order to be efficient, a solar cell should absorb a large fraction of the solar spectrum, minimize the amount of photon energy that is converted in heat and guaranty an optimal

collection of charge carriers at the electrodes. Understanding and controlling each one of these processes is a fundamental topic in photovoltaic science [19]. The processes leading to light energy harvesting span many different timescales can be summarized in steps: (1) Photon with energy $E_{ph} > E_g$ are absorbed by the active layer, generating electron-hole pair. Electron is excited in the conduction band, the hole in the valence band (2) Generated electron-hole pair recombine and release energy in the form of photons or result in lattice vibrations (phonons). To extract useful work out of the generated electron-hole pair, they need to be separated and not recombine with each other or get trapped. These processes are discussed in details in Chapter.2. (3) To avoid recombination, electron and hole selective interfaces are placed on the sides of the active layer, aiming to separate the generated electron-hole pair. (4) The energy stored in the separated electrons and holes is used by passing through an external electric circuit.

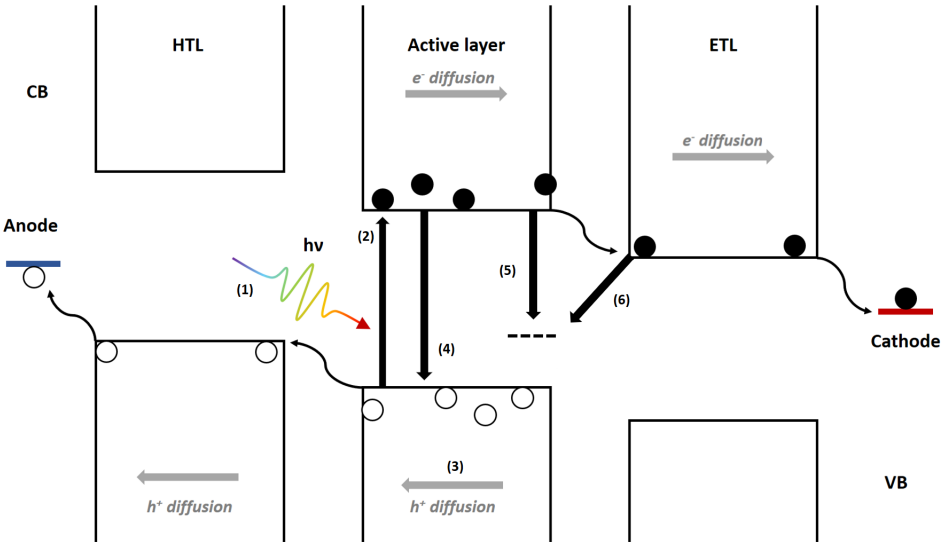

Figure 1.3: Principle of a single junction solar cell. (1) Photon absorption and (2) generation of free charge carriers (electron and holes) in the conduction (CB) and valence band (VB), respectively. (3) Charge carriers diffusion. Different charge recombination source: (4) Radiative recombination, (5) Trap-assisted or grain boundaries recombination, (6) interfacial recombination.

Single junction solar cell architectures

Several single junction solar cell architecture exist, as shown on Fig. 1.4.a. A $p-i-n$ or a $n-i-p$ junction refer to undoped intrinsic semiconductor i region between a p-type semiconductor (positively doped, with larger hole concentration than electron concentration) and an n-type semiconductor (negatively doped) region. The mesoscopic $n-i-p$ structure shown is the original architecture of the perovskite photovoltaic devices and is still widely used to fabricate high-performance devices [20]. The main advantages of the mesoscopic

architecture compared to the planar one is to drastically enhance the interaction surface between the active layer and the ETM. The larger the surface area, the more electrons have the probability to pass in the ETM material and to be separated from holes.

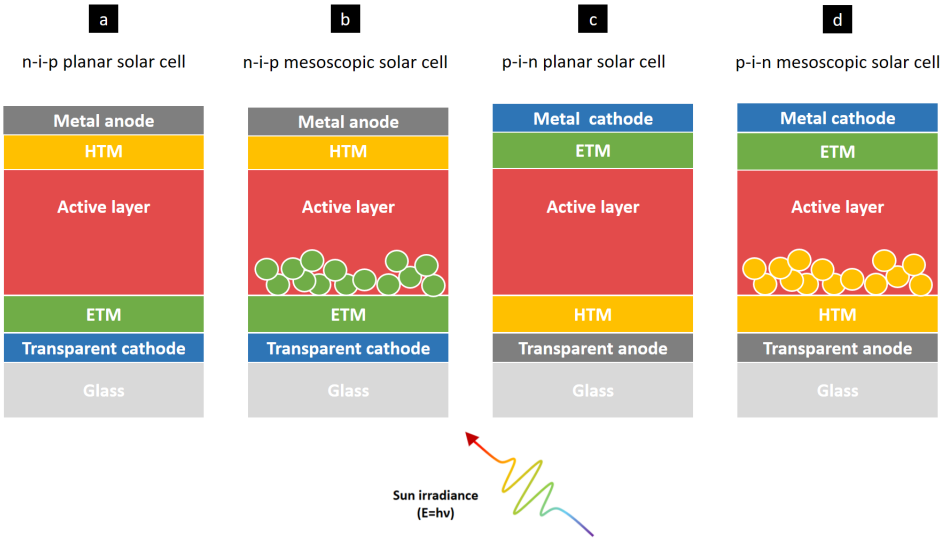

Figure 1.4: Different architectures of single junction solar cell with n-i-p junction (a,b) and p-i-n ones (c,d). (b,d) Mesoscopic structure enhances the interaction surface between active layer and ETL.

Key role of the semiconductor active layer

As discussed previously, the choice of the semiconductor active layer is highly important, as the solar cell performance relies heavily on its ability to absorb and separate charges as much as possible in order to generate the maximum amount of electrical power. In the case of a single junction solar cell, the maximum theoretical efficiency of a solar cell using a single p-n junction to collect power is constrained by the Shockley-Queisser limit was calculated to be 33.7% of efficiency with an ideal band gap of 1.34 eV, represented in yellow on Fig. 1.5. The efficiency of the solar cell strongly relies on the absorption properties of the chosen active layer and therefore on its band gap E_g. Indeed, if the band gap E_g is to high, photons are more difficult to absorb (Fig. 1.5, red). If the active layer material band gap is too small, the photogenerated carriers has low energy and relax more easily to the conduction and valence band edges. This mechanism induce thermal losses and a lower voltage ((Fig. 1.5, blue). Therefore, band gap engineering and choice is a key step in the choice of active layer for solar cell. Band gap engineering is one the numerous advantages of LHPs material.

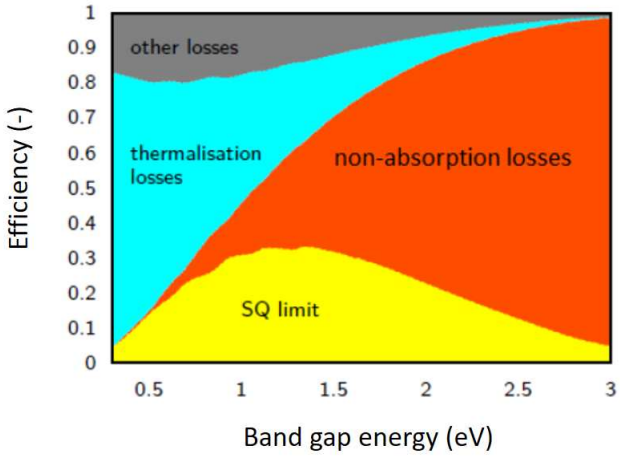

Figure 1.5: Diagramm representing the efficiency of a single junction solar cell as a function of the band gap energy of the active layer. Schokley-Quiesser limit (yellow), thermalisation losses originating from low band gap (blue), non-absorption losses due to high band gap (red) and other losses (grey). Extracted from [21]

Photovoltaics emergence and categories

Many types of active layers are used in solar cells. First of all, it is necessary to differentiate two main types of solar cells: the single junction that we have discussed previously and which are limited by the Schokley-Queisser limit and the multijunction solar cells. These latter are solar cells with multiple p–n junctions made of different semiconductor materials. Each material's p-n junction produces electric current in response to a particular wavelengths of light. Multijunction solar cell allows the absorbance of a broader range of wavelengths, improving its global electrical energy conversion efficiency. In this work, we only focus on single junction solar cell (Chapter.7.3).

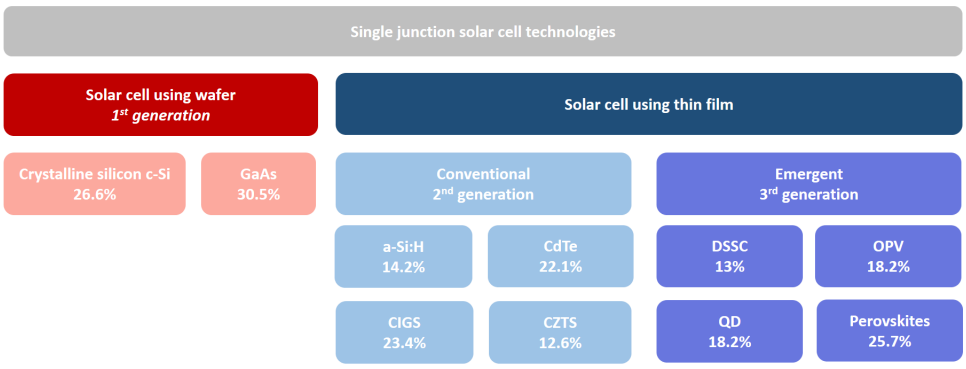

Figure 1.6: Single junction generations and maximum efficiency.

Fig. 1.6 shows the different generations of solar cells by, separating 1^{st} generation using wafer

to 2^{nd} and 3^{rd} generations using solution printed thin films, including perovskite solar cells. The term perovskite in photovoltaic application refers particularly to LHPs. This material has been used in a single junction solar cell for the first time in 2009 [22] and yet the efficiency of solar cells using it as an active layer has allowed them to compete with silicon single junction. This material has since interested the community enormously, notably for its many intriguing and interesting properties, described in Chapter.3. Indeed, perovskite solar cells are a favorable candidate for next-generation solar systems with efficiencies comparable to Si photovoltaics [23], but their long-term stability must be improved to commercialization and some of their fundamental properties still need clear explanation. Fig. 1.7 shows the solar cell efficiency throughout the years and the skyrocket increase of perovskite single junction solar cell's efficiency are represented (yellow dot surrounded by red, purple triangle surrounded by red).

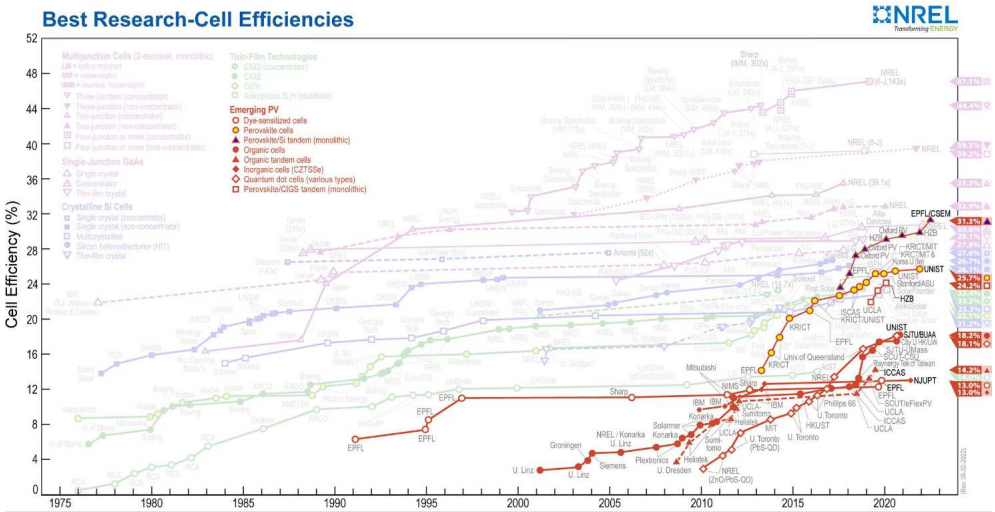

Figure 1.7: Best Research-Cell Efficiencies chart 2018 by the National Renewable Energy Laboratory [24].

1.1 Perovskites: from discovery to solar cell active layer

1.1.1 Discovery and perovskite structure

German mineralogist Gustav Rose discovered the $CaTiO_3$ mineral structure in the Ural Mountains during the 19th century and named it after the Russian mineralogist Lev Perovski. Since, the name *perovskite* is applied to all materials of empirical formula ABX_3 bearing the same atomic arrangement as $CaTiO_3$, as shown on Fig. 1.8. The ideal perovskite structure is the cubic structure, that belongs to the space group $Pm-3m$.

The stability of the perovskite structure has been described by Goldschmidt with respect to

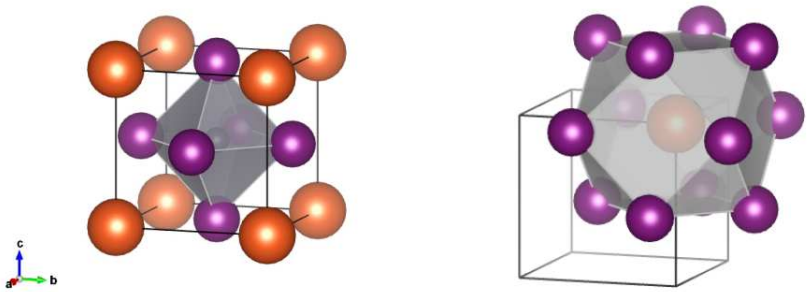

Figure 1.8: Perovskite structure representation: octahedral representation (left) and cuboctahedral representation (right). ABX_3: A in orange, B in grey and X in purple. Extracted from [25]

the ionic radii of its components.The ideal ratio that allows perfect ionic coordination is:

$$t = \frac{r_A + r_X}{\sqrt{2}r_B + r_X} \tag{1.1}$$

with r_A, r_B and r_X are the effective radii of the cations A and B as well as anions X, respectively. The ideal cubic structure is formed when the tolerance factor t is equal to 1, with no octahedral tilting or distortion in the ground state structure at 0 K. [26]. Small deviations (t comprised between 0.8 and 1.1) are tolerated within which the typical perovskite ionic coordination is conserved. However, these deviations determine the lowering of symmetry to tetragonal, orthorhombic or monoclinic type of unit cells due to the tilting of the BX_6 octahedra. One of the goal of this thesis is to dynamically control these tilting angles on ultrafast time scales. Undersized A-cations result in tilted octahedral structures ($t < 1$), while oversized A-site cations ($t > 1$) can lead to ferroelectric distorted structures with a B-site cation off-center displacement [27, 28, 29, 30].

One of the main advantages of metal halide perovskites is the possibility to play with the chemical composition of all the cation and anion-sites. This induces a modification of the material band gap E_g, as well as structural and other optoelectronic properties. The metal halide perovskites can therefore meet a multitude of needs by changing only their chemical composition. The first perovskite active layer used for solar cell application was the hybrid lead halide perovskite $MAPbI_3$ [22], with only one A-site organic cation and X-site halide anion. Many other chemical compositions were subsequently tried. The main elements and molecules usually used for photovoltaic applications are shown on Fig. 1.9 and can be listed as follow: (i) Methylammonium (MA), Formamidinium (FA), Guanidinium (GA) and Cesium (Cs) in the A-site cation ;(ii) Lead (Pb) or Tin (Sn) in the B-site cation; (iii) Iodine (I), Bromide (Br) or Chloride (Cl) in the X-site halide anion [31]. The advantages and disadvantages of these components are actively investigated in Chapter.3, especially in the case of the study of perovskite with quadruple A-site cation.

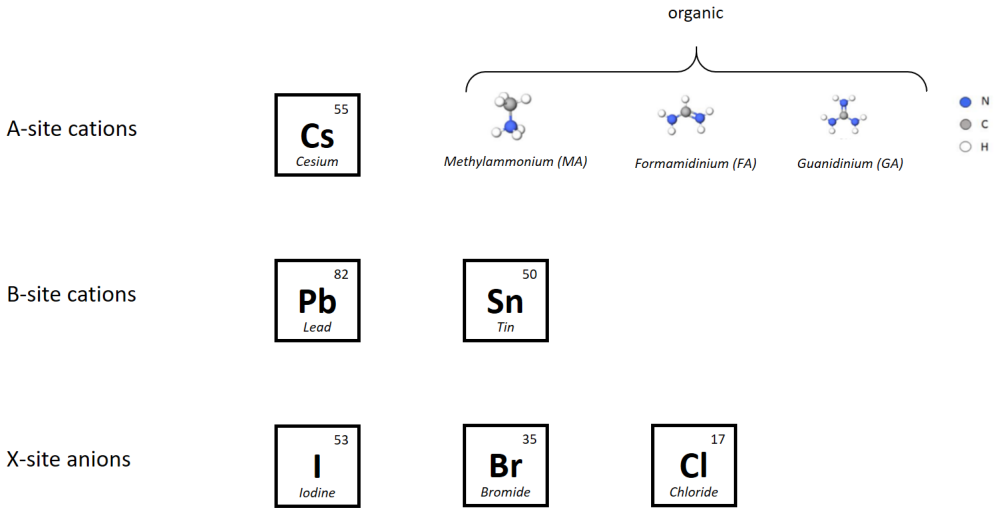

Figure 1.9: Main A-site and B-site cations as well as X-site anions used metal halide perovskites chemical composition.

1.1.2 Intriguing properties of metal halide perovskites

Metal halide perovskite-based solar cell stands out in particular thanks to their easy fabrication. Indeed, high-quality thin films and single crystals can be fabricated by simple chemical solution processes due to apparent defect tolerance [32]. This opens the possibility to integrate perovskite processing into an industrial roll-to-roll fabrication process, allowing scalable mass production at low cost. This metal halide perovskite technology can thus allow the elaboration of rigid but also flexible solar panels, increasing considerably the possibilities of commercial applications. Furthermore, solar applications are not limited to single junction solar cells anymore: the chemical tuning of the material bandgap E_g makes it especially interesting for application in multijunction, also known as tandem solar cells.

The chemical instability noticed in the first $MAPbI_3$ type perovskites can be improved by playing on the chemical composition but also by using metal halide perovskites of different dimensions in the design of solar panels [32]. Many dimensions of perovskites have been studied lately, from 3D bulk to 0D, through 2D and 1D. Playing on chemical composition and material dimension can drastically enhance the stability of the metal halide perovskite, particularly sensitive to water.

These semiconducting materials also exhibit many useful and interesting optoelectronic properties, including large absorption coefficient, intense photoluminescence, low or high exciton binding energies E_B in 3D or 0D/1D/2D respectively [33]. Quantum confinement is particularly high in the later low dimension perovskites [34]. Metal halide perovskites also demonstrate high dielectric constants, long carriers diffusion length L_D and despite this, low mobility μ. Low nonradiative recombination rates of the photogenerated carriers are

also observed, which is essential to achieve respectable lifetimes and diffusion lengths, and therefore high solar cell efficiency. [35, 36]

Interestingly, metal halide perovskites possess a combination of high-quality average structural order and defect tolerance with significant dynamic disorder [37]. A-site cation in hybrid and all-inorganic halide perovskite is dynamically disordered at room temperature [38, 39] while large amplitude displacement and dynamic disorder of the lead-halide Pb-X sublattice is observed at room temperature. [39, 40] One hypothesis is that the highly polar and anharmonic lattice of metal halide perovskites influences their optoelectronic properties through dynamic charge carrier screening. These materials also show intrinsic local ferroelectric polarization as well as high spin-orbit coupling in the case of LHPs [41, 42, 43], which could lead to the appearance of Rashba-splitting.

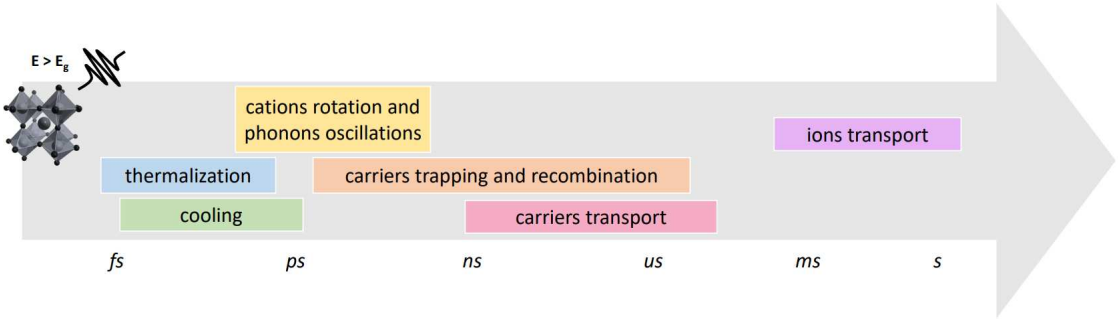

Figure 1.10: Timeline of ultrafast and other process occuring in lead halides perovskites and studied in this research work.

The origin of dynamics in LHPs, and in particular the ultrafast dynamics of electrons and lattice vibration, are still much debated. The understanding of these phenomena is however fundamental for the improvement and optimization of devices using LHPs. It is necessary to use spectroscopic tools that can scan all the timescales of these processes, in particular the ultrafast dynamics (femto to picoseconds) as well as the relatively slower dynamics (nanoseconds to microseconds), as depicted on Fig. 1.10.

1.2 Thesis motivation and approach

1.2.1 Scientific objectives

One of the main goals of contemporary research about LHPs is the understanding of correlation between their macroscopic properties and their internal microscopic dynamics. This work focuses on a precise study of MHPs, and particularly of its most interesting forms for applications, namely in 3D form (bulk single crystal, thin films) but also in 2D form, as well as by modifying the chemical composition of the A-site cation. Absolute advanced techniques are needed to study the ultrafast lattice and charge-carrier dynamics in these materials. We

propose to used ultrafast spectroscopy techniques on the order of femto- (10^{-15} s) and picoseconds (10^{-12} s) to measure and understand these properties. More specifically, we will focus on the following key questions, also resumed on Fig. 1.11 :

- Is the dominating lattice polarizability which allows for charge carrier screening on sub-ps (= THz) time scales What is their level of involvement in charge screening?
- Does the large tolerance of hybrid perovksites to the electron trapping originates from organic cation screening?
- Does the Rashba coupling exist and can it be observed directly by following the conduction band dynamics?
- What is the impact of A-site cation tuning for radiative recombination, charge relaxation and device stability?

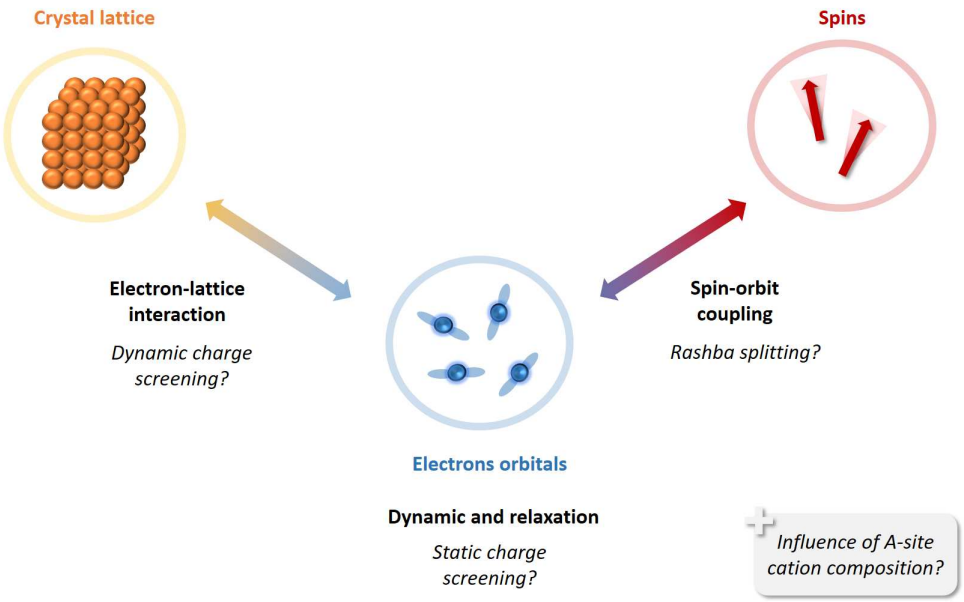

Figure 1.11: Main subsystems and parameters studied in this research work.

These questions lead us to study with the help of ultrafast excitation techniques taking place at equivalent or different time scales, explicited on Fig. 1.10. In a first part, we use Kerr effect spectroscopy to gain new insights into the fundamental mechanisms of lattice-electron coupling and coherent phonon polarizability, using optical (OKE) (Chapter 6.1) then Terahertz (TKE) pumping source (Chapter 6.2, Chapter 6.3). Second, we will use time- and angle-resolved photoemission (tr-ARPES) (Chapter 7.1) to characterize electron dynamics in different types of lead halide perovskites, such as $MAPbI_3$ (Chapter 7.1), 2D (Buthylammonium)-$MAPbI_3$ (Chapter 7.2) and high performance quadruple A-site cation perovskites (7.3). A theoretical

part allows the readers to follow the basics of all the notions necessary to the good understanding of the mechanisms put in play and discussed (Chapter 2). The experimental techniques used are explained in Chapter 4 for Kerr effect spectroscopy and Chapter 5 for time-resolved ARPES.

1.2.2 Experimental organisation

This work is the result of multiple collaborations. First of all, this thesis is carried out in co-direction between the Ecole polytechnique and the Fritz Haber Institute of the Max Planck Society. TKE experiments were performed under the supervision of Dr. Sebastian Maehrlein at the Fritz Haber Institute of the Max Planck Society (Germany), in the department of Prof. Martin Wolf. Time-resolved ARPES experiments were performed at Ecole polytechnique and Synchrotron Soleil under the supervision of Prof. Luca Perfetti. The work concerning the OKE spectroscopy was done during a research stay at Columbia University (USA), under the direction of Prof. Xiaoyang Zhu, lead by Sebastian Maehrlein. Numerous collaborations have been realized for the elaboration of the samples and for some characterizations, notably with Prof. Sanjay Mathur group of University of Cologne (Germany), Prof. Xiaoyang Zhu group from Columbia University (USA), Prof. Emmanuelle Deleporte group of ENS Paris-Saclay (France) and from Prof. Kaibo Zheng group from the Technical University of Denmark (Denmark).

2 Theoretical background

This research works aim to understand numerous and different interactions in LHPs. A brief introduction of the main physical concepts particularly charge recombination in semiconductors, electron-phonon interaction, Rashba splitting and light-matter interactions are discussed in this section.

2.1 Charges recombination in semiconductors

This section describes charge generation in LHPs materials and in their electronic band structure, as well as the following recombination and relaxation dynamics.

2.1.1 Photogenerated charge carriers and early-time relaxation dynamics

A semiconductor material absorbing a photon with an energy $h\nu$ equal or superior to its own electronic band gap creates electron-hole pairs [44]. The excited photogenerated electrons are located in the conduction band, while the holes are located in the valence band.

Then in the early stage after photogeneration, the charge-carrier distribution is out of equilibrium and subsequently relaxes through different processes towards the band edge (conduction band minimum in the case of electrons). Carrier relaxation mechanisms in LHPs follow the main steps as in typical semiconductors such as GaAs.

Loss of coherence

In the case of excitation with coherent laser system, the photoexcited electron-hole pairs might initially have a fixed phase relationship or coherence between excited states wavefunctions and the laser pulse. This coherence is lost typically on the femtosecond scale through scattering events, such as electron-phonon interaction or other charge carriers. [45]

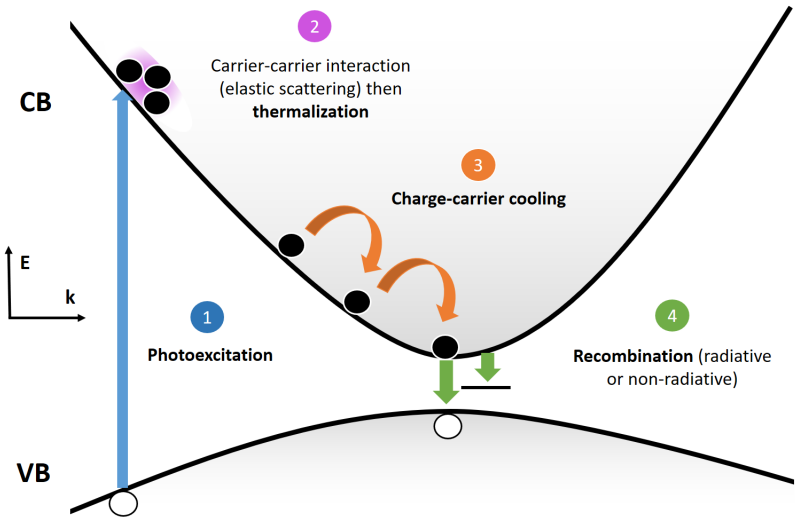

Figure 2.1: Early-ime relaxation dynamics after photoexcitation.

Charge-carrier thermalization

The nonresonnant photoexcitation originating from the incoming photon immediately leads to a nonthermal charge-carrier distribution in the material. In less or equal to picoseconds, the nonequilibrium distribution of charge carriers relaxes within the electronic bands through carrier scattering. They establish a thermalized Maxwell-Boltzmann distribution, which is characterized by the carrier temperature T_c. [45]

Charge-carrier cooling

The carriers are described as hot when the charge-carrier temperature T_c is higher than the lattice temperature T_L. Carrier cooling mechanism is established through interactions with the lattice. A primary and fast carrier-cooling rate takes place during interactions between longitudinal optical (LO) phonons, which are modes of the inorganic sublattice in the case of LHPs [46, 47]. A subsequent and slower cooling originates from thermal equilibrium being reestablished between longitudinal optical phonons and acoustic phonons. For elevated excited charge carriers density, longitudinal optical phonon modes may increase their population way more effectively than accoustic modes. This leads to significant phonon bottleneck, keeping charge carriers hot for an extended time period [48]. In LHPs, the hot-phonon bottleneck effect prolongates the cooling period of hot charge carriers. The cooling time generally occurs on the picosecond timescale. A thorough understanding of the charge-carrier cooling is extremely important in the context of photovoltaics as hot charge carriers can be harvested at the charge-extracting contacts of the solar cells, improving their efficiency.

Band gap renormalization (BGR) and Burstein-Moss state filling

In the case of high carrier density, charge-carrier dynamics are highly influenced by many-body and state-filling effects. The band-gap renormalization (BGR) leads to a red shift of the band edge and originates from the Pauli principles which prevents fermions (such as electrons) with identical spin from occupying the same state and the Coulombic repulsion which maximizes the distance between charges. Lowering or red shift of the band-gap energy is the signature of this resulting energy minimization [49]. In contrast, state-filling Burstein-Moss effect [50, 51, 52] leads to a blue shift of the band gap due to the finite density of states available for fermionic occupation.

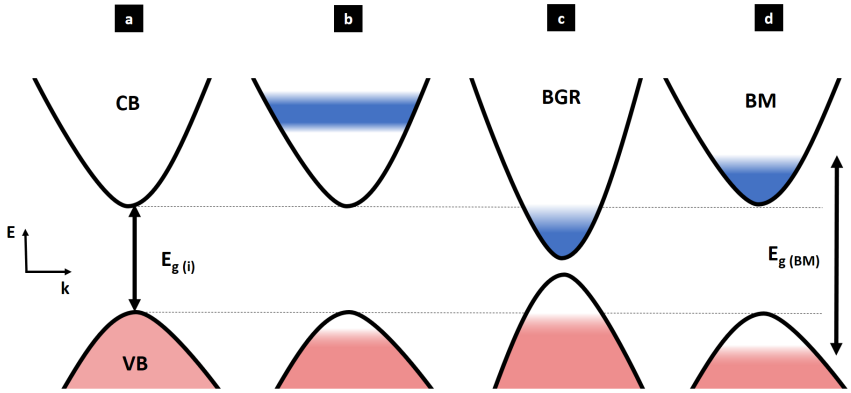

Figure 2.2: (a) Semiconductors bands in the steady states. (b) After photoexcitation of the charge carriers, the CB fills up while VB extrema decreases. (c) Band gap renormalisation (BGR) takes place just after photoexcitaion, before that electrons and holes have cooled down to the band extrema. (d) When the carriers density n increase considerably, smallest energy for an optical transition increases and a Burstein-Moss effect (BM) gives rise to a new ephemeral band gap $E_{g(BM)}$.

2.1.2 Charge-carrier recombinations

Charge-carrier recombination mechanisms highly impact electronic device performance such as solar cells. In photovoltaic cell, charge-carrier lifetime limits the charge extraction [53]. Decay of free-charge-carrier density $n(t)$ can be expressed with the Shockley-Read-Hall (SRH) model equation, taking into account three contributing mechanism:

$$\frac{dn}{dt} = -k_3 n^3 - k_2 n^2 - k_1 n \tag{2.1}$$

with k_1, k_2, k_2 the rate constant of monomolecular (or trap-assisted), bimolecular and Auger recombination respectively.

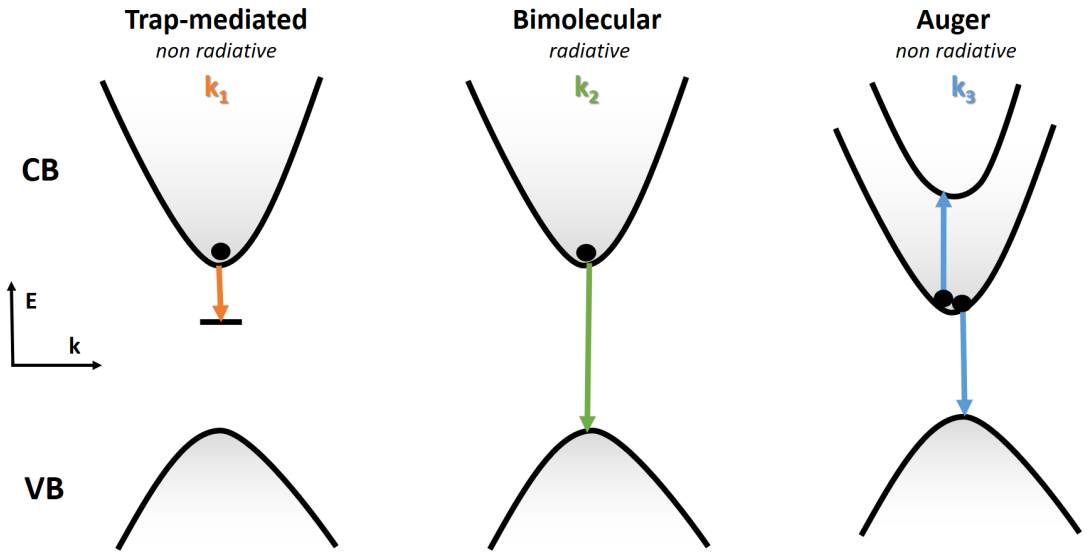

Figure 2.3: Schematic representation of the three charge-carrier recombination mechanism.

Monomolecular or non-radiative trap-assisted recombination

Monomolecular or non-radiative trap-assisted recombination (k_1) describes an individual carrier (electron or hole) recombining via in a trap.

Bimolecular or radiative recombination

Bimolecular or radiative recombination (k_2) depends on both electron and hole densities which lead to $n_e n_h = n^2$ for photoexcitation. This process results from the recombination of an electron in the conduction band with a valence band hole, resulting in the emission of a photon at the bandgap energy E_g. This radiative recombination sets a fundamental intrinsic limit to charge-carrier diffusion length in material, once trap-assisted recombination process have been eleminated.

Auger recombination

Auger recombination is a non-radiative many-body process in which electron and hole recombine and when the energy of the photogenerated carrier is dissipated not by photon emission, but rather by increasing the kinetic energy of another free carrier.

Recombination mechanism and charge-carrier diffusion length

The three recombination mechanisms form the total recombination rate $r(n,t)$ which influences the charge-carrier diffusion length L_D [53, 44]:

$$r(n) = k_3 n^2 + k_2 n + k_1 \tag{2.2}$$

$$L_D(n) = \sqrt{\frac{\mu k_b T}{r(n) e}} \tag{2.3}$$

with μ the charge-carrier mobility, T the temperature, k_B the Boltzmann constant and e the elementary charge.

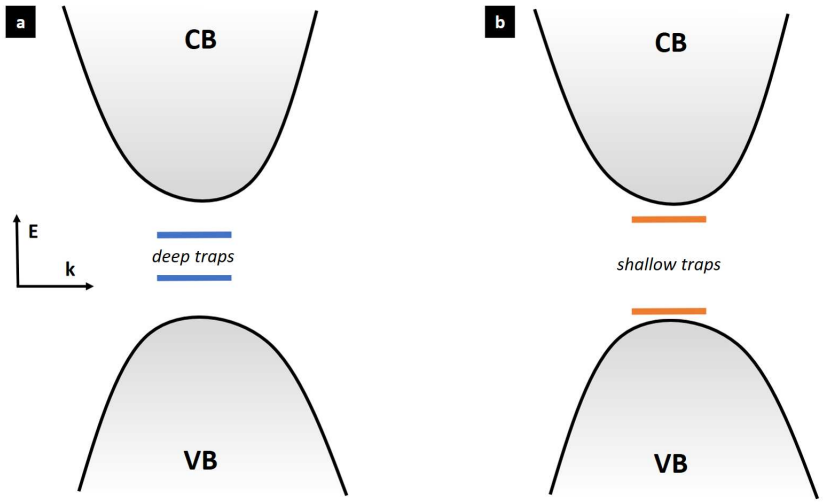

Figure 2.4: Shallow versus deep trap, adapted from [54, 55]. These terms refer to the binding energy of the defect or its energy level within the bandgap: shallow defects are near a band edge (not as recombination-active), while deep defects are in the middle of the gap. (a) A deep defect is detrimental to carrier lifetime, (b) in contrary to shallow defect, which can affect mobility but have little impact on electron-hole recombination.

Free electrons can experience slightly different radiative recombination, depending on the presence of a direct or indirect band gap in the material. A process of splitting of the conduction and valence bands called Rashba splitting can also occur.

2.2 Electron-lattice interaction

2.2.1 Coherent phonons and anharmonicity

The atoms of a crystal lattice are far from being immobile, they vibrate. These vibrations are quantified and the quantum of energy associated is called phonon. The phonons can be described as collective excitations of the lattice displacement. Lattice vibrations in crystals underpin a large number of material properties, such as the volumetric and constant-pressure heat capacities, the Helmholtz and Gibbs free energies and the thermal conductivity. Furthermore, they also provide important spectral signatures as the infrared-active (IR) and Raman-active modes, that are often used as routine identification and characterisation tools. Phonon modes are also a key part of describing physical phenomena such as superconductivity, ferroelectric phase transitions that play a critical role in the performance of emerging functional materials.

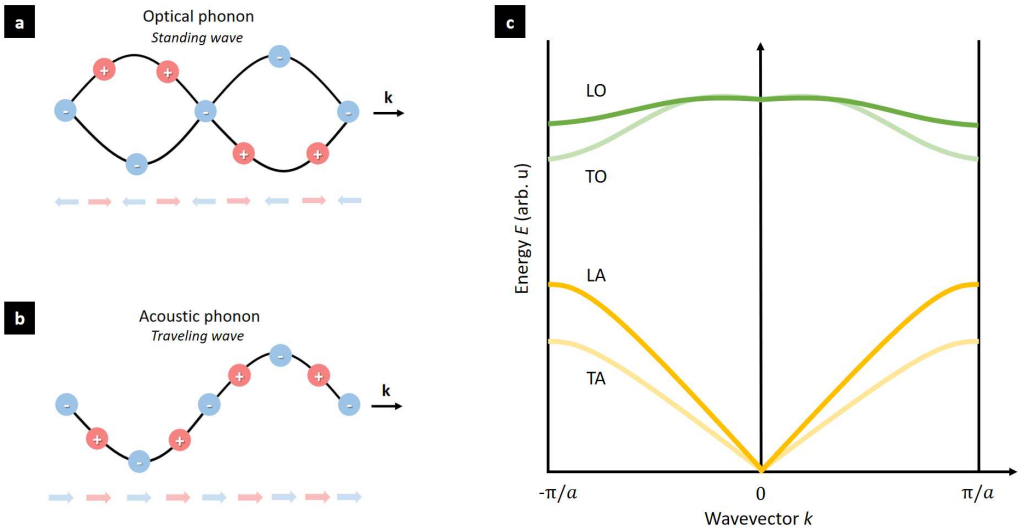

Figure 2.5: Atoms vibration in the case of (a) optical and (b) acoustic phonons. (c) Dispersion relationship for a diatomic crystal.

The lowest frequency modes are called the acoustic phonones. They describe vibrations whose frequency varies linearly in q in the limit of long wavelengths ($q \rightarrow 0$). The other one and describing the highest frequency modes is called optical phonons. These branches describe vibrations having frequencies which do not cancel for long wavelengths. Atomic vibration and travelling wave of optical and acoustic phonon are represented in Fig. 2.5.a and Fig. 2.5.b, respectively. Fig. 2.5.c represents the theorical dispersion relationship in diatomic crystal. In general, acoustic and optical modes can be represented on the first Brillouin zone. Both optical and acoustic phonons can have transverse (TO and TA, respectively) or longitudinal modes (LO and LA, respectively).

Lattices are able to form in-phase oscillations along a certain direction of the crystal and keep this coherent motion on a macroscopic length scale. In other words, the excited phonon is coherent, meaning the atomic motion is phase-locked across the entire photo-excited area and that the atoms move back and forth in perfect synchrony. This leads to correlations between the quantum phonon states and lead to a non-vanishing classical amplitude $Q(t)$. Amplitude $Q(t)$ can be used in the damped harmonic oscillator picture with and external driving force F. The isolated motion of the coherent phonon along a normal coordinate is described by the equation of motion:

$$\frac{\partial Q(t)}{\partial t^2} + 2\gamma \frac{\partial Q(t)}{\partial t} + \omega^2 Q(t) = \frac{F(t)}{m^*} \tag{2.4}$$

with γ the oscillator damping constant, m^* the reduced mass and ω the phonon eigenfrequency. The harmonic approximation is based on the assumption that the atoms do not move very far away from their local minimum at equilibrium and that a second order expansion of the energy around the minimum is sufficient to describe atomic vibrations. Therefore, the harmonic approximation breaks down when the atoms move significantly far away from equilibrium and higher-order terms need to be considered, i.e in the case of anharmonicity.

Different kind of driving force F are discussed in Section. 2.4.4, including the direct ones such as resonant electric field coupling to IR-active optical phonons and the indirect ones such as Raman excitations, mediated by electron-phonon coupling and the polarizability we will discuss later in Section.2.4. The driving force can also originate from the coupling to other excited phonons. This phonon-phonon coupling necessarly needs anharmonic potentials.

2.2.2 Polaron and Fröhlich interaction

An electron moving in a periodical potential of a rigid crystal moves as a free electron but has an effective mass different from the one in the vacuum. As previously discussed, the crystal lattice is deformable and the displacements of the atoms from their equilibrium positions are described in terms of phonons.The moving electrons interact with the atoms displacements, leading to electron-phonon coupling. In 1933, Lev Landau proposed a first approach of the polaron definition, considering an electron trapped in a defect of the crystal lattice. Later, Solomon Pekar proposed that the electron was dressed with the lattice polarization, which could be described as a cloud of virtual polar phonons. Such an electron could still propagate freely across the crystal but with an higher effective mass. These different visions lead to the final definition of a polaron: a quasiparticle used to understand the interactions between electrons and atoms in a solid and which can be described as a moving charge in a dielectric crystal where atoms displacement from their equilibrium positions screen the charge-carrier and known as a phonon cloud. The generation of a polaron is explained by the fact that a charge placed in a polarizable medium will be screened and can be describe through the dielectric theory by the creation of a polarization around the charge carrier. The induced polarization follows the moving charge on its path in the medium and they can be described

as one physical entity, the polaron. Electrons are not the only particle that could lead to a polaron, any other charged particle allowed to interact with a phonon can.

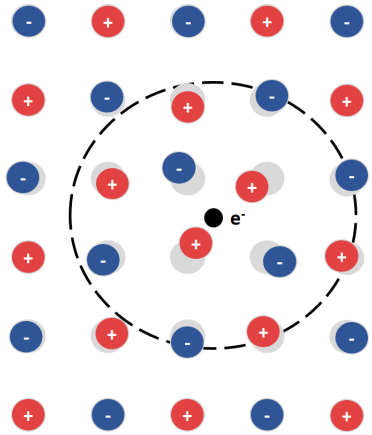

Figure 2.6: Sketch representing polaron formation from interaction between a charge carrier (here an electron) and the ionic lattice of the crystal.

Usually, in covalent semiconductors the couplings of electrons with lattice deformation is weak and the formation of polarons does not occur. In polar semiconductors the electrostatic interaction with induced polarization is strong and polarons are formed at low temperature. Another class of materials where polarons are observed are molecular crystals, where the interaction with molecular vibrations may be strong. In the case of polar semiconductors the interaction with polar LO phonons is described by the Fröhlich Hamiltonian. Nevertheless, Fröhlich picture is too simplified in case of anharmonic phonon-phonon coupling, as later discussed in Section.3.4.

The strength of electron-phonon interaction is determined by the dimensionless coupling constant α_{e-ph} on Table.2.1 [56, 57, 58]:

Material	α_{e-ph}
GaAs	0.068
CdTe	0.29
$MAPbBr_3$	1.54
$CsPbBr_3$	2.64
$SrTiO_3$	3.77

Table 2.1: Electron-phonon coupling constant in different materials.

2.3 Rashba splitting

2.3.1 Spin-orbit coupling (SOC)

Spin-orbit coupling or also called spin-orbit interaction, is described in quantum physics as a relativistic interaction of a particle's spin with its motion inside a potential. A crystalline solid, such as a semiconductor, can be characterized by its band structure. In the overall scale, including the core levels, the spin-orbit coupling is a small perturbation. Nevertheless, it plays a relatively important role in the bands close to the Fermi level, i.e the conduction and valence band. The atomic spin-orbit interaction can induce a band splitting of states which would be otherwise degenerate if the crystal or an interface lacks inversion symmetry. This mechanism gives rise to Rashba splitting in the conduction and valence band of a solid system.

2.3.2 General description of Rashba effect

Basic principles

Rashba effect is a spin degeneracy lift originating from spin-orbit coupling (SOC) under inversion symnetry breaking. More precisely, it is a momentum-dependent splitting of spin-polarized bands in bulk crystals and low-dimensional condensed matter systems, such as heterostructures and surface states. The splitting is a combined effect of spin–orbit interaction and asymmetry of the crystal potential (i.e inversion symmetry breaking), in particular in the direction perpendicular to the two-dimensional plane. This effect is named in honour of Emmanuel Rashba, who discovered and explained it using group theory in 1959 [59] for three-dimensional systems and afterward with Yurii A. Bychkov in 1984 for two-dimensional systems [60, 61, 62]. Perdew et al. proposed recently a local explanation of Rashba-Dresselhaus effect [63]. Spin splitting occuring in Rashba effect may have various consequences on the solid-state systems and is particularly interesting for spintronics application [64, 65]. In photovoltaic applications, spin splitting can also have a high impact on the absorption as well as on transport properties of the materials. Indeed, the presence of spin and angular momentum forbidden transitions can slow down or even cancel electron-hole recombination [66]. Furthermore, a spin splitting would have a strong impact on semiconductor, by transforming a direct band gap semiconductor into an indirect band gap one.

The Rashba effect is the consequence of the breaking of inversion symmetry in the crystal in a direction orthogonal to a k-point sampling plane and is described by the Bychkov-Rashba Hamiltonian [68]:

$$H = \frac{p_{\parallel}^2}{2m} + \underbrace{\frac{\alpha^{'}\hbar E_z}{4m_0^2c^2}}_{\alpha/\hbar}(\sigma \mathrm{x} p_{\parallel}).z \tag{2.5}$$

with, $p_{\parallel}$ the linear momentum, α' the Rashba primary correlation factor, σ the Pauli spin

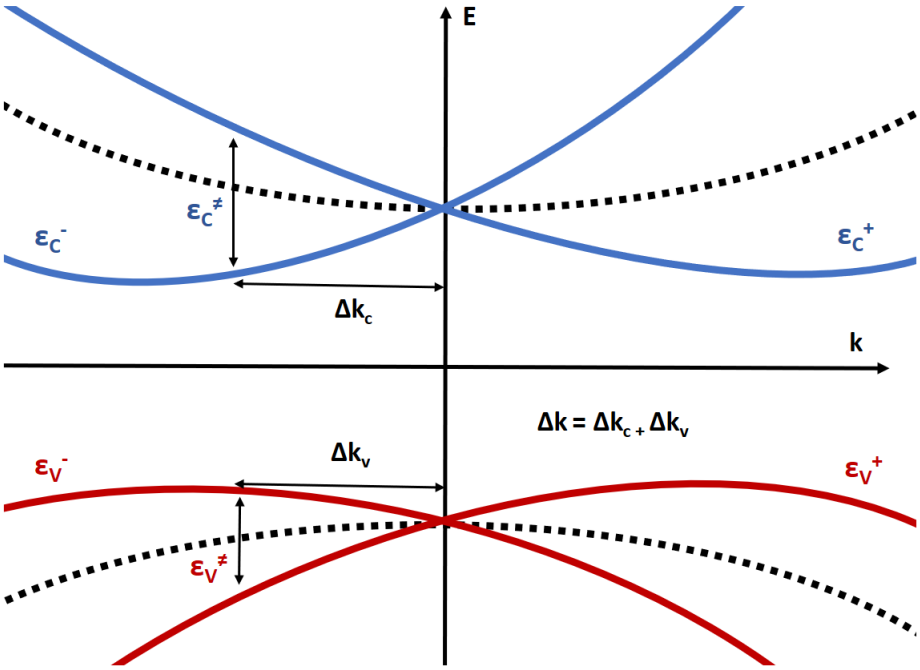

Figure 2.7: The valence and conduction bands (VB and CB) in the presence (absence) of Rashba splitting are the solid red and blue (dashed) lines, respectively. The Δk-shifted absorption and radiative recombination processes are also illustrated. Adapted from [67].

matrices, $-E_z z$ originating from the gradient operator of the electrostatic potential V. The electric field projection can be included into the Rashba interaction coefficient α. Dispersion energy splitting can be derived by diagonalizing the Hamiltonian in the k-space:

$$\epsilon_{\pm}(k) = \frac{\hbar^2}{2m}k^2 \pm \alpha k \tag{2.6}$$

We indicate by $\epsilon_{\pm}(k)$ the energy difference between branches with opposite spin polarization, calculated at the particular k point where the conduction band has its minimum sets. The Rashba interaction coefficient α can be retrieved by:

$$\epsilon^{\neq} = 2\alpha\Delta k \Rightarrow \alpha = \frac{\epsilon^{\neq}}{2\Delta k} \tag{2.7}$$

With $\pm\Delta k$ and $\epsilon_{\pm}$ indicating the wavevector and energy coordinate of the conduction band minimum with respect to origin, i.e namely the position where the minimum would be in absence of Rashba splitting. $\epsilon^{\neq}$ defines the difference between the two energy curves at the vertex positions as shown on Fig. 2.7.

2.4 Light-matter interactions

2.4.1 Linear optics and fundamental definitions

In this subsection, fundamental concepts of linear optics used in the following experimental and simulation work are clarified. Let us considering the dipole moment per unit volume or polarization *P(t)* of a material system depending on the strength of an applied optical field *E(t)*. If the induced polarization depends linearly on the electric field, it can be described by this relationship :

$$P(t) = \epsilon_0 \chi^{(1)} E(t) \tag{2.8}$$

with ϵ_0 the vacuum permittivity, $\chi^{(1)}$ the first order susceptibility of the material. In materials where susceptibility is anisotropic, meaning which is different depending on direction, susceptibility is represented as a tensor known as the susceptibility tensor. Electric susceptibility measures the ability of a material to become transiently polarized.

The electric susceptibility χ is a constant that can be defined as the degree of polarization of a dielectric material in response to an applied electric field:

$$\chi = 0, \qquad \text{in the vacuum} \tag{2.9}$$

$$\chi = \epsilon_r - 1, \qquad \text{in a material} \tag{2.10}$$

with epsilon$_r$ the relative permittivity or dielectric constant, which is a ratio between the relative permeability of a material and the vacuum electric permeability.

Materials with no free charges are called dielectrics. Electric susceptibility χ, related to the refractive index n is convenient to describe interactions of light and matter material:

$$n^2 = \frac{\epsilon}{\epsilon_0} = 1 + \chi \tag{2.11}$$

This relation is convenient in the case of electrons oscillating at the same frequency than the electric field E, meaning when the intensity of the electric field stays relatively low. In the case of nonlinear materials and intense laser beam with high electric field, new electromagnetic waves with different frequency components are generated, as described in Section.2.4.3.

2.4.2 From microscopic to macroscopic polarizability

Microscopic polarizability is expressed by term α, while macroscopic polarizability is represented by χ. A dielectric material is said to be polarized when induced electric dipoles are present. The presence of induced electric dipoles within the dielectric causes the electric field both inside and outside the material to be modified. Polarizability α can be defined as a measure of the ability of a material to become polarized in the presence of an applied electric field. It occurs in both polar and nonpolar materials.

Three different types of polarizibality

Two kind of polarization exist depending on its origin. The distortional or also called deformational polarizibility and the orientational or dipolar polarizibility. The first one, the distortional polarizibility, can be distinguished in two types: the electronic α_e and the ionic or atomic α_{ion}. Both of them are characterized by relative displacement of charges, either between electron orbits and nuclei, or between ions. The both deformation results from the application of an external electric field. The second origin of polarization is orientational and lead to the orientational, or so called dipolar polarizability α_{mol}.

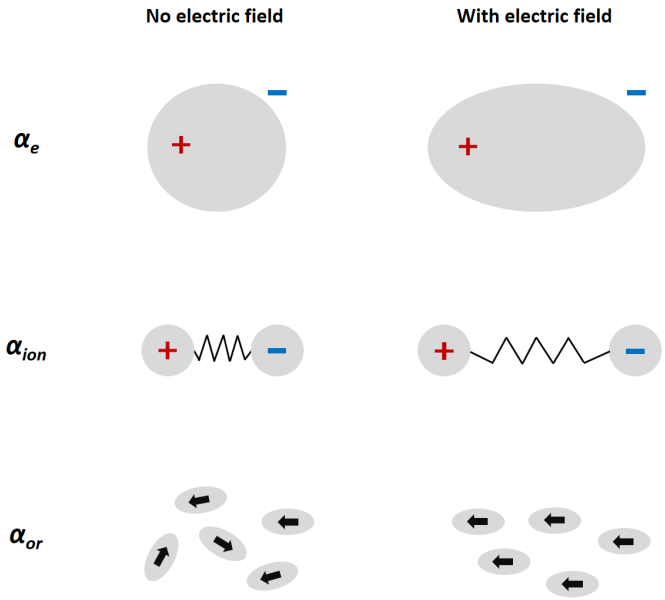

Figure 2.8: Electronic polarizability α_e and ionic or atomic polarizability α_{ion} originate from distortional polarizability, while orientation (dipolar) polarizability α_{mol} originate from orientational change.

When an external electric field is applied, it generates a small displacement of the center of negative charge of electrons distribution relatively to the center of positive charge in the nucleus. Therefore, atoms acquire an electric dipole moment and each atom can be character-

ized by an electronic polarizability α_e. The displacement of the negative charges is usually called electron cloud. The value of electronic polarizability should increase with the number of electrons, knowing the outer shells' electrons in multielectronic atoms are less bonded to the nuclei.

When ions experience an external electric field, they also undergo displacement from their equilibrium positions. This gives rise to ionic or also called atomic polarizability α_{ion}. As ions and atoms have considerably higher mass than electrons, their polarization leads to a slower process than the electronic polarization.

The third existing polarizability is the orientational or dipolar polarizability α_{mol}. A polar dielectric, for example molecules or group of molecules, can exhibit a permanent dipole moment due to their structure. By applying an external electric field on it, the dipoles tend to aligned with the direction of the later, therefore changing their initial orientation.

The total polarizability α of a material can be written as follows:

$$\alpha = \alpha_e + \alpha_{ion} + \alpha_{mol} \tag{2.12}$$

where α_e, α_{ion}, α_{mol} are the electronic, atomic (or ionic), orientation polarizabilities relative to the molecular orientation, respectively.

The dielectric behavior of a polar solid is significantly influenced by the temperature and the interactions between molecules and groups.

In the case of materials with no significant permanent dipole, the polarizability of individual particles is related to the average electric susceptibility of the medium by the Clausius-Mossotti relation, which expresses the dielectric constant (or relative permittivity) ϵ_r of the material in terms of the atomic polarizability α:

$$\frac{\epsilon_r - 1}{\epsilon_r + 2} = \frac{N\alpha}{3\epsilon_0} \tag{2.13}$$

with ϵ_r the material dielectric constant, ϵ_0 the vacuum permittivity and N the number density of the particles (number per cubic meter).

The ratio of the induced dipole moment to the applied field is called the polarizability α of the molecule. As previously discussed, we can define the microscopic polarizability p as followed:

$$p = \alpha E \tag{2.14}$$

The SI unit for α is C.m^2.V^{-1}. The equation suggests that p and E are in the same direction –

but this is so only if the electrical properties of the medium are isotropic.

For the sake of the simplicity and merging equations (2.19) and (2.20), induced microscopic polarizability p can be expressed as follow:

$$p = \sum_{i}^{n} p_i^{(static)} + p_i^{(ind)} \qquad p_i^{(ind)} = (\alpha_e + \alpha_{ion} + \alpha_{mol}) \tag{2.15}$$

In the Teraherz-induced Kerr spectroscopy measurements presented in Chapter 6.2, the microscopic polarizibility cannot be directly observed. Nevertheless, a measurement of the macroscopic refractive index n occurs. The link between lattice polarizibility p and refractive index n through material susceptibility χ is discussed in this section.

2.4.3 Nonlinear optics

In this thesis, some of the phenomena studied take place on ultrashort time scale, from femto- (10^{15} s) to picosecond (10^{-12} s). Their time-resolved observation is possible using pump-probe techniques, requiring laser pulses with short pulses. Moreover, intense laser light is needed in order to excite the material and to create desirable observable dynamics, such as change in refractive index n to follow α_e and α_{ion}. Therefore, interaction of intense laser light with matter is an important point of this thesis. In the case of intense laser light, nonlinear optics rules have to be taken into account.

Nonlinear optics allows to study the interaction between intense laser light with matter. Nonlinear optic field began with the discovery of second-harmonic generation by Franken et al. in 1961 [69]. The term *nonlinear* is attributed when the response of a material system is nonlinear to the optical field applied. For example, the process of second-harmonic generation we will discuss in the following subsection occurs as a result of the part of the atomic response that scales quadratically with the strengh of the applied optical electric field. Thus, the intensity of the light generated at the second-harmonic frequency increases as the square of the intensity of the applied laser.

In the case of a conventional linear optics, the induced polarization (or dipole moment per unit volume) depends linearly on the electric field strengh, as described by equation 2.8: , where $\chi^{(1)}$ is the first order and linear susceptibility. In the case of high electric field strengths being comparable to the characteristic atomic field E_{at}, as commonly reached with lasers, the linear response approximation is not valid anymore [70]. The laser intensity I_{at} associated with a peak field strength of E_{at} can be written as the following [71]:

$$I_{at} = \frac{1}{2}\epsilon_0 c E_{at}^2 = 3.5x10^{20} W/m^2 = 3.5x10^{16} W/cm^2 \tag{2.16}$$

An interpretation of the nonlinearities appearing in polarization comes from the microscopic

aspect of matter. Each atom of a dielectric material[I] is surrounded by an electronic cloud capable of deforming under the action of E and creating an electric dipole. This dipole, for a small deformation, is proportional to E, but if the deformation is too large, this is no longer the case. The sum of all the dipoles gives rise to a non linear, macroscopic polarization. Nonlinear terms have to be added to the optical response, which is described by expressing the induced polarization as a power series in the field strength:

$$P(t) = \epsilon_0[\chi^{(1)}E(t) + \chi^{(2)}E^2(t) + \chi^{(3)}E^3(t)...] = P^{Lin}(t) + P^{NL}(t) \tag{2.17}$$

with $\chi^{(2)}$ and $\chi^{(3)}$ the second- and the third-order nonlinear optical susceptibilities, respectively. It is relevant to note $\chi^{(1)}$ is a second-rank tensor, $\chi^{(2)}$ a third-rank tensor and so on for the following nonlinear terms.

Second-order nonlinear optical interactions can only take place in noncentrosymmetric crystals, meaning crystals that do not display inversion symmetry. Inversion symmetry takes place in liquids, gases, amorphous solids as in many crystals. The second order susceptibility χ^2 vanishes identically for such media and consequently these materials cannot produce second-order nonlinear optical interactions because of space inversion (E becomes $-E$). However, third-order nonlinear optical interactions can occur for both centrosymmetric and noncentrosymnetric media.

Second-order nonlinear processes

In this subsection, we discuss the optical processes occuring in second-order nonlinear medium. Polarization has a key role in the description of nonlinear optical phenomena because time-varying polarization acts as the source of new components of the electromagnetic field. The wave equation of a nonlinear and dielectric media is described as:

$$\nabla^2 E - \frac{n^2}{c^2}\frac{\partial^2 E}{\partial t^2} = \frac{1}{\epsilon_0 c^2}\frac{\partial^2 P^{NL}}{\partial t^2} \tag{2.18}$$

with n the linear refractive index, c the light velocity. Let us consider one component of an incident light field $E(t)$ of two distinct frequencies:

$$E(t) = E_1 \exp^{-i\omega_1 t} + E_2 \exp^{-i\omega_2 t} + \text{c.c.} \tag{2.19}$$

[I] A dielectric medium is an electrical insulator that can be polarised by an applied electric field. Placed in an electric field, its electric charges do not flow through the material as they do in an electrical conductor. As they have no loosely bound or free electrons that may drift through the material, they only shift slightly from their average equilibrium positions, inducing dielectric polarisation. The material may exhibit electrostatic dipoles at the atomic scale, which will interact with an applied external electric field. This interaction results in the creation of a polarization $\vec{P}$ related at the microscopic level to this electric field by the polarizability, and at the macroscopic level, by the electric susceptibility χ.

with ω_1 and ω_2 the distinct frequencies of the light field. Nonlinear response of a material to an intense laser field causes the generation of new frequency components. The second-order nonlinear polarization term $P^{(2)}$ contains the following frequencies, assigned to distinct nonlinear second-order processes:

$$\begin{aligned} \omega &= 2\omega_{1,2} && \text{Second harmonic generation (SHG)} \\ \omega &= \omega_1 + \omega_2 && \text{Sum frequency generqtion (SFG)} \\ \omega &= \omega_1 - \omega_2 && \text{Difference frequency generation (DFG)} \\ \omega &= \omega_{1,2} - \omega_{2,1} = 0 && \text{Optical rectification (OR)} \end{aligned} \tag{2.20}$$

Usually only one of the frequency components is present with a high enough intensity in the radiation generated by the nonlinear optical interaction. This is due to the phase-matching condition, required to ensure that a proper phase relationship between the interacting waves is maintained along the propagation direction [72].

Second-harmonic generation (SHG), sum-frequency generation (SFG), difference-frequency generqtion (DFG)

Second-harmonic generation can be defined a nonlinear process in which two photons interact, are combined and generate a new photon. Let's first focus on the second harmonic generation (SHG), the sum frequency generation (SHG) and the difference frequency generation (DFG), sketched on Fig. 2.9. SHG leads to the generation of a radiation with the double frequency of the incident electric fields. As illustrated on Fig. 2.9, the SHG can be described as two incident photons with the same frequency ω exciting a system from its ground state to a virtual state. While relaxing, a photon with frequency 2ω is emitted. This process is indeed used in the FemtoARPES setup to generate second harmonic for two-photon photoemission using nonlinear barium borate (BBO) crystals (Chapter 5).

Sum-frequency generation (SFG) is analogous to the SHG, except that it takes place when the incident field consists of two distinct frequency components. This process is definitely useful as an output of frequency-tunable visible laser[73]. Second-harmonic and sum-frequency generation (SHG/SFG) spectroscopy is a powerful technique to study surfaces and interfaces. It uses the fact that optical responses of a surface and bulk of a medium follow different selection rules. Indeed for media with inversion symmetry, SHG/SFG is forbidden in the bulk. However, it is not the case at the surface or interface, where the symmetry is naturally broken. This leads to strong suppression of the process in the bulk, leaving it to stand out at the surface [74].

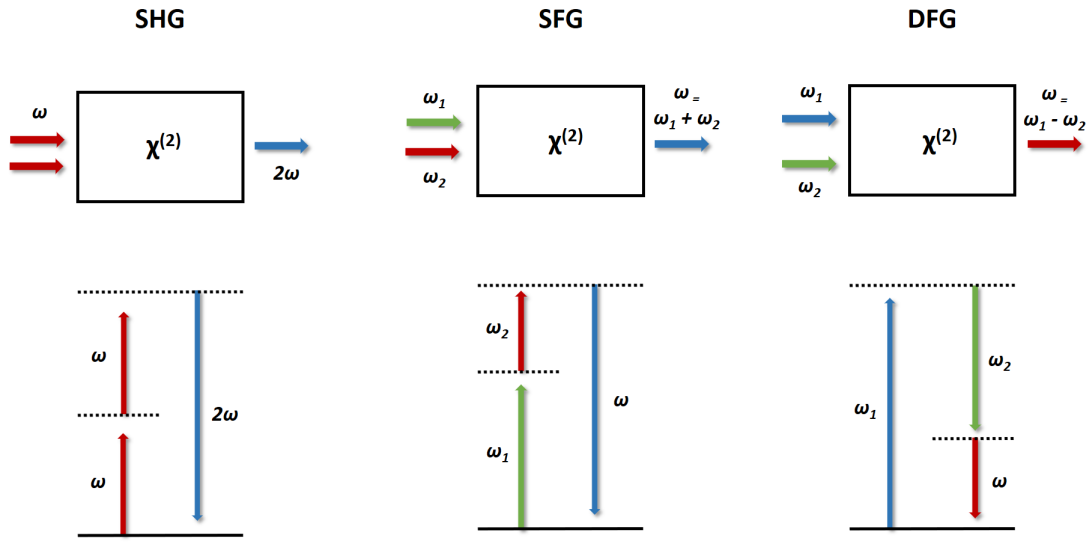

Figure 2.9: Second-harmonic (SHG), sum-frequency (SFG) and difference-frequency generation processes. Solid lines represents the atomic ground state, dashed lines the virtual levels.

Difference-frequency generation process, illustrated on Fig. 2.9, consists in the generation of a radiation with frequency ω, which is the difference of the ones of the applied fields, respectively ω_1 and ω_2. Considering ω_1 as the photon with the higher frequency and ω_2 the lower, the latter will be amplified through the process, while an output photon with frequency ω is generated.

Optical Rectification

Optical rectification (OR) can be described as a difference frequency mixing of two photons with different frequencies ω_1 and ω_2 originating from the same light pulses. As pulses have a finite bandwidth, this leads to the generation of low frequency pulses. In the case of short pulses, the OR contribution expands to cover part of the THz spectral region. In particular, the OR is used in our Terahertz Kerr effect experiments to generate high-intensity ultrashort THz pulses using nonlinear Lithium niobate $LiNbO_3$ crystal (Chapter 4).

Phase-matching condition

Phase matching is required because nonlinear process has to fulfill both energy conservation and wave vector conservation. Phase matching occurs when generated waves at diverse points in the nonlinear crystal are able to interfere constructively along the propagation pathway of the initial generation pulse. In all nonlinear mixing processes, minimizing the wave vector

mismatch Δk is therefore a key to achieve maximum conversion efficiency.

$$\Delta k = k_1 + k_2 - k_3 \tag{2.21}$$

with the wavevector k_n of the respective frequency waves ω_n.

Third-order nonlinear process

In non centrosymmetric crystals, third order nonlinear phenomena have lower efficiency than second order ones. However, they play a very important role in nonlinear optics. In the case of centrosymmetric materials, we have seen that there is no second order nonlinearity. The third order nonlinearity corresponds in this case to the first observable nonlinear effect. Several third-order nonlinear optical processes exist, such as the third-harmonic generation process [71, 70], which correspond to the generation of a 3ω frequency created by an applied field with ω frequency. However, this phenomenon is not particularly interesting because in practice it is more efficient to generate the third harmonic by means of two second order processes in cascade, using frequency doubling or the then sum of frequencies.

An interesting third-order nonlinear process is the intensity-dependent refractive index (i.e isotropic Kerr effect). In the presence of this type of nonlinearity, the refractive of a material index displays an intensity dependance and can be described as the following relationship:

$$n = n_0 + n_2 I(t) \tag{2.22}$$

with n_0 the usual and linear refractive index, n_2 the second-order index of refraction and $I(t)$ the time-dependent intensity of the field E, described as: $\mathrm{I} = 2\mathrm{n}_0\epsilon_0 c|E(t)|^2$

The intensity dependence of refractive index is also known as the Kerr effect, which we discuss in Chapter 4. We are particularly interested in the THz-induced Kerr effect and how to probe the lattice polarizability with it.

2.4.4 Lattice control through coherent phonons

The previous subsection about linear and nonlinear optics discussed non-resonant interaction of light with electronic degrees of freedom. This subsection focuses instead on the coupling of light to phonon resonances, either via a direct or indirect. We particularly discuss the origin of coherent phonon mode excitations also discussed in the Section.6.3 and Section.6.3.

A phonon mode can be selectively excited through the absorption of a photon. The energy has to be equal to the energy difference between the two vibrational states in the case of IR absorption. An alternative excitation mechanism is Raman scattering, in which the incident light excites the system to a high-energy state (virtual energy state). Raman scattering found its name from C. V. Raman, who was awarded the Nobel prize in 1930 for his discovery of the

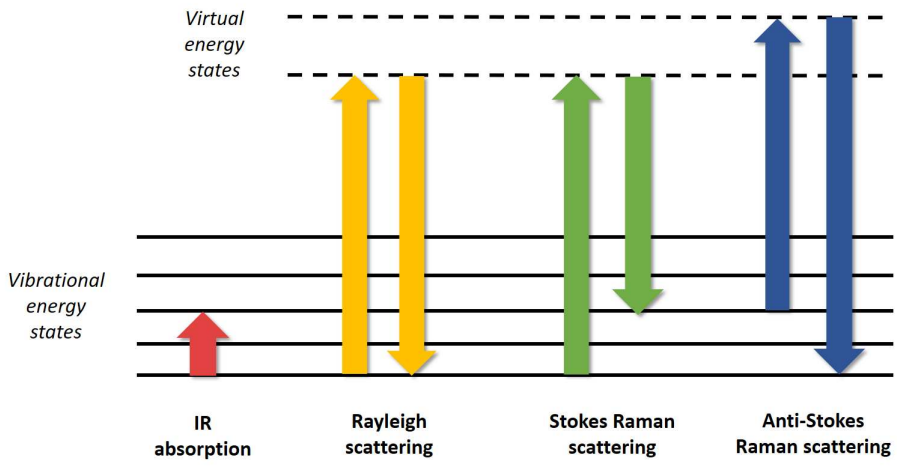

Figure 2.10: IR, Rayleigh and the Stokes and anti-Stokes Raman scattering, with the phonon picture. Resonance are described by a ground state and an excited state. Virtual intermediate states are represented with dotted lines.

inelastic light scattering from molecules. In the context of phonon physics, it refers specifically to the inelastic light scattering from optical phonons.

In the following, we consider consider interactions of light with coherent phonons. Light coupling with phonon mode can be simply model as the interaction of an electromagnetic field with a damped harmonic oscillator. Equation of motion of the later can be obtain from Taylor expansion of the polarization in the material P and the classical Lagrangian for a single normal coordinate Q [75]:

$$m\ddot{Q} = \frac{\partial V}{\partial Q} + \frac{\partial P(Q,0)}{\partial Q}E + \epsilon_0 \frac{\partial \chi(Q)}{\partial Q}E^2 \tag{2.23}$$

with Q and E in function of the time. The term is equivalent to the restoring force of the harmonic oscillator. The two other E-dependent terms are the external driving forces of the oscillator. Under the assumption of weak perturbation (i.e harmonic potential), the equation of motion can be extended:

$$\frac{\partial^2 Q(t)}{\partial t^2} + 2\gamma\frac{\partial Q(t)}{\partial t} + \omega^2 Q(t) = \frac{1}{m*}\left(\frac{\partial P(Q,0)}{\partial Q}E(t) + \epsilon_0 \frac{\partial \chi^{(1)}(Q)}{\partial Q}E(t)^2\right) \tag{2.24}$$

The equation contains the two main interaction of a light electric field with a specific phonon mode. The first term on the right describes the direct coupling of the light with IR-active phonon modes, while the second corresponds to the indirect coupling of light with Raman-active phonon modes, via nonlinear coupling of the electric field. The mutual exclusion principle implies that only one of the two coupling can take place at the same time, in the case

of inversion-symmetric materials.

IR-active phonons (one wave interaction)

Figure 2.11: Classical representation of IR-active phonon.

Typical vibration frequencies in molecules and optical phonon frequencies in solids are in the order of several THz, i.e in the IR region of the electromagnetic spectrum. The movement of atoms in a molecule has a natural vibrational frequency related to the strength of their bonds. When the vibrational frequency of a bond is equal to the frequency of IR-active radiation directed at it and if the mode has an dipole moment, then the bond absorbs the radiation [76]. The specific IR frequencies absorbed by the bonds in a molecule give rise to an IR spectrum of the molecule. In order for a resonance to cause IR vibration, the phonon modes must generate oscillating electrical dipoles, as the displacement of oscillating charges cause polarisation. IR spectroscopy is performed either by measuring the transmission or reflection of IR radiation. TO phonon modes of polar solids strongly couple to light waves in the IR spectral region when their frequencies and wave vector match with each others.

Since dipole moment activated in IR-region is parity-odd, i.e its sign changes upon inversion, only the parity-odd modes (i.e antisymmetric by inversion) are considered as IR-active modes. This selection rules apply to centrosymmetric crystals where phonons are classified as parity-even and parity-odd. Parity-even phonon are classified as Raman-active phonons. Therefore, light-matter interaction gives information about the phonon vibration in a material, but also about the dipole moments and the polarizability of the lattice modes. For example, during the symmetric stretching vibration of the linear CO_2 molecule, its polarizablitiy gets smaller during the stretching as opposed to the compression. This vibration is Raman-active (and IR-inactive). In contrast, during the asymmetric stretching vibration, the polarizability does not change, and the vibration is Raman-inactive (but IR-active). We now discuss the case of Raman-active phonons.

Raman-active phonons (two waves interaction)

When photons interact with a molecule, the light produces a coherent polarization in the medium. The interaction of the light with the molecule can induce a motion of the electron cloud of the molecule which leads to instantaneous electronic polarizability. A molecule has specific energy transitions related to its intramolecular bonds, in which polarizability shifts occur that activate the Raman-active modes. The frequency of the Raman shift is related to

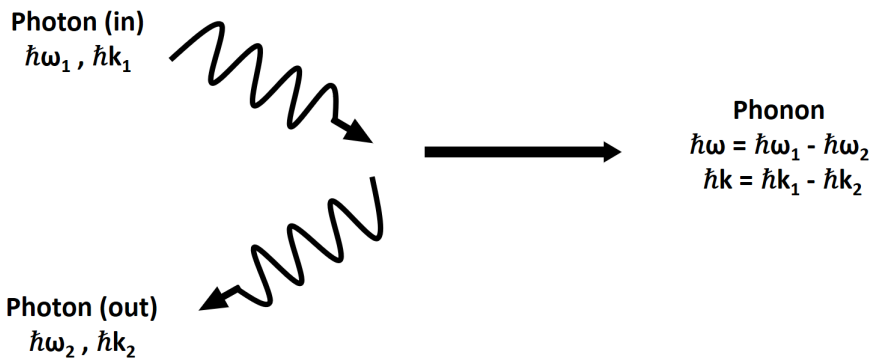

Figure 2.12: Classical representation of Raman-active phonon.

the type of bond excited and also strongly dependent of the polarizabily of the mode.

According to Eq.2.24, the Raman-active driving force is proportional to the product of two electric fields E(t), i.e $F(t) \propto |E(t)|$. The strength of this so called Raman interaction generated when applying a field $E(t)^2$ is given by χ, which contains all the modes and resonances.

The strong-field THz used in this research work (Chapter.4) allows nonlinear light-matter interactions at THz frequencies [77]. This frequency range approaches the phonon resonance frequency and could drive difference as well as sum frequency to excite them. This opens a new way to control specific lattice modes.

Photonic and phononic pathways

In this subsection, we summarise the different excitation pathways observable in our TKE experiments (Section.6.2), in order to better explain the experimental results of Section.6.2.

Two main excitation pathways are candidate to explain the observation of Raman-active modes: the phononic and the photonic process [78, 79, 80], represented in Fig. 2.13. They can each be divided into two categories. In the case of the photonic pathway, which requires strong Terahertz polarizibility, the two mechanism are: (i) In the case of coherent and nonresonant excitations below the material bandgap, the Impulsive stimulated Raman scattering (ISRS) mechanism takes place, in which a virtual electronic state serves as the intermediate energy level for the Raman scattering of the incoming light by the phonon. The difference frequency of the two photons in the light pulse is resonant with a vibrational transition of the phonon mode; (ii) The sum-frequency excitation (SFE), the counter part equivalent to ISRS, where incident photon adds up to reach a phonon state. This mechanism consists in the excitation of a phonon state in a material which does not possess infrared-active phonons and require only low-energy excitation by Terahertz radiation.

Phononic pathways are also separated in sum- and difference-frequency processes and requires anharmonicity: (iii) Conventional ionic Raman scattering via difference-frequency (DF-IRS) excites Raman-active phonons via scattering with infrared-active phonons. The mechanism consists on infrared-active phonon coherently excited by light and which serve as intermediate state for Raman scattering. This process mediated through anharmonic phonon-phonon coupling and is less dissipative than its photonic counterpart due to the lower excitation energy involves; (iv) Sum-frequency counterpart of ionic Raman scattering (SF-IRS), consisting in the excitation of a phonon state via a phonon scattering.

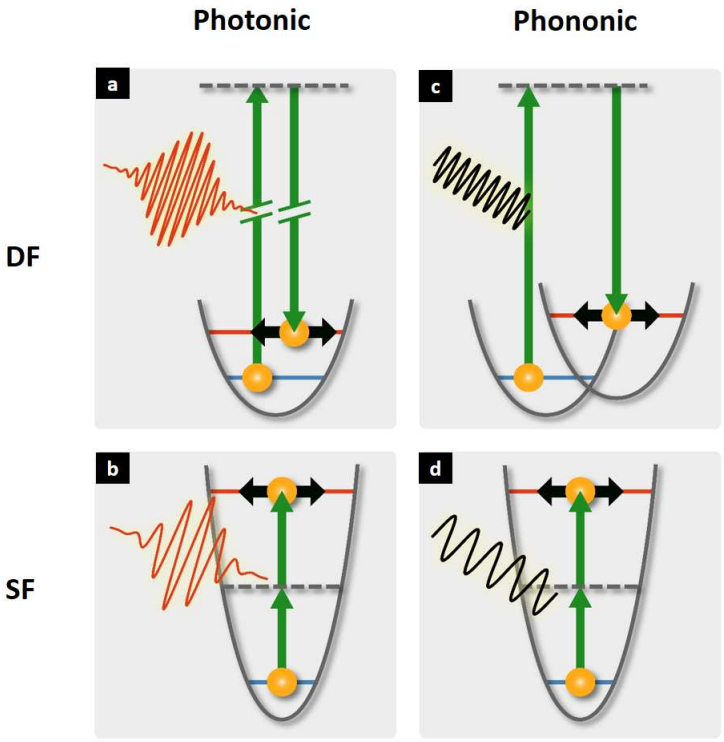

Figure 2.13: Representation of the (a-b) photonic and (c-d) phononic excitation pathway, in difference or sum-frequency process respectively. Extracted from [79].

Each of the four phonon modes mechanism proposed earlier can be predict using the general equation of motion for the excitation of phonons:

$$\ddot{Q} + \kappa \dot{Q} + \frac{\partial}{\partial Q} V(Q) = \sum_i Z_i E_i + \epsilon_0 \sum_{ij} R_{ij} E_i E_j \tag{2.25}$$

with Q the normal mode coordinate (i.e amplitude) of the phonon at the Brillouin-zone center, κ the damping coefficient, $V(Q)$ the lattice potential of the phonon (harmonic or anharmonic, depending of the mechanism), Z_i the Born effective charge [II], E_i the electric field component

[II] An ionic crystal can be described as a periodic arrangement of punctual charges. In this simplified model, the

of the exciting light pulse, R_{ij} the Raman tensor. In a centrosymetric crystal and if the phonon modes is Raman-active, the term $\sum_i Z_i E_i$ is equal to zero.

The photonic pathway requires strong THz polarizability in order to excite Raman-active phonon. As $Q_R \propto E_{THz}^2$, we assume that the transient birefringence cause by the THz pump should be proportional to Q_R:

$$\Delta n_{TKE} \propto Q_R \tag{2.26}$$

In the case of the photonic pathway, we assume to have a harmonic lattice potential The term $V(Q_R) = \frac{\Omega_R^2 Q_R^2}{2}$, leading to the following equation:

$$\ddot{Q}_R + \kappa_R \dot{Q}_R + \Omega_R^2 Q_R = \epsilon_0 R E^2 \qquad \text{(nonlinear photonic)} \tag{2.27}$$

In the second pathway, which is the phononic one, we suppose that the THz pump first excite IR-active phonon mode, which later excites Raman phonon mode. Ionic Raman scattering is described by a quadratic-linear coupling of IR-active with Raman-active phonon. Therefore, the anharmonic lattice potential can be expressed as:

$$V(Q_R, Q_{IR}) = \frac{\Omega_R^2 Q_R^2}{2} + \frac{\Omega_{IR}^2 Q_{IR}^2}{2} + c Q_{IR}^2 Q_R^2 \tag{2.28}$$

with c the quadratic-linear coupling coefficient. The equation of motion of phonon can be obtained be re-writting equation (5.11), which lead to the following equation of motion [81, 80, 78]:

$$\ddot{Q}_{IR} + \kappa_{IR} \dot{Q}_{IR} + (\Omega_{IR}^2 + 2cQ_R) Q_{IR} = Z_{IR} E(t) \qquad \text{(linear phononic)} \tag{2.29}$$

$$\ddot{Q}_R + \kappa_R \dot{Q}_R + \Omega_R^2 Q_R = c Q_{IR}^2(t) \qquad \text{(nonlinear phononic)} \tag{2.30}$$

We notice that in the case of a Raman-active phonon excitation via photonic mechanism, the driving force should be quadratic in electric field E, as expected. While in the case of the phononic process, the driving force is quadratic in the phonon field of the infrared-active phonon Q_{IR}^2 and thus also proportional to E^2.

displacement of an ion from its equilibrium position causes a polarization change simply equal to the charge of the ion multiplied by the displacement. For a more realistic calculation, the Born effective charge is defined as the polarization change in a direction α caused by a displacement of an ion in a direction β.

2.5 Summary

This chapter has allowed us to grasp the fundamental notions and concepts about the vibrational modes of the lattice, focusing on anharmonicity and their different mechanisms of excitations. The fundamentals of optics and nonlinear processes, widely used in this work, were discussed. Finally, we have also enlightened the reader about the different relaxation and recombination processes of free charges, in particular electrons, as well as the potential mechanisms they could undergo such as Rashba splitting or charge carrier screening via a polaron. These phenomena and properties seem to be particularly important in LHPs. The following chapter serves to link the theoretical mechanisms of this chapter with the state of the art and expectations in LHPs.

3 State-of-the-art of lead halide perovskites (LHPs)

This chapter aims to give readers an accurate overview of the latest findings on LHPs. This research topic is currently attracting many researchers, resulting in a dense, extremely diverse and rapidly evolving scientific literature. We focus on the topics related to the experimental results in Chapter.6 and Chapter.7.

3.1 Compositional engineering

3.1.1 Global overview

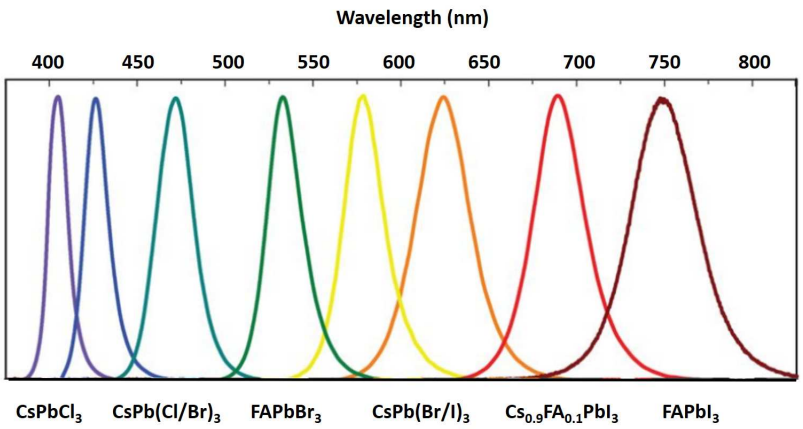

Figure 3.1: Band gap tuning and compositional variation in lead halide perovskite materials, inducing diverse wavelength photoluminescence emission. Adapted from [82].

Among the best known and studied LHPs are the lead halide perovskites with a single A-site cation, such as $MAPbBr_3$, $MAPbI_3$, $FAPbBr_3$ or $CsPbBr_3$. LHPs have the great advantage of being easily tunable and thus able to play with their optoelectronic properties, such as the band gap (Fig.3.1). Nevertheless, these single A-site cation perovskites have limitations, notably in terms of resistance to humidity or temporal degradation [83]. Numerous studies

have been carried out to find chemical compositions that are more stable for photovoltaic applications [84, 85]. In this research work, we will focus on double A-site cations such as (MA,FA)$PbBr_3$, but also on the much more complex quadruple A-site cation called (4cat)$PbBr_3$.

3.1.2 From conventional (simple) to complex A-site cation

The most promising results in terms of absorber stability were obtained by making thin films optimally intermixing different cations on the A-site and halide anions on the X-site of the ABX_3 structure [86, 87, 88]. The main objective of chemical engineering are to obtain a cubic phase thin film, which is stable within the operation temperature range of the photovoltaic device, but also which displays low carrier recombination rates to enhance solar cell performance. Maintaining a reasonably low bandgap E_g is also an important parameter, in order to absorbe as much photons as possible. Among the most interesting elements incorporated in compositional engineering is Guanidinium (GA). The addition of a small dose of this cation, with a much wider ionic radius than the others, enables to modulate the morphology and drastically alter charge recombination dynamics in lead halide perovskites, by means of larger grain size, trap passivation and reduced hysteresis effects [87, 88, 89, 90].

Methylammonium MA^+ cation is an excellent light harverster, but also suffers from its low thermal and chemical stability, originating from its fully organic composition. Formamidinium FA^+ displays a broader absorption of the solar spectrum because of its lower band gap [91, 92] and displays higher affinity to form hydrogen bonds with the inorganic Pb-X lattice [93], leading to an improved stability. This optimal embedment of MA^+ and FA^+ stabilizes the pseudocubic structure with respect to the tetragonal phase that is observed in pure $MAPbX_3$ under standard condition. Nevertheless, $FAPbX_3$ is known to undergo a phase transition into the nonphotoactive and hexagonal δ-phase [94]. This phase is undesirable and leads to a large bandgap insulator with unefficient absorption properties for a solar cell photoactive layer. Nonetheless, the δ-phase formation can be hindered by incorporating small amounts of Cesium Cs^+ cations [94]. This one increases the structural stiffness, inhibit the formation of the undesired δ-phase, improves the thermal stability and homogenized the distribution of the halide mixture throughout the material. The addition of Guanidinium GA^+ decreases the formation of halide vacancies and minimizes nonradiative charge carrier recombination at the grain boundaries [86]. Besides, it has been reported to stabilize both FA^+ and MA^+ based perovskites because of an increased number of H bonds with favorable orientation within the inorganic framework. In fact, compared with the 1–2 H bonds per MA molecule, the introduction of GA^+ increases the number of interactions to six H bonds within the inorganic framework [95].Furthermore, the GA^+ cation improves stability with its high pK_a value (13.6) and almost completely prevents deprotonation [I]. Section.7.3 and Section.6.3 discuss electron relaxation, lattice dynamics and solar cell implementation of an innovative (4cat)$PbBr_3$.

[I] Deprotonation is a chemical reaction in which an H+ proton is removed from a molecule to form its conjugate base. The propensity of a molecule to release a proton is measured by its pK_a (measure of acidity).

3.2 Dimension properties

In our experimental investigations, we will mainly study 3D bulk LHPs, in the form of single crystals and thin films. We will also present some preliminary data on the 2D perovskites. The dimension of the material obviously plays a large role in the diversity of these optoelectronic properties, the main ones of which are commented in this section.

3.2.1 Single crystal and thin films (3D)

LHPs can be grown both as single crystals or thin films. Single crystals provide information about a crystalline and ordered material, facilitating for example Raman-active mode characterisations or defect tolerance properties. However, thin films are more likely to be used in practical applications. They are printed and used as the active layer in LHPs solar cells.

Thin films are by definition less pure and contain many grains, as well as grain boundaries, which impact the material's characteristics (especially regarding halide migration and trap-recombination).

3.2.2 Two-dimensional material (2D)

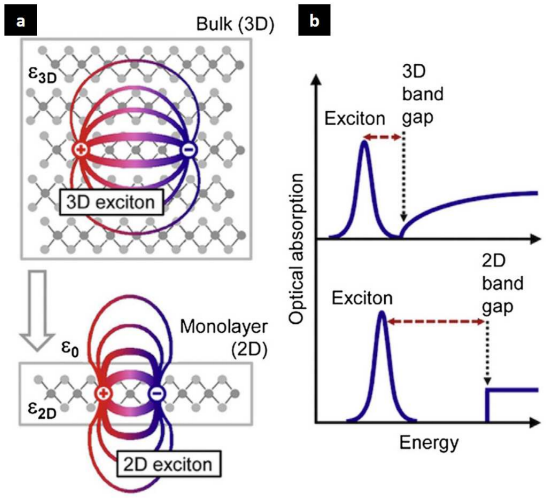

Figure 3.2: (a) Exciton electric field in 3D and 2D materials. (b) The change in dimension lead to a separation between the exciton and band gap peaks in optical absorption measurements. Extracted from [96].

Two dimensional (2D) LHPs are usually obtained by slicing the 3D bulk perovskite structure along the (100) plane and incorporating large spacer cations (usually long-chain ammonium cation LA) between the perovskite layers. This gives rise to the general formula $(LA)_2(A)_nM_nX_{3n-1}$, with n corresponding to the number of LHPs layers. 2D perovskite structures behave as natural multiple quantum wells, in which the inorganic perovskite layers act

as potential well and the organic layers act as barriers because of their difference dielectric function [97]. The quantum confinement as well as reduced dielectric screening increases the exciton binding energy (E_b) in 2D LHPs, leading to the dominance of excitons [II] instead of free carriers from above band gap excitations [98]. Optical and electronic properties of 2D LHPs can be readily tuned by the thickness of the inorganic wells n and the nature of organic spacer cations. Broadband emission with a large Stokes shift has been demonstrated in some n= 1 structures, attributable to the strong coupling between an exciton and the polar modes, leading to self-trapped exciton formation [99]. Excited-state properties start to resemble those of their 3D counterparts when the quantum well thickness increase as shown on Fig.3.2 [100, 101, 102].

3.3 A-site cation

3.3.1 Defect tolerance

Perovskite materials have interesting property of being relatively defect tolerant, as they mostly form defect states close to the valence band or conduction band (shallow traps) [18]. They are less prone to form defect states in the vicinity of the bandgap (deep traps). Defect states within the valence band or the conduction band do not lead to non-radiative recombination, whereas defect states deep in the bandgap can do it. Defect states within the valence band, conduction band or near the band edge arise due to very unusual band structure of perovskite materials. In optoelectronic devices, it is particularly essential to avoid non-radiative processes that convert electronic to thermal energy via defects. Indeed traps lower the efficiency and can trigger device breakdown. It turns out that many of the low energy point defects in halide perovskite can be considered as inert, which is one of the reasons for the materials success.

DFT simulation and experimental studies concluded that the most prominent defect states are shallow trap depths (near the band edge), while no deep traps have been found [103, 104, 105]. Elemental vacancies such as missing lead or halide are also present. Trap density varies largely from lead halide perovskites thin film (in the range of 10^{16}-10^{17} cm^{-3} to single crystal 10^{9}-10^{10} cm^{-3}), which shows the significant impact of grain boundaries and interfaces in the trap creation.

Regarding radiative charges recombination, bimolecular recombination rate constant k_2 is reported in the range of 0.8-20x10^{-10} $cm^{-3}s^{-1}$ in $MAPbI_3$ [53, 106]. For very high quality direct bandgap materials, such as GaAs, the radiative recombination of carriers can be the ultimate limit to device efficiency [107]. Therefore, radiative recombinatin rate in LHPs solar cell active layer should be delayed as long as possible.

[II] Coulomb interactions between electrons and holes affect the operation of solar cells because the resulting bound state, called exciton, has an associated binding energy E_b that needs to be overcome for electrons and holes in order to contribute to the photocurrent [44]. In the case of $E_b > kT$, thermal energies may be enough to dissociate exciton, making exciton binding energies lower than thermal energies at room temperature ($\approx$ 26 meV) highly desirable for applications.

3.3.2 Consequences of phase transition on dielectric function and surface

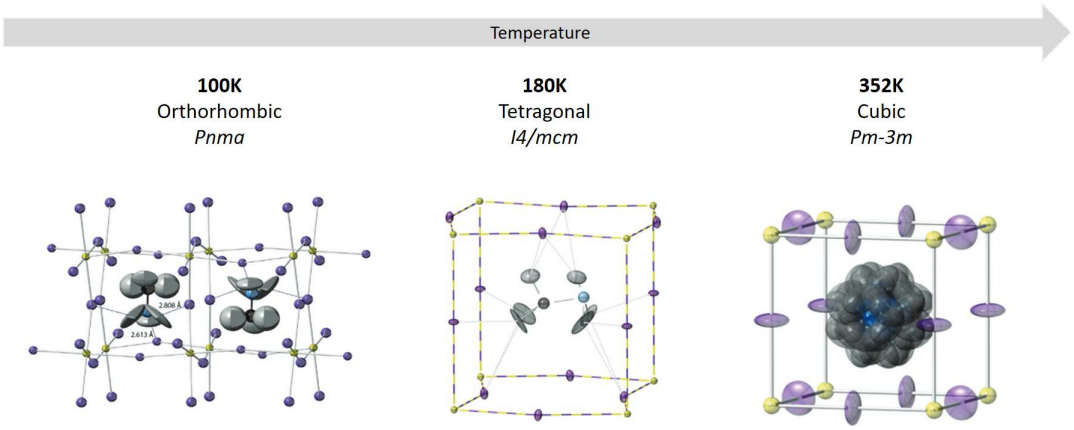

Figure 3.3: Unit cell of $MAPbI_3$ at different temperatures. The ellipsoids represents the 90% probability of presence. Lead is represented in yellow, iodine purple, carbon in black, nitrogen in blue and hydrogen in grey In the orthorhombic phase, MA^+ cations are fully ordered with the $-NH_3$ groups aligned and directed into the distorted square face of the orginal unit cell. Four-fold orientation disordered of the MA cation, orientational disorder in the cubic phase. Original simulation from Weller et al [108]. Equivalent A-site cation motion is observed at low temperature in LHPs.

Dielectric function is an important property in the phase transition of LHPs. If we take the example of A-site Methylammonium cation, the latter has an asymmetric charge distribution resulting in a net dipole moment [109]. The phase structure of the material and particularly the inorganic Pb-I cage shape has an important impact on MA^+ cation dynamics, as pictured on Fig. 3.3. Depending on the temperature, the organic cation undergoes the modulations of the inorganic structure via the hydrogen bonding linking its hydrogen atoms to the different halide anions. It results in a variation of the methylammonium cation rotational freedom inside the metal halide lattice, from rotating, going through tilt or finally being completely frozen. In the orthorhombic phase $Pnma$, the rotational disorder and fluctuations of the organic cation is inexistant [108]. By increasing the temperature and entering in the tetragonal phase $I4/mcm$, the rotational motion of MA^+ cation has more degree of freedom. It is still restricted but small tilting are possible, leading to an important increase of the dielectric function, as described by Anusca et al. and as shown on Fig. 3.4 [110]. The tetragonal-to-cubic transition is linked to the anisotropy of the molecular disorder, as well as inorganic octahedral deformation and tilting, which evolves from predominantely two dimensions in tetragonal phase to three dimensions in the cubic phase [111]. In the cubic phase $Pm-3m$ the dipolar MA^+ cation rotate almost freely inside the inorganic cage inducing a high disorder. This leads to a high dielectric screening at low GHz frequencis (i.e on ns time scales) compared to inorganic and nondipolar cations, as in $CsPbI_3$ [110, 112]. It has been proposed that organic cation MA^+ plays an important role in the optoelectronic properties of the hybrid perovskites, as promoting the formation of free charges during photoexcitation or favorising polaronic effects leading to charge carrier lifetime improvment [113, 114]. Nevertheless, it is demonstrated

by previous work that the LHPs community and our results that it is the Pb-Br cage (and inorganic sublattice Pb-X cage in general) which seems to dominate the ultrafast for charge carrier screening. Combining our complementary techniques, we propose a new and global picture of Pb-X bonding and A-site cation role, considering the Pb-X bonding are responsible for the screening of dynamic electric field of moving charges, while the A-site cations are responsible for static field screening, therefore reducing trap and defect recombination.

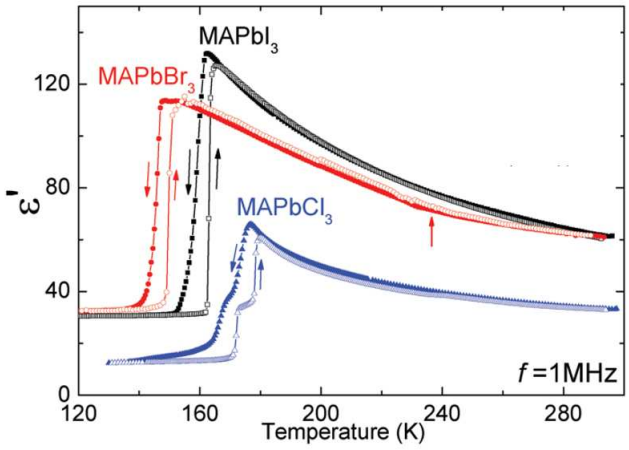

Figure 3.4: Temperature dependences of the real part of the dielectric permittivity for different halide X of $MAPbX_3$, measured at a frequency of 1 MHz. A huge drop of the dielectric permittivity is observed at the orthorhombic phase transition in all of the composition. The dielectric permittivity used in our research as been extracted from this research from Anusca et al. [110]

Indeed, ionic polarization and dielectric function play a fundamental role in the optoelectronic properties of hybrid perovskites. In the experiments shown in Section 7.1, we discussed the effects of polar fields on the dynamics of phoexcited carriers on $MAPbI_3$ single crystal surface in different crystallographic phase using two photon photoemission (2PPE) spectroscopy. We particularly investigated the tetragonal-to-orthorhombic phase transition, where the methylammonium cation display the order to disorder phase transition leading to a sudden jump of dielectric permittivity (Fig. 3.4). LHPs samples being easily damageable with a probe beam, studying the samples at low temperature reduces the risk of damaging the material by overheating it, which could lead to surface destruction. Surface termination and architecture is a parameter that greatly impacts the properties of the latter.

3.3.3 Surface termination and polar catastrophy

As in all materials, surface presents different properties than the bulk and atomic reconstructions. In the case of $MAPbI_3$, the surface displays two possible terminations, the zigzag and the dimerized one, both featuring a net positive charge of +0.25 eV in the topmost CH_3NH_3-I layer, as shown on Fig.3.5 [115]. The net charges on the CH_3NH_3-I and Pb-I_2 layers are alternatively positive and negative, implying the buildup of a domain with permanent dipole moments

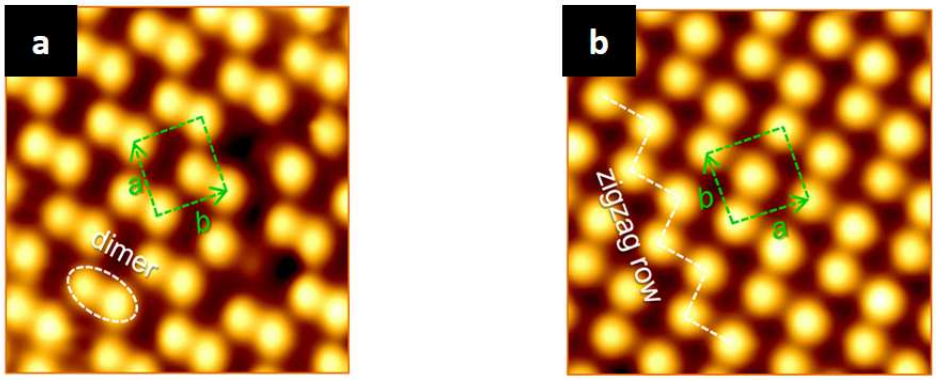

Figure 3.5: High-resolution scanning tunneling microscopy images of the zigzag (a) and dimer structures (b). The unit cells are denoted by dashed rectangles. A zigzag row is denoted by dashed line in (b) and an iodine dimer is denoted by a dashed ellipse in (a), from [115].

perpendicular to the surface [116]. This process is common to ionic termination and in the case of $CH_3NH_3PbI_3$ may play a role in the hysteretic behavior of IV curves [117]. If capable of penetrating sufficiently in the crystal, the local electrostatic potential generated by the charged terminations would induce an accumulation of photoexcited electrons at the surface. In this context, the of polarizabitity of MA^+ cations of organic cations may play an essential role. For example, the reorientation of surface MA^+ dipoles, which strengthens the interactions with surface iodine anions, might be responsible for the surface iodine dimerization. Therefore, the surface MA^+ dipoles weaken the surface polarity, leading to a stabilization of the surface structures.

3.4 Inorganic sublattice Pb-X_3 and moderation of electronic properties

3.4.1 Fröhlich polaron model

As discussed in the introduction, LHPs possess unique structural and optoelectronic behavior still under debate and their possible relationship deserve serious scrutinity (Fig. 3.6). One of the main questions about LHPs properties is the existence of strong electron-phonon interactions leading to charge carrier screening, which could explain the moderate carrier mobility compared to classic semiconductor as well as their relatively high carrier diffusion length and defect tolerance [118, 119]. The role of strong electron-phonon in LHPs mechanism has been frequently discussed, in particular the electron-phonon interactions leading to the formation of a polaronic state, where an electron or a hole deforms the lattice in its vicinity and becomes more localized [120, 121]. A polaron formation should lead to an increase in the effective carrier mass [122] and should significantly impact the electrical and optical properties of the material. Until recently, conventional Fröhlich interaction (discussed in Section.2.2.2)

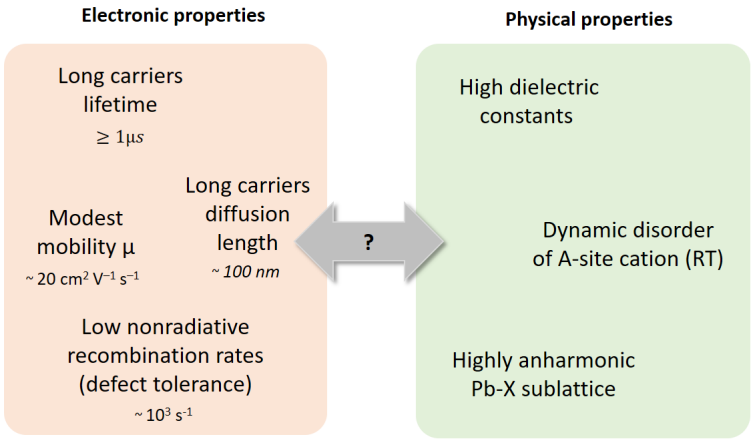

Figure 3.6: Main remarkable LHPs electronic and physical properties, as well as possible relationship between them.

and coming from the ionic nature of perovskite crystals has been mainly considered to be the polaron formation mechanism in halide perovskites [19, 119, 123]. Experimental and theoretical evidence suggested that room-temperature charge-carrier mobilities in LHPs are fundamentally limited by Fröhlich interactions between charge carriers and the electric fields associated with the longitudinal optical (LO) phonon modes of the ionic lattice Pb-I [118, 124, 125, 58, 126, 110]. Fröhlich mechanisms are known to dominate the high-temperature regime for many ionic semiconductors. But surprisingly, lead halide perovskites as $MAPbBr_3$ and $CsPbBr_3$ have and electron and hole mobility values limited around 200 $cm^2.V^{-1}.s^{-1}$, while classical ionic semiconductors, such as GaAs, have a room-temperature hole and electron-mobility of 450 and 9000 $cm^2.V^{-1}.s^{-1}$, respectively [127]. The lower value of carrier mobilities in lead halide perovskites can be explained by a relatively strong ionicity of the metal-halide bond, the low energy of the longitudinal optical phonon mode involving the oscillation of heavy lead atoms, as well as the slightly larger effective charge-carrier masses [128]. At room temperature, strong anharmonicity and dynamic disorder have been observed in several methylamnonium lead halide by Sendner et al., such as in MAPbBr, $MAPbI_3$, $MAPbCl_3$ [123]. Using Fröhlich's polaron theory and Feynman extension, polaron's effectiv mass m^* and the Fröhlich coupling constant α were determined. As shown on Fig. 3.7, effective mass and Fröhlich coupling constant of $MAPbBr_3$ are one order magnitude higher than the one of classical semiconductor GaAs. Furthermore, the polaron mobility is clearly lower in the case of methylamnonium lead halide than in GaAs, as expected. Despite only moderate polaron masses, the low LO phonon frequency and high ionicity of the LHPs fundamentally limit the charge carrier mobilities in these materials. Nevertheless, charge extraction properties in LHPs remains excellent as shown through the charge diffusion length which depends on the charge-recombination lifetime, which is equal to higher than the one in typical GaAs. Carrier diffusion length was generally reported around 50 μin GaAs [129], around 100 nm in polycrystalline $MAPbI_3$ [35] and from 10 μm to even exceeding 3 mm in single crystal $MAPbI_3$

[130, 131].

	Effective mass[a] m^*_{ex}/m_0	Ionic screening $1/\varepsilon^*$	Coupling constant α	Polaron mass m_P/m^*_{ex}	Polaron radius l_P [Å]	Mobility μ [$cm^2 V^{-1} s^{-1}$]
$MAPbI_3$	0.104[53]	0.17	1.72	1.36	51	197
$MAPbBr_3$	0.117[53]	0.18	1.69	1.35	43	158
$MAPbCl_3$	0.20	0.22	2.17	1.48	27	58
GaAs[57]	0.067	0.016	0.068	1.01	40	7000

[a] In units of the free electron mass m_0.

Figure 3.7: Determined polaron parameters and LO phonon scattering limited carrier mobilities at room temperature. Extracted from [123].

Strong ionicity of the LHPs could link the charge-carrier mobilities with their composition: using smaller halides could lower the charge-carrier mobilities, while substituting lighter metal as Tin could increase the longitudinal phonon frequencies and then improving mobility values. As the longitudinal optical phonon is primarily associated with the oscillation of the ionic metal-halide sublattice, the A-site cation should have almost no influence on the intrinsic charge-carrier mobility limits.

3.4.2 Solvation picture and strong phonon anharmonicity

While the Fröhlich interaction plays an essential role in ionic crystals, the strong phonon anharmonicity of halide perovskites should also be considered as it may lead to the formation of unconventional polarons [121]. Recent experiments lead to question the well-accepted Fröhlich carrier-phonon interaction and to take much more into account the liquid-like Debye relaxation mode at low frequencies of lead halide perovskites, as well as their soft and anharmonic characteristic , wherein the A-site cation size and halogen nature could strongly influence the softness of the lattice and optical modes damping through a coupling of acoustic and optical phonons. [132].

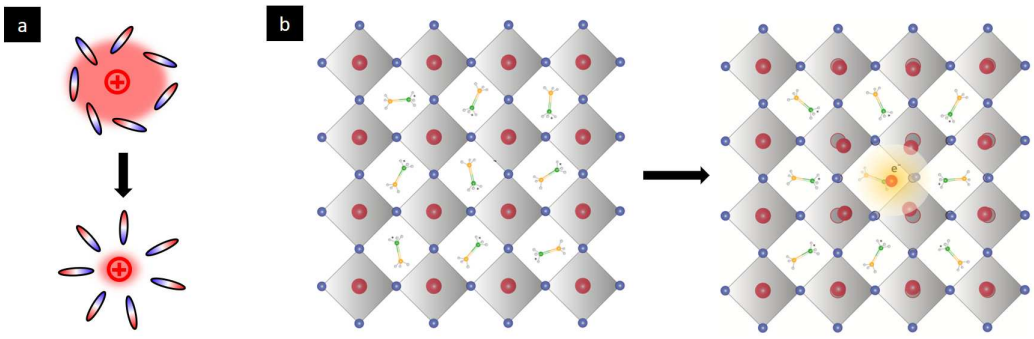

Figure 3.8: (a) Schematic representation of charge solvation in liquids. (b,c) Representation of lead halide perovskite multiple unit cells with A-cation being MA^+, before and after charge injection, respectively. Negatively charged electron gets screened by MA^+ molecules and Pb-X sublattice. Adapted from [133]

One of the main scientific questions in LHP field is to obtain relevant indicators to prove the relationship between charge carrier screening and lattice dynamics, leading to a protection of the particle against scattering and trapping, being able to explain the outstanding properties of LHPs. Having a clear picture of the electron-lattice interaction during charge excitation would help to understand how the lattice gets involved in this process. The chemical process of solvation is a good example to approximate what is going on in the LHP lattice. Solvation is described as the interaction of solvent with dissolved molecules. As pictured on Fig. 3.8.a, a charged particle placed in a solvent has a certain initial long-range Coulomb potential (red circle) caused by its charge. Furthermore, the randomly oriented and charged solvent dipoles will interact with the charged particle. More precisely, the solvent dipoles will tend to reoriente, leading to a reduction of the particle's Coulomb potential. This description of how a long-range Coulomb potential might be reduced by charge rearrangment is a very simplified picture to describe what might be going on in LHPs. Fig. 3.8.b presents several Methylammonium lead halide lattice unit cells. When an electromagnetic wave with an higher energy than the bandgap of the material is sent on it, mobile charges are generated. As previously described with the solvation model, the long-range Coulomb potential of the negatively charged electron is screened by the diverse charged molecules and ions located in the unit cell, as shown in Fig. 3.8.c. Reducing the Coulomb potential of the electron induces that the probability of interaction between the electrons with charged defects and other charges are lowered.

This liquid-like relaxation of polar phonons (originating from the ionic lattice) gives also rise to the dielectric solvation of their excited states, as shown by the temperature-dependent Stokes shift between absorption and emission in $MAPbBr_3$, $CsPbBr_3$ and $FAPbBr_3$ single crystals. [134] The temperature-dependences can be well-described by the solvation model explained above, but not by the Fröhlich polaron model anymore. Indeed, the Fröhlich model assumes that one electron is coupled to one isolated LO-phonon mode, based on the harmonic approximation. Nevertheless, we already discuss the strong anharmonicity as well as the liquid-like dynamic disorder of lattice modes in LHPs, making the Fröhlich polaron model incomplete.

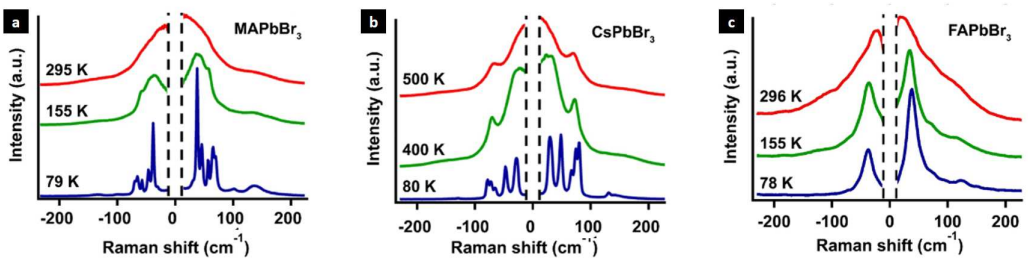

Figure 3.9: Temperature-dependent Raman spectra of hybrid and inorganic LHP crystals of (a) $MAPbBr_3$, (b) $CsPbBr_3$ and (c) $FAPbBr_3$ at different temperatures. Extracted from [135, 136].

Indeed, LHPs show high anharmonicity and dynamic disorder in the phonon modes, as presented in Fig.3.9. They are reflected in the broad central peaks in the low-frequency Raman

spectra of different single crystals ($MAPbBr_3$, CsPbBr3 and $FAPbBr_3$) in the room temperature phases [135, 136], therefore suggesting liquid-like local polar fluctuations. The nonzero modulation of the central peak in cross-polarized Raman spectra shows that the liquid-like fluctuation behavior is related to the PbX_3 sublattice motions. The anharmonic phonons with weak restoring forces as well as the large amplitude displacements contribute to the local polar fluctuations [39, 134, 135]. While former works proposed the role of organic cations to explain the solvation model, [137, 138, 139], the current consensus tends to believe that the responsible dipoles result mainly from the polarization of the Pb-X sublattice, irrespective of the cation type [140, 141]. This would imply that the polaronic stabilization of a charge carrier (i.e dynamic screening) comes mainly from the Pb-X sublattice [142]. The efficient dielectric screening present in LHPs could reduce scattering of charge carriers with others and with charged defects, which may explain the long carrier diffusion length and lifetimes in these materials [126, 143]. Moreover, long-lived charge carrier dynamics have been observed in ferroelectric semiconductor such as SbSI [144] and were explained by charge carrier interactions with thermally stimulated soft-phonon excitations, supporting the idea electron-soft phonon interaction could be harnessed to provide efficient charge carrier screening and leading to long charge carrier lifetimes.

3.4.3 Lattice vibrations in lead halide perovskites

Vibration modes in LHPs were particularly investigated during the last decade, using a plethora of different techniques. In order to have a better vision of the state of the art and the vibration modes involved in the anharmonicity of the structure, here is a summary from the recent literature.

IR spectra and Raman spectroscopy are common techniques used to study lattice and molecular vibration in materials. These techniques showed that Pb-X lattice vibrations take place in the lower frequencies range from 30 to 300 cm^{-1} (i.e 1-5 THz) [35], while molecular vibration of MA^+ cations are located at highest frequencies in mid-IR ranges as shown on Fig.3.10[135, 136, 145, 146, 147]. In the case of polar material such as $MAPbX_3$, longitudinal optical phonon frequency is higher than the transversal optical phonon frequency, inducing a LO-TO splitting. At room temperature, $MAPbI_3$ shows a mode at 63 cm^{-1} (equivalent to 66 cm^{-1} in $MAPbBr_3$) originating from disorder of the lead-halide framework that is coupled to fast reorientations of the methylammonium cation [113] and possibly accompanied by strongly anharmonic hopping of Pb and/or I [135].

Even though the conventional Fröhlich polaron picture is not sufficient, it might be important to consider the multiple LO phonons mode that were observed and attribute to this model [119, 151, 152]. In the case of $MAPbI_3$, 1 THz mode was attributed to the Pb-I-Pb twisting mode.

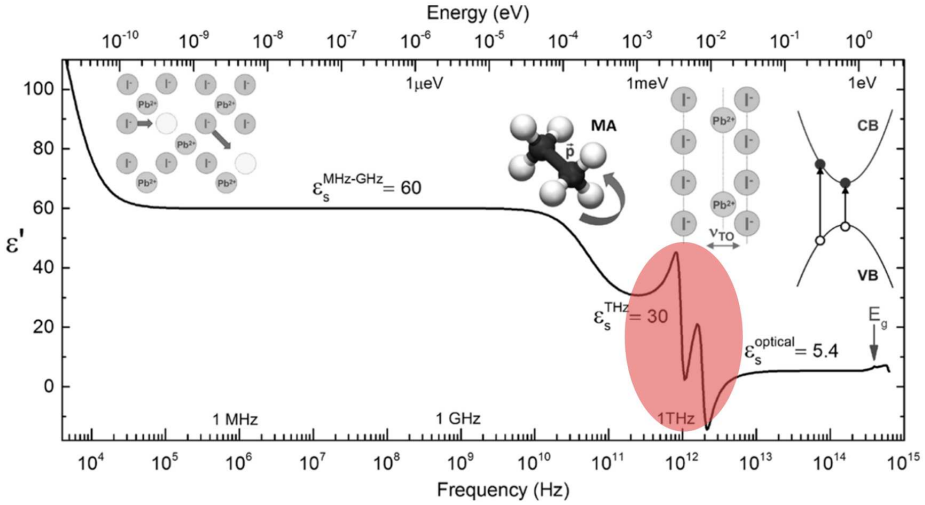

Figure 3.10: Frequency-dependent relative permittivity (real part) of $MAPbI_3$ at room temperature, derived from literature reports [146, 53, 148, 110, 149].Features around 48×10^{14} Hz are associated with electronic interband transitions, while the strong resonances near 1-2 THz derive from optical phonon resonances of inorganic sublattice. The increase near 100 GHz is related to collective reorientation of MA cations. The rise in the value of permittivity toward the low frequency regime originates from slow migration of ions. Adapted from [150].

A dominating mode at 3.5 THz was also observed, attributed to stretching mode, as well as a 5.1 THz mode related to the librational MA^+ modes. In $CsPbBr_3$, the dominating LO phonon was observed at 4.8 THz, and was related to stretching. The TO twisting mode Pb-X-Pb was also proposed to lead polaronic state by Park et al [153]. After performing transient absorption spectroscopy and photoexcitation at room temperature on $MAPbI_3$ sample, they observed a major influence coming from the Pb-I-Pb twist mode.

It is important to remind that despite a clear separation in energy between the low-frequency modes associated to the inorganic sublattice Pb-X_3 and the high-frequency modes associated with the A-site cation (Fig.3.10), significant coupling for them was found [154]. Soft modes were found at the boundary of the Brillouin zone of the cubic phase, consistent with displacive instabilities and anharmonicity involving tilting of the PbI_6 octahedra around ambient temperature.

3.4.4 Inorganic sublattice and electronic bandgap

Lead-halide bondings Pb-X have other highly important roles for perovskites properties. Pb-X-Pb bond angles influence particularly the bandgap, which is a crucial property for solar cell and photoemission application [155, 156]. The evolution of the band gap E_g is a consequence of the VB and CB position. Their energy is influenced by the orbital interactions, thus the

lattice size and lattice distortion. Band structure calculations show that the top of the valence band involves hybridized metal s and halide p orbital states. The orbitals s and p are related to the metallic and halide element's electronegativity χ, which therefore influence the top of the valence band energy. Playing with chemical composition of the metal-halide has an influence on the electronic properties, knowing that $\chi_{Pb} < \chi_{Sn}$ and $\chi_I < \chi_{Br} < \chi_{Cl}$ [157]. The bottom of the conduction band consists of metal p and halide s orbital states. The orbital overlap in the conduction band is smaller than in the valence band, therefore the hybridization is less pronounced. This leads to an higher ionic bond with a conduction band dominated by metal state. Furthermore, the conduction and valence band are both dependent of the lattice size, which is determined by the ionic radii of both anions and cations. A smaller lattice would for example lead to more confinement effects, which would shift the atomic levels slightly upward and therefore affecting valence and conduction band energy.

3.4.5 Electron-phonon coupling and polaron lifetime

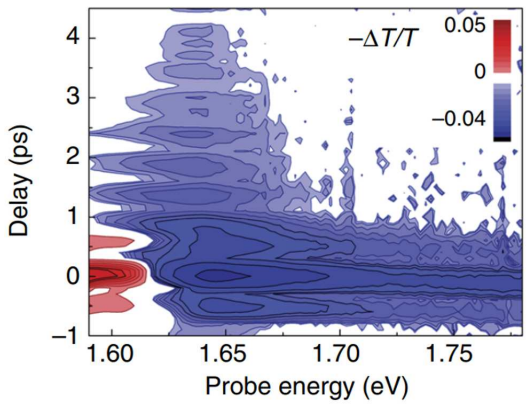

Figure 3.11: Strong electron-phonon coupling in $MAPbI_3$, between the 1.1 THz twisting Pb-I-Pb mode and the bandgap. Extracted from [158].

Strong electron-phonon coupling has been detected so far in LHPs, for exemple in $MAPbI_3$, related to twisting/bending Pb-I-Pb angle [158]. Kim et al used transient absorption spectroscopy to probe optical band gap modulation as shown on Fig. 3.11.a. They observed a coupling with the bandgap of the 1 THz mode. It would mean that the Pb-X-Pb twisting mode can modulate the bandgap in LHPs, and therefore that the equivalent 1.1 THz mode in $MAPbBr_3$ should exhibit strong electron-phonon coupling. Guo et al. [159] observed a coupling between the bandgap and an equivalent mode to 1.1 THz in $MAPbBr_3$ at 80K, assigned to a symmetric A_g mode. Finally, Bretschneider et al. [160] used THz time-domain spectroscopy to extract an approximate polaron formation time of 0.4 ps in $MAPbI_3$, $FAPbI_3$ and $CsPbI_3$.

Due to the soft lattice and the important anharmonicity, especially at room temperature, it is very hard to observe the phonon dynamics (likely related to polaron formation) in an excited

state, i.e. after the injection of free electrons into the structure. In this research work, we are focusing on the study of phonon systems in lead bromide perovskites ($MAPbBr_3$ and $CsPbBr_3$) in the electronic ground state. The objective is to excite the perovskites samples below the bandgap to avoid any charge carrier injection, using a THz wavelength, and get in resonance with the most polarizable phonon modes (Section.6.3 and Section.6.2). We aim to study the dynamic polarization response of the lattice to the THz excitation and to observe the phonon modes dynamics. Finding the main mode which dominates the dynamic lattice polarization response in the electronic ground states is indeed required to understand the carrier screening in the excited states.

3.4.6 OKE spectroscopy and looking-like coherent dynamics

There was no direct observation of polaron formation until Miyata et al.[58] studied LHPs with time-resolved optical Kerr effect (tr-OKE) spectroscopy, a technique usually used to study liquid-like systems such as water [161, 162]. The technique is explained in Section.6.1. This work provided a direct time domain view of below and above bandgap dynamics in $MAPbBr_3$ and its all-inorganic counterpart $CsPbBr_3$. While pumping far below and close to the band gap (respectively in the nonresonant and in the preresonant regime) at room temperature on single crystal $MAPbBr_3$, Miyata et al. observed significantly different dynamics depending on the A-site cation. In the case of the organic $MAPbBr_3$, they observed a flat non-oscillatory signal, decaying after few picoseconds and with a decay time depending on the pump pulse energy (Fig. 3.12.a). No particular frequency was observable in the Fourier Transform (Fig. 3.12.b) Interestingly in the case of the fully inorganc $CsPbBr_3$, long-lived oscillations appeared (Fig. 3.12.c), with frequency again highly dependent on the pump energy (Fig. 3.12.d). In the carrier injection regime, both $MAPbBr_3$ and $CsPbBr_3$ showed an exponential decaying dynamic. The below-bandgap signals in $MAPbBr_3$ were attributed to the transient polarization anisotropy caused by liquid-like reorientation dynamics of organic cations and lattice disorder, while the above-gap excitations were discussed in relation to polaron formation. On the other hand, the oscillatory features in $CsPbBr_3$ were attributed to potential coherently excited collective modes, such as phonons. Nevertheless, the strong dependence of the oscillatory frequency on pump energy contradicted this approach.

Studying nonresonnant and preresonnant regime below the LHPs bandgap is fundamental as several important process might take place in this range of energy, such as stimulated emission, polariton condensation, superfluoresence or photon recycling [163, 164, 165, 166]. Moreover, in order to establish the photophysical mechanism in LHPs, it is necessary to understand the ultrafast polarization response to light fields and the subsequent generation of charge carriers or excitons. As discussed previously, two main polarization contributions are commonly discussed in perovskite community : the deformation of the inorganic lattice cages and the reorientational motion of the organic cations, in the case of $MAPbBr_3$. It was suggested that these processes could subsequently lead to dynamic screening models and

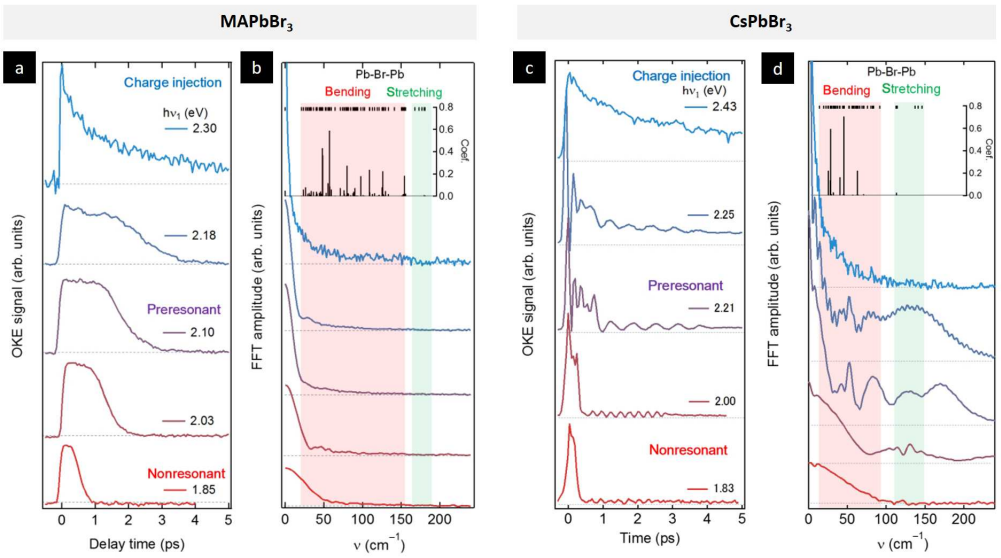

Figure 3.12: Time-resolved OKE spectra of $MAPbBr_3$ (a) and $CsPbBr_3$ (b) as a function of pump energy, with their Fourier components, (c) and (d) respectively. Black lines on top show calculated frequencies of normal mode. Reproduced from [58].

polaron formation.

3.4.7 Towards the concept of dynamical Rashba effect

Rashba effect in LHPs

As discussed in Section.2.3.2, Rashba effect is intimately connected to the presence of heavy nuclei, such as lead and possibly iodine in LHPs, which have a high SOC constant, and to the presence of inversion symmetry breaking [44, 167, 42, 103, 168, 169, 170]. Therefore, Rashba effect might appear in LHPs.

Understanding the reasons behind the reduced carrier recombination rate in LHPs, exceeding the predicted Langevin limit by 5 orders of magnitude [171], is one of the hottest topics in current perovskite research. It might also be one of the main reasons behind the impressive rise of photovoltaic efficiency of perovskite solar cells, now exceeding 22%. The heavy nature of lead and halide ions leads to significant spin-orbit coupling in many hybrid perovskites. This lowers the band gap and in absence of inversion symmetry may cause a splitting of the conduction band states with the lower, split-off band forming the conduction band minimun [44, 167, 42, 169]. As mentionned in Section 2.3, the indirect band gap of this electronic structure would slow down the radiative electron-hole recombination. The Rashba splitting and its origin are well studied in 3D hybrid perovskites such as $MAPbI_3$ [93, 93, 68, 172, 67, 173, 174, 175, 176]. However, the connection between the Rashba effect and the long carrier

lifetime remains controversial, as more detailed studies reveal no evidence for spin forbidden optical transitions in perovskites [172].

The different Rashba splitting experienced by valence band and conduction band introduce the different Rashba splitting terms, such as Δk the splitting wavevector and α the Rashba coefficient. It is important to note that both the splitting energy and the Rashba coefficient are much more prominent in the conduction band than in the valence band. This originates from the different density of states at the conduction and valence band edges. Indeed, the Rashba band splitting arises from the spin–orbit coupling effect and is dependent on the total angular momentum J of the electrons. As as consequence, it is expected that p-electrons experience a larger Rasbha splitting than s-electrons. VB maximum of the LHPs mainly consists of the $5p$ of I and a large portion of the $6s$ of Pb, while the CB maximum mainly consists of Pb $6p$ [177, 178] . Therefore, the Rashba splitting energy and coefficient at the CB is expected to be way larger than that of the VB. This property, may explain the recombination process in LHP solar cells. Indeed, the photogenerated carriers of conduction and valence band would thermalize at band extrema located at a different points in k-space. Therefore, radiative recombination which preserves k would be hindered as in the case in indirect band gap semiconductor.

Rashba effect in 2D LHPs

2D LHPs have particular interest to us, because their low dimensionality favor the apparition of the inversion symmetry breaking, particularly at surface terminations and interfaces [174, 179, 180]. Yu et al. recently investigated the magnitude and origin of Rashba splitting in 2D perovskites and demonstrated the correlation between the splitting magnitude and the octahedron distortions [181]. Furthermore, they noticed that different numbers of inorganic layers, spacer cations, and A-site cations have a great influence on the Rashba splitting through different mechanisms. Experimental studies showed that introduction of a halogen atom such as Chlorine or Bromide could lower the crystal symmetry, leading to non-centrosymmetric structures [182]. Others experimental and theoritical works studied of spin relaxation supporting the presence Rashba splitting in 2D LHPs [183] and predict a giant Rashba effect with a splitting energy of 40 meV [184]. Nonetheless, it remains unclear how the structure parameters influences the structural distortion and the splitting magnitude, and more importantly how to directly observe the conduction and valence band splitting.

Dynamical Rashba effect

The Rashba splitting requires in principle a noncentrosymmetric crystal symmetry. However, the assignement of the main LHPs space group symmetry is still debated. For exemple, $MAPbI_3$ was proposed for the space group symmetry $I4/mcm$ [38] as well as $I4cm$ space group [185], which may allow for polar ferroelectric distortion. Therefore and despite many attempts, $MAPbI_3$ crystal structure in the tetragonal stable phase at ambient temperature has not been fully understood, including the position of the organic cations. It is likely that the material

does not exhibit macroscopic ferroelectric behavior at room temperature [186] which would in principle prevent the occurrence of a static Rashba band-splitting. However, it has been proposed that structural fluctuations, possibly present at room temperature, might give rise to local ferroelectric domains which could extend beyond the characteristic Rashba length scale of few nanometers [187]. Therefore, a macroscopic and static lack of inversion symmetry might not be necessary since local electric field could give rise to a dynamical Rashba effect, i.e a spatially local Rashba splitting fluctuating on the picosecond timescale which is typical of MA^+ cation dynamics. [140, 188, 189].

3.5 Summary and open questions

This part allowed us to have a better understanding of the state-of-the art in LHPs and to summarize their properties, notably as a function of their size and chemical composition. The main properties are summarised in Fig. 3.13. The research presented in this thesis has the following objectives:

- Understanding the origin of the oscillations in OKE signal (Section 6.1).
- Control and characterize Raman-active mode dynamics in single and quadruple A-site cation LHPs using strong field THz pump source (Section.6.2 and Section.6.3). This would provide information on the most polarizable sublattice phonon modes that can participate in dynamical charge screening.
- Compare electrons relaxation dynamics in the conduction band of $MAPI_3$ in tetragonal and orthorhombic phase to understand the relationship between organic A-site cation and possible static screening (Section 7.1).
- Taking the first steps in the analysis of Rashba splitting in 2D perovskites using time and angle-resolved photoemission (Section 7.2).
- Characterise electron relaxation and charge recombination in quadruple A-site cation LHPs and compare their solar cell device performance with single A-site cation LHPs (Section 7.3).

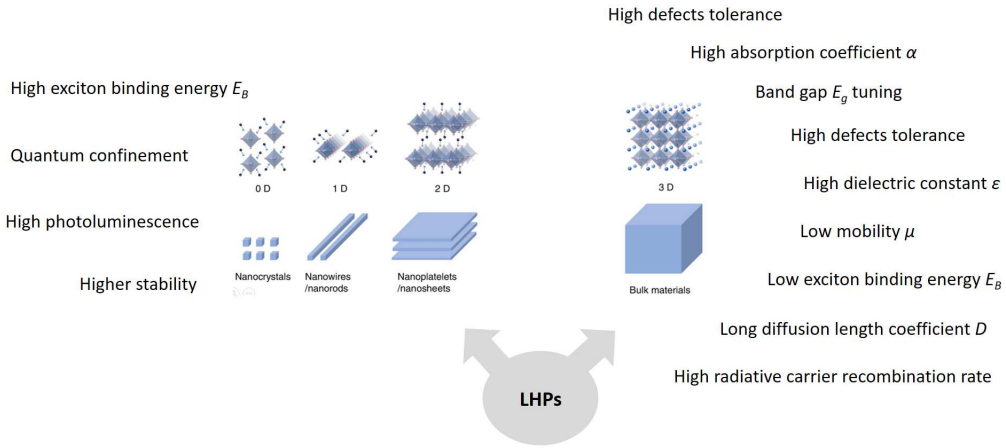

Figure 3.13: Main properties of LHPs.

4 Kerr Effect spectroscopy

The Kerr Effect spectroscopy is widely used in this research work, first through optical and then with Terahertz excitation. This chapter aims to give the reader a better understanding of Kerr Effect spectroscopy, what phenomena it allows us to study as well as giving a precise introduction to the experimental setup employed.

First, we define the Kerr effect through its widely spread experimental techniques, the optical Kerr effect (OKE). Second, an innovative technique of time-resolved Terahertz Kerr spectroscopy (TKE) is described. The later is used in order to observe Pb-Br lattice dynamics in different chemical composition of LHPs. In general Kerr spectroscopy, the electric field of a linearly polarized pump laser pulse creates transient anisotropy in the sample and the resulting birefringence is detected by the polarization rotation of the probe pulse, allowing to measure the system's response on a femto- to picosecond timescale. In this experiment, the lattice's sample are excited through a THz pump pulse. The general operation and parameters of the setup are discussed in this chapter.

4.1 Introduction to general Kerr Effect

4.1.1 Basic principles

Kerr effect was discovered in 1875 by the Scottish physicist John Kerr [190, 191]. Also called the quadratic electro-optic effect, it is defined as a nonlinear optical effect which can occur when light propagates in a medium. It can be represented as a change in refractive index of the medium caused by electric fields, and being proportional to the square of the electric field strength. Two different forms of Kerr effect does exist: the Kerr electro-optic effect (DC Kerr effect) and the optical Kerr Effect (AC Kerr Effect).

Kerr electro-optic effect takes place when a slowly varying electric field is applied to a medium, e.g. to a piece of glass using two electrodes. A light beam passing the medium can then experience a polarization-dependent change of optical phase which is proportional to the square of the voltage applied to the electrodes, i.e., to the square of the electric field strength.

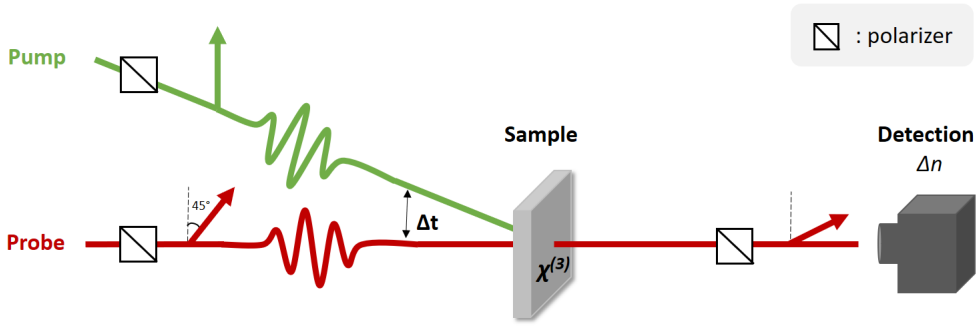

Figure 4.1: Basic sketch representing OKE experiment. Probe pulse (red) is polarized at 45° with respect to the excitation pump pulse (green). The birefringence Δn induced in the sample is measured by the change of polarization of the probe by the detection system. $\chi^{(3)}$ is the third-order electric susceptibility of the sample, connecting the different electric fields involved in the FWHM process.

In this work, we focus on the second form of Kerr effect, the optical Kerr effect (OKE). The later occurs without an externally applied electric field but is based on the electric field of a electromagnetic light wave only going through a medium (Fig. 4.1). The Kerr effect is originating from an instantaneously occurring nonlinear response, which can be described as a modification of the medium's refractive index. In the case of high intensity light beam, the refractive index is modified according to:

When a strong electric field E (e.g from an intense laser source) is applied to a medium, it induces an optical anisotropy in it. Therefore, the material can be characterized by two different refractive index values. One is parallel to the applied electric field E ($n_\perp$), the other is perpendicular to it ($n_\parallel$). The birefringence generated results in a phase difference Φ between the two parallel and perpendicular components [162]. Moreover, the induced birefringence $\Delta n = n_\parallel - n_\perp$ is related to the squared electric field:

$$\Phi = \frac{2\pi l}{\lambda}(n_\parallel - n_\perp) = 2\pi l B E^2 \tag{4.1}$$

with λ the light's wavelength, l its length traveled throughout the sample, B a constant.

In order to detect this birefringence variation, we consider that the electric field goes through two cross polarizers placed before and after the sample, then is detected by a diode detection system. When no birefringence is generated in the sample, no electric field is detected after the last polarized. When birefringence occurs in the sample, it results in a partial depolarization

of the light electric field and the diodes system detects an intensity signal I. The later depends on the phase shift Φ in the medium:

$$I = I_0 sin^2(\frac{\Phi}{2}) \tag{4.2}$$

with I_0 the initial intensity. For small values of Φ, the transmitted intensity is proportional to the square of the phase difference.

OKE belongs to the family of four-wave mixing (FWM) processes and involves four electric fields, which are the electric field of the incident beam probing the birefringence (i.e the probe); the electric field of the beam inducing the birefringence (i.e the pump), which acts at the second power according to Eq.2.17; and finally the light emerging from the sample. OKE is described by the third-order of nonlinear polarization $P^{(3)}_{NL}(t)$:

$$P^{(3)}_{NL,i}(t) = \int_{-\infty}^{t} dt' \int_{-\infty}^{t'} dt'' \int_{-\infty}^{t''} dt''' \chi^{(3)}_{ijkl}(t,t',t'',t''') E^{pr}_{j}(t') E^{pu}_{k}(t'') E^{pu}_{l}(t''') \tag{4.3}$$

with $\chi^{(3)}_{ijkl}$ the third-order electric susceptibility of the sample, while subscripts refer to the polarization directions of the different electric fields involved in the FWM process. The three electric fields on the right side correspond to the incident probe beam (E_j) and the two exciting pump beams (E_k, E_l), with their applied times t^n. On the left side, the time-dependent third-order nonlinear polarization refers to the fourth generated electric field from FWM, polarized along i.

In our time-resolved experiments, the electromagnetic fields are applied in the form of ultra-short light pulses of few femtoseconds, implying that the $P^{(3)}_{NL,i}(t)$ has a full physical meaning and can refer to ultrafast mechanism dynamics in the excited medium. The experiments can described as an intense excitation pump I_{pu} inducing birefringence at a given time in the sample and setting the time origin t_0 of the experiment, while a probe pulse I_{pr} is probing the residual birefringence induced by the pump in the medium with a variable delay τ (Fig.4.1). The detection system measured the intensity of the probe pulse transmitted after the second polarizer of the experiment as a function of time delay [162]:

$$S(t) \propto \int_{-\infty}^{+\infty} dt I_{pr}(t-\tau)[\int_{-\infty}^{t} R(t-t') I_{pu}(t')]^2 \tag{4.4}$$

with $R(t)$ is the response function of the system, related to third-order nonlinear susceptibility terms. The response function contains the electronic, ionic and molecular dynamics and is thus related to the several polarizability processes, as discussed later in Section.4.4.3 [162, 77].

In this research work, we use Kerr effect with two different objectives. Firstly, we propose an innovative experimental and theoretical approach of ultrafast polarization occuring in LHPs. For this purpose, Section.6.1 present our work using optical Kerr effect (OKE), meaning that the studied materials are excited with a laser-generated pump pulse having an energy of the optical electromagnetic domain. Secondly, we characterize the highest polarizable lattice

mode of diverse LHPs using Terahertz-induced Kerr effect (TKE). In this technique, the pump is not in the optical domain anymore, but in the THz region. The results of this work are presented and discussed in Section.6.2 and Section.6.3, while the technique is discussed in the following section.

4.2 Terahertz Kerr effect spectroscopy (TKE)

4.2.1 THz excitation

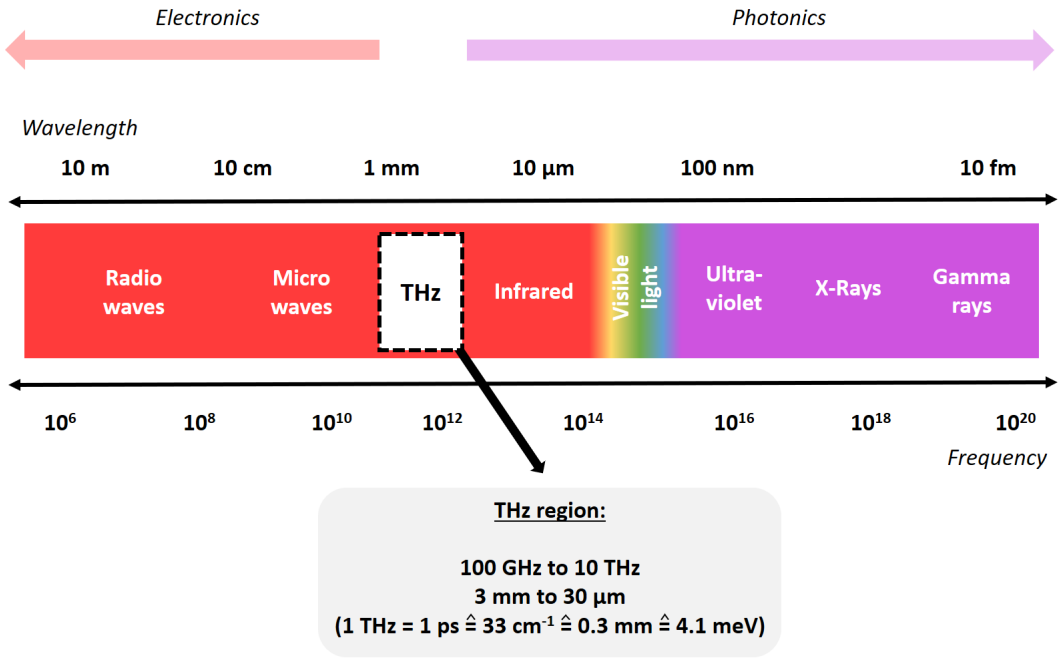

Figure 4.2: Frequency and wavelength regions of the electromagnetic spectrum, with a focus on the THz region.

It is important to remind here that most elementary excitations of solid state physics occur on THz energy and time scale. The photon energy of a THz radiation is resonant to lattice vibration (phonons) [192, 193]. Fig. 4.2 shows were the THz region is located in the frequency and wavelength regions of the electromagnetic spectrum. More exactly, 1 THz = 10^{12} Hz ≙ 1 ps ≙ 33cm^{-1} ≙ 4.1 meV. The THz electromagnetic wave can linearly probe phenomena having the same timescale, such as charge carrier scattering, electron-phonon equilibration or lattice dynamics

The lattice structure and its vibration determine numerous solid state properties, such as mechanical, thermal and electric ones. Therefore, the observation and the dynamic control of the lattice vibration might be very promising for phononic applications and to better

understand fundamental properties of certain materials such as LHPs [194, 195]. Among these, phonons are new key players to control ultrafast solid-state processes, notably using the lattice degree of freedoms to command these dynamics [196, 197, 198, 199]. In this research project, we worked with a novel nonlinear excitation mechanism able to couple with Raman-active phonon modes of LHPs sublattice using intense THz pump pulses. This aims to better understand the lattice dynamics in its electronic ground state (i.e without any carriers excitation) and to later have a better understanding of the lattice-carrier interaction inside these materials, such as carrier screening.

4.2.2 Motivation for THz-induced Kerr spectroscopy (TKE)

THz-induced Kerr measurements have already been successfully performed to study molecular orientation dynamics [77], as later discussed in Section.4.4.3. Time-dependent THz-induced Kerr signal has the particularity to highlight all the polarizibility processes related to the medium studied, namely always fast electronic response and potentially ionic dynamics or molecular orientation [162]. The magnitudes of the observed Kerr signals scale quadratically with the THz electric field amplitude expected, as expected for a nonlinear $\chi^{(3)}$ process (Eq.2.17).

THz wavelength allows to excite IR-active modes and nonlinearly Raman-active modes, in the case of strong fields. Lattice vibration modes and their dynamics and relaxation can be probed using time-resolved pump-probe experimental setup. Phonon lifetime in perovskite being in the range of about picosecond [135], a femtosecond laser system is necessary to resolve it. Furthermore, THz wavelength were often used as a probe in pump-probe experiment [148, 200, 201, 202] but rarely with such an intense pump. Indeed, before the last decade THz field strengths have been too small to induce observable higher-order nonlinear effects [77]. Femtosecond optical pulses have been used to produce a THz pulse, for example through optical rectification. To excite a material like LHPs, the THz pump pulse should have a relatively high power, which was made possible using amplified laser system.

Electro-optic sampling depends on the different timescales on which the pump and probe fields evolve. The THz pump pulse used in these experiments has a period of about 1 ps, while the probe pulse envelope is only 20 fs long. In order to reconstruct the material response to the THz field, the experiments requires many repetitions of the experiment with different pump-probe delays τ. The probe pulse has to be shorter than the sample property evolution to be able to observe them, meaning the probe pulse duration limits the temporal and frequency resolution of the pump-probe experiment. Moreover, the phase matching should also be optimal between the phase velocity of the pump and the group velocity of the probe. The scientific achievements of this thesis require a specific THz source, that combines high intensity and short pulse durations for the probe. To meet these expectations, a high power THz laser system was used.

4.3 High power THz laser system

4.3.1 MHz oscillator

The whole laser system and time characterization from data acquisation and delay stage are seeded by an ultrafast pulse Coherent laser oscillator which acts as a clock and the reference time, with its 78.77 MHz repetition rate and 20 fs pulse duration. This system is a mode locked oscillator composed of the common laser components (gain medium, cavity, pump energy source).

The seed pulses then exit the oscillator and are separated into two paths: one is used for the probe and will not be modified (neither in wavelength nor in power). The other one used for seed pulses which will be routed to the kHz amplifier and then to the $LiNbO_3$ crystal to generate THz pump pulses.

4.3.2 kHz amplifier

In order to provide intense THz pulse, the oscillator pulse energies need to be amplified, which also requires a decrease of their repetition rate, reduced to 1 kHz. Pulse amplification need severals steps, explained in the following subsection.

Regenerative amplifier

kHz regenerative amplifier (Coherent Legend Elite Duo USP). The oscillator beam is separated by a pass filter, with one path being used as the probe, and the other one for the pump. This beam first propagate through 2 Faraday isolators, in order to prevent back reflections into the oscillators, that could cause severe damage.

The main goal of the amplifier is first to stretch the pulse, then to amplify a lot their power using gain medium and finally to compresse the high energy pulse. Thus, the seed pulses are stretched by a grating stretcher before entering in the regenerative amplifier (RegA). To prevent excessive peak intensity able to damage the optical components, this grating stretcher induces a large group velocity dispersion that stretch the femtosecond pulses to the order of picosecond pulses.

The stretched seed pulse go through a first Pockels cell[I] (PC1) , which rotates its polarization, allowing the seed to go through the cavity windows. Then, the seed pulses are coupled into

[I]Pockels cell: device consisting of an electro-optic crystal [II], having electrodes attached to it and through which a light beam can propagate. The phase delay in the crystal, originating from Pockels effect, can be modulated by applying a variable electric voltage. The Pockels cell acts such as a voltage-controlled waveplate.

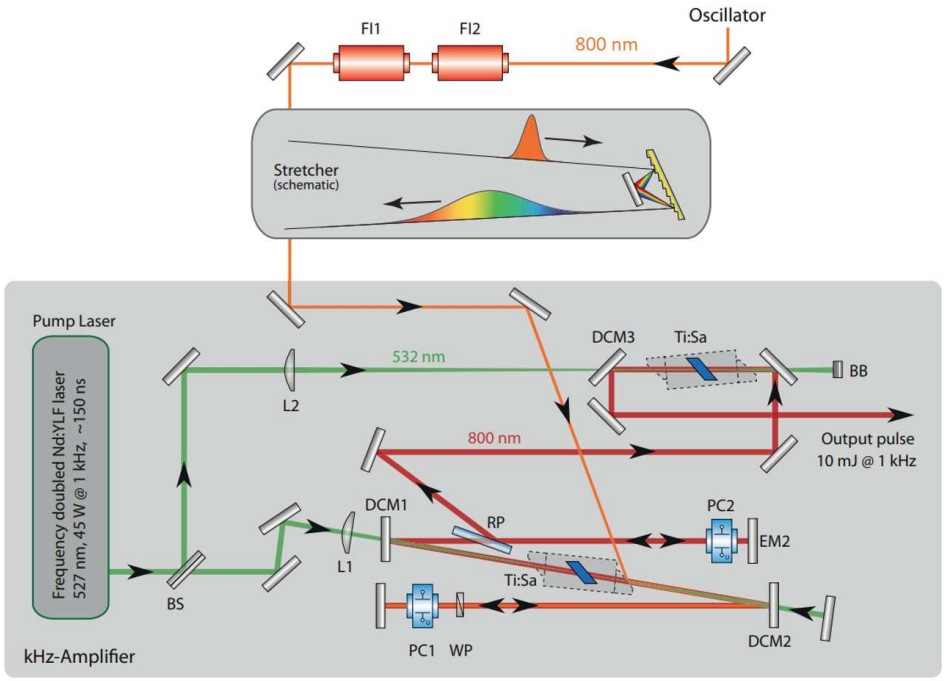

Figure 4.3: Sketch of the regenerative amplifier (RegA) and single pass amplifier (SPA). Oscillator seeds first go throught two Faraday isolators (FI1 and FI2) preventing back reflections. Then, they are stretched by a grating stretcher before entering the RegA. A waveplate (WP) and the switching of the Pockels Cell (PC1) allows the seed pulses propagation through the first Ti:Sapphire crystal (Ti:Sa). Ti:Sa is pumped by a 527 nm pump LASER, which is recycled between the two dichroic mirror (DCM1 and DCM2) The polarization of the generated 800 nm pulses rotate after switching the second Pockels cell (PC2) and are further amplified in the a second Ti:Sa crystal (Ti:Sa). Extracted from [75].

a laser cavity composed of a Ti:Sapphire crystal in order to amplify the stimulated emission over several roundtrips in the cavity. At the same time, the Ti:Sapphire crystal is pumped by a frequency doubled Nd:YLF laser (Coherent Evolution-HE, 527 nm, 45 mJ at 1 kHz repetition rate, about 150 ns pulse duration).

Single pass amplifier

The pulse is again amplified by propagating through a single-pass amplifier, which is another Ti:Sapphire crystal (Ti:Sa), pumped by the same Nd:YLF pump laser used in the regenerative amplifier. This last one and the second pass amplifier leads to uncompressed output pulses with 10 mJ pulse energies at a repetition rate of 1 kHz and a central wavelength of 800 nm. The pulses are then further amplified in a cryogenic single pass amplifier.

Cryogenic pass amplifier

This single pass amplifier is again composed of a Ti:Sapphire crystal as active medium for amplification. Its particularity is to be enclosed in a Helium cryostat operating at 62K under a 10^{-8} mbar pressure. These cryogenic conditions are necessary to ensure the amplified and highly powerful pulses coming from the previous single pass amplifier are not damaging the Ti:Sapphire crystal. Furthermore, it also takes advantage of the temperature dependent gain profile, leading the final pulse energy to a 18 mJ power. The active medium is pumped by two Revolution laser.

Compression

The pulses are then separated by beamsplitters and directed to three different path of compressors. Each of them are composed of a pair of parallel fold reflection gratings that recompress the pulses to 35 fs, leading to a gain in peak power. The kHz amplifier system finally produces three output beams, including the output later used to generate THz. It provides 5 mJ pulse energy with a pulse duration of about 35 fs at a central wavelength of 800nm.

4.4 THz Kerr Effect Setup

4.4.1 THz generation : optical rectification in $LiNbO_3$

Exciting Raman-active phonon modes in LHPs requires high field THz to allow nonlinear excitation process. Therefore, amplified pulses coming from the kHz amplifier are directed to an optical rectification setup where single-cycle THz pulses are generated using tilted-pump-pulse-front scheme in a $LiNbO_3$ crystal [203].

THz pump pulse generation and path

The beam coming from the Cryo-amp is directed to the THz generation setup Fig. 4.4. This beam is a 800nm central wavelength beam with 6 mJ pulses stretched to approximatively 80 fs at 1 kHz repetition rate. The pulses are used to excite a Lithium Niobate $LiNbO_3$ crystal through the tilted pulse front method [204, 203]. The tilted pulse front is achieved by imaging the laser spot on a grating (G) followed by two cylindrical lenses (CL1 and CL2) into the $LiNbO_3$ crystal. A half-waveplate allows to tune the grating efficiency and therefore the pulse power applied on the $LiNbO_3$ crystal. THz pulses are generated by the optical rectification process in the $LiNbO_3$ crystal and reach a short focal length parabolic mirror (PM1). The THz radiation is cleaned from the remaining 800nm pump beam using a Teflon scatterer (TS). For the purposed of our experiments, a THz vertically-polarized polarizer fix the polarization of the radiation (TP1), that is then collimated by a 2-inch parabolic mirror (PM2). In order to control the THz radiation power, two other polarizers are placed on the beam path: a motorized THz polarizer

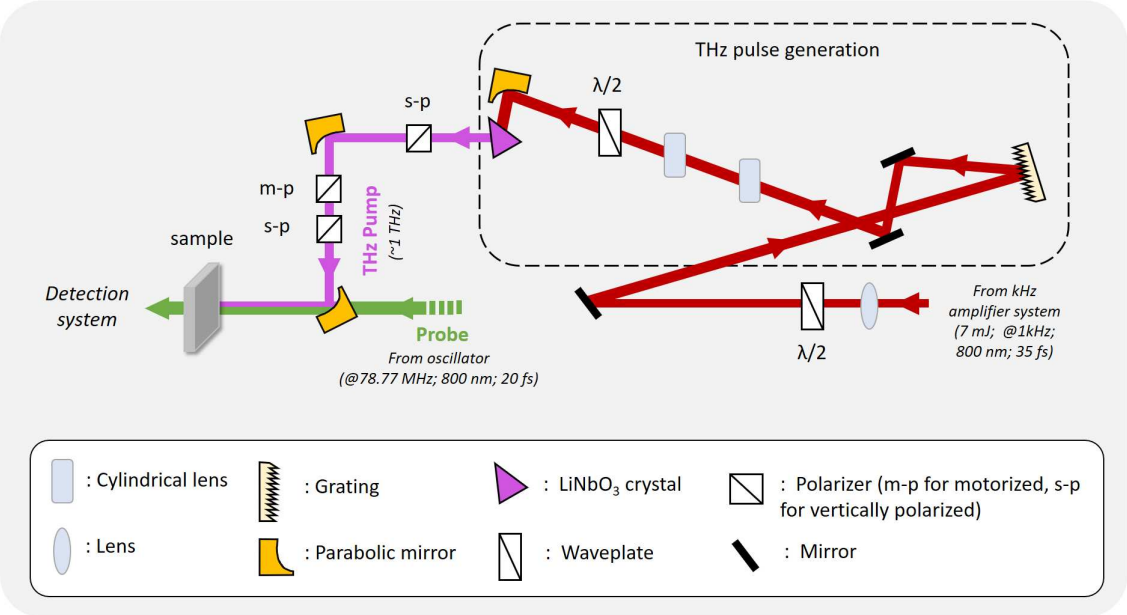

Figure 4.4: THz generation setup.

(TP2) and again a fixed THz s-polarizer. Finally, the THz radiation is focussed with the probe beam on the sample by a parabolic mirror (PM3) [205].

Optical rectification

Several THz sources use optical rectification to convert strong laser pulses to THz frequency range pulses. Optical rectification consists on the simultaneaous interaction of two intense light waves with respective frequencies ω_1 and ω_2 and with a large second order nonlinear susceptibility term $\chi^{(2)}$, that enables the generation of a nonlinear polarization response $P_{NL}^{(2)}$. $P_{NL}^{(2)}$ contains a non-oscillating term $\omega = \omega_{1,2} - \omega_{2,1} = 0$ which is called *rectified* term [71]. In our case, we are using ultrashort laser pulses containing a spectrum of frequencies, broadening the initial spectral line $\omega = 0$ and finally reaching finite frequencies around the THz range. Unlike typical generation crystals as GaSe or ZnTe, $LiNbO_3$ crystal requires even more drastic condition to achieve high conversion efficiencies, particularly for the phase matching Δk. Indeed, the pump pulses group velocity necessarily have to match the THz field's phase in the crystal in order to minimize the phase mismatch and therefore to generate efficiently THz single pulses. For this purpose, a pulse front tilt is realised, meaning that the pulse front experiences a delay across the cross section of the beam, while the phase front of the NIR beam remains perpendicular to the travel direction. It is equivalent having the beam laterally segmented and the segments continuously delayed in time. This segmentation of the beam is made possible by a combination of the reflective grating (G) and a 4f telescope, as shown on Fig.4.5. The $LiNbO_3$ crystal has one side face cut in the same angle, allowing to

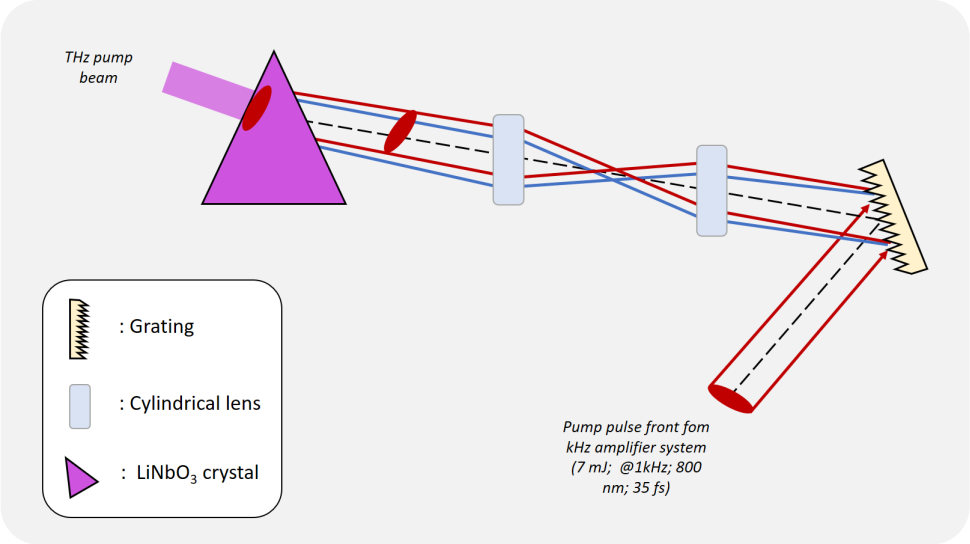

Figure 4.5: Optical rectification in $LiNbO_3$ and generation of THz pump pulses.

emit THz radiation with wavefronts perpendicular to the surface [206]]. A 1.3 mol-% MgO doped stoichiometric LiNbO3 crystal is used. The pump pulse front tilt inside the crystal generates a THz spectrum centered at ≈1 THz. The Lithium Niobate source generates 1 ps duration, near single cycle pulses with a spectrum from 0.1 – 2.5 THz peaked at about 1.2 THz and field strengths of up to 1.5 MV/cm at the sample as shown on Fig. 4.6 . The typical THz spot diameter on the sample is ≈ 300 µm (gaussian FWHM diameter). The THz electric field evolution was determined with electro-optic sampling method (EOS) in a 50 µm z-cut quartz.

The linearly vertically-polarized THz pulse then lead onto the sample with three parabolic mirrors. The generated excitation and dynamics in the sample are probed by the probe pulse arriving from the amplified system oscillator output (repetition rate @ 78.77 MHz). The optical probe parameters are detailed in the following subsection. The probe is collinearly overlapped and temporarily delayed with respect to the Terahertz pump path. The probe polarization is set at 45° with respect to the s-polarised (i.e vertical) THz pulse. The later induces change in birefringence in the sample because of Kerr effect [77]. This induced birefringence causes probe field to acquire phase difference between the polarization components parallel and perpendicular to the pump field. The phase difference is later detected by a combination of half-waveplates $\lambda/2$ (HWP) and quarter-waveplate $\lambda/4$ (QWP), followed by a Wollaston prism which spatially separates the incoming light beam into two separate linearly polarized outgoing beams with orthogonal polarization. The intensity of these two beams is detected by two photodiodes. As the induced birefringence is relatively small, the difference intensity between the two photodiodes is proportional to the induced birefringence. The precise detection mechanism is further explained in the following subsection.

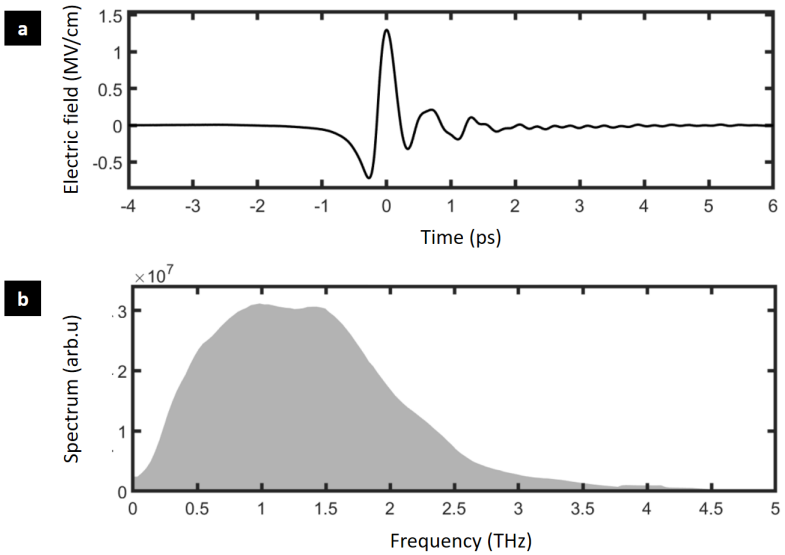

Figure 4.6: THz electric field spectrum from $LiNbO_3$ source with (a) temporal and (b) frequency spectra.

In these Terahertz Kerr effect experiments, a linearly polarized optical probe with a wavelength energy smaller than the bandgap of the semiconductor we want to study is used to interrogate the sample properties, particularly to follow the change of birefringence in the material. In our setup, a ≈ 1 nJ, 25 fs linearly polarized pulses with 800 nm central wavelength with 80 MHz repetition rate pulses coming from the oscillator is used to probe the sample dynamics. For the purpose of pump-probe measurement, the probe pulses are mechanically delayed with respect to the THz pulses with a motorized linear translation stage (NEWPORT GTS-150 controlled by a NEWPORT XPS controller). The optical probe beam is focussed through a hole in the parabolic mirror (PMx) in order to follow the sample response. The probe beam properties, particularly its intensity and its polarisation are translated into an electrical signal in the detection system detailed below.

4.4.2 Detection Mechanism

Electro-optic detection

The electro-optic detection system used in the setup is represented on Fig. 4.7. A motorized broadband half-waveplate ($\lambda/2$) controls the probe polarization. The probe spot size on the sample in the focus is around 50 µm (gaussian FWHM diameter). During the interaction with the samples excited with THz pump pulse, the linearly polarized probe can acquire polarization rotation θ or ellipticity change ν. The change in polarization is detected by the balanced detection setup. It consists in a quarter-waveplate, a motorized half wave plate, a Wollaston

prism and balanced photodiodes. The quarter waveplate ($\lambda/4$) converts the incoming probe beam with ellipticity ν to a linear beam. The motorized half-waveplate compensates the polarization rotation created by the sample. The Wollaston prism (WP) aims to split the beam into two orthogonally polarized component beams, respectively recorded on photodiodes, able to resolve 80MHz pulse train. The both photodiodes (PD1 and PD2) record the difference of the two component beams. When there is no probe polarization change because of the absence of pump induced polarization change, the two components have equal intensity on the photodiodes. In contrary, a probe beam polarization rotation θ leads to an imbalance of the two component beam intensities and generates signal in the photodiodes.

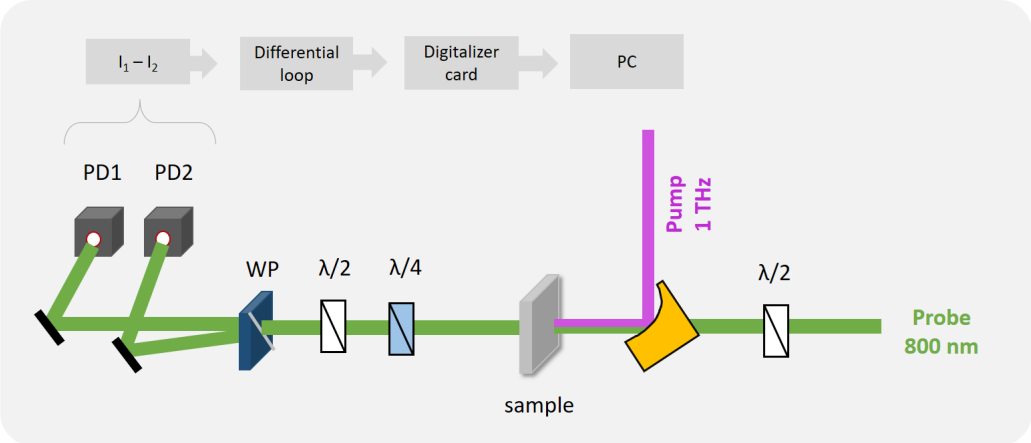

Figure 4.7: Detection system.

The difference signal between the two photodiodes ΔI directly measures the change of polarisation:

$$\Delta I = \frac{1}{2}\epsilon_0 c(|E_1|^2 - |E_2|^2) = I_0 \sin\Gamma \tag{4.5}$$

with ϵ_0 the vacuum permittivity, E_1 and E_2 the electric field measured by the photodiode 1 and 2 respectively, Γ the relative phase retadation between the two projections E_1 and E_2.

Data acquisition and signal-to-noise improvment

Signal(τ) is reconstructed by varying the pump-probe delay τ and repeat the measurement. The motorized translation stage is operated in a "fast scan mode", allowing to scan the entire pump-probe delay range in one continuous motion while recoding the position whenever an electrical signal arrives on the photodiodes. The motorized delay stage position is synchronized to the 1 kHz laser repetition rate. This detects the pump induced modulation of the difference current of the two photodiodes $\Delta I = I_1 \neg I_2$ due to polarization changes of the probe.

To detect and isolate the pump-induced dynamics in the samples, electrical background subtraction was performed using a specific electronic delay line [75, 205]. The latter behaves as an interferometer : the electrical signal j containing the pulse and obtained on the diode is separated by a voltage divider dimensioned for the experiments, which separates the incoming pulses into a transmitted and a deviated part. The transmitted pulse $(j+1)$ got sign reversed because of reflection at the end of the delay line and is superimposed with the deviated pulse j. The transmitted pulse signal is finally $\delta_1 = (j+1)–j$, leaving only the pump induced signal change $\delta 1$, which is then amplified x100 in a broadband signal amplifier before the data acquisition. The same process happens to the pulse j and $j-1$, which are again superposed, allowing to isolate the signal δ_2 = -δ_1. These two signal components are detected by the digitizer card.

4.4.3 From polarization to lattice dynamics

Relation between n and $\chi^{(3)}$

Initial linear refractive index n_0 is described as Eq.4.6 and the nonlinear refractive index n is obtained by its Taylor expansion as shown on Eq.4.7:

$$n_0^2 = 1 - \chi^2 \tag{4.6}$$

$$n^2 = n(E)^2 = 1 + \frac{\partial P}{\partial E} = 1 + \chi^{(1)} + \chi^{(2)} E + \chi^{(3)} E^2 \tag{4.7}$$

As LHPs are supposed to be centrosymmetric, χ^2 term is cancelled. Δn is obtained by approximating the difference of Eq.4.6 and Eq.4.7, leading to a relationship between the variation of probe polarization Δn and the pump electric field E:

$$n(E)^2 - n_0 = 2 n_0 \Delta n \propto \chi^{(3)} E^2 \tag{4.8}$$

A relationship can finally be set up between Δn and the polarizability α of the medium:

$$\Delta n \propto (\alpha_e + \alpha_{ion} + \alpha_{mol}) \tag{4.9}$$

Polarizability measurement

This subsection provides a short overview of the Terahertz Kerr spectroscopy used in the following experiments, as well as a state of the art of the previous use of THz-induced Kerr effect. We focus on the physical processes observed by this techniques (Fig. 4.8).The balanced detection system measured the change of birefringence by following the probe polarization angle Θ, which can be defined as followed:

$$\Theta \approx \frac{\Delta n \omega_{probe} L}{c} \tag{4.10}$$

with $\Delta n = n - n_0$ the change in refractive index compared to the original probe polarization, L the thickness of the sample, c the electric field velocity. The nonlinear polarization originating from the four wave mixing (FWM) emits a cross polarized new signal field which mixes with the transmitted probe field and thereby creates an effective change of the total transmitted light field's polarization at frequencies close to probe frequencies. This gives information of polarizability dynamics in the studied material. It is important to be careful with the term of n as a physical refractive in our experiments: the change of birefringence that we measured on the diode with the rotation of the probe by the angle Θ is not correlated to the linear refractive index of the sample but to the nonlinear electric field generated in the sample by nonlinear FWM process. Thus, the change in birefringence that we observe is only related to the third order of nonlinearity $\chi(3)$.

The induced polarization $P(\omega_{probe})$ can be expressed with linear and nonlinear term, as a function of probe and squared pump frequency. The nonlinear term $\chi^{(2)}$ is considered null in the case of LHPs which are considered centrosymmetric on a macroscopic scale:

$$P(\omega_{probe}) = \epsilon_0(\chi^{(1)}E(\omega_{probe}) + \chi^{(3)}E(\omega_{pump})E(\omega_{pump})E(\omega_{probe})) = \epsilon_0\chi_{eff}E(\omega_{probe}) \tag{4.11}$$

with $\chi^{(1)}E(\omega_{probe})$ is equivalent to linear polarisation response, while the term with $\chi^{(3)}$ originates from the third-order nonlinear polarization $P^{(3)}_{NL}$. Using the Eq.4.8, a relationship is obtained between the change in refractive index obtained at the photodiodes Δn and the third-order non linear susceptibility $\chi^{(3)}$, related to the microscopic polarizability of the material:

$$n^2 - n_0^2 \approx 2n_0\Delta n = \chi_{eff} - \chi^{(1)} = \chi^{(3)}|E(\omega_{pump})|^2 \propto \Delta n \tag{4.12}$$

Therefore, the two THz electric field E_{THz} interactions (originating from nonlinear Kerr definition) lead to THz polarizability-related transient birefringence, which is probed by the visible probe pulse E_{pr} in an effective 3^{rd} order nonlinear process.

$\chi^{(3)}$ response follows the polarizibality dynamics in LHPs. The change of birefringence Δn enables to access to both the instantaneous electronic polarizability α_e and ionic lattice contribution α_{ion} as discussed in Chapter 2. In principle, the molecular reorientation polarizability is also accessible with these experiments, but the pump frequency might not be able to excite the one in the lead halide perovskite system.

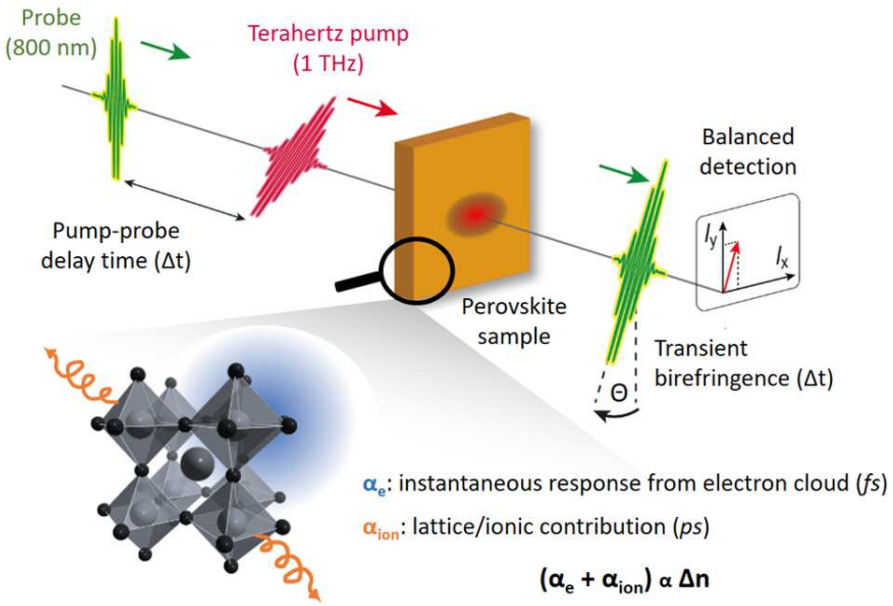

Figure 4.8: Sketching representation of the Terahertz Kerr spectroscopy applied on lead halide perovskites. The sample is excited by a pulse centered at ≈ 1 THz. The instantaneous electronic response α_e as well as the lattice dynamic contribution α_{ion} are detected by the change in birefringence of the linearly polarized probe. The signal is obtained by the balanced double-diodes detection system, measuring Θ variation. Adapted from [133].

TKE in liquids

LHPs was never studied with Terahertz Kerr spectroscopy so far, but Terahertz induced Kerr effect was already performed on liquids [77] as well on some solids as Diamond [207]. Fig. 4.9.a shows Terahertz Kerr signal for various liquids. A main peak at $t = 0$ ps is observed in all liquids, related to the instantaneous electronic response α_e. It is followed by some decay features, which vary in function of the chemical composition of the liquids. These oscillations correspond to molecular reorientation vibration α_{mol}. In order to ensure that the observed physical process originating from the Terahertz kerr effect are observed, it is necessary to verify that the allegedly Kerr signal is quadratic to the electric field strength as demonstrated on Fig. 4.9.b. In comparaison, Fig. 4.9.c shows a Diamond THz-induced Kerr signal. In this material, only the instantaneous electronic polarizibility α_e is visible, given that the ionic lattice mode vibration is at 40 THz. Therefore, it cannot be excited and observed with a ≈ 1 THz pump, as the one used in our experiment.

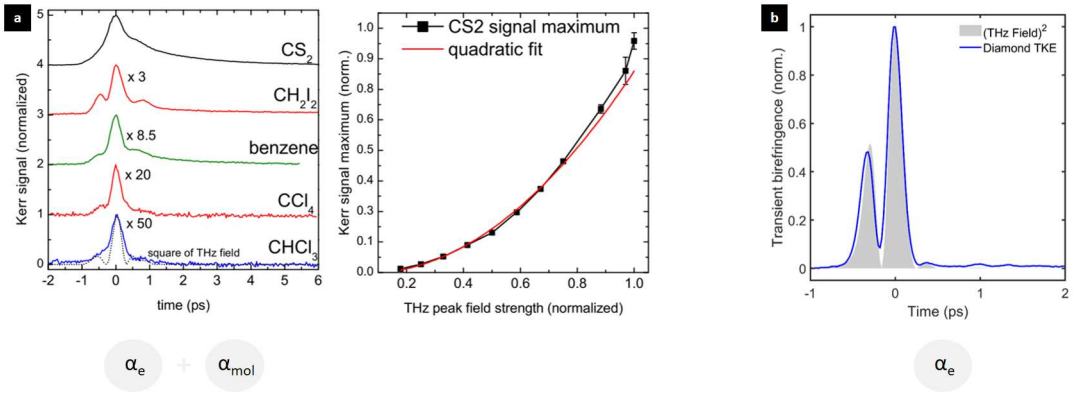

Figure 4.9: (a) TKE signal for various molecules extracted from [77]. Instantaneous electronic response α_e and molecular polarizability α_{mol} are observed. (b) TKE signal of Diamond. Only the instantaneous electronic response α_e is observed, as diamond lattice modes are to high frequency ($\approx$ 40 THz) to be excite by our $\approx$ 1 THz excitation pulse.

4.5 Materials

4.5.1 Single crystals for OKE

$MAPbBr_3$ and $CsPbBr_3$ single crystals

For the synthesis of $CsPbBr_3$ single crystals, the precursor solution (0.38 M) was prepared by F. Wang and B. Xiang from X.-Y. Zhu group at University of Columbia, using mixing cesium bromide (CsBr, Aldrich, 99.999%) and lead bromide (PbBr2, Aldrich, 98%) with molar ratio of 1:1 in dimethylsulfoxide (DMSO, EMD Millipore Co., anhydrous 99.8%). After being fully dissolved, the solution was titrated with methanol (Alfa, 99.9%). Then it was further stirred at 50 ∘C until a yellow permanent suspension formed. The solution above the yellow precipitate is filtered and serves as the precursor solution for the crystal growth. Methanol was used as the anti-solvent for slow vapor diffusion and the crystal growth was quenched when the desired morphology was achieved. A similar method was used for the preparation of $MAPbBr_3$ single crystals. All the details can be found in the supporting information of [133].

(4cat)$PbBr_3$ thin films

Glass substrates including BK7 glass and microscopic slides were cleaned with Hellmanex 2% water solution followed by sonication, then sonication in aceton and isopropyl alcohol, and dried with nitrogen flow. Glass substrates were further treated in UV–ozone chamber before the deposition of perovskite layer. The aforementioned chemical compositions were composed by mixing the appropriate amounts of powder precursors in DMF and DMSO solvents. The perovskite solutions were deposited with spin coating and the optimized program for each

composition and thickness. For all samples except $CsPbBr_3$, 200 of chlorobenzene was poured on the spinning sample. The layers were annealed at 100°C during 1 hour in a nitrogen-filled glove box.

5 Time and angle-resolved photoemission spectroscopy

5.1 Photoemision

5.1.1 A technique for electronic properties studies

Photoemission is a resulting process of the photoelectric effect, discovered by Hertz in 1887 [208] and explained later by Einstein in 1905 [209]. It can be explained as the emission of so called photoelectron after the interaction of an electromagnetic radiation, such as light, and a material. In a condensed matter systems, electrons occupied distinct states of well-defined binding energy. When a light quanta $h\nu$, also called photon, delivers more than the specific binding energy to an individual electron, the later might be emitted into free space with excess energy (also named kinetic energy E_k). The kinetic energies distribution of the binding energies give important information about the binding energy distribution in the atomic, molecular or crystalline system.

Photoemission is not limited to studies of core levels, it can also analyze valence and conduction electrons. The wave functions of these electrons combine to form delocalized states over the entire solid so-called Bloch states [I] in a periodic crystal. A Bloch state corresponds to the coherent propagation of an electronic wave characterized by a wave vector. These states form a continuum (also called energy band) which determines electronic properties, for example charge transport. The wave vector is determined from the emission angle of the photoelectrons making it an important element for precision measurements.

The first experimental determination of a band structure by photoemission was obtained by Spicer et al. in 1964 on a copper sample [210]. The particularity of this type of photoemission is that it allows a conservation of the component parallel to the surface of the wave vector.

[I] In a periodic potential, Bloch's theorem states that solution to the Schrödinger equation take the form of a plane wave, modulated by a periodic function. Functions of this form are known as Bloch functions or Bloch states. In condensed matter physics, they are suitable basis for the wave functions or electrons state in crystalline solides. They are written : ϕ(r) = e(ik.r)u(r) , where ϕ is the wave function, k the wave vector represents the crystal momentum vector, r the position, u a periodic function with the same periodicity than the crystal.

The conservation laws of the energy and the wave vector (its parallel component) enable to obtain the band structure in angle-resolved photoemission experiments. From the energy and the angle of emission of the photoelectron, it is possible to determine the energy and the wave vector of the initial state of the electron and thus to obtain information on its dispersion relations, i.e. on the band structure of the material.

Within a solid, the mean free path of electrons, i.e the average distance between two inelastic shocks, is very short in matter. With photon energies from IR, UV to X, the photoelectrons come from the atomic planes in the immediate vicinity of the surface. Photoemission is therefore a surface sensitive technique which requires to master the preparation and the non-roughness of the surface. As in my experiments, the samples are cleaved under ultra-high vacuum (<10^{-9} Torr) to avoid the presence of impurities.

ARPES allows to determine experimentally the band structures of the samples as well as the dispersion relations and the topology of the Fermi surface [II], which is crucial for many physical properties such as electronic transport. It also gives access to the energy, the wave vector, the spin as well as some symmetries such as the parity of the Bloch states. It has a central role in the study of surface states, especially in the case of low dimensional systems with complex electronic properties. It is a spectroscopic technique particularly well adapted to the study of systems with strong correlations. Indeed, its high energy resolution allows to study in detail low energy excitations such as band gap opening or to highlight electron-electron interactions.

5.1.2 Principle of electrons photoemission

We have seen that the absorption of light, or more precisely radiation, by the electrons of a material, whether it is a solid, a molecule or an atom, can lead to their extraction from the solid. For this to happen, light must provide the energy necessary to break the bond that holds the electron to the rest of the system. The study of photoemitted electrons then provides information on the spectrum of occupied states of the material.

There are two types of electrons that can be distinguished according to the following categories: (i) the core electrons that are located on an atom and thus have a marked atomic character.

[II] In the case of metals, the band theory imposes that the valence band is filled with electrons up to the Fermi energy and denoted E_f. In quantum physics, Fermi energy can be described as the kinetic energy of the highest occupied state. Fermi energy is often used to refer to a different but close concept, called the Fermi level or electrochemical potential. The Fermi energy is only defined at absolute zero, while chemical potential is defined for any temperature. Because of wave-particle duality, the energy of each electron is described by a wave vector associated with it, written k. Electrons with an energy equal to the Fermi energy E_f have a wave vector whose norm is given by $k_F = \frac{\sqrt{2mE_F}}{\hbar}$. All these vectors form a closed surface known as Fermi surface. The properties of the metal are determined by the shape of the Fermi surface in reciprocal space.

(ii) the valence electrons are delocalized in states associated with chemical bonds and can extend over the entire system. These are less bound to the solid and form a continuum, also called energy band. This band is filled by satisfying Pauli's rule of one electron per state and is called the valence band. The energy of the last occupied state in a metal defines the Fermi level or energy. This Fermi level corresponds to the zero state of the binding energy E_B. The binding energy of a state is the energy needed to bring the electron to the Fermi level. The work function corresponds to the energy necessary to extract an electron from the Fermi level and send it to out of the crystal with zero kinetic energy (this energy reference is called the vacuum level). Typically, the workfunction of most materials is between 4 and 6 eV. The core electrons, strongly bound to the atoms, need photons of about ten to a few tens of keV to be photoemitted (of the order of X-rays), while the valence and conduction band electrons will need only a few eV.

In the case of a free particle, the relation between the energy and the wave vector, called the dispersion relation, is an isotropic quadratic form:

$$E(\vec{k}) = \frac{\hbar^2 k^2}{2m} \tag{5.1}$$

In a solid, the interaction with the atoms necessarily makes this relation more complex and the knowledge of the dispersion relation E($\vec{k}$) is essential for the understanding of the electronic properties of the solid. In the case of a valence or conduction state, the photoemission technique measures both the kinetic energy $E(k)$ and the wave vector of the photoelectron K, therefore making possible to reconstruct the wave vector of the electron in the solid k and its dispersion relations. This type of measurement based on angular resolution is called angle-resolved photoemission spectroscopy.

5.2 Angle-resolved photoemission spectroscopy (ARPES)

5.2.1 General description

Angle-resolved photoelectron spectroscopy (ARPES) consist in the excitation of a electron by an incident photon with energy $h\nu$, so called photoelectron, which is then emitted outside the characterized material. Photoelectrons are later collected by an electron energy analyzer, which measures both their kinetic energy E_{kin} and their momentum K by detecting the polar emission angle Θ and the azimutal emission angle Φ. These values allow to extract information on the momentum k of the electrons in the solid and on the binding energy E_B. ARPES experiment geometry is represented on Fig. 5.1, while the energy balance of the photoemission process between the characterized solid and the analyzer is sketched on Fig. 5.2.a.

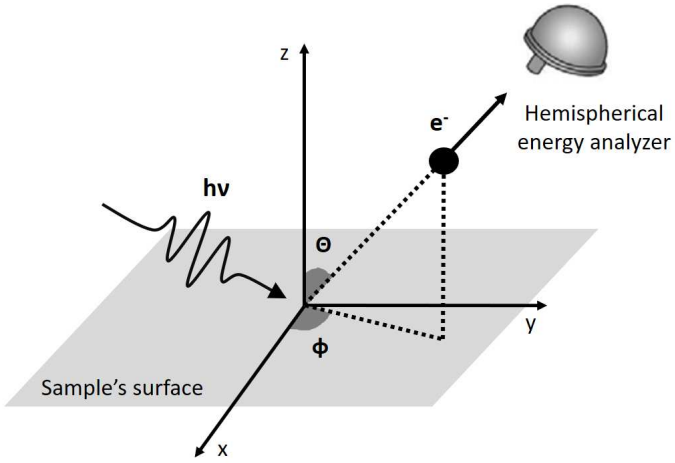

Figure 5.1: Experiment geometry of the ARPES technique.

Photoemission spectroscopy is based on the laws of conservation of energy and momentum. It is possible to determine the band structure of the solid from the measurement of the energy and emission angles (Θ and Φ) of the photoelectrons. In vacuum, the energy of the photoelectron is:

$$E_{kin} = h\nu - E_B - \phi \tag{5.2}$$

$$k_f - k_i = k_{h\nu} \tag{5.3}$$

with E_B the binding energy, $k_{h\nu}$ the incoming phonon wavevector, k_f and k_i respectively the final and initial wavevector. The photoelectron wave vector is $K = p/2m$. The modulus is $K = \sqrt{2mE_{kin}}/\hbar$ while the parallel $K_\parallel$ ($K_\parallel = K_z + K_x$) and perpendicular $K_\perp$ ($K_\perp = K_y$) components to the sample surface are obtained from polar θ and azimuthal ϕ emission angles:

$$K_x = \frac{1}{\hbar}\sqrt{2mE_{kin}}\sin\theta\cos\phi \tag{5.4}$$

$$K_y = \frac{1}{\hbar}\sqrt{2mE_{kin}}\sin\theta\sin\phi \tag{5.5}$$

$$K_z = \frac{1}{\hbar}\sqrt{2mE_{kin}}\cos\theta \tag{5.6}$$

When the electron reach the surface, the translational symmetry in $x-y$ plane is preserved, inducing $k_{\parallel} = K_{\parallel}$ and therefore:

$$k_{\parallel} = \frac{2\pi}{\hbar}\sqrt{2mE_{kin}}\sin\theta \tag{5.7}$$

The momentum parallel resolution can be expressed as:

$$\Delta k_{\parallel} = \frac{2\pi}{\hbar}\sqrt{2mE_{kin}}\cos\theta\Delta\Theta \tag{5.8}$$

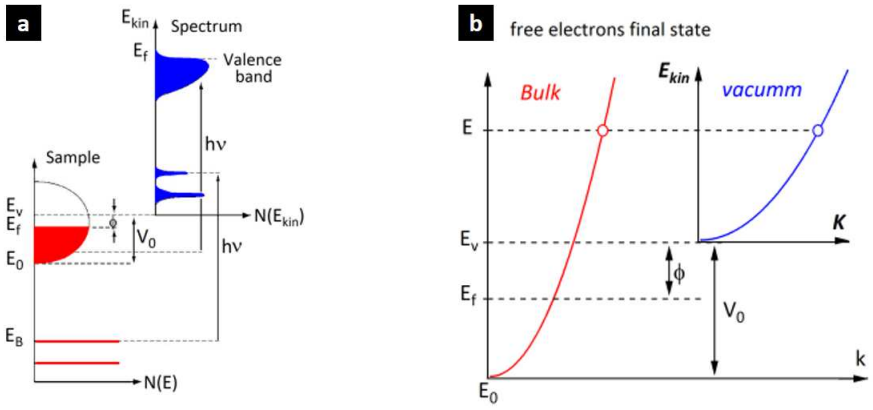

Figure 5.2: (a) Energy distribution of the photogenerated measured as a function of their kinetic energy E_{kin}. Density of states of the solid in terms of the binding energy (left), with Fermi level E_F corresponding to the zero binding energy. (b) Free-electron dispersion comparison in the vacuum (right) and in the final bulk state (left) Extracted from [211, 212].

The translational symmetry leads to the conservation of $K_{\parallel}$ but it does not impose a condition for perpendicular $K_{\perp}$. Indeed, the symmetry is broken in this direction and $k_{\perp}$ is not conserved. The relation between $k_{\perp}$ and $K_{\perp}$ is a function of the band structure of the material and the internal potential V_0. Since photoelectrons have a high kinetic energy, it is possible to neglect the periodic potential of the solid and to consider that the final states in the solid can be described by the free electron approach, i.e assumption is made for the dispersion of the electron final state $E_f(k)$, which is represented by a parabolic dispersion as shown on Fig. 5.2.b. The electron final state can be expressed as follow:

$$E_f(k) = \frac{\hbar k^2}{2m} - |E_0| = E_{kin}\sin^2(\Theta) + \frac{\hbar k_{\perp}^2}{2m} - |E_0| \tag{5.9}$$

with E_0 the energy at the bottom of the valence band. Using equation 5.2, the perpendicular component of the electron inside the solid is written as follow:

$$k_{\perp} = \frac{1}{\hbar}\sqrt{2m(E_{kin}+V_0)cos^2(\Theta)} \tag{5.10}$$

with V_0=$|E_0| + \phi$ defined as the inner potential, i.e the energy of the bottom of the valence band referenced to the vacuum level. The determination of $k_\perp$ is therefore reduces to the determination of the inner potential V_0, which can be obtained either experimentally with an hemispherical analyser or from theoretical band structure calculations. In ARPES, the complete knowledge of the crystal wavevector are challenging, but in the case of 2D system, the dispersion of the z-axis is negligeable [213].

5.2.2 Hemispherical analyser

After photoemission from the sample, photoelectrons are detected in the vacuum by a detector measuring their kinetic energy E_k and their direction of emission K. As discussed previously, these measurements allow to determine the energy and the component parallel to the surface of the wave vector $k_\parallel$. Fig. 5.3.b represents the energy balance of the photoemission process from the solid to the analyser, where the Fermi level E_F is taken as a zero reference. The left part of the diagramm represents the density of states of the electron inside the sample we aim to characterize. The photoelectron spectrum measured by the analyser is drawn on the right part. Photoelectron are extracted from the sample at the energy $E_F - E_B$. The black electrical link represents the electrical contact between the sample and the spectrometer. The chemical potential of the coupled system is separated from the vacuum level (dot line) by the spectrometer work function Φ, defining the minimum thermodynamic work required to remove an electron from the solid to a point in the vacuum immediately outside the solid surface. Using the energy conservation law and measuring the kinetic energy E_k allow us to retrive the binding energy E_b indicating the primary energetical position of the photoelectron, from Equation 5.2:

$$E_B = h\nu - \phi - E_k \tag{5.11}$$

In the case of hemispherical electron analyzer (Fig. 5.3.a), the analyzer entrance slit contains an electro-optical lens which enable a selection of the photoelectron analyzed in function of their kinetic energy. In the hemispherical detector, the photoelectron beam is deflected by electrostatic fields. The trajectory of the electrons depends on their kinetic energy, which allows the selection in energy of the photoelectrons. The detectors also monitor the emission angle of the photoelectrons, which allows to derive the their wave vector k as a function of the emission angle. The simultaneous knowledge of the two quantities E_k and k is necessary to obtain the initial state of the electrons.

In our FemtoARPES setup, an hemispherical electron energy analyzer collects the emitted photoelectrons and measures their kinetic energy E_{kin} and their momentum, using two emission angles: the polar angle θ and the azimutal angle ϕ. From these values, it is possible to find out the binding energy E_B and the momentum k of the electrons of the sample surface, to later defines its electronic band structure.

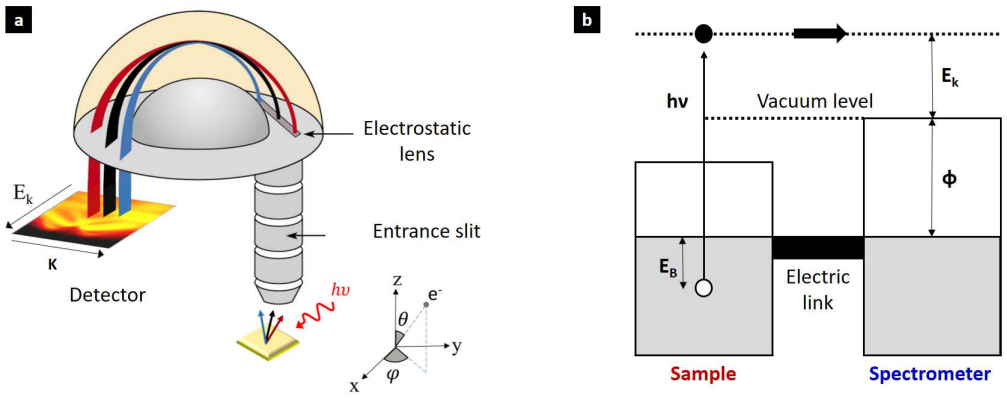

Figure 5.3: (a) Schematic view of a hemispherical electron analyzer, adapted from [214]. (b) Energy relation between sample and analyzer.

In order to extract the binding energy E_B, the analyzer's work function has to be taken into account. This offset-value can be beforehand experimentally measured. Fig. 5.3.b shows how the Fermi level E_F of the sample and the analyzer can be lined up by considering them connected by an electrical contact. The binding energy E_B is determined using this reference.

5.2.3 Photoemission intensity

To obtain the initial state of electrons in a solid, it is first necessary to understand the different mechanisms taking place, from the absorption of the photon by an atom to the detection of the emitted electron. The simplest model is the three-step model that divides photoemission in three separate processes: the optical excitation, the propagation towards the surface and the refraction of surface.

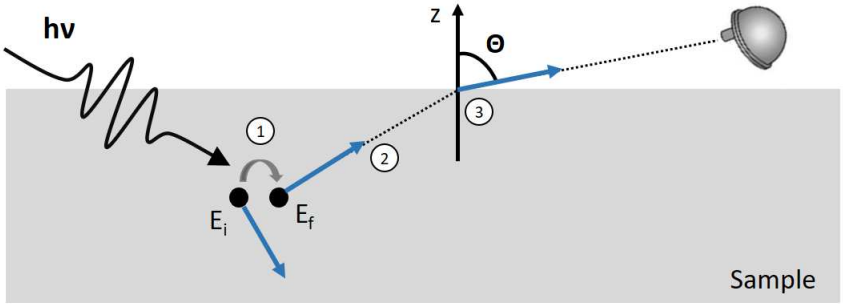

Figure 5.4: Three steps model representation with (1) optical excitation, (2) propagation towards the surface, (3) surface crossing and detection.

Optical excitation

First, a photon of energy $\hbar\nu$ is absorbed by an electron of energy E_i. This step is called optical excitation. The final state is an excited state $E_i + \hbar\nu$. The probability of this electronic transition depends on the energy and polarization of the photon, the initial and final states and the geometry of the experiment. One can also define this transition as an optical transition between two states of an infinite crystal. This type of transition satisfies the conservation of the wave vector, which implies that the initial and final states are characterized by the same wave vector $\vec{k}$, defined inside the first Brillouin zone. We note them $\langle\phi_k^{(i)}|$ et $\langle\phi_k^{(f)}|$, so that the transition probability is written :

$$w_{fi} = \frac{2\pi}{\hbar} |\langle\phi_k^{(f)}| \hat{H_{int}} |\phi_k^{(i)}\rangle|^2 \delta(E_f(\vec{k}) - E_i(\vec{k}) - \hbar\omega) \tag{5.12}$$

with H_{int}, the interaction Hamiltonian. Thus, final state $E_f(\vec{k})$ depends on the initial phonon energy used. The matrix element $|\langle\phi_k^{(f)}|\hat{H_{int}}|\phi_k^{(i)}\rangle| = M_{fi}$ contains the essential physics of the transition process and the Dirac δ [III] corresponds to energy conservation law.

Propagation towards the surface

The second step is the propagation of the photoelectron in the solid from its position during the absorption of the photon. A priori the photoelectron can propagate in all directions but only the electrons propagating towards the surface will be able to leave the solid and be detected in the detector. In solids, high energy electrons interact strongly in the medium, which leads to inelastic collisions. The photoelectrons that have lost some of their energy have also lost the information of the initial state. These electrons are called secondary electrons and contribute only to the background noise, visible in the experimental spectra. Only the electrons that have not collided are of interest for photoemission, they are called primary electrons. However, inelastic scattering mechanisms limit the depth probed by photoemission and only the electrons emitted near the surface can leave the solid without having undergone inelastic scattering. Inelastic collisions are described phenomenologically by the inelastic mean free path (IMFP), which represents the average distance between two inelastic shocks experienced by an electron in a solid. These inelastic shocks limit the lifetime of the electronic state of the photoelectron. Inelastic collisions are described by the inelastic mean free path parameter λ, which represents the average distance between two inelastic shocks experienced

[III] The Dirac distribution or Dirac function, can be informally considered as a function which takes an infinite value at 0, and the value zero everywhere else, and whose integral over $\mathbb{R}$ is equal to 1. The Dirac δ function is very useful as an approximation of functions whose graphical representation has the form of a large narrow point. It is the same type of abstraction that represents a ponctual charge, mass or electron. By extension, a Dirac or a Dirac peak, is used to designate a function or a curve peaked at a given value.

by an electron in a solid. These inelastic shocks limit the lifetime of the electronic state of the photoelectron. The inelastic mean free path depends on the kinetic energy of the electrons. This energy dependence is called universal because observed in all materials. This graph shows that to be less sensitive to the surface, it is necessary to use either photons of high energy (several keV) or photons of very low energy (less than 10 eV).

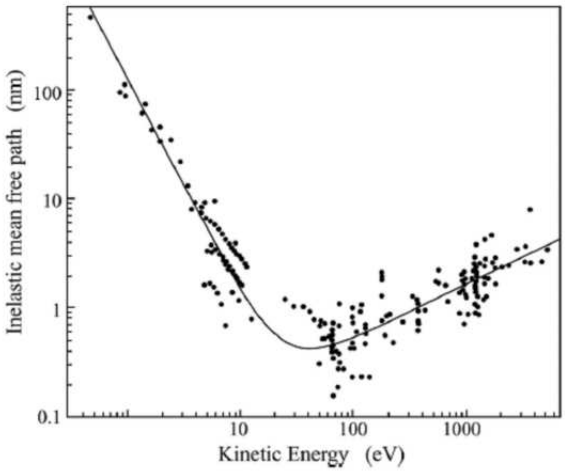

Figure 5.5: Universal mean free path for electrons inside solids depending on their kinetic energy [215]

The inelastic mean free path depends on the kinetic energy of the electrons. As the probability that a photoelectron created at distance z from the surface does not undergo an inelastic shock varies in $exp^{-z/\lambda}$. The photoemission yield I(z) decreases exponentially with the depth as a consequence of the inelastic scattering:

$$I(z) \propto I_0 e^{-z/\lambda \cos(\theta)} \tag{5.13}$$

with I_0 the initial beam intensity, z the initial depth of the photoelectron, λ the wavelength of the excitation pulse, and θ the angle of photoemission with respect to the normal of the surface. This explains why the photoemission only probes a thickness of the order of lambda below the surface. The surface sensitivity of this technique has important consequences, since it requires surface preparation to ensure atomic scale order, as well as ultra-high vacuum technology to keep the surfaces clean.

Surface crossing and detection

The last step is the crossing of the surface which constitutes a potential barrier for the electrons. This process obeys to conservation laws associated with the symmetry of the problem. The surface constitutes a potential barrier which breaks the invariance by translation of the

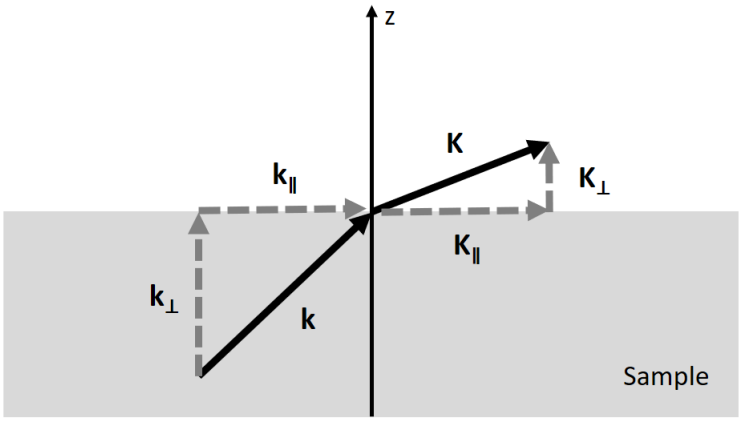

Figure 5.6: Surface crossing and evolution of parallel and perpendicular wave vectors.

crystal in the perpendicular direction. This barrier absorbs part of the kinetic energy of the photoelectrons and decreases the component of the wave vector perpendicular to the surface $K_{\perp}$ (Fig. 5.6).

5.3 Two-photon photoemission (2PPE) for time-resolved ARPES (tr-ARPES)

5.3.1 Studying time-resolved electron dynamics

Characterizing ultrafast dynamics of electrons in materials such as lead halide perovskites is technically feasible using time-resolved pump-probe spectroscopy with short laser pulse duration (around hundred femtoseconds). The combination of time-resolved and angle-resolved spectroscopy enable to probe the electronic structure dynamics with k-space resolution.

In time-resolved ARPES, two femtosecond laser pulses are used in a so-called pump-probe configuration. The different components of TR-ARPES are depicted on Fig. 5.7.a and Fig. 5.7.b respectively. The pump pulse is a femtosecond pump pulse ($h\nu_1$) creating an out of equilibrium excited state in the sample at time zero t_0, while the probe pulse ($h\nu_2$) is used to eject the electrons from the surface into the hemispherical analyzer, to measure its kinetic energy E_k and momentum K. This technique is commonly named two photon photoemission (2PPE). Pump pulse can create different excited states in a semiconductor, by promoting electrons from the valence to the conduction band. The probe pulse is used to detect these different excited states and to follow their dynamics. By gradually delaying the arrival time of the probe pulse with respect to the pump pulse (Δt), the relaxation process are characterized in time, from tenth of femtoseconds to hundreds of picosecond. The different steps of relaxations processes we aim to study in lead halide perovskites are therefore accessible, such as electron-electron scattering, electron-phonon scattering and Rashba splitting.

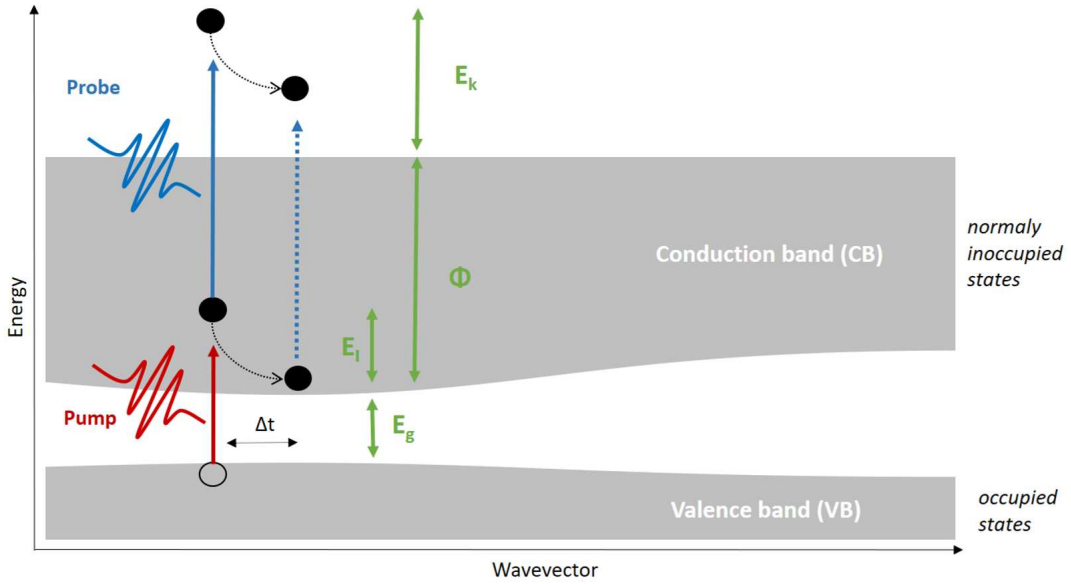

Figure 5.7: Sketch representation of two photon photoemission process. Electrons are excited from the valence band to the conduction band by the pump pulse. Their relaxation dynamics in the conduction band is enable by the probe pulse and time-delay variation Δt between the probe and pump pulses.

5.3.2 Experimental setup

Ultrafast laser system

The time-resolved measurements on FemtoARPES are performed using a femtosecond laser system represented on Fig. 5.8. The laser system consist in Ti:Sapphire laser system (RegA Coherent), delivering 6 µJ per pulse with 50 fs duration at FWHM at 250 kHz repetition rate. It is composed by a diode LASER (Verdi 523 nm), with a wavelength between 780 nm and 820 nm, at 45 nm bandwidth and a 80 MHz repetition rate. The Verdi pulses are splitted in two: a first beam is used to pump the Ti:Sapphire oscillator (Micra-18), the second one the amplifier (RegA Coherent 9040). Short laser pulses are generated using a mode-locking system in the Micra oscillator, while being continuously pump by he Verdi laser, with a 5W power. The optical cavity of the oscillator is an active mode-locking system controlled by an acoustic-optic modulator. Depending on the cavity length, only certain modes are allowed. Indeed, only the ones forming standing waves in the cavity and having a frequency separation equal to the inverse of cavity round-trip time are allowed. When many modes get macroscopically populated in the gain medium, a soliton called pulse is generated.

The outcoming pulse from the oscillator further propagate to a SILHOUETTE pulse shaper composed of liquid crystals. This measures and controls the spectral phase and amplitude of

the laser pulses, helping to compensate eventual unwanted phase distortion after compression.

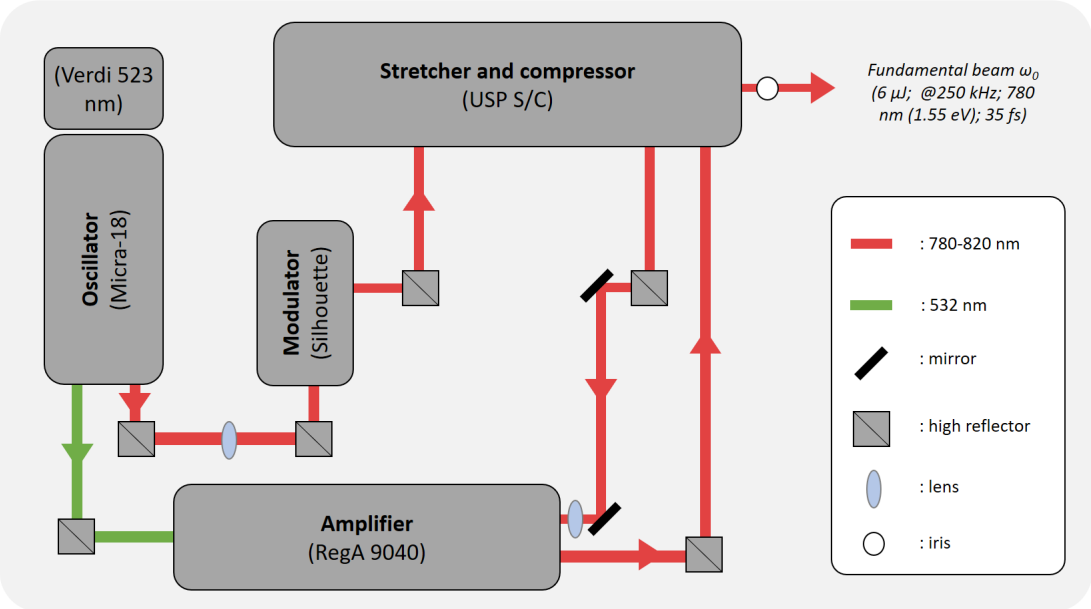

Figure 5.8: Ultrafast laser system.

As pictured on Fig. 5.9, the ultrafast laser pulse are amplified following a pathway including stretching, amplification and finally compression. In order to enhance the energy per pulse thus to prevent damage on the optical components as the gain medium in the amplifier, the oscillator seeds sent to the stretcher where are temporally chirped to roughly 100ps. The stretched pulses are then amplified in a regenerative amplifier (RegA-Coherent). An acoustic-optic modulator injects some of the oscillator seeds in the cavity of the Regenerative amplifier. Then, the induce stimulated emission of identical photon wavelength through a Ti:Sapphire crystal, excited by the second split beam of 12W from the Verdi 18 laser. The same acoustic-optic modulator later ejects the amplified pulsed into the compressor. A grating system similar to the one used in the amplifier system is used to compress the pulses to 50 fs FWHM pulses. The outcoming pulses have a 6 μJ pulse energy and a 250 KHz repetition rate.

Half of the outcoming pulse is split as the probe beam, the other half is used as pump pulse to excite the sample. Depending on the properties we want to characterize in the sample (valence band, electron relaxation in the conduction band..), the photon energy of the probe and the pump pulses have to be optimized.

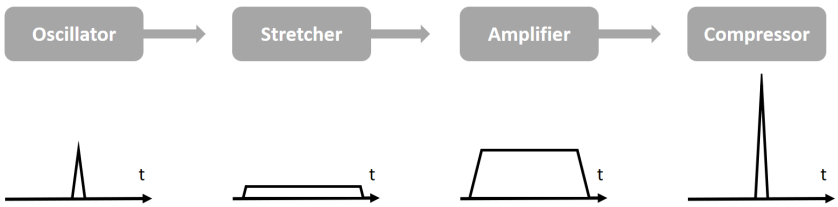

Figure 5.9: Amplification process diagramm

Harmonic generation beam path

Pump and probe energy have to be tune in order to be relevant for a specific sample characterization. Nonlinear optical processes are setup in this optical beamline to allow it, using higher-harmonic generation as explained in Chapter 2.4.3 . FemtoARPES setup enables to generate the 2th (3.15 eV), 3th(4.7 eV) and 4th (6.25 eV) harmonic of the fundamental laser wavelength (1.55 eV) [216]. β-barium borate crystal (BBO) are used at each steps of harmonic generation, as shown on Fig. 5.10.

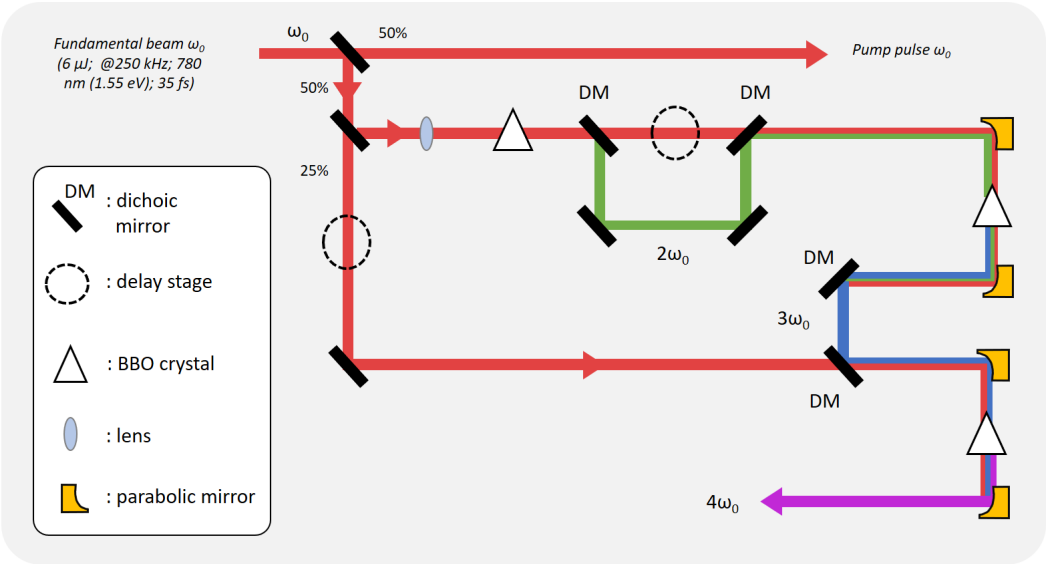

Figure 5.10: Generation of second, third and fourth harmonic from fundamental beam ω_0 and using BBO crystals. Mechanical delay line are used to shift delay time between pump and probe pulses.

Ultra-high vacuum chamber and hemispherical analyzer

As tr-ARPES is a surface sensitive characterization technique, the environnement surrounding the sample as its surface should necessarily be uncontaimined. For this purpose, the sample

cleaving and the tr-ARPES experiments take place in a ultra-high-vacuum (UHV) chamber. The samples are first loaded in a load-lock chamber (10^{-8} mbar). Then, they are placed in the preparation chamber (5.10^{-10}mbar) where they are cleaved manually with a metallic wooble stick. The sample is then ready for characterization and is transfered to a transfer chamber (1.10^{-10} mbar) where it is fixed to a 5 axis cryogenic manipulator. The sample is them moved to the photoemission chamber (5.10^{-11} mbar), where the tr-ARPES measurement takes place.

5.4 Materials

The samples were obtained through collaborations with different research groups. A short introduction to the sample fabrication methods is introduced in this sub-chapter.

5.4.1 $MAPbI_3$ single crystal

$MAPbI_3$ single crystal were grown by Gaelle Trippé-Allard, from Emmanuelle Deleporte's group LuMIn of University Paris-Saclay/ENS Paris-Saclay (France). $CH_3NH_3PbI_3$ single crystal has been grown by the inverse temperature crystallization method. Methylammonium iodide (0.78 g, 5 mmol) and lead iodide (2.30 g, 5 mmol) were dissolved in gamma-butyrolactone (5 mL) at 60 ° C. It lead to a yellow solution (2 mL) which was placed in a vial and heated at 120° C during few hours.

5.4.2 2D $(BA)_2(MA)_{n-1}Pb_nI_{3n+1}$ single crystals

2D perovskite single crystals where grown by Weihua Lin from Kaibo Zheng's group from the Technical University of Denmark (Denmark). The bulk single crystal of $(BA)_2(MA)_{n-1}Pb_nI_{3n+1}$ (n = 1, 2, 3) were obtained by the temperature gradient growth method. PbI_2 (99 %), methanamine hydriodide (98 %, MAI), butylammonium iodide (98 %, BAI), hypophosphorous acid solution (50 % in water; 5 ml) and hydroiodic acid (57 % in water; 0.25 ml) were formulated as the precursor solutions in 20 ml glass bottles. For n = 3, the PbI_2/MAI/BAI contents are 1.5 mmol/2.5 mmol/2.0 mmol, respectively. Then, precursor solution was sealed and stirred at room temperature for 30 minutes. They were later heated at 80 °C until solutions become completely clear. The bulk single crystals were grown from the clear solutions at a cooling rate of 0.5 °C/day starting from 55 °C.

5.4.3 (4cat)$PbBr_3$ single crystal

The quadruple cation single crystals were synthesized in a nitrogen environment using inverse temperature crystallization (ITC) approach at 107 °C. Precursor materials were dissolved in γ-butyrolactone solvent and seed growth was then performed under isothermal conditions [217].

Thin films were prepared via spin coating under a nitrogen environment in mixed DMF/DMSO solvent system followed by antisolvent quenching using toluene.

6 Ultrafast lattice polarization response in lead halide perovskites

This chapter focus on the experimental results obtained using several types of time-resolved Kerr spectroscopy on LHPs. First, we use optical Kerr effect spectroscopy (OKE) and focus on signals resembling coherent phonons but originating from nonlinear electronic polarization and light propagation (Section.6.1). Then, we present a THz-induced Kerr effect spectroscopy (TKE) to study the inorganic sublattice polarizability. With this technique, we first study simple A-site cation LHPs such as $MAPbBr_3$ and $CsPbBr_3$ (Section.6.2), as well as more complex A-site cation perovskite, so called (4cat)$PbBr_3$, in order to analyze the importance of the choice of the chemical composition of the cations in the coherence time of the phonons (Section.6.3).

6.1 Optical Kerr effect to decode the ultrafast polarization response

6.1.1 Motivation

As discussed in Section.3.4, the defect tolerance responsible for the excellent optoelectronic properties of lead halide perovskites may be explained by the formation of large polarons. Their highly anharmonic sublattice and associated dielectric responses have led to the large polaron proposal in which the dynamically screened coulomb potential minimizes charge carrier scattering with defects, other charges or LO phonons. Nevertheless, their formation and the impact of organic cations on it remain a burning issue in the perovskites community. Based on the room temperature results of Miyata et al discussed in Section.3.4, we focus our interest in studying MAPbBr3 and $CsPbBr_3$ with temperature-dependent OKE spectroscopy. The aim was to see a coherent phonon response as a reaction to charge carrier injection slightly below the bandgap (accounting for the binding energy of a large polaron). These experiments can be performed with one excitation pulse (1D-OKE) or two (2D-OKE), the later allowing to increase the accuracy of the measurements in terms of energy. One of the most interesting features of this experiment is that it allows to energetically dissect broadband light propagation and thus to obtain a superior excitation energy resolution.

Having joined the project along the way and for a limited time, I participated in results interpretation as well as the experimental verifications of 1D-OKE at low temperature to confirm 2D-OKE experiments, made by coworkers Sebastian Maehrlein, Prakritri Joshi, Feifan Wang, Xiaoyang Zhu et al [133]. The simulations were performed by Lucas Huber.

6.1.2 Dispersive and anisotropic light propagation

Experimental results using 1D-OKE

Fig. 6.1.a shows the first 1D-OKE response obtained with $CsPbBr_3$ single crystal at room temperature. As previously discussed in the Miyata et al. paper, an oscillatory signal is observable. Interestingly, the oscillation features frequency seem to evolve in function of the pump-probe delay. Indeed, it is possible to dissequate the oscillatory signal in three frequency domain. The Fourier transform of this spectrum in function of the pump-probe delay (Fig. 6.1.b) enables to see clearly the frequency jump, around 5.3 THz before 1 ps, decreasing to 2 THz at 2.5 ps. This sudden jump in frequency cannot be correlated to coherent phonon dynamics and relaxation, and must therefore originate from another physical process.

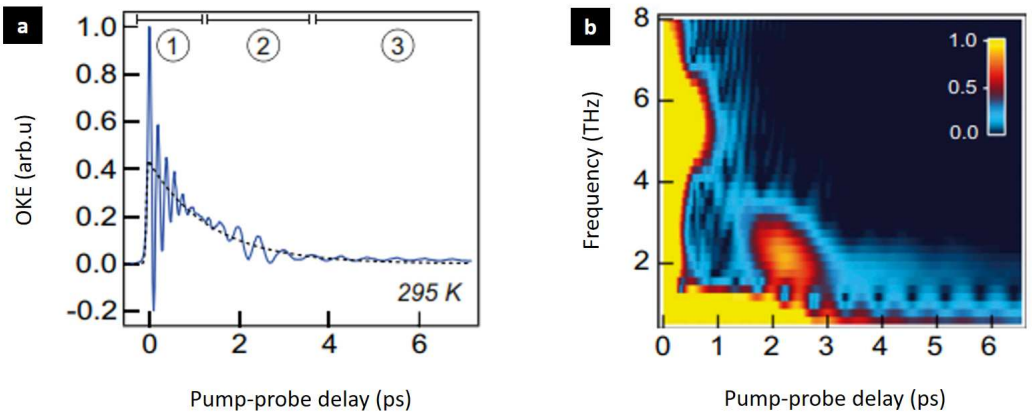

Figure 6.1: (a) Time-resolved single pulse (1D) OKE spectrum of single crystal $CsPbBr_3$ at 295K. Polarization dynamic includes three distinct regions (circled numbers). (b) Pseudocolor representation from a moving-window Fourier analysis of the OKE signal of figure (a), unveiling highly nonlinear frequency evolution. Pseudocolor was obtained from FT amplitude. Figures extracted from [133].

Taking into account the preliminary results of this research, Kerr spectroscopy experiments were reproduced on these same two crystals by studying their characteristics at different temperatures, and thus in different phases.

Experimental results using 2D-OKE

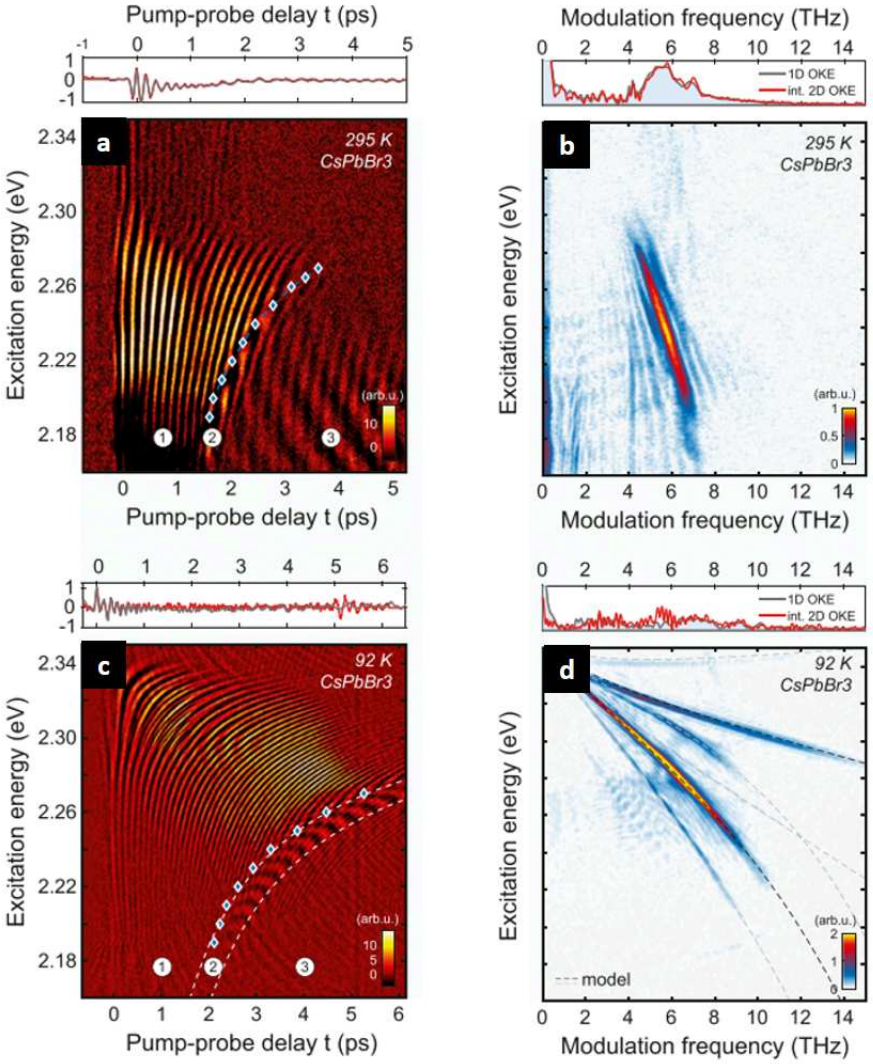

Figure 6.2: Energy-time domain 2D-OKE signal of $CsPbBr_3$ at 295K (a) and 92K (c), given by the Fourier transform of the transient birefringence $S(t,\tau)$ with respect to the pump-pump delay τ. The three distinct regions are identified by circled numbers. End of the region 1 ($t_{1,-}$) is identified with blue markers. Dashed lines in (c) fits $t_{1,-}$ (left) and $t_{2,-}$ (right) to determine the refractive index and group index. Correlation between excitation energy and modulation frequency, derived from the energy domain 2D-OKE by Fourier transform with respect to pump-probe delay t is represented again for $CsPbBr_3$ at 295K (b) and 92K (d). Frequency-frequency correlation branches agree with the model (dashed lines): defined by FWM phase matching (black) and higher(order side bands (gray). Above all plot take place integrated 2D OKE signal and 1D OKE signal under identical experimental conditions, which show perfect agreement [133].

.

To decode the oscillatory features below and close to the bandgap, 2D-OKE was perform to obtain precise excitation energy resolution, while maintaining a femtosecond time resolution, as explained in the paper from Maehrlein et al [133]. The excitation energy-dependent transient birefringence as a function of pump-probe delay t from $CsPbBr_3$ is presented in Fig. 6.2.a and Fig. 6.2.c, respectively at T=295K and 92K. The energy-time domain 2D-OKE signal in pseudocolor is obtained using the real part of Fourier transform of the signal, with respect to the pump-pump delay time τ. At the top of each plot from Fig. 6.2, the excitation energy integrated 2D-OKE is shown in red with the equivalent single pulse excitation experiment from 1D-OKE. They perfectly agree for all samples, which fully validates the consistency of using 2D-OKE technique and proves its absence of systematic artifacts. It allows us to treat each horizontal line cut of constant energy E_{ex} as a third order nonlinear polarization response as a function of pump-probe delay. To obtain the OKE frequency spectrum, a second Fourier transform was performed along the pump-probe axis and its absolute value, i.e amplitude, is presented. It leads to 2D frequency maps representing the correlation between the excitation energy and the modulation frequency, i.e the oscillatory features obtained with the OKE technique. As observed in 1D-OKE setup, a strong oscillatory feature is noticed. The oscillation frequencies are again strongly dependent to the excitation energy, as oscillation frequencies decrease while excitation energy is increasing, giving rise to an underlying fanlike structure present at both temperatures. Indeed, the oscillatory features seem to live for a longer time when the pump energy is increased. This feature can be understood as a strong dependence of modulation frequency on excitation energy. The whole dynamics can be decomposed in three domains, as discussed previously about the 1D-OKE. In region 1, oscillatory features are visible until reaching the fanlike structure, generating a bumplike feature we call region 2. This sudden stop is followed by long-lived low-frequency oscillation, belonging to region 3. Such sudden change in oscillatory frequency is unphysical for coherent phonons or any coherent particles relaxation, but is consistent with the dispersive propagation model developped in the following parts. Fig. 6.2.c and Fig. 6.2.d shows the Fourier transform of the left side signal with respect to the pump-probe delay t. The anticorrelation between the modulation frequency and excitation energy is clear at both temperatures. Nevertheless, a dominant anticorrelation branch is observable at 295K, while multiple branches with different slopes appear at 92K. The 2D-OKE traces integrated (red trace) are in good agreement with the 1D-OKE (gray and blue) traces.

2D-OKE spectra of $CsPbBr_3$ crystal in the orthorhombic phase at 295K and 92K is represented on Fig. 6.2. This orthorhombic phase is anisotropic and thus birefringent. The same 2D-OKE experiments have been repeated on a $MAPbBr_3$ single crystal, at 295K in its non birefringent cubic phase (Fig. 6.3.a) and 104K in it birefringent orthorhombic phase $Pnma$ (Fig. 6.3.c). In the cubic phase, $MAPbBr_3$ presents the same constant signal and non-oscillatory signal. The 2D-OKE unveils an abrupt decay of the Kerr signal after few picosecond, i.e again dependent on the excitation energy. The signal vanishes towards the bandgap around 2.1 eV due to an increase of absorption and thus a decrease in penetration depth. The Fourier transform shows

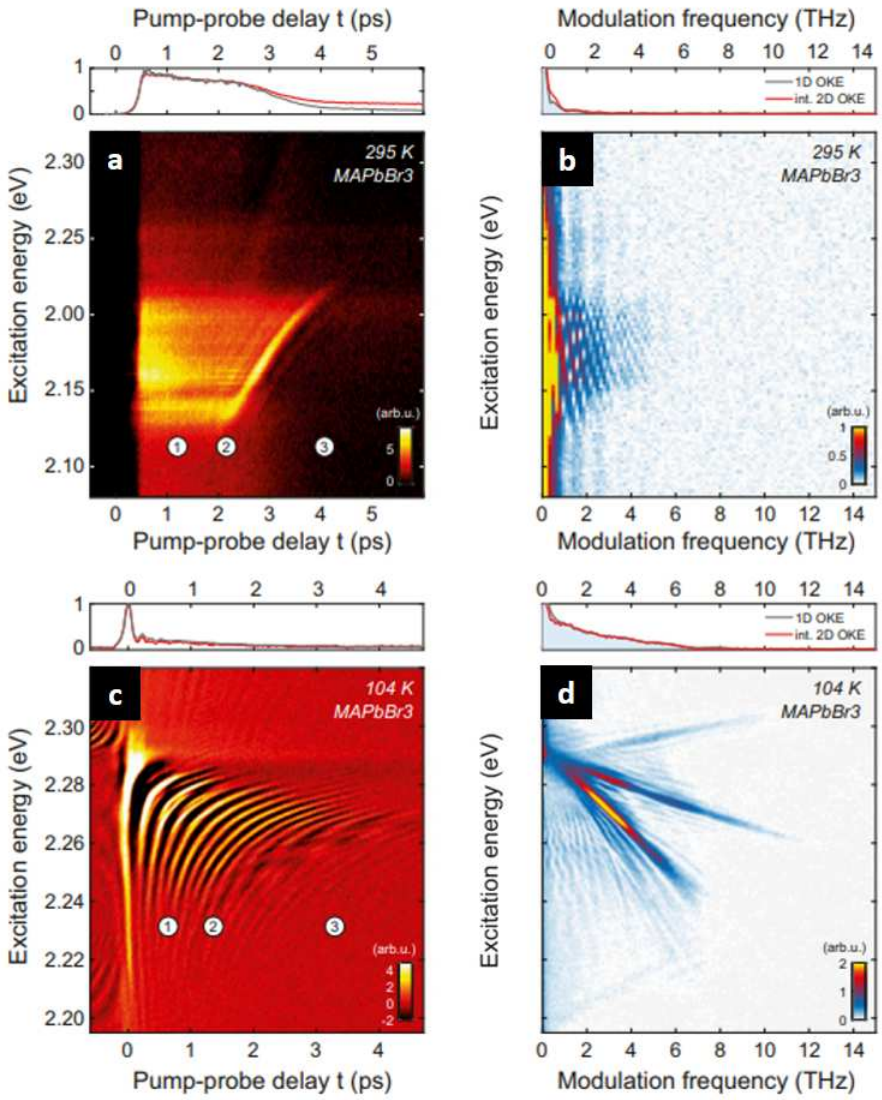

Figure 6.3: Energy-time domain (a) and energy-frequency domain (b) of the 2D-OKE signal in cubic-phase $MAPbBr_3$ at 295K, analogous to Fig. (c and d) same as (a) and (b), but in the orthorhombic-phase $MAPbBr_3$ at 104K. The clear similarity between orthorhombic $MAPbBr_3$ and orthorhombic $CsPbBr_3$ unveils the structural phase and its birefringence properties as the main source for high contrast between cubic-phase $MAPbBr_3$ and $CsPbBr_3$ OKE at room temperature [133].

.

a broad zero-frequency feature (Fig. 6.3.b). The 2D-OKE signal in the cubic non-birefringent $MAPbBr_3$ phase is different from the one obtained in the birefringent orthorhombic phase by lowering the temperature (Fig. 6.3.c). Indeed, a strong oscillatory feature is observed at 104K, similar to the responses obtained in the orthorhombic phase of $CsPbBr_3$. As well, the three

different time domain are present. The Fourier transform of the 2D-OKE with respect to the pump-probe delay t again reveals the anticorrelation between the modulation frequency and excitation energy (Fig. 6.3.d). Two branches are apparent in the orthorhombic phase, with frequency magnitude varying between 1 to 10 THz.

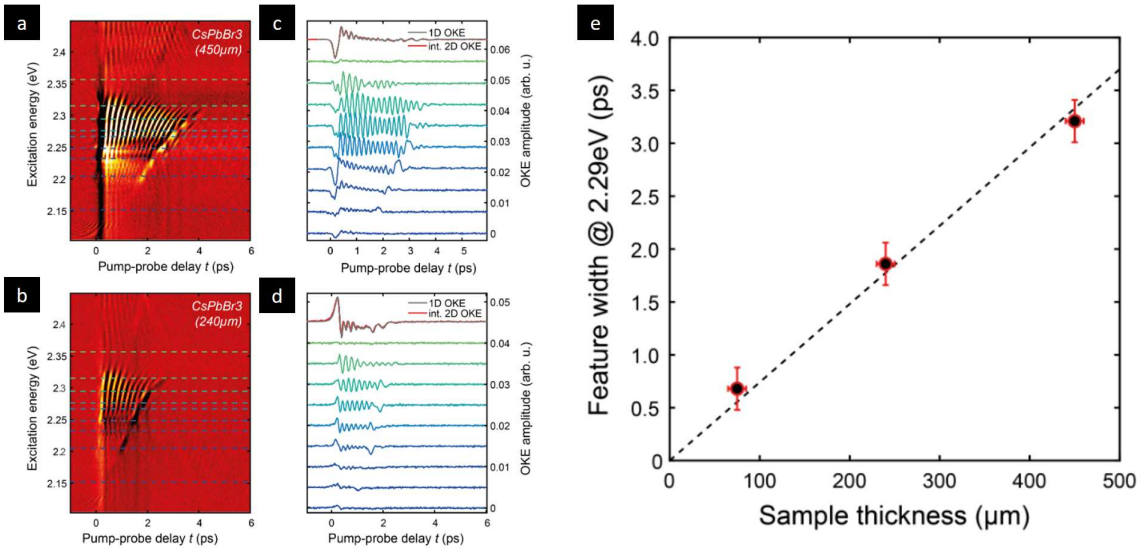

Figure 6.4: (a,b) 2D-OKE signal of $CsPbBr_3$ single crystal and (c,d) its corresponding constant excitation energy cuts, for 450 µm and 240 µm crystal thickness, respectively. (e) Thickness dependence for 2.29 eV excitation energy for different thickness of $CsPbBr_3$ single crystal. The duration of the main 2D-OKE feature scales linearly with the thickness, demonstrating the role of propagation in the observed nonlinear polarization spectra. Extracted from [133].

.

Thickness-dependent 2D-OKE measurements

Thickness-dependent 2D-OKE spectroscopy was then performed on three $CsPbBr_3$ with different thicknesses (75 µm, 240 µm, 450 µm). The 2D-OKE spectra of the two thicker are presented to Fig. 6.4.(a,b), as well as their corresponding constant energy cuts to visualize the temporal width of the main oscillatory signal on Fig. 6.4.(c,d). Fig. 6.4.e represents the feature width (i.e the duration of the first oscillatory region) for an energy cut of E_{ex} = 2.29 eV for the three samples. Interestingly, we notice on Fig. 6.4.e that the oscillatory feature width is dependent and proportional to the sample thickness. This is a first clue to the hypothesis that the oscillatory feature observed is not due to a coherent phonon response but to a propagation effect in the material, as the lifetime of coherent phonons should not be dependent on the thickness.

Propagation in LHPs

The previous results and observations force us to reconsider the idea that the observed oscillations are rather resulting from of complex light propagation in the samples. It is important to clarify the crystallographic structure of the studied LHPs as a function of temperature (Fig. 6.5.a) and the impact of the phase on the propagation of light in the material (Fig. 6.5.b,c). As shown on (Fig. 6.5.a), $CsPbBr_3$ is orthorhombic in all studied temperature, i.e from room temperature 300K to 80K. However, $MAPbBr_3$ is in the cubic phase from 300K to 230K, then transits into the tetragonal phase below 230K and until 135K, temperature at which it finally reaches the orthorhombic phase. The particularity between cubic and orthorhombic phase is that they differ in term of refractive index: indeed, the cubic phase is isotropic, which means that the refractive index is not different depending of on the light's polarization with respect to the crystal axes. When probe and pump pulses co-propagate in the LHP sample (Fig. 6.5.b), they undergo a walkoff, i.e a spatial and temporal distance between the two pulses originating from refractive index dispersion. Moreover, the excitation pump pulse undergoes a group velocity dispersion (GVD) when its energy is getting closer to the electronic bandgap E_g, due to the high refractive index dispersion being non negligeable at used excitation energies. The third-order nonlinear polarization $P_{NL}^{(3)}$ observed with 1D and 2D-OKE depends on the nonlinear $\chi^{(3)}$ mixing term, taking into account these evolving interactions between pump and probe pulse.

Pump-probe walkoff as well as pump pulse group velocity dispersion are also present in the orthorhombic phase, but another process is derived from anisoptropy of this phase. Orthorhombic structure has the particularity of being birefringence, which means that light propagates anisotropically. In a birefringent medium, the refractive index is not unique and depends on the direction of polarisation of the light wave. Therefore, the pump pulse can be considered by two distinct components orthogonal E_x^p and E_y^p to each other, and moving at different velocity due to the difference in refractive index between the orthogonal polarizations. When pump and probe propagate, the static birefringence results in an oscillating cross-polarized $\chi^{(3)}$ mixing term, causing third-order nonlinear polarization $P_{NL}^{(3)}$ oscillating features. In order to clearly understand the propagation effect in LHPs and the observed oscillating features and their modulation frequencies, a model has been developped and is explained in the later subchapter. It takes into account the third-order nonlinear electric polarization $P_{NL}^{(3)}$, which serves as an in situ probe of the LHPs polarizability and also governs the ultrafast macroscopic response of the material to an incident exciting field.

6.1.3 Model

The abrupt decay at t_1 (i.e end of region 1) in the Kerr signal observed in the orthorhombic phase of $CsPbBr_3$ and $MAPbBr_3$ seems particularly unphysical for coherent phonons or other collective modes, and might originate from light propagation. Co-workers developped a model

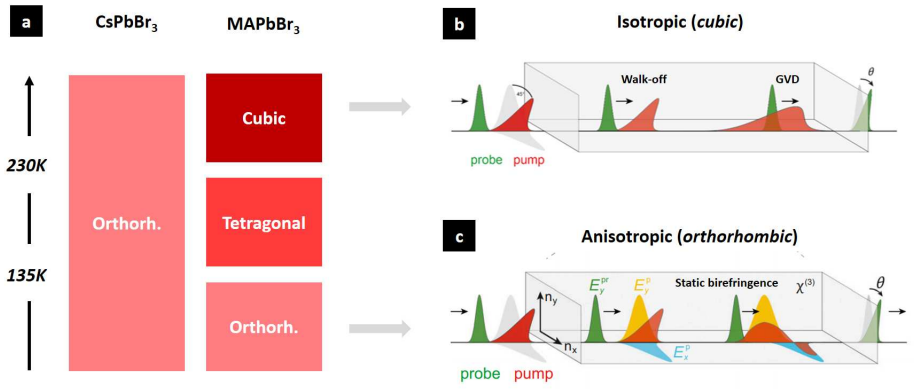

Figure 6.5: (a) Temperature-dependence phase transition diagram in $CsPbBr_3$ and $MaPbBr_3$. Scheme of light propagation in the isotropic cubic (b) and in the anisotropic orthorhombic phase [133] (c). In the cubic phase, the pump undergo pump-probe walkoff induced by different wavelength refractive index, as well as group velocity dispersion (GVD), mainly in the vicinity of the bandgap E_g. In orthorhombic phase, additional process appear: the anisotropy and dispersion of light propagation are dominated by nonlinear $\chi^{(3)}$ mixing of perpendicular pump field projection E_x^p and E_y^p while interacting and propagating with respect to the probe field E_y^{pr} [133].

.

where are considered an instantaneous electronic polarization (originated from hyperpolarizability) and several propagating light fields in single crystal [218]. The influence of spectral dispersion, the static birefringence and the nonlinear mixing are taken into account in the third-order nonlinear susceptibility $\chi^{(3)}$. The propagation of all three interacting light fields that mix through $\chi^{(3)}$ are traced to produce a new polarization component, $P_{NL}^{(3)}$:

$$P_{NL}^{(3)}(t,z) = \epsilon_0 \int_{-\infty}^{t} dt' \int_{-\infty}^{t'} dt'' \int_{-\infty}^{t''} dt''' \chi_{jklm}^{(3)}(t,t',t'',t''',z) E_k^{pr}(t',z) E_l^{p}(t'',z) E_m^{p}(t''',z) \quad (6.1)$$

with $P_{NL}^{(3)}$ the third-order nonlinear term of polarization, ϵ_0 the vacuum permittivity, E^{pr} the probe field component, E^p the pump fields components, the collinear propagation along z. The instantaneous Kerr response arising from the hyperpolarizability is modelled by $\chi_{jklm}^{(3)}(t,t',t'',t''',z)$ which is set to a product of δ-function in time, i.e instantaneous response function, in order to separate the different interactions in the model. It leads to $\chi_{jklm}^{(3)}(t,t',t'',t''',z) \sim \chi_{jklm}^{(3)} \delta(t-t')\delta(t'-t'')\delta(t''-t''')$. Therefore, this term is assumed to be constant, while the linear refractive index tensor $n_0(\nu)$ exhibits a strong dispersion near the bandgap and static birefringence in the orthorhombic phase. It also includes properties originated from the group velocity dispersion (GVD), such as the pump-probe walk-off from group velocity mismatch as $n_G(\nu_p) > n_G(\nu_{pr})$ (group refractive indices) and the temporal spread of the pump pulses.

As discussed in the paper from Maehrlein et al [133], simulation reproduces absolutely well the experimental 2D-OKE responses. It confirms that the abrupt decay of Kerr signal toward the bandgap in region 1 is originating from the strong group velocity dispersion and walk-off of each nonlinear polarization component from the pump and the probe pulses. The abrupt bump-like feature in region 2 results from the interference of the pump pulse with itself at the backside of the sample. In agreement with the modelled energy-time domain 2D-OKE signal and the experimental frequency map, the model reproduces all the features previously discussed. The frequency-frequency correlation branches observed experimentally in the orthorhombic phase (Fig.6.2.d) are also clearly reproduced by the simulation. Interestingly, these predicted branches fit perfectly with the experimental frequency-frequency correlation branches, offering a clear consistency of the model.

Discussion

Using the four-wave mixing model, experimental 1D-OKE as well as 2D-OKE energy and frequency correlations were reproduced, which enabled to establish polarization-dressed light propagation in LHPs, originating from δ-like (i.e electronic material) response . The blue markers Fig.6.2.a,c represent pump-probe delay t_{1-} and is proportional to the thickness of the crystal. We can define two important parameters, $t_1,-$ the latest overlap of the probe pulse with the faster co-propagating pump-field at the sample backside, and $t_1,+$ counter propagating (i.e reflected) pump pulse. The strong anticorrelations are caused by the hyper-polarizability experienced by light propagation in highly dispersive and anisotropic region near and below the bandgap. Polarization contributions from the inorganic lattice or the cation reorientation would require slightly retarded response functions, depending on inertia and resonance frequencies of the structural lattice dynamics as we will discuss in Section.6.2. The interpretation of OKE signals as ultrafast dynamics dominated by orientational or lattice contributions in hybrid LHPs should be carefully considered, particularly when the excitation wavelength is close to the optical bandgap or when a thickness dependence is observed. The discussed dominating hyperpolarizability in lead halide perovskites suggests the picture of intense light fields traveling with nonlinear polarization clouds in the near-bandgap region. This work enabled to obtain an unified origin of strong optical Kerr response observed in lead halide perovskites and to maintain awareness on quick interpretation of oscillating features in these materials. Finally, this work highlights how importantly anisotropic and dispersive light propagation dressed with instantaneous 3^{rd} order nonlinear polarization and how much we need to take it into account in our later THz-induced Kerr effect measurements.

6.2 Terahertz Kerr effect and polarizibility in $MAPbBr_3$ and $CsPbBr_3$

6.2.1 Motivation

This section focuses on the confirmation of the dynamic charge carrier screening by looking at coherent phonon excitations using wavelength excitation resonant to lattice modes. One way to study lattice dynamics is to excite it with THz wavelength (Section.4.2), as THz lattice excitation is a powerful tool to study and control mechanisms in condensed matter, while electronic degrees of freedom in their ground state (without free carriers). We therefore study the ultrafast polarization response of the hybrid LHPs $MAPbBr_3$ and $CsPbBr_3$ when exposed to transient electric fields in the form of intense, single-cycle THz pulses. By probing the THz-induced Kerr effect (TKE), we aim to probe the THz polarizability and ultrafast polarization dynamics of the inorganic sublattice Pb-Br.

All the TKE experiments as well as data analysis were performed by myself with coworker Max Frenzel at the Fritz Haber Institute of the Max Planck Society. The samples were synthesized by Feifan Wang and Bo Xiang from Columbia university. The simulations were written by Lucas Huber and adapted to our study case.

6.2.2 Experimental results

First, THz-induced Kerr effect spectroscopy was performed on $MAPbBr_3$ and $CsPbBr_3$ single crystals at room temperature, with a thickness of about 500 µm and 200 µm respectively. The TKE signals are presented on Fig. 6.6(a,d) and present the transient birefringence as function of time, with time zero t = 0 ps, being the peak field of the THz pulse. A first important observation is that both LHPs ($MAPbBr_3$ in blue, $CsPbBr_3$ in green) are strongly polarizable to the THz electric field, shown by the high main peak at time zero. The THz electric field squared is represented in light grey, showing an undeniable similarity with the THz signal on the first picosecond. The main peak is originating from the instantaneous electronic polarizability α_e generated from the interaction between the Terahertz pump pulse and electron clouds. Pump fluence-dependent experiments have been performed and the main peak scaled quadratically with the maximum of the THz electric field, as shown on Fig. 6.6(b,e). As previously discussed in Chapter.4, having the TKE peak scaling quadratically with the THz electric field is a evident signature of a Kerr effect.

Nevertheless, both TKE signals are really different from one to another A-site cations: in the case of $MAPbBr_3$, the main peak coming from the instantaneous electronic polarizability α_e is followed by an exponential decay, while in $CsPbBr_3$, the exponential decay seems to be mixed with longer-lived oscillatory features. $MAPbBr_3$ and $CsPbBr_3$ are in the isotropic cubic phase and anisotropic orthorhombic phase at ambient temperature, respectively. Moreover, THz wavelengths are partly absorbed by $MAPbBr_3$ and $CsPbBr_3$, as the linear refractive index undergoes important dispersion from 0.5 to 5 THz, leading to a decrease of the penetration depth and increase of absorption. Fig. 6.7.a presents TKE signal at room temperature (300 K) in

$MAPbBr_3$ single crystal with different thickness $MAPbBr_3$ single crystals (132 µm, 547 µm and 972 µm). For all considered thicknesses, the exponential decay tail have similar time constants. The TKE main peak does not scale linearly with thickness as shown in the absorption model box. This can be explained by the significant absorption in the THz region. Fig. 6.7.b presents the calculated penetration depth and absorption coefficient as a function of frequency in the THz range. Only low frequencies below 1 THz penetrate the considered single crystal significantly.

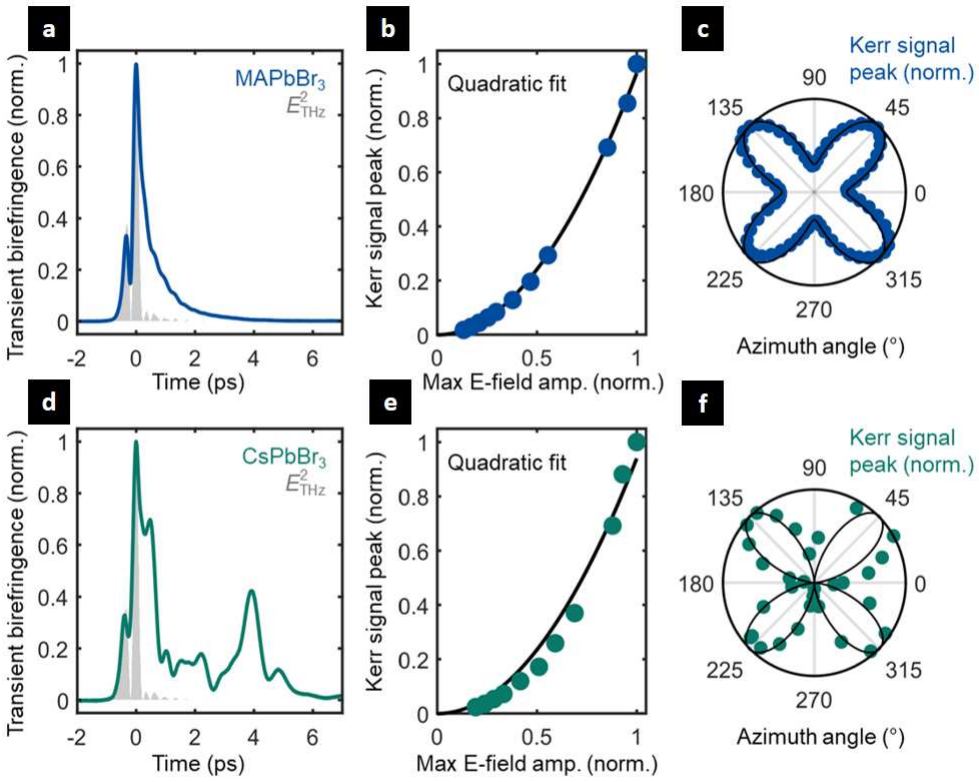

Figure 6.6: Strong THz-induced birefringence in $MAPbBr_3$ and $CsPbBr_3$ at room temperature. (a) Room temperature TKE in $MAPbBr_3$ and (d) $CsPbBr_3$ single crystals, respectively. (b) and (e), THz fluence dependence of main peak amplitude with quadratic fit, demonstrating the Kerr effect nature of the signals. (c) and (f), azimuth angle dependence of main peak showing its 4-fold rotational symmetry.

The TKE signal in the anisotropic orthorhombic phase is more specific than in the cubic phase and oscillatory features are observed in $CsPbBr_3$ shown on Fig. 6.6.d.

Azimuth angle dependence measurements have been performed in order to verify the expected 4-fold rotational symmetrical dependence for a cubic and orthorhombic crystal structure from the $\chi^{(3)}$ tensor. As shown on Fig. 6.6(c,f), the 4-fold rotational symmetrical was well respected. By considering the symmetry of the crystal structures and focusing only on the

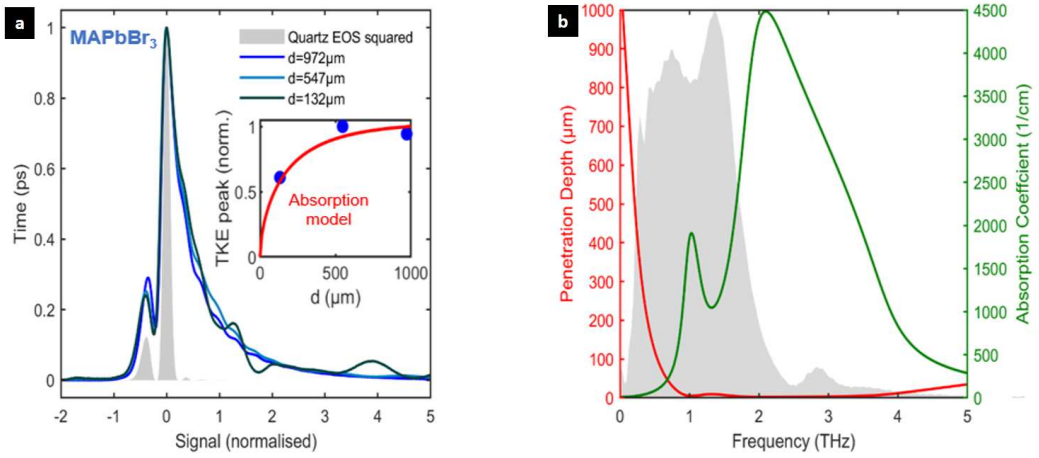

Figure 6.7: (a) $MAPbBr_3$ single crystal TKE peak signal as a function of crystal thickness. The tail has similar time constants for all considered thicknesses. The TKE main peak does not scale linearly with thickness, which can be explained by the significant absorption in the THz region. (b) Calculated penetration depth and absorption coefficient as a function of frequency in the THz range. Only low frequencies below 1 THz penetrate the considered single crystal significantly.

non-zero tensor elements, the TKE azimuthal angle dependence was fit to obtain the ratio of diagonal to off-diagonal S of $\chi^{(3)}$ tensor elements, with:

$$S = \frac{d_{diag}}{d_{offdiag}} \tag{6.2}$$

This ratio S is 1.59 in the hybrid material $MAPbBr_3$ and $S = 1$ in the all-inorganic material $CsPbBr_3$. It has been proposed by Yaffe et al. [39] that highest and not uniform ratio in $MAPbBr_3$ might be a signature of an additional isotropic disordered induced by MA^+ cation rotation at room temperature, similar to the dynamic disorder observed in the low frequency of Raman spectra (Fig. 3.9).

According to the Raman spectra previously discussed on Fig. 3.9, lowering the temperature should allow to distinguish several Raman phonon modes. Temperature-dependence TKE measurements were performed on $MAPbBr_3$ samples at the same temperature range than the Raman spectroscopy experiments from Guo et al, from 300K to 80K. The temperature range enables to reach the three different crystallographic phases known for $MAPbBr_3$: cubic above 230K, tetragonal from 230K to 135K (including a tiny incommensurable tetragonal II phase below 145K) and the orthorhombic phase below 135K. Furthermore, these temperature-dependent TKE measurements were performed both on 500 µm single crystal and 400nm thinfilm on a 500 µm BK7 glass substrate. By lowering temperature, single crystal transient birefringence presents more and more oscillatory features (Fig. 6.8.a). The tetragonal phase

at 180K presents some few short-lived oscillatory features until 4 ps and might reflect cubic-tetragonal structural change in the single crystal, while strong and long-lived oscillations are observed in the orthorhombic phase at 80K. As discussed earlier, LHPs thick single crystal as $MAPbBr_3$ can undergo propagation effect and show oscillatory features originating not from lattice vibrations but from dispersive light propagation and mixing $P_{NL}^{(3)}$ electric field in the anisotropic orthorhombic phase. In order to rule out the propagation theory, the same experiment was performed on thin film. Propagation effect is by definition thickness-dependent and therefore should only produce short-lived oscillations in a thin film.

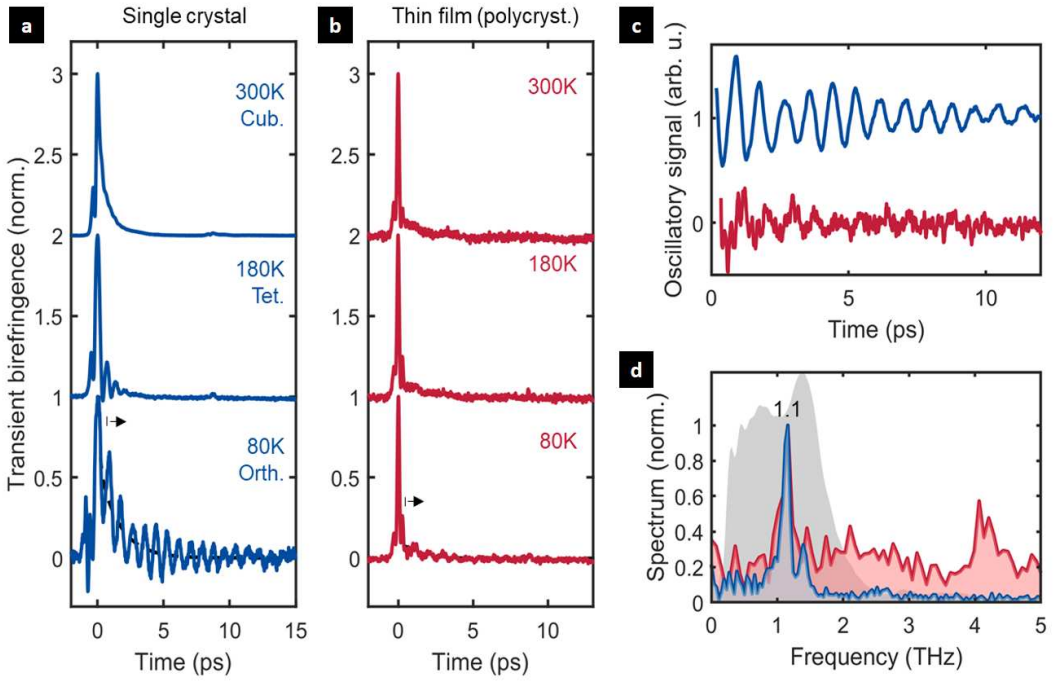

Figure 6.8: TKE signal of respectively $MAPbBr_3$ (a) single crystal and (b) thin film on glass substrate, at room temperature, 180K and 80K. Oscillatory features at 80K appear clearly by removing the exponential decay tail and zooming on it (c), in single crystal (blue) and thin film (red). (d) Fourier Transform of the oscillatory features above. Frequency peaks correspond to Raman-active phonon modes [135]. The thin film being polycrystalline, 1.1 THz peak might be an anisotropic A_g mode. 4 THz peak is supposed to correspond to an LO phonon mode but its origin still remains under debate as it does not appear in the single crystal.

Temperature-dependent TKE experiments are presented on Fig. 6.8.(b). A first observation is the absence of the exponential tail at 300K, compared to single crystal. This might be due to the thinner thickness of the thin film, reducing the propagation effect due to pump-probe walk-off and absorption in the sample. As the TKE signal strength is dependent on the crystal thickness, the signal in thin film is globally lower and more noisy. Nevertheless, oscillatory features are one more time clearly visible in the orthorhombic phase at 80K. More interestingly,

long-lived oscillations are observed until 12 ps, ruling out the possibility of the oscillatory features to originate from propagating effect. Could it be originating from Raman coherent phonon oscillation?

The lifetime of a phonon can be obtained from the FWHM of the Fourier transform peak. The lower lifetimes at higher temperatures are mainly due to the anharmonic decay of optical phonons into low-energy phonons [219, 220]. The increased phonon damping is observed above approximately 30 K, together with a reduced phonon intensity. An anharmonicity of the hybrid halide perovskite lattice is expected to play a considerable role in electron–phonon interactions [221, 121]. The anharmonicity manifests at room temperature, where optoelectronic devices and solar cells are usually operating [132].

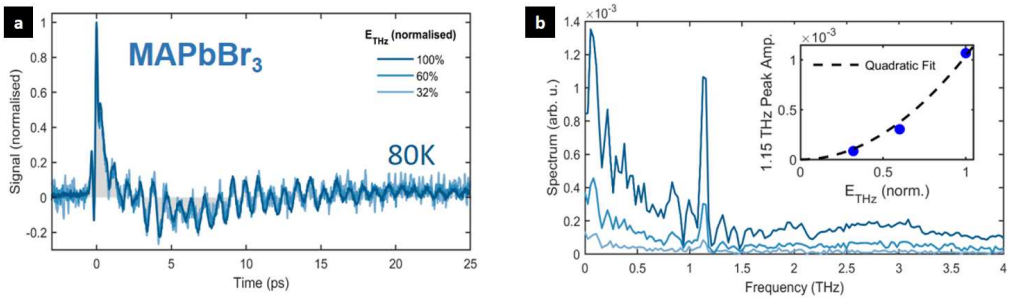

Figure 6.9: (a) TKE at 80K for different THz pump fluences in $MAPbBr_3$. The amplitude of the oscillations scale with the TKE peak. (b) The inset shows that the dominating oscillatory amplitudes also scales with the square of the THz electric field, 1.1 THz for $MAPbBr_3$. This demonstrates that the oscillations correspond to nonlinearly excited Raman active phonons.

In order to analyze more qualitatively the oscillatory features, the TKE signal was substracted from its biexponential decay from t_0 to remove the signal upcoming from the THz electric field, as shown on Fig. 6.8.(c). The Fourier Transform of the resulting oscillatory signal is presented on Fig. 6.8.(d). A clear mode appears in both single crystal and thin film at 1.1 THz (36.7 cm^{-1}), in agreement with Raman-active phonon modes observed in static Raman spectroscopy [135]. This mode is supposed to be an isotropic A_g mode, meaning according to the group theory that the mode is non-degenerate [I] and symmetric mode, i.e the same mode should be observable regardless of sample orientation and the diagonal value of the Raman tensor are supposed to be equal. The single crystal is crystallographically oriented by definition, while the thinfilm have no particular crystallographic orientation due to the random orientation of its grain boundaries. Nevertheless, the 1.1 THz mode is predominant in their both Fourier Transform, reinforcing the idea the 1.1 THz mode is an isotropic mode, meaning independent of the orientation. A fluence dependency of the TKE signal in $MAPbBr_3$ at 80K and of the Fourier transform of the 1.1 THz mode have been performed. The 1.1 THz peak signal scales

[I] An energy level is degenerate if it corresponds to two or more different measurable states of a quantum system. A non-generate level corresponds to only one quantum state.

quadratically with the THz electric field as expected in Raman-active excitation (Fig. 6.9.a) and the oscillations scale with the amplitude of the time-zero peak (Fig. 6.9.b). These two elements are solid proofs that the 1.1 THz mode observed is a nonlinear excitation of Raman-active phonon mode and that $MAPbBr_3$ has a strong THz lattice polarizability. In opposite to the TKE spectra at ambient temperature depending entirely on the instantaneous electronic response α_e, the oscillatory features observed at 80K originate from both α_e in the case of the main peak at $t = 0$ ps and from the lattice polarizibility α_{lat}. The phonon lifetime has been extracted for oscillatory signal at 180K, 140K and 80K (Fig. 6.10.(d)) using a Lorentzian fitting method. The FWHM of the frequency peak studied is extracted from the Fourier transform (intensity spectrum, i.e squared amplitude) and called $\delta\nu$. Phonon lifetime τ is then obtained with the formula $\tau = \frac{1}{2\pi\delta\nu}$. 1.1 THz Raman-active phonon mode lifetime of the single crystal τ_{sc} and of the thinfilm τ_{tf} are 1.7 ps (± 0.42) and 1.5 ps (± 0.52), respectively. The shorter phonon lifetime in the case of thinfilm has been proposed to be caused by increased crystalline disorder, associated with grain boundaries and strain [152]. Due to the increase of lattice anharmonicity and thermal-induced vibration at higher temperature, phonon lifetime decreased and reached 0.3 ps (± 0.05) and 0.27 ps (± 0.05) at 140K and 180K, respectively. Interestingly, the shift of the center frequency from 1.72 THz at 140K to 1.5 THz at 180K seems similar to the frequency shift observed in static Raman spectroscopy [135] and might originate from the lattice disorder at higher temperature.

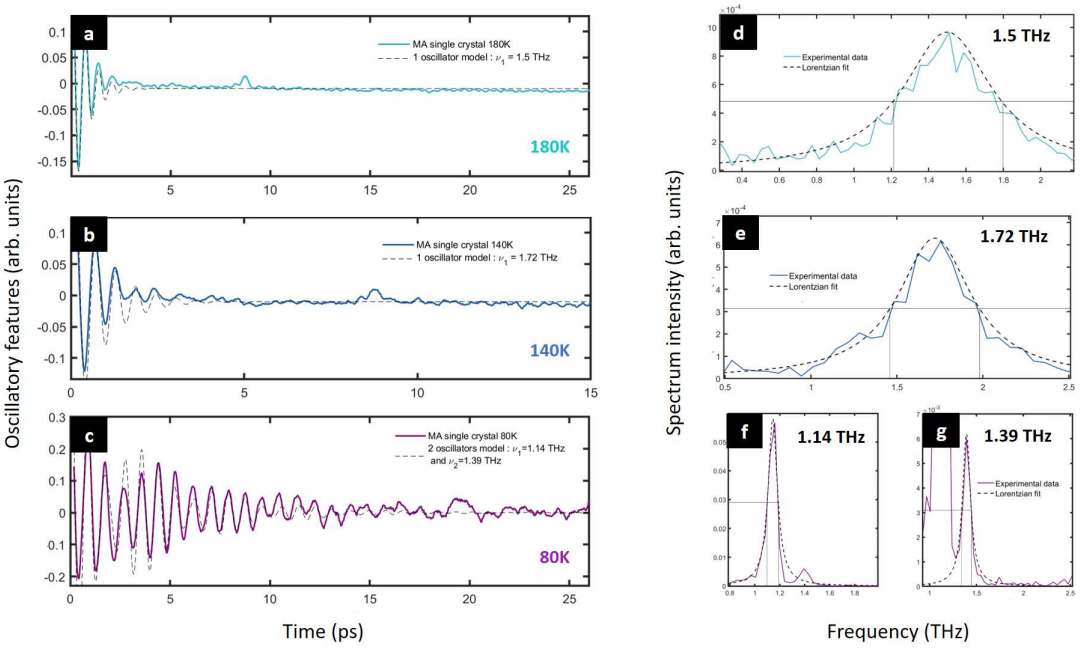

Figure 6.10: (a-c) Oscillatory features obtained after subtracting biexponential decay from the initial TKE signal for $MAPbBr_3$ single crystal at 80K, 140K and 180K. (d-f) Phonon lifetime $\tau_{(I)}$ deduced from linewidth at FWHM $\delta\nu$ (g-i).

According to several research papers [113, 148], 1.1 THz phonon mode in $MAPbBr_3$ is ascribed to the Pb-Br-Pb bond, equivalent to the twisting of the octahedra as shown on Fig. 6.11.a.

This octahedral twist corresponds to dynamic change of $PbBr_6$ octahedron rotation angle [29] and should be associated to a TO phonon. This bonding is a major ingredient of the phase transition as a soft mode [222, 223]. Nevertheless, the phonon frequency is really close to the one responsible of the octahedral distortion, associated to longitudinal and transversal phonon, as depicted on Fig. 6.11.b. 1.1 THz phonon mode also strongly agree with the bandgap coupled mode observed in $MAPbI_3$ by Kim et al [158], as discussed previously, leading this octahedral twist mode to be a good candidate to explain dynamic screening in LHPs. The lattice polarizability observed with TKE allows to assign the most polarizable Raman-active mode 1.1 THz to an octahedral twisting mode of LO phonon.

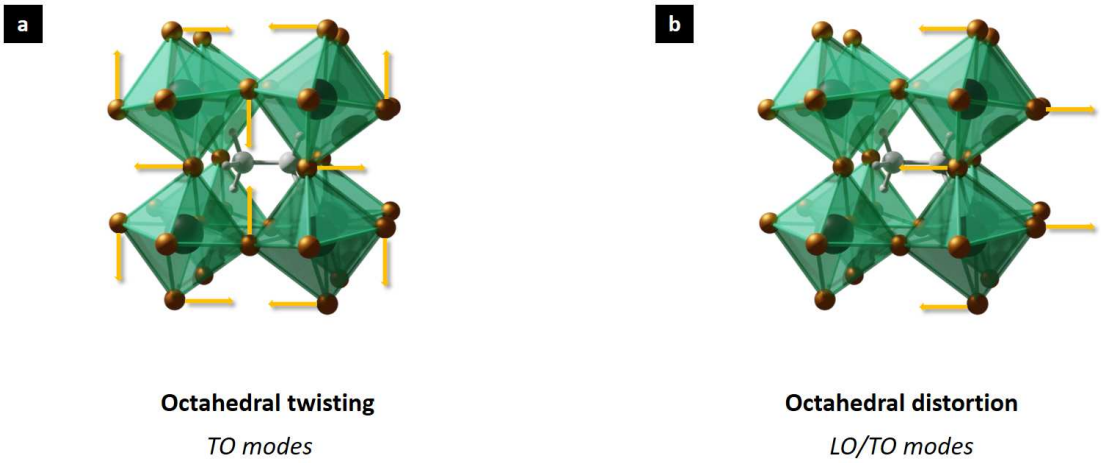

Figure 6.11: Schematic representations of the vibrational modes geometries experimentally observed in $MAPbBr_3$ in the cubic phase: (a) Twisting mode of the octahedra and (b) octahedral distortion. Adapted from [113].

Interesting peaks also appear on the oscillatory signal Fourier Transform, with lower amplitude. In single crystal, a peak at 1.4 THz (46.7 cm^{-1}) with 1.5 ps (± 0.15) lifetime appears. It is also in agreement with static Raman spectroscopy [135]. This peak is not clearly visible or inexistant in the thin film Fourier Transform, suggesting it is rather an isotropic phonon mode. In the thin film, another particularly broad peak is observed at 4.1 THz. This frequency could be in agreement with a Raman mode that split at really lower temperature [134], but could also come from some artefact in the first 2 ps of the temporal domain, such as Fabry-Pérot resonance.

The same experiment has been performed at 80K on $MAPbBr_3$ with different orientation of the crystal axis. Oscillatory features after substraction of the main TKE peak exponential decay as well as its Fourier Transform are shown on Fig. 6.12, for the both crystal orientation 0 degree and 45 degree with respect to the main crystal axis. 1.1 THz Raman-active mode is visible in both axis configuration, providing an additional argument for considering this mode of vibration as isotropic. Interestingly, the second peak present at 1.4 THz at 0 degree does not seem present or easily observable in the 45 degree orientation, also confirming the anisotropy

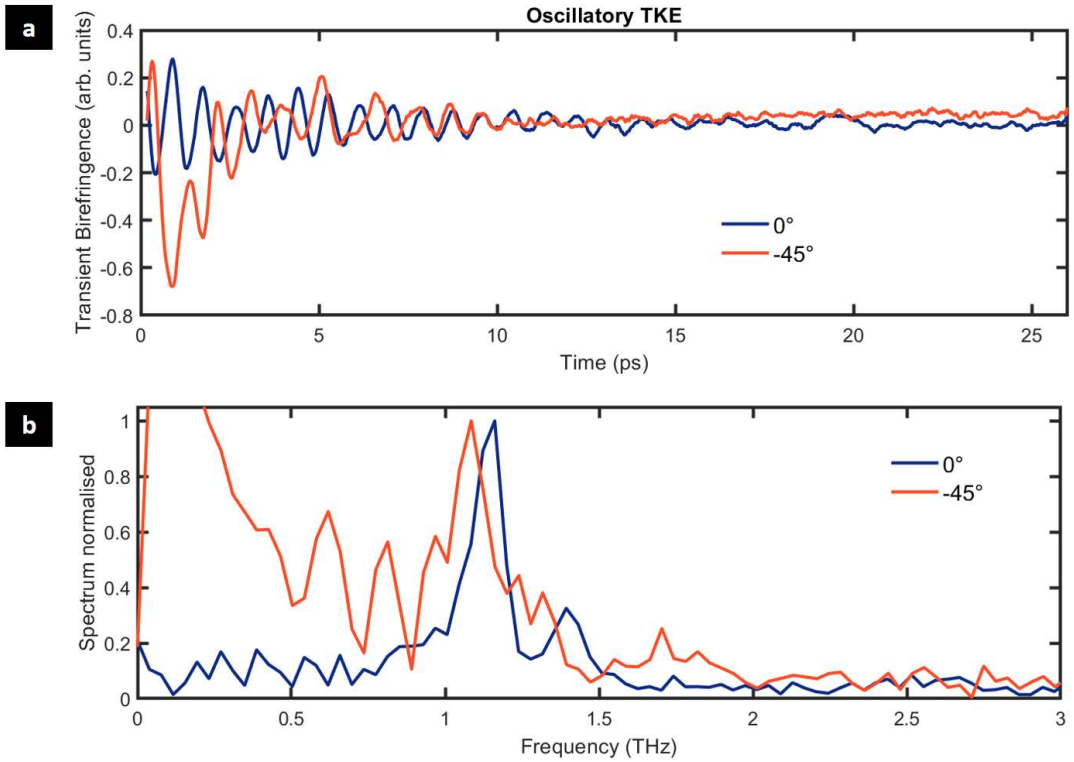

Figure 6.12: (a) Oscillatory signal after substraction of the biexponential tail and (b) Fourier transform for 0 degree of rotation (blue) and 45 degree (orange).

of this phonon mode. Another mode is visible in the 45 degree configuration around 0.85 THz. This would agree with one Raman mode observed in static Raman spectroscopy [135], but its lower amplitude and the higher background do not allow to assert a strong presence of this mode.

Helium measurement were performed on $MAPbBr_3$ single crystal down to 5K as shown on Fig.6.13. As expected, the phonon lifetime even increased by lowering the temperature. Temperature-dependent time-resolved THz spectroscopy recently enabled to observe Pb-X-Pb mode splitting in $MAPbI_3$ in the orthorhombic phase [148]. More precisely, the mode splitting took place for the mode 1 THz, which is the equivalent of the 1.1 THz mode in $MAPbBr_3$. The splitting was clearly visible at 20K and resulted in two modes at 1 THz and 0.8 THz. Nevertheless, we observed only one main 1.1 THz mode at Helium temperature in $MAPbBr_3$ crystal and absolutely no splitting of the main 1.1 THz mode. According to La-O-Vorakiat et al., the mode was infrared-active, which could explain why it is not visible in our TKE experiments. Indeed, this technique only enable to study Raman mode. IR modes can only be observed if they couple in a way of later resulting in a Raman mode, for exemple via difference-frequency excitation or sum-frequency excitation (SFE). Interestingly, some new peaks are visible at 1.5 and 3.1 THz, which could be some other Raman-active modes excited via THz-SFE.

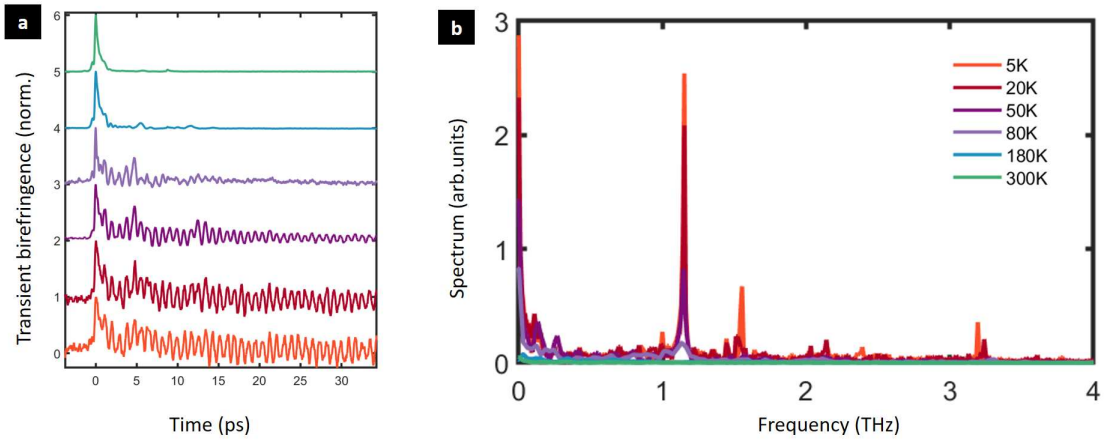

Figure 6.13: (a) TKE signal of $MAPbBr_3$ at Helium temperature and (b) its Fourier transform.

6.2.3 Model and simulation

In order to confirm our theory that the observed oscillations are indeed due to coherent phonons and not to light propagation, we again use the four-wave mixing simulation as explained in Chapter.4 to simulate the propagation of light in an anisotropic and dispersive medium, namely $MAPbBr_3$ in orthorhombic anc cubic phases. In these simulations, the temporal response $\chi^{(3)}$ was either defined by a electronic response model (Equ.6.3) only or by the sum of electronic and phonon-lattice response model (Equ.6.4), expressed as follows based on the Lorentz oscillator model:

$$R_e(t,t',t'',t''') = R_{(e,0)}\delta(t-t')\delta(t'-t'')\delta(t''-t''') \tag{6.3}$$

$$R_p(t,t',t'',t''') = R_{(p,0)}\delta(t'-t'')\delta(t''-t''')\exp^{-\Gamma(t-t')}\sin\sqrt{\omega_{ph}^2-\Gamma^2(t-t')} \tag{6.4}$$

with $\omega_{ph}/2\pi$ the specific phonon frequency, $\frac{1}{2\gamma}$ the phonon lifetime.

Our simulation takes fully into account THz pump electric field as it has been measured experimentally, meaning that the amplitude and phase as a function of frequency are taken into account. In the case of the probe electric field, we assumed a Fourier limited Gaussian spectrum. Therefore, the simulated probe field is considered to have a center wavelength of 800 nm and a pulse duration of 20 fs. Materials properties were also include in the simulation, such as the $MAPbBr_3$ refractive index in the THz region obtained from Sendner and coworkers' work [123]. As no refractive index in the THz region were accessible in the case of $CsPbBr_3$, we include in the simulation its known optical refractive index. As well as in the OKE simulation

explained in Section 6.1 [133], we used the static birefringence model in the anisotropic medium, resulting with different refractive index for the parallel and perpendicular electric field axis to the propagation field. In the case of isotropic simulation in the cubic phase, there is no static birefringence. As previously observed in OKE measurements (Section.6.1), the third order of nonlinear polarization $P_i^{(NL)}$ is generated by four-wave mixing process of exciting and probe pulse and is measured by the difference signal between the Kerr signal and the the probe polarization in balanced condition.

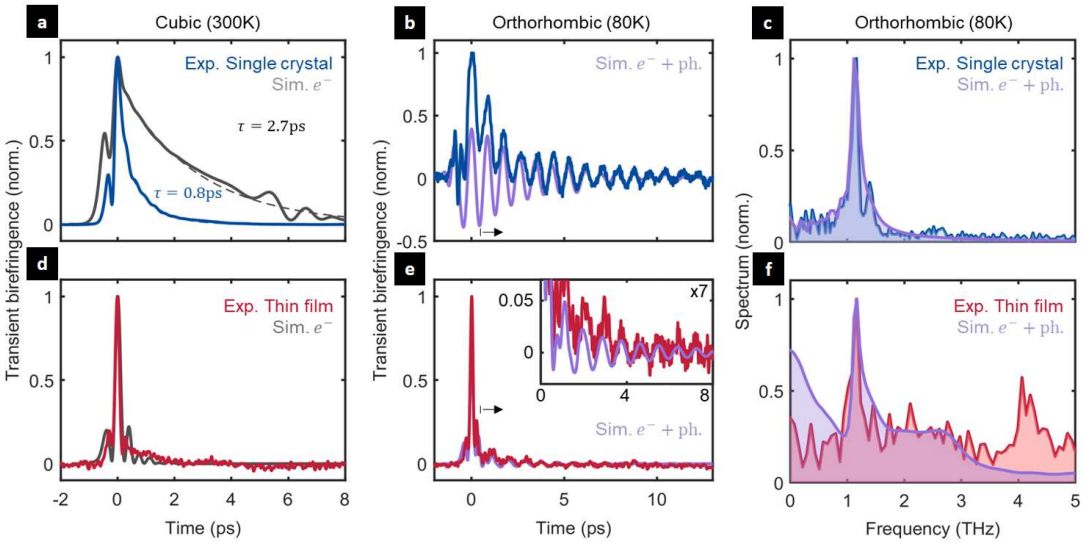

Figure 6.14: 4-wave mixing simulations versus experimental data in MAPbBr3. 300K temperature: (a) Single crystal and (d) thin film experimental TKE versus simulation for (a) 500um and (d) 0.4um thick model system neglecting static birefringence and assuming electronic response only. 80K temperature: (b) Single crystal and (e) thin film TKE vs simulation for model system with static birefringence and added phonon response. (c), (f) Fourier transform of experimental data and simulation results from (b) and (e) showing good agreement.

Fig. 6.14 presents both experimental and simulation of the TKE signal at room temperature in the cubic phase (a-d), in the orthorhombic phase at 80K (b-e) and its Fourier transform, for the single crystal (blue) and the thinfilm (red). Firstly, in the case of the $MAPbBr_3$ single crystal, we can notice that the simulation for a 500 µm crystal shows a longer exponential tail than the one obtained experimentally. The diminution of the exponential decay constant in the experiments is due to the THz absorption inside the sample. Nevertheless, the close simulation shape to the experimental one is a good observation to confirm the dominating electronic polarizability in $MAPbBr_3$ in the cubic phase. The exponential decay shape observed in both $MAPbBr_3$ and $CsPbBr_3$ single crystals shown on Fig. 6.6 is originating from the dispersive light propagation dressed by the instantaneous $P_{NL}^{(3)}(t)$, and more particularly is generated by the pump-probe walkoff induced by the refractive index difference between the both pulse. The oscillatory features observed in $CsPbBr_3$ shown on Fig. 6.6.d are also originating from the dispersive light

propagation in the sample, and particularly from the static birefringence caused by the two distinct orthogonal pump components having different refractive indexes [133]. At ambient temperature, we can conclude that LHPs are dominated by the electronic polarizability α_e and phonon dynamics are not observed. By lowering the temperature and adding birefringence (Fig. 6.14.b), we observe that the oscillations resulting from light propagation appear around 1.4 THz. The simulated oscillatory signal is originating from electronic only contribution which accounts for static birefringence. The oscillation features are caused by the co-propagating pump and probe pulse. However, the Fourier transform (Fig. 6.14.c) provides some difference between the simulated and the experimental signal: simulated main frequency peak (black) has a frequency of about 1.4 THz, slightly shifted from the main experimental one located at 1.1 THz (See Annexis Fig. A.10). More importantly, the stimulated peak is particularly wider than the simulated one. Therefore, it is hardly comparable to the long-lived real phonon modes observed experimentally at 80K, which tends to indicate that despite the fact the both main frequency peak are quite close, the propagation effect might not explain the oscillation observed at 80K and lattice polarizibility might be dominating.

As previously proposed, we compare now the experimental TKE signal with the simulated third order nonlinear polarization term together in the case of a thin film. The TKE signal at room temperature seems quite similar for the both experimental and simulation taking only into account the electronic response model (Fig. 6.14).d, despite the fact short-lived oscillatory features seem more pronounced in the simulation. Moreover, the simulation follows without tail-like shape, strengthening the idea that the exponential tail observed in single crystal originates from the light propagation through the sample and is dependent of the thickness. The difference between the propagation simulation and the experimental signal is obvious at 80K, where the experimental phonon oscillation are visible until 10 ps while the propagation oscillatory features only survived 2 ps. The most interesting observation might come from the Fourier transform (Fig. 6.14.f). The simulated Fourier transform does not show any main and clear frequency peak, in opposition to the experiment. Therefore, static birefringence should not be responsible of sharp frequency peak as shown by the black curve, which is a good agreement with the 1.1 THz mode observed experimentally to be a real Raman phonon mode originating from the lattice polarizibility and not due to light propagation.

Simulation assuming electronic and phonon contributions to describe more precisely the time and frequency domain experimental signals for the thin films are displayed in purple on Fig. 6.14.e and Fig. 6.14.f , with $\frac{\omega_{ph}}{2\pi}$ = 1.1 THz. The simulation fits really well the experimental results, This is further evidence that we observe both electronic and lattice polarisability due to the 1.1 THz phonon mode.

We now turn our interest to another A-site cation lead halide perovskites, the fully inorganic $CsPbBr_3$. We performed temperature-dependent TKE experiments on a 800 µm thick single crystal. Although the TKE signal at 80K has several similarities in terms of features and does not qualitatively change, it also presents important and long-lived oscillatory features that

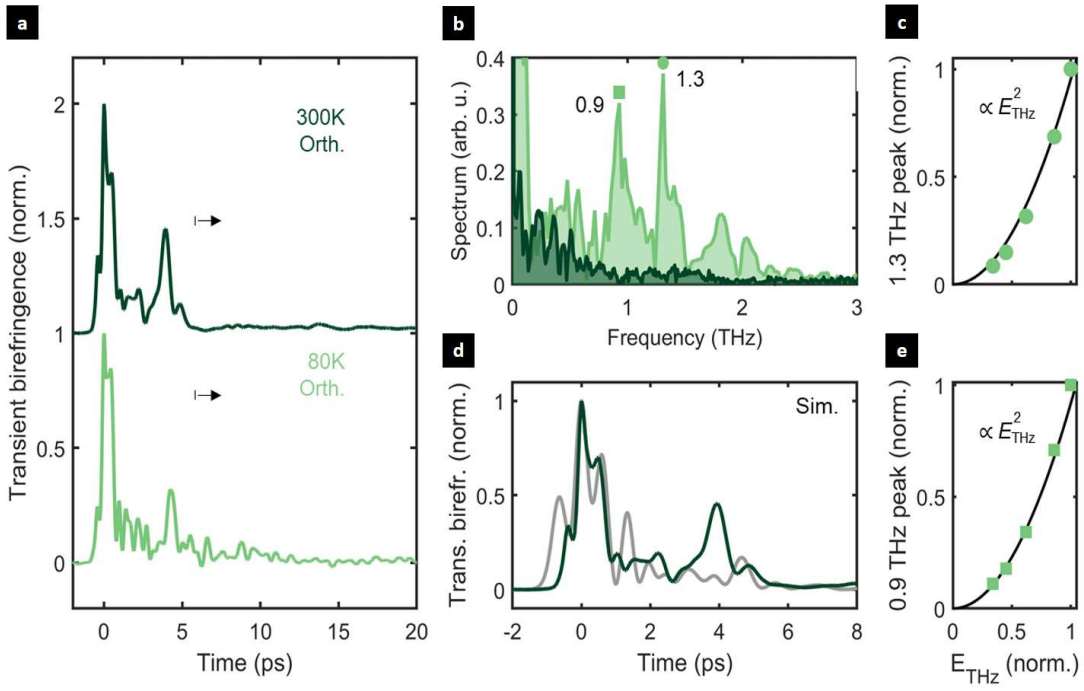

Figure 6.15: $CsPbBr_3$ single crystal (a) TKE signal at different temperature, (b) Fourier transform and (c) simulation.

do not appear in the room temperature spectra (Fig. 6.15.a). The Fourier transform of the signal show a clear evidence of two frequency mode appearance, at 0.9 THz and 1.3 THz respectively (Fig. 6.15.b). The extracted lifetime from the Lorentzian fit is $\tau_{1.3THz} = 3$ ps ($\pm$ 1). These frequency modes are in good agreement with static Raman spectroscopy [135] and they also scale quadratically with the THz electric field, conforting the idea these modes are non-linear Raman-excited ones (Fig. 6.15.c, e). The simulation of the dispersive and birefringent orthorhombic phase at 80K is represented with the experimental TKE signal on Fig. 6.15.d. The electronic response simulation do not fit perfectly well with the experimental TKE signal, but the both are assumed to be particularly complex.

6.2.4 Discussion

Photonic or phononic excitation pathway ?

THz-induced Kerr measurements enabled to follow for the first time time-resolved dynamics of Raman-active mode in $MAPbBr_3$ and $CsPbBr_3$ perovskites, consistent with the ones observed in static Raman spectra. [39, 135, 136, 224, 225]. In the case of $MAPbBr_3$, the Raman-active mode corresponds to the single 1.1 THz dominating phonon mode resulting from the Pb-Br-Pb

bond angles originating from the octahedral twisting [113]. This mode is an anisotropic and symmetric A_g and is present in both single crystal and polycrystalline thinfilm. On the other hand, two dominating Raman-active phonon modes are observed at 0.9 THz and 1.3 THz in $CsPbBr_3$ single crystal, also in agreement with static Raman spectra.

The Raman-active origin of the coherent phonon modes has been proven by the quadratic relationship of phonon amplitude $Q(t)$ with the THz electric field. The nonlinear excitation of the mode is consistent with Raman-type probing via TKE. Nevertheless, the specific excitation pathway of these Raman-active mode excitation is not entirely solved. Two main excitation pathway could explain our observation: the phononic and the photonic process, as discussed in Section.2.4. The phononic pathway would require significant phonon anharmonicity, whereas a direct coupling of two THz fields to the Raman tensor in the photonic pathway would require strong THz polarizability. To know which of the difference- or sum frequency (DFG/SFG) excitation pathway could be responsible of the Raman-active phonon modes excitation in the case of the photonic pathway, we simulate a SFG/DFG force spectrum knowing the THz pump field. Fig. 6.16.a describes the strength of the $LiNbO_3$ spectrum to excite modes at a particular frequency using either SFG or DFG. We can see that at 1.1 THz both SFG and DFG seem equally likely. In the case of the phononic pathway shown in Fig. 6.16.b, there is also comparable probability for this paths to drive the 1.1 THz mode. So far, it is not possible to rule out a precise excitation mechanism for any of the four possible nonlinear excitation pathway.

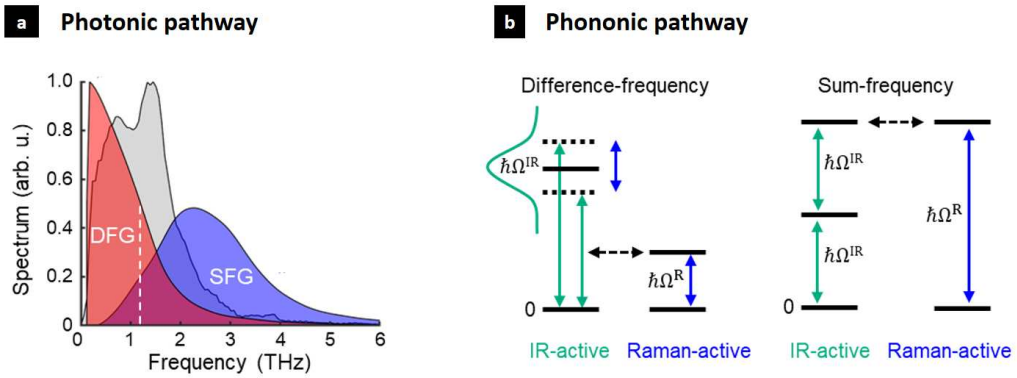

Figure 6.16: (a) Difference and sum frequency excitation for photonic pathway force spectrum (b) Possible phononic pathway driven by the polarization of IR-active phonons.

Octahedral tilting: a signature of polaron formation?

We previously discussed the clear phonon mode observed in $MAPbBr_3$ and $CsPbBr_3$ as the most polarizable lattice mode. Several works proposed that the 4 THz mode was related to a possible Fröhlich phonon, which could lead to charge screening [123, 119, 152, 226, 151]. This

higher frequency phonon modes is not observed in our TKE experiments. Furthermore, the later discussed sum frequency-force spectrum shows that THz pump pulse might not have enough spectral strength to excite higher frequencies, which could be a clue to understand why the 4 THz mode does not appear on our TKE.

The equivalent of the 1.1 THz TKE mode observed in $MAPbBr_3$ was found to transiently modulate the electronic bandgap in $MAPbI_3$ by Kim et al [158]. Moreover, this mode has a frequency and corresponding half-cycle time of $\approx$ 0.5 ps, which is consistent with estimates for the polaron formation time in LHPs [160]. It is therefore a likely candidate for the phonon mode contributing to polaron formation and dynamic screening. The very similar polaron formation dynamics observed by Bretschneider et al. [160] for the three different LHPs also points out the critical role of the inorganic sublattice for polaron formation, rather than the A-site cations.

As discussed later in Chapter.7, freely moving A-site cations have a contribution for static but not dynamic screening. It seems the molecular reorientation coming from A-site cation dynamics do not contribute to the polarization in our TKE experiments. According to our simulation, the exponential tail-like feature is only originating from instantaneous electronic polarization and dispersive light propagation. Moreover, the THz pump frequency should not be able to excite the vibrational mode of the A-site cation, located in way higher frequency region (800 cm^{-1}), while rotational resonances are located as much lower frequencies (< 100 GHz) [113]. Despite the fact TKE spectroscopy enables the observation of inorganic lattice vibration, the diversity of signals obtained between $MAPbBr_3$ and $CsPbBr_3$ is a signature of the cation's role to moderate the degree of polarizability. This signature was also observable in the diverse Raman spectra observed for different A-cations [135, 136].

LHPs phase transition previously described are similar to the one in well studied oxide perovskites, such as $SrTiO_3$. The phase transition takes place when antiferrodistortive distortions appear, originating from the octahedra rotation [222, 227, 228, 229]. The twisting of the octahedra leads to a slight modification of the Pb-Br-Pb angle. During the cubic to tetragonal phase transition, only 1 tilt appears, while 3 microscopic ordered-tilts are possibles during the tetragonal to orthorhombic phase transition [223, 230]. These twisting modes are the soft modes which govern the structural phase transition in LHPs. Recently, Raman spectra of double-perovskite $Cs_2AgBiBr_6$ showed particularly well this implication of the twisting soft modes [231]. The soft phonon mode of the cubic to tetragonal transition is highly more displacive than the ones in the tetragonal to orthorhombic transition, as for $MAPbBr_3$, and lead to rotation of octahedra. The softening of the 1 THz twist mode in Raman spectra of $MAPbI_3$ (equivalent to the 1.1 THz mode in $MAPbBr_3$) has been studied in several research works, suggesting it should be the soft mode responsible for the phase transition [223, 232, 40]. In comparison, the tetragonal to orthorhombic phase transition is a primarily order-disorder type of phase transition, originating from MA cations and Pb-X framework coupling [223, 233]. The main factors influencing the rotation angle of the octahedral tilt are the A-site cation via

the steric effects [II] [234, 235, 236, 237], as well as the hydrogen bonding between the Pb-X framework and the A-cation, when the later is organic [238, 239, 240]. These octahedral tilting motions contribute significantly to dynamic disorder in LHPs and present the strongest polarization response to quick varying electric field on sub-picosecond timescales [39], indicating its likely contribution to dynamic carrier screening and polaron formation. Therefore, the formation of a large polaron may be linked to a transient phase instability.

6.3 THz Kerr Effect : $APbBr_3$, with A-site a quadruple cation

The previous subchapter discussed the most polarizable Raman-active phonon modes in $MAPbBr_3$ and $CsPbBr_3$, using THz-induced Kerr spectroscopy technique to identify them and to follow their coherent dynamics. This section focuses on compositional engineering of the A-site cation, investigating the coherent Raman-active phonon dynamics in $FAPbBr_3$, $(MA_{0.2},FA_{0.8})PbBr_3$ and the quadruple cation lead halide $(GA_{0.015},Cs_{0.046},MA_{0.152},FA_{0.787})PbBr_3$ perovskite, lnown as (4cat)$PbBr_3$ in our discussion.

6.3.1 Motivation

Previously, we studied conventional and simple A-cation LHP like $MAPbBr_3$ and $CsPbBr_3$. Compositional engineering explored different chemical compositions of the A-site cation. Adding a small amount of Cs in the A-cation composition was found to enhance the stability of the material [94]. Moreover, the A-site cation influences the exciton binding energy, which has been reported to be lower with Cs-containing mixed compounds than in simple $MAPbI_3$ [241, 242]. More precisely, the exciton binding energy with Cs and mixed (I,Br) is even lower than for pure $MAPbBr_3$ and $MAPbBr_3$ at room temperature. Being able to tune the exciton binding energy is an important tool, knowing that large exciton binding energy is a problem for solar cell application, since smaller exciton binding energies are beneficial for the charge separation and therefore the charge extraction in the device. This emphasizes the excellent suitability of multiple-cation mixed-halide perovskites for photovoltaics [38]. Simple A-site cation perovskite generally have poor photostability and thermal stability. Highly crystalline and compositionally photostable material with mixed-cation lead mixed-halide perovskite show better performance when used as absorber for tandem solar cells [31]. In general, cation engineering contributed to power-conversion efficiency enhancement in photovoltaic solar cell [24]. A study of the crystallographic structure of the complex mixed A-site cation seems important, knowing that suppression of phase transitions is crucial to maintain a stable performance for many application. Indeed, phase transitions change the crystal structure and thus affects the electronic structure. It is possible to observe phase transition via photoluminescence, optical spectroscopy and electronic bandgap change [241]. Temperature-dependent bandgap energy of Cs incorporation and (Br,I) halide mix did not show any phase-transition

[II] Steric effects originates from spatial arrangement of atoms and are nonbonding interactions influencing the shape and reactivity of ions and molecules.

related jumps or kinks compared as pure $MAPbI_3$ or $MAPbBr_3$ case [241]. This is a first indication of the suppression of the phase transition in these multiple-cation mixed-halide perovskites. The above arguments reinforce the idea that there is a need to deeply study and develop complex mixed A-cations lead halide perovskites in order to produce highly stable, defect tolerant and efficient absorber material for solar energy application.

As discussed in the previous section, it is still debated that carriers scattering in LHPs is dominated by solvation model, i.e between charge carriers and optical phonon modes. Moreover, LHPs are known to have high lattice anharmonicity, particularly at room temperature. This phonon scattering is believed to be the key fundamental factor in establishing the intrinsic limit of the charge carriers mobility. More specifically, it has been recently suggested that this limit is set by the lower-energy LO modes (3–20 meV). The observed presence of such modes in different A-site cation compounds [119] seems to be the reason for the relatively low mobilities compared to classical inorganic semiconductors like Si and GaAs. This work aims to understand the influence of A-site cation composition on the instantaneous electronic α_e and lattice polarizibility α_{ion} as a response to a single-cycle THz electric field, by investigating numerous conventional and simple then complex A-site cation LHPs with time-resolved TKE. We are interested in investigating how A-site cation compositional engineering influence Pb-Br sublattice polarizability and dominating coherent phonon response. First, in the case of complex (4cat)$PbBr_3$, we aim to characterize its temperature-dependent crystallographic structure, as well as its optoelectronic properties and charge carrier dynamics.

6.3.2 Lattice polarizibility dependence to A-site cation chemical composition

The samples were synthesized by our collaborators at the University of Cologne, who also performed the additional characterizations (see Annexis.A.1) mentioned later in the discussion.

THz-induced Kerr spectroscopy method was performed on 350 nm thick thin film on BK7 glass substrate with different A-site cation composition at 80K, to observe the coherent Raman-active phonon response. The temporal dynamics are normalised and shown on Fig. 6.17.a, with a focus on the instantaneous electronic polarizibility α_e happening in the first 0 to 2 ps, and the lattice polarizibility until 6 ps. (4cat)$PbBr_3$, $MAPbBr_3$, (MA,FA)$PbBr_3$ and $FAPbBr_3$ shown all short instantaneous electronic polarizibility α_e, in contrast with the $CsPbBr_3$ thin-film which shown a longer exponential tail during approximately 2 ps. In all the thin films, small amplitude oscillatory features appear from 1 to 2 ps, with a frequency of 4 THz. These oscillations are reproductible in all thin film and do not originate from the BK7 substrate, as the later has really low signal compare to the TKE signal generate from perovskite as shown on Fig. 6.18.b. Furthermore, the BK7 signal does not change significantly from room temperature to 80K, which further confirms the latter points (Fig. 6.18.a).

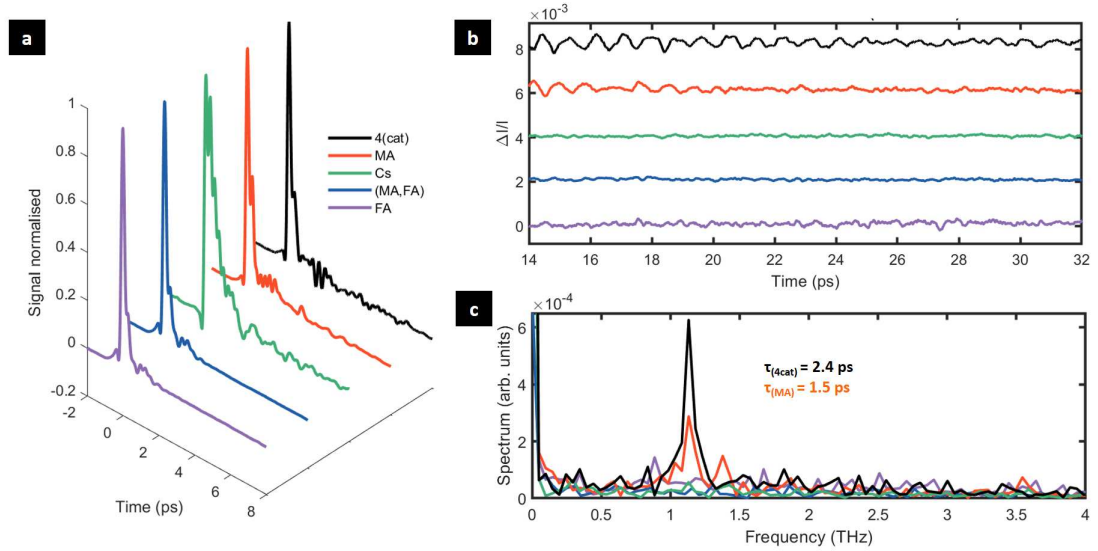

Figure 6.17: (a) TKE signal for different A-site cation lead bromide thin films. All are 350 nm thick. (b) Oscillatory features at 80K appear clearly by removing the exponential decay tail and zooming on it. (c) Fourier Transform of the oscillatory features above.

(4cat)$PbBr_3$, $MAPbBr_3$ and $CsPbBr_3$ show oscillatory features after 2 ps and lasting at least until 6 ps, in opposition to (MA,FA)$PbBr_3$ and $FAPbBr_3$, which show absolutely no signal after 2 ps. The oscillations are shown on Fig. 6.17.b, with a temporal focus on the long-lived oscillations from 13 ps to 31 ps, and its Fourier transform is shown below in Fig. 6.17.c. $MAPbBr_3$ and $CsPbBr_3$ signals are comparable to what was described in the first work we performed on both single crystal and thin films, with Raman-active phonons modes respectively at 1.1 THz for $MAPbBr_3$, with an additional small peak visible around 1.4 THz, and 0.9 THz for $CsPbBr_3$ (not shown on this Fourier transform). It is clear that at 80K, TKE signal and phonon modes as well as phonon lifetimes highly depend on the A-site cation chemical composition. Furthermore, dominating inorganic lattice mode in (4cat)$PbBr_3$ remains the same as in $MAPbBr_3$, despite distortion and increased lattice disorder. Very interestingly, (4cat)$PbBr_3$ and $MAPbBr_3$ have a main polarizable mode at 1.1 THz, with different lifetime $\tau_{(4cat)}$ = 2.4 ps (± 0.37) and $\tau_{(MA)}$ = 1.45 ps (± 0.54).

It is particularly interesting as in comparison to other A-site cation containing Formamidinium (FA), (4cat)$PbBr_3$ is the only one showing long-lived oscillatory features. $FAPbBr_3$ is highly anharmonic and only broad and extremely short-lived phonon oscillation should be observed, according to static Raman spectra at 80K [136]. Its TKE signal does not allow to even observe the Raman-mode frequency we might observed in FA. The extremely short-lived inorganic lattice modes in FA coumpounds may be connected to a different dynamics of the FA cation and its coupling to the perovskite sublattice, by comparison to the MA cation [132]. According to nuclear magnetic resonance (NMR) measurements [243], the broader nature of the optical

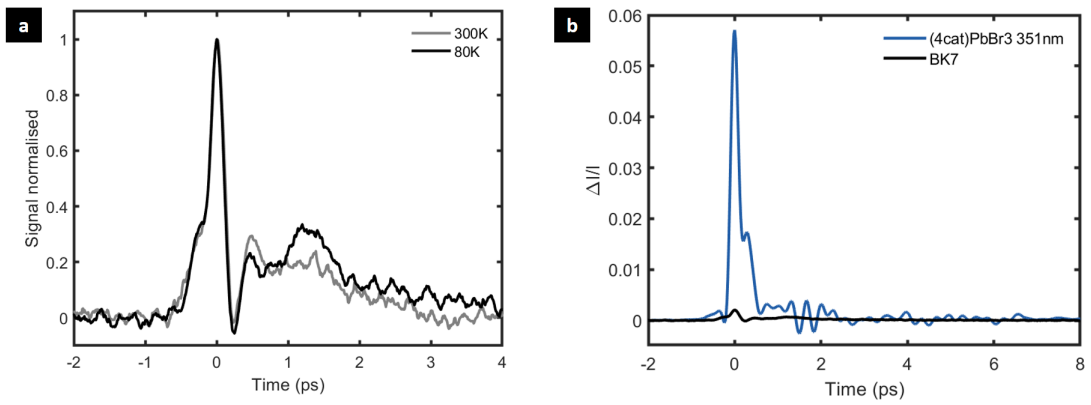

Figure 6.18: (a) THz induced Kerr signal in 500µm BK7 glass substrate, at 300K (grey) and 80K (black). (b) Comparison of THz induced Kerr signal at 80K between BK7 substrate (black) and (4cat)$PbBr_3$ 351 nm thick thinfilm (blue). BK_7 does not affect the quadruple cation LHPs signal.

modes of FA-based compounds, compared to their MA-based counterparts, may be attributed to the fact that the FA reorientation in FA-containing materials is faster than that of MA in the MA-based perovskite, despite the fact that FA is larger than MA. This has an impact on the charge carriers lifetime in these compounds. In addition, the acoustic phonon density of states is located at lower energy in FA-based compounds as compared to the MA based [132], thus leading to enhanced scattering between acoustic and optical phonons and related increased anharmonicity [244]. The lack of dispersion of the lowest LO-phonon frequency mode in MA-based LHPs is not related to cation (molecular) but pure lattice vibration, in contrast to FA-based LHPs, where broader phonon modes are observed and involve molecular vibration. The origin of broader phonon peaks can be either due to a larger damping or related to moderately dispersive phonons in FA-based halide perovskites [132]. In $FAPbBr_3$, phonon damping and reduced phonon amplitude make it difficult to properly assign the exact contribution of each phonon mode to the overall spectra at higher temperatures [132].

In our THz-induced Kerr signals (Fig. 6.17.a), both (MA,FA)$PbBr_3$ and pure $FAPbBr_3$ do show extremely short-lived lifetime but interestingly (4cat)$PbBr_3$ with (4cat) being composed of an 78% of FA shows really long-lived phonon modes with the same frequency as pure $MAPbBr_3$ coumpound. 1.1 THz mode is highly dominating the sublattice vibration in (4cat)$PbBr_3$, as in $MAPbBr_3$, despite the fact there is only a few percentage of MA in the A-site. As the 1.1 THz mode is pretty clear for $MAPbBr_3$ (4cat)$PbBr_3$ composed of A = ($GA_{0.015}$,$Cs_{0.046}$,$MA_{0.152}$,$FA_{0.787}$), but absolutely not existing for the ($MA_{0.2}$,$FA_{0.8}$)$PbBr_3$, we should consider the role of GA and Cs in the reinforcement of the MA cation signature. According to our latest knowledge, the coupling between GA^+ cation has not been investigated and solved so far. Our observation allows to suggest a hypothesis: as the 1.1 THz mode observed in $MAPbBr_3$ and (4cat)$PbBr_3$ is

linked for sure to the Pb-Br bonding, the current chemical composition of Formamidinium, Guanidiniuum and Cesium may lead to a stabilization of the overwhole lattice behavior as in $MAPbBr_3$, despite the diverse cation size. Therefore, the MA^+ cation would be the only one to still interact with the sublattice. Due to the weaker overall cationic disorder induced by the quadruple cation composition, the most polarizable vibration mode could appear more intense.

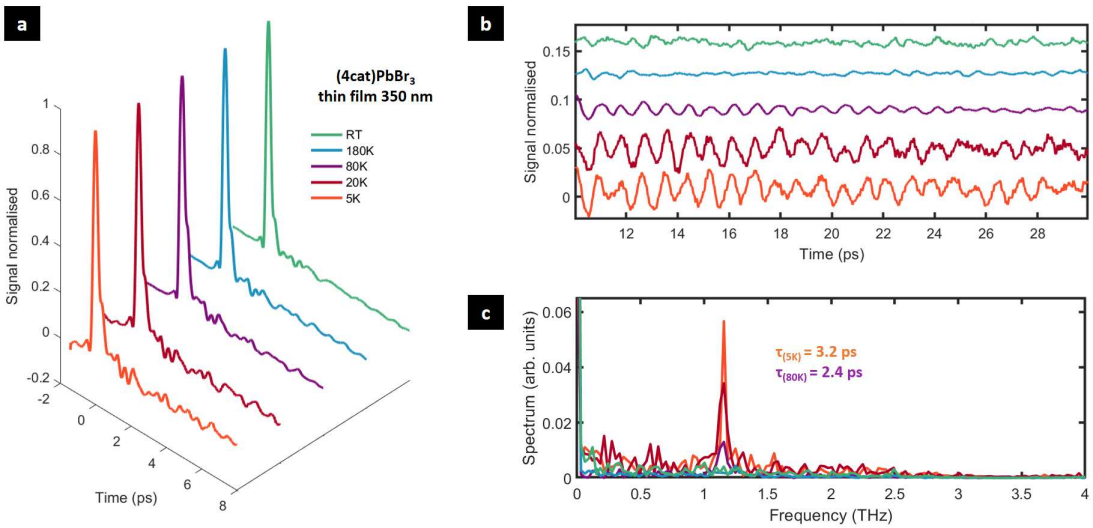

Figure 6.19: (a) Normalised temperature-dependent THz-induced Kerr signal in quadruple cation lead bromide perovskite (4cat)$PbBr_3$ thin film (350nm), its (b) oscillatory features and (c) Fourier transform from 10 ps. 1.1 THz phonon mode appears more clearly while decreasing temperature. Phonon lifetime τ evolution is written on the plot.

6.3.3 Intriguing most polarizable Raman-active mode

The dynamics of (4cat)$PbBr_3$ is further studied by looking at the evolution of the THz-induced birefringence as a function of temperature. We repeated the same protocole of temperature-dependent THz-induced Kerr spectroscopy experiments (Section.6.2) from room temperature to 5K, as it is necessary to cool down to the lowest temperature in order to reduce phonon damping and to be able to observe sharp optical phonon features. Fig. 6.19.a shows the normalized temperature-dependent electronic polarizibility α_e. The first 2 ps are quasi-equivalent, while some oscillatory feature get more and more proeminent at lower temperature. The oscillatory signal after the substraction of the biexponential decay is represented in Fig. 6.19.b, while its Fourier transform is shown on Fig. 6.19.c. Clear 1.1 THz oscillatory features appear at 80K and get even stronger by lowering the temperature. It is explained by the fact two-photon photon absorption has to be avoid by decreasing the probe power, therefore lowering the final detected transient birefringence signal. Nevertheless, the Fourier

Transform show a clear narrowing of the 1.1 THz peak by approching 5K, making no doubt of the existence of this mode. The smaller the temperature is, the higher the phonon lifetime is, as we obtained using Lorentzian fitting from the Fourier transform, with τ_{80K} = 2.4 ps (± 0.37) and τ_{5K} = 3.2 ps (± 0.29), respectively.

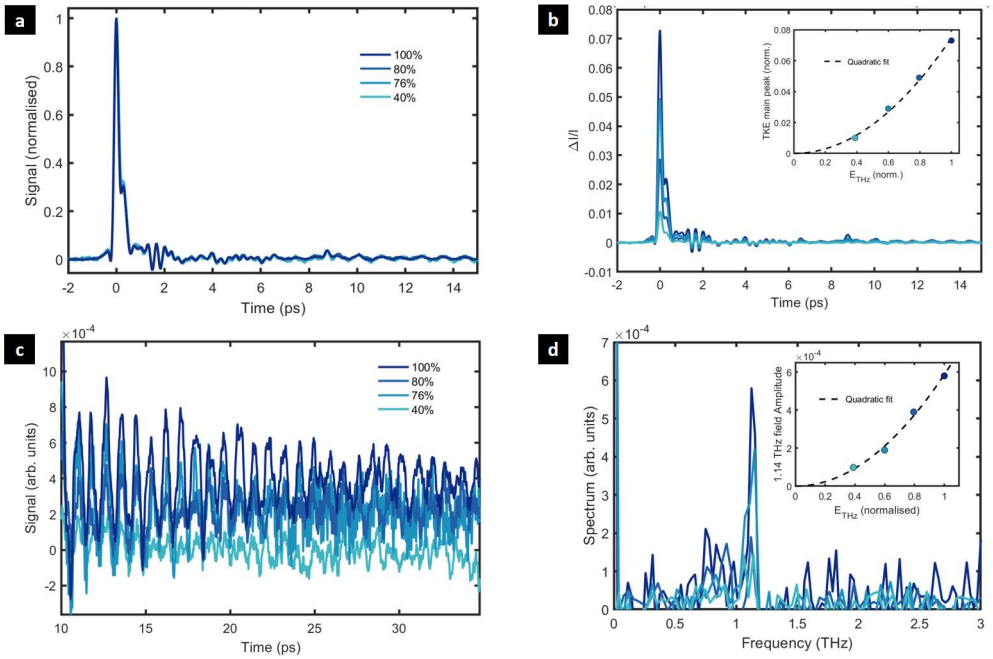

Figure 6.20: Normalised and not normalised TKE at 80K for different THz pump fluences in (4cat)$PbBr_3$ 350nm thin film. The amplitude of the oscillations scale with the TKE peak. The inset shows that the dominating oscillatory amplitudes also scales with the square of the THz electric field, 1.1 THz for $MAPbBr_3$. This demonstrates that the oscillations correspond to nonlinearly excited Raman active phonons.

In order to confirm the Raman-active origin of the observed 1.1 THz mode in (4cat)$PbBr_3$, fluence-dependent measurement where performed at 80K. Fig. 6.20.a and Fig. 6.20.b show that the main peak originating from the instantaneous polarizibility and the 1.1 THz phonon modes scale with the oscillation and that the signal scale quadratically with the incoming THz electric field.

The 1.1 THz mode is not the only visible mode in the (4cat)$PbBr_3$. The previous discussion focussed on the extremely long-lived frequency, visible even after 14 ps on Fig. 6.19.c, while Fig. 6.21.a focuses on the one observed after 1.5 ps. When Fourier transform are performed from 1.1 ps after the main instantaneous electronic response peak, four relatively short-lived modes also appear from 80K that are not observed in other A-cations lead bromide perovskite: at 73 cm^{-1} (2.2 THz), 86 cm^{-1} (2.6 THz), 103 cm^{-1} (3.1THz) and 110 cm^{-1} (3.3 THz). They get even more observable and their lifetime seems to increase while the temperature decrease. A fifth mode might even exist at 56 cm^{-1} (1.7 THz), but is less obvious than the four others.

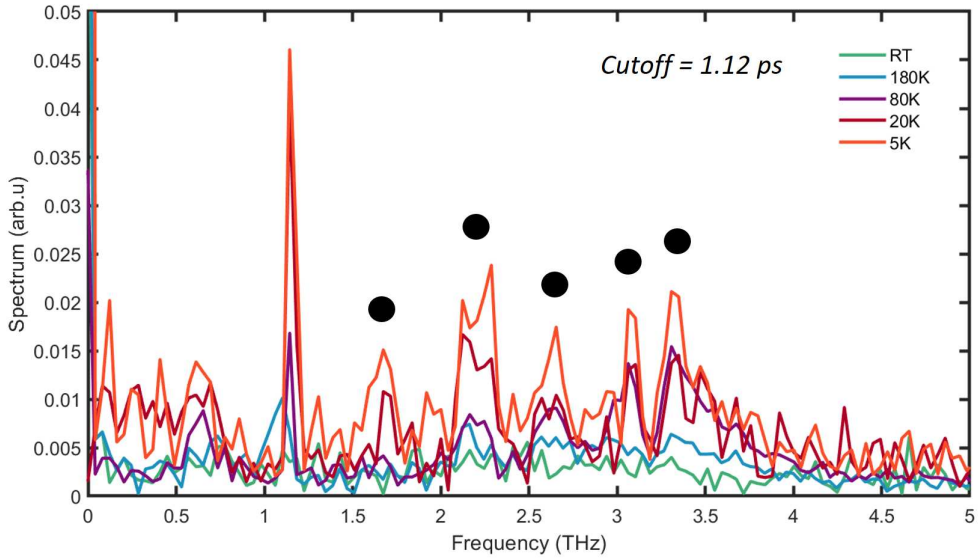

Figure 6.21: Temperature-dependent Fourier Transform of the (4cat)$PbBr_3$ TKE oscillatory signal after t = 1.1 ps. In addition to the sharp phonon mode at 1.1 THz, several other shorter-lived frequency peaks are observed (black dots). Their frequencies get clearer by lowering down the temperature. A cutoff = 1.12 ps was used, i.e Fourier transform is performed on all temporal signal after t = 1.12 ps.

Unfortunately, fluence dependence was not possible on these modes to investigate their excitation pathway.

As the specific $(GA_{0.015},Cs_{0.046},MA_{0.152},FA_{0.787})PbBr_3$ has been only studied once in the litterature [245], no static Raman spectroscopy has been performed on it yet. One of our next research step is to realize a temperature-dependent static Raman spectroscopy on a (4cat)$PbBr_3$ single crystal, to verify the existence of these short-lived Raman-active phonon modes in this material.

In order to ensure that these four new modes originate from the material and not from a propagation effect or another artefact, thickness-dependence TKE experiments have been performed. All the (4cat)$PbBr_3$ perovskites layer were deposited on the same 500 µm-thick BK7 glass substrate and the following thickness were studied: 260 nm and 351 nm. There transient birefringence signal as a function of the pump-probe delay are represented in Fig. 6.22.a and their Fourier transform are shown on Fig. 6.22.b and .c. For the 260 and 351 nm-thick sample, the temporal TKE signals slightly different, but their Fourier transform and main frequency peak are similar after 12.68 ps, indicating the mode is only material-related (Fig.6.22.c). The Fourier transform of the 260nm and 350nm thick thin film after 1.1 ps (Fig. 6.22.b) show that the four other modes at 2.2 THz, 2.6 THz, 3.1THz and 3.3 THz are observable independently

of the thinfilm thickness, adding a strong proof to the hypothesis these modes are related to the A-site cation chemical composition and not from an external artefact. According to the FWMH of the four newly observable phonon modes, they should be shorter-lived than the main 1.1 THz mode.

All these observations open the discussion about the possible link between the coexistence of the four relatively-short lived modes, the long lifetime of the 1.1 THz in (4cat)$PbBr_3$ and the 1.1 THz mode similarity with $MAPbBr_3$ at T < 80K. The complexity of this A-site cation could explain the presence of these short-lived phonon modes, but their exact mode nature still require investigation. The size of the mixed cations and the nature of the halogen (Bromide in our case) are additional features known to strongly influence the softness of the lattice [246]. They also have a direct impact on the damping of the optical modes. Therefore, this suggests that the coupling between acoustic and optical phonons may play a role in the harmonicity of the lattice, besides nonlinear coupling between optical phonons [132, 159].

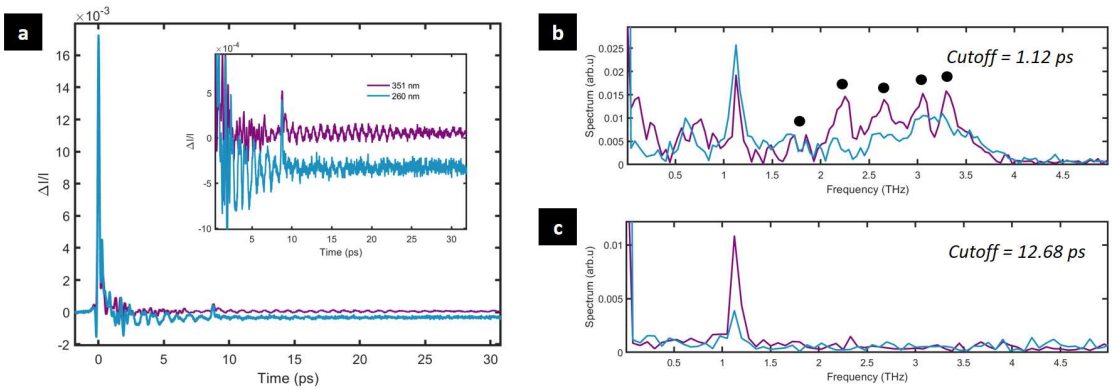

Figure 6.22: Thickness dependence of the (4cat)$PbBr_3$ thin film: (a) Transient birefringence and Fourier transform after to different cutoff in the t direction (b) at 1.1 ps and at (c) 12.68 ps. In both thinfilm, short-lived oscillations with closed frequency are observed.

6.4 Summary and discussion

This chapter has discussed the many applications of the Kerr effect in the field of hybrid perovskite characterisation. In Section 6.1, optical Kerr effect alerted us to the need to take into account dispersive light propagation in anisotropic media, especially in the orthorhombic phase of perovskites, and not to confuse them with coherent phonon dynamics. Terahertz induced Kerr effect allowed to follow nonlinear coherent excitation of the 1.1 THz main polarizable and Raman-active mode in $MAPbBr_3$ and (4cat)$PbBr_3$ perovskites, as described in Section 6.2. These modes are possible candidates to explain the dynamic charge screening in lead halide perovskite. This finding highlights the role of the inorganic lattice for dynamic carrier screening and the related mechanism of charge carrier protection. Comparison with

the vibrational modes obtained for other A-site cations lead bromide perovskites has shown the role of the cation-inorganic sublattice interaction on the dominant vibrational modes, even though polaronic stabilization of a charge carrier comes mainly from the latter and particularly from PbX_3 polarization. Four-wave-mixing simulations showed how crucial it is to account for anisotropic and dispersive light propagation in the interpretation of the measured TKE signals. Interestingly, the complex (4cat)$PbBr_3$ also has a most polarizable phonon mode at 1.1 THz, thus opening the question concerning the usefulness of having a cationic disorder and its impact concerning the lattice vibration. Crystallographic measurements have shown that (4cat)$PbBr_3$ is still potentially in the cubic phase at 80K while the highest polarizable lattice modes obtained are similar to those observed in $MAPbBr_3$. Optoelectronic as well as SEM measurements have confirmed the better structural and optoelectronic properties of (4cat)$PbBr_3$ compared to simple A-site cation LHPs, which may be a key to understanding the previous TKE resultes. The next step would be to exctract the Urbach energy of the different A-site cation thin film to understand if the decreasing static disorder with an increasing number of cations might indicate an improved structural order, as proposed by Zeiske et al [247]. As THz-induced Kerr effect technique is extremely promising for studying phonon modes with a frequency close to Terahertz, further investigations on 2D perovskites are also a next step to better understand the interplay between the inorganic structure and the organic spacer cation.

7 Femto- to picosecond electron dynamics in lead halide perovskites

This section presents the experimental results obtained using the 2PPE or tr-ARPES techniques presented in Chapter.5. The impact of static defect screening in MAPbI3 is studied through the tetragonal to orthorhombic phase transition in Section.7.1. Then, the first experimental results concerning a possible Rashba splitting in 2D (BA)-$MAPI_3$ are presented in Section.7.2. Finally, we discuss in Section.7.3 the passivation of the recombination centers increase the lifetime of charge carriers in quadruple A-site cation $(GA_{0.015},Cs_{0.046},MA_{0.152},FA_{0.787})Pb(I_{0.815}Br_{0.185})$ and the impact of solar cell properties.

The 2PPE and tr-ARPES experiments were performed by myself and co-workers on the FemtoARPES set up of the Ecole Polytechnique, as well as the analysis of ultrafast time-resolved phenomena. The other techniques were performed by collaborators from University of Cologne or Synchrotron Soleil.

7.1 Tetragonal to orthorhombic phase in 3D $MAPbI_3$ perovskites

7.1.1 Motivation

Metal halide perovskites are highly studied during the last decade because of their excellent performance in photovoltaic devices and optoelectronic applications. As for any other semiconductor, the transport and photovoltaic properties of these compounds can be influenced by disorder and impurities. However, the excellent tolerance to defect scattering in metal halide perovskites is the subject of considerable debate [248, 249, 250]: the high charge-collection efficiencies and open-circuit voltage in the lead halide perovskites solar cells suggest that both the carrier recombination rate and trapping rates are particularly low [245]. Besides, the solar cell active layer is nearly always a polycrystalline thin film, having grain boundaries which could create a large amount of trapping centers. Some research works linked the exceptional electronic properties of metal halide perovskites to the polarizability of the nuclear lattice [110, 251]. Permittivity measurements of the tetragonal phase of MAPbI3 have shown that collective reorientations of organic cations result in a dielectric constant, attaining values larger than 120

below 1 GHz [110, 149]. Furthermore, trapping centers generate a massive dipole relaxation which has no analogous property in conventional semiconductors: any carrier approaching a charged defect will not be affected, unless coming closer than two unit cells [110]. The defect tolerance originating from the large dielectric screening prevails in $MAPbI_3$ tetragonal phase, where the orientation of organic dipoles can be very easily switched. It is the opposite of the orthorhombic phase, where the organic moiety freezes in an ordered structure, leading to a sudden drop of the dielectric function from 120 to 30. [110, 149] This should lead to a visible impact on the dynamics of photocarriers, originating from charged traps and polar interfaces of the grain boundaries. This evidence has so far remained elusive. In this section, we investigate if the organic cations MA^+ are capable of efficiently screen charged defects or polar interfaces. For this purpose, a study of $MAPbI_3$ surface and surface-to-bulk electronic band bending is proposed.

7.1.2 Organic cation and screening in $MAPbI_3$

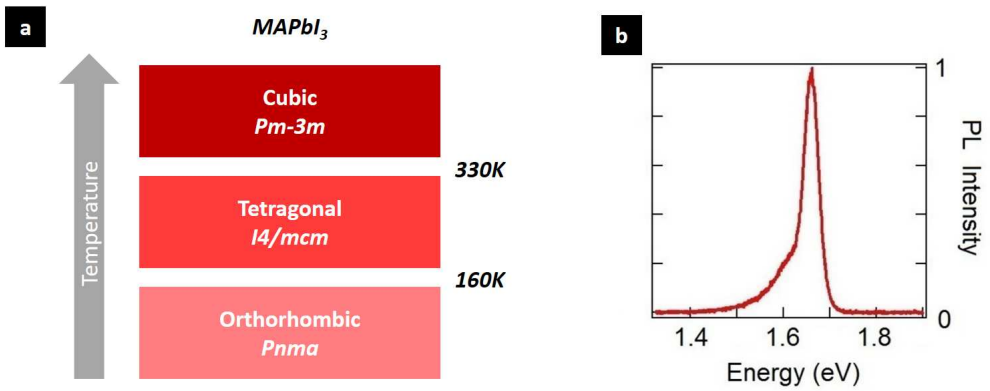

Figure 7.1: (a) Phase transition and space group of $MAPbI_3$ at different temperature in Kelvin. (b) Photoluminescence spectrum of $MAPbI_3$ in the orthorhombic phase at 130K, from [252]. An electronic bangap of E_g = 1.66 eV is extracted from it.

This work treats particularly about the electron dynamics in lead halide perovskite single crystal with different chemical composition of the inorganic cage, more specifically iodide ions instead of bromide ions in the halide position X_3 (Fig. 7.1.a). As $MAPbBr_3$, $CH_3NH_3PbI_3$, also written $MAPbI_3$ or MAPI, is one of the most intensively studied perovskite during the last decade by the scientific community and is still considered as a reference chemical composition in the field. MAPI phase transitions differs slightly from the $MAPbBr_3$ one (Fig. 7.1.a). Despite certain debate about the exact space group for each temperature and according to several group studies [113, 108], we will consider in this section that MAPI is in the cubic phase $Pm-3m$ above 330K, in the tetragonal phase $I4/mcm$ from 330K to 160K, and finally in the orthorhombic phase $Pnma$ below 160K. Chen et al observed an abrupt phase tetragonal-to-orthorhombic phase transition in $MAPbI_3$ at around 160K using temperature-dependent

photoluminescence and an electronic bandgap of 1.66 eV in the orthorhombic transition at 130K [252]. Single crystals of MAPI grown by inverse crystallization method were used for these experiments, as explained in Chapter 5.4.

7.1.3 One and two-photon photoemission experimental details

In order to access the energy of the electronic states and ultrafast dynamics of the excited carriers in tetragonal and orthorhombic phase, one photon and two photon photoemission techniques have been performed in this work. The principle of photoemission and two photon photoemission (2PPE) has been already detailed in characterisation techniques (Chapter.5). The photoemission measurements discussed in this section have been performed with the FemtoARPES setup, using a combination of direct and two photon photoemission. The fourth harmonic (6.3 eV) have been used to characterize the valence band photoelectron. Then, the second (3.15 eV) and the third harmonic (4.7 eV) has been used to transiently populate and subsequently probe the photoelectron dynamics in the conduction band. In this experiments, the pump beam is absorbed in a penetration depth of about 50 nm and generates an electron density of 5 x 10^{18} cm^{-3}.

7.1.4 Conduction band dynamics at the phase transition

First, a precise analysis of the core levels and the valence bands have been performed in the tetragonal phase at 180K and in the orthorhombic phase at 120K, using hard X-ray photoelectron spectroscopy (HAXPES). The HAXPES spectra displayed both core levels and valence band at different temperature on Fig. 7.2. A shift towards lower energy is observed when the perovskites is in the lower symmetry phase, meaning the orthorhombic phase. This suggests we are observing a band offset so called type II, when both VB and CB lower their energy with respect to the tetragonal structure. The similar core levels were observed in previous XPS studies [253].These spectra are accurate indicators of the composition and chemical bonds present on the surface of the $MAPI_3$, as the total accumulation time was performed in a very short amount of time corresponding to few minutes, in order to limit the degradation of the sample by the 3 keV photons. The lack of any other appreciable change in the spectral shape at the two temperatures indicates that the electronic density of states and atomic valences are almost unaffected by the structural transition.

Photoelectron intensity map of the $MAPbI_3$ surface is shown on Fig. 7.3 and was collected at a pump probe delay of 1.5 ps as a function of temperature. The kinetic energy position of the chemical potential is obtained from the Fermi level of a copper reference that is in Ohmic contact with the sample [I]. The y axis represents the energy considering the chemical potential to be at zero. Fig. 7.3.a represents the conduction band minimum (CBM) and the secondary electrons replica (SER), originating from electron energy loss due to inelastic scattering and

[I] Ohmic contact is a metal-semiconductor contact with a very low contact resistance. It is said to be ohmic when the current I is proportional to the voltage V with a proportionality factor 1 / Rc.

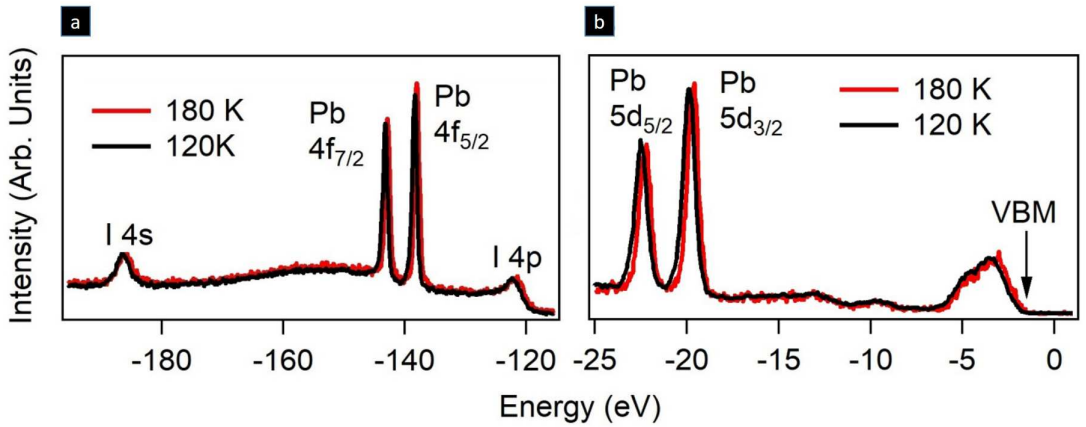

Figure 7.2: HAXPES spectra of $MAPbI_3$ (a) core levels and (b) valence band in the tetragonal phase at 180K and in the orthorhombic phase at 120K. A rigid shift decrease of the valence band energy is observed by lowering the temperature.

corresponding to electrons having zero kinetic energy [252]. The intensity map has been acquired using a probe photon energy of 4.7 eV, using the third harmonic of the fundamental beam (pump-on minus pump-off signal is displayed to reduce background noise). In the tetragonal phase, a signal at roughly around 0.4 eV above the chemical potential is observed. It originates from electrons that have relaxed near the conduction band minimum. After cooling the sample temperature down to 159K and thus reaching the tetragonal-to-orthorhombic phase transition, the signal becomes brighter. The brightest signal is now at -0.1 eV. The lowering of the conduction band minimun observed means that the positively charge surface termination are less screened in the orthorhombic phase than in the tetragonal one. Furthermore, the major increase of the photocurrent intensity in the lowest symmetry phase is the signature of electron accumulation due to a local electrostatic potential. This takes place because organic cations freeze out and the dielectric polarizability drops by a factor four when the structure enters in the orthorhombic phase.

The photoelectron intensity map of the valence band and the valence band maximum (VBM) is displayed in Fig. 7.3.b. The valence band maximum is identified by the threshold where the photocurrent intensity drops below the noise level, and is represented as a dashed white line. Below 159K and thus after the tetragonal-to-orthorhombic phase transition, the valence band maximum shifts by -0.2 eV. This observation is in agreement with the HAXPES measurements discussed in Fig. 7.2. The experimentally estimated electronic bandgaps are 1.58 eV and 1.67 eV, respectively in the tetragonal and the orthorhombic phase, and are identified by the white arrows. These values are comparable to the electronic bandgap observed in the temperature dependent photoluminescence experiments displayed on Fig. 7.3.c. The blue shift of the electronic bandgap in the orthorhombic phase is explained by the tilting of PbI_3 octahedra and the freezing of the organic cation in the orthorhombic ordered structure [106,

53]. Notice that our data confirm the presence of a type II band offset. A mixed phase of $MAPbI_3$ would favor the separation of charge carriers, because of the electrons accumulation in the orthorhombic structure and holes accumulation in the tetragonal one. This would imply that in photoexcited $MAPbI_3$ being in the orthorhombic phase but still having tetragonal inclusions, a photoluminescence peak due to the recombination of electron-holes trapped at the domain boundary between tetragonal and orthorhombic inclusions could be observed.

The measured energy distance between CBM and SER is ξ = 0.4 eV in our crystal. This value can depend on the stoichiometry and can shrink down to 0.1 eV in surfaces with the deficiency of organic cations [252]. We can later extract the energy separation between the vacuum level and the VBM, also known as ionization energy (IE). The value IE = 5.9 eV is obtained by adding the band gap (1.6 eV) and subtracting ξ to the probe photon energy (4.7 eV). According to Emara et al. the obtained IE of approximately 6 eV indicates that our sample has nominal stoichiometry [254].

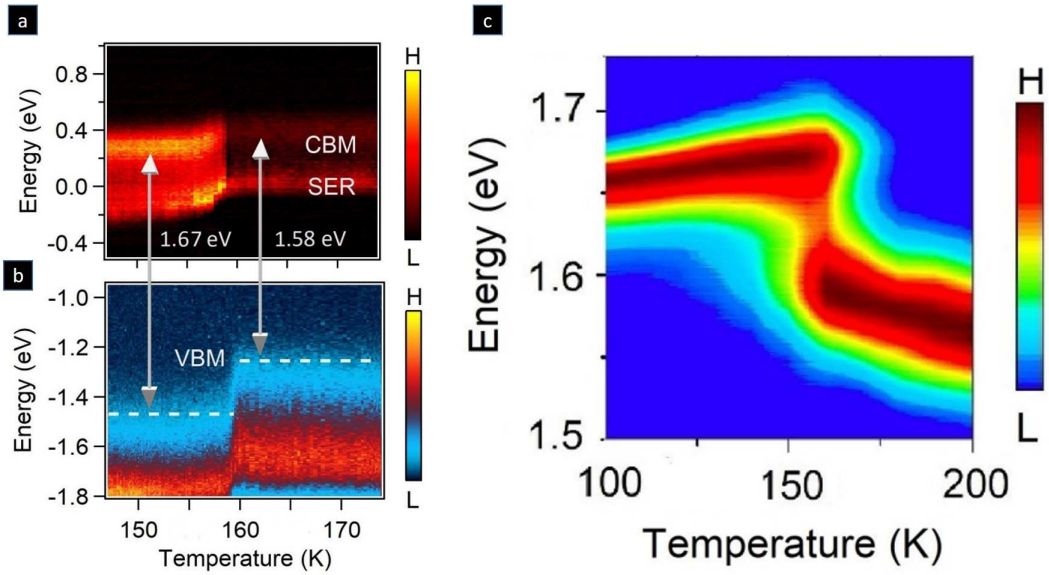

Figure 7.3: Photoelectron intensity map of $MAPbI_3$ single crystal collected at a pump probe delay of 1.5 ps.(a) Conduction band minimun (CBM) and secondary electron replica (SER) and (b) valence band minimum are observed, as function of temperature. (c) Photoluminescence intensity map as function of temperature.

Then, we investigated the carrier dynamics when changing the temperature across the phase transition, using 2PPE. Previous studies of $MAPbI_3$ tetragonal phase have demonstrated that collective reorientations of organic cations lead to a dielectric constant attaining values larger than ϵ = 120 below GHz [110, 149]. This high value of the dielectric constant is due to the molecular dipole of the cation which are not freezed in this crystallographic phase. It ensures that charged surface terminations are efficiently screened by the polarization of the

dynamically disordered organic cations. Since a local electrostatic potential cannot build up, the band stay flat near the surface interface. Later, the photoexcited electrons cool down in order of 0.25 ps by dissipating their excess energy by electron-phonon scattering (Fig. 7.4). The electrons are fully thermalized in the conduction band after 500 fs. The carriers finally recombine with holes in a typical recombination time of 1.2 ns.

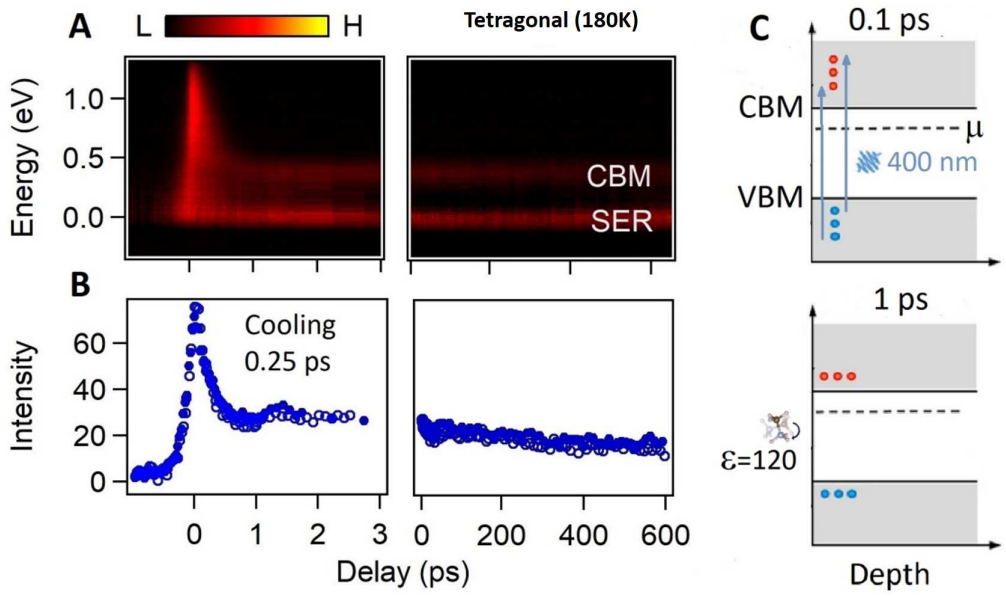

Figure 7.4: (a) Photoelectron intensity map of $MAPbI_3$ acquired in the tetragonal phase at 180K. (b) Photoelectron intensity integrated in an energy interval of 0.1 eV around the CBM as a function of the pump probe delay, always at 180K. The two process of cooling and recombination are indicated on the plot with their lifetime. (c) Sketch of carrier relaxation at the surface of the tetragonal phase.

The same experiment has been performed, this time at 140K in the orthorhombic phase. In the lower crystal symmetry, the build up and the relaxation of the electronic signal is different (Fig. 7.5) compared to the previously discussed one in the tetragonal phase. Indeed, the photoelectron intensity gets particularly bright after 1 ps. This is due to a drift of photoexicted electrons towards the surface, induced by local electric fields. The presence of built-in fields near to the surface of the orthorombic phase is due to the organic cations locked in a specific orientation inside the inorganic Pb-I cage, therefore freezing the orientational degrees of freedom of their dipoles. Thus, the screening efficiency of the cations is compromised and the dielectric constant drops to $\epsilon = 30$. The positively charged terminations of the cations now induce a surface potential, responsible of the conduction and valence band bending downward, with respect to the bulk reference. The surface can be seen as a series of capacitors, with the positively charged part being the MA^+ oriented cations and the negatively charged part the Pb-I octahedra. The polarisation difference between the MA cations and the negative Pb-I octahedra generates a local potential difference, also called polar catastrophy. This potential cascade does not continue infinitely and ends in the bulk, which naturally tends to

stabilise. Indeed, MA^+ cations, although still frozen in the inorganic Pb-I cage, have a tendency to countereact the polar catastrophe when the internal field becomes too large.

Afterwards, the accumulated electrons get trapped by interstital defects and vacancies usually present on ionic surfaces. This localization explains the decay of the 2PPE intensity on a time scale of 60 ps, which is visible in Fig. 7.5. Indeed, strongly localized states induce a signal equally distributed at all wavevectors and below the CBM, most of which escapes from our detection window. After 200 ps, the CBM intensity follows the nanosecond decay that has been also reported for the tetragonal phase. Because the latter is a slow process, we evince that surface traps do not act as recombination centers but are neutralized once filled by electrons. The drift decay time has been obtained from a single exponential fit, and the trapping thus recombination time from a biexponential fit.

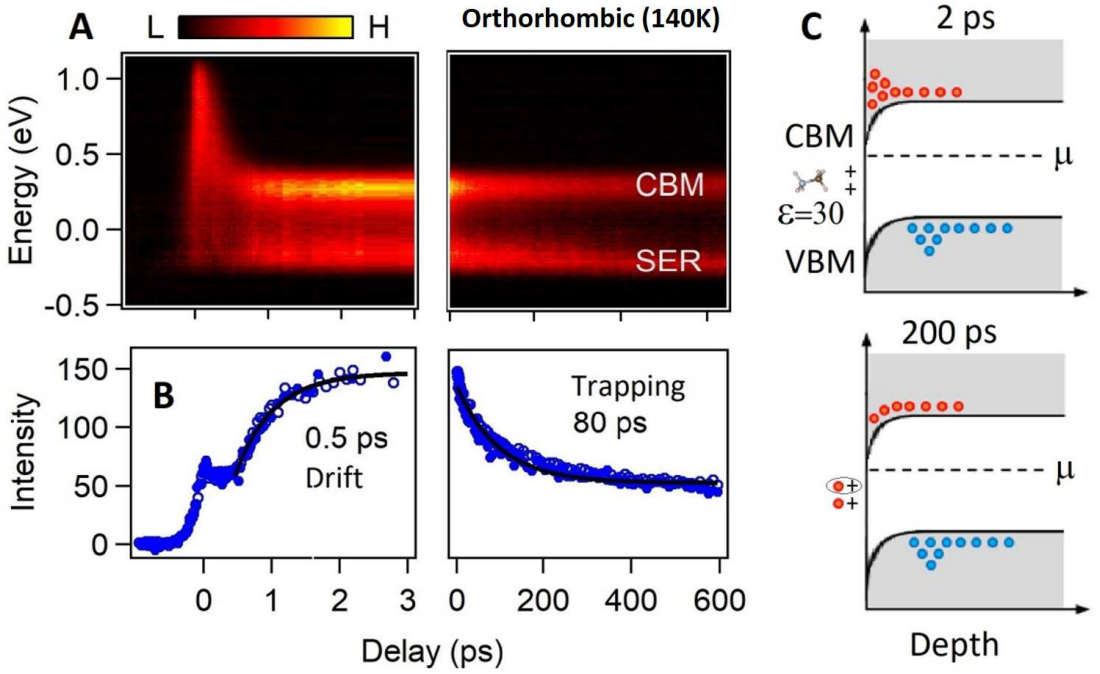

Figure 7.5: (a) Photoelectron intensity map of $MAPbI_3$ acquired in the orthogonal phase at 140K. (b) Photoelectron intensity integrated in an energy interval of 0.1 eV around the CBM as a function of the pump probe delay, always at 140K. The two process of drift and trapping are indicated on the plot with their lifetime. (c) Sketch of carrier relaxation at the surface of the orthorhombic phase.

Finally, two-photon photoemission experiments, coupled with hard X-ray photoelectron spectroscopy allowed novel insights on the defect tolerance in $MAPbI_3$ single crystal. The specific electron dynamics in tetragonal and orthorhombic phase provided information about the large polarizability of organic cations above 160K. This explains the modest impact that defects and grain boundaries have on perovskites performances. Characterizing the $MAPbI_3$ single cyrstal's surface is a first approach to understand what is going on in the bulk, which can

be summarized by light carriers generated in the PbI_3 bands and strong screening of charged defects by MA^+ cations, ultimately favorising charge carriers mobility.

7.2 Conduction and valence band dispersion in n-layered 2D perovskites

7.2.1 Motivation

The objective of this experimental project is to observe for the first time the conduction band dispersion of a 2D LHPs using the time-resolved ARPES technique. This observation is particularly difficult due to the possible degradation of 2D perovskites under the laser beam and to the damage caused by thermal diffusion in the material. The second aim of this work is to observe the relaxation dynamics in the conduction band of 2D and report the presence (or not) of a Rashba splitting.

Although some theoretical and experimental works via transient absorption spectroscopy have proposed the existence of dynamic Rashba splitting in perovskites (see Chapter.3), the conduction band of 2D perovskites and the potential Rashba splitting has never been directly observed via time-resolved ARPES. We provide here preliminary experimental results on this subject.

7.2.2 Conduction band dispersion using tr-ARPES

Time-resolved ARPES spectroscopy was performed on (BA)-$MAPbI_3$ single crystal sample, with n=3. The material details are presented in Chapter.5.4. Knowing that the types of perovskite lead halide used were very delicate, especially to the low-energy electron diffraction (LEED) technique, it was impossible to orient the crystal in the desired high symmetry direction. In order to minimize the deterioration of the sample, the experiment was performed at 130K. This experiment allowed us to generate the first proof of concept proving the ability to directly observe the conduction band in 2D LHPs.

Fig. 7.6 shows the conduction band minimum in a random crystal orientation of the reciprocal space at t = 50 fs. Bright features represent the electron intensity as a function of kinetic energy E_k and the wave vector k. One side of the conduction branch seems much more intense than the other one, probably due to the matrix element effects of the photoemission process. Indeed the observed states are strongly emitting when the electric field of the probing photons have an out of plane component. Due to the geometry of the experiment and the rotation of the sample, this takes place only for the data corresponding to positive wavevector. The blue fit represents the dispersion we could expect with a Rashba coupling in this material. The latter was generated using Equation 2.6. An effective mass of m^*_{eff} = 0.13 m_0 and a Rashba coupling $\alpha \leq 0.7$ eV/Angstrom were exctracted from it. It is the first time where the effective

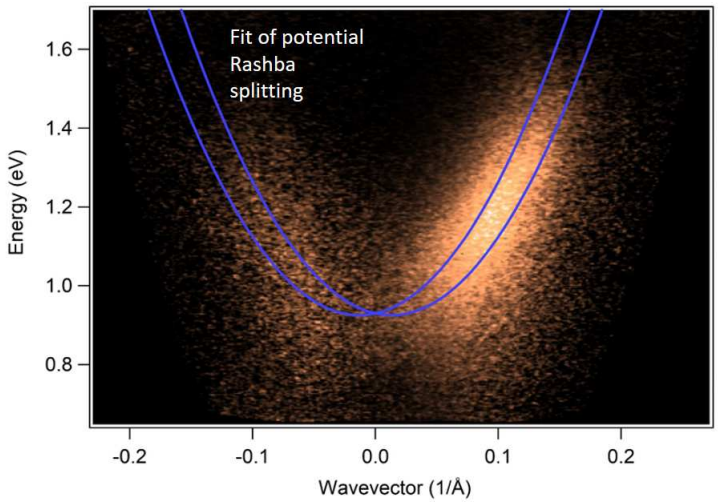

Figure 7.6: Electron intensity map (bright features) as a function of kinetic energy E_k and the wave vector k and fit of a potential Rashba splitting (blue).

mass m^*_{eff} is directly exctracted from an experimental observation of the conduction band in 2D lead halide perovskite. The experimental Rashba value α gives an upper limit of the Rashba coupling we could observe in this sample, which should be the same, smaller or even not existent. This value is in the same order of magnitude of the one observed from transient spectroscopies by Zhai et al (1.6 eV/Angstrom) [184].

This proof of concept is a first step in our study of Rashba splitting in 2D lead halide perovskite crystal. The next steps are to extend this work to different time scales, to evaluate the presence or not of a conduction band evolution. We also plan to orient the crystal properly to study the global minimum of the conduction band and to try this experiment on different number of layers n.

7.3 Towards high efficiency and time stable photovoltaic absorbers

The previous chapters discussed in particular the fundamental microscopic properties of various types of perovskite lead halides. This part will focus on macroscopic physical properties, such as charge recombination at grain boundaries or lifetime of hot carriers, with a more applicative view on photovoltaic cells. We will focus particularly on complex 4-cation $APb(Br,I)_3$ perovskites with A = (MA,FA,GA,Cs), in order to discuss their improved performance compared to single A-site cation perovskites. In addition, time-resolved spectroscopy techniques are also used, notably to understand the relaxation of electrons within the conduction band. This work was carried out in very close collaboration with the team of Prof. Sanjay Mathur from the University of Cologne (Germany) and was printed as a peer-reviewed publication [245].

7.3.1 Motivation

As introduced in Chapter.3, LHPs have been attracting the attention of the scientific community for more than a decade because of their extremely interesting optoelectronic properties, especially for photovoltaic applications. In the context of a photovoltaic cell, LHPs thin films are used as absorber semiconductor materials, capable of generating free charges (electrons and holes) from a certain energy from the electromagnetic spectrum of sunlight. Nevertheless, LHPs still face many problems, such as externally induced stability issues that are highly problematic for large-scale commercial applications. It is still an ongoing debate wheter the introduction of multiple cations to the A-site cation of the perovskite structure can alter the charge carrier dynamics. Moreover, the effect of trap passivating properties of Guanidinium cations are still not perfectly understood [88, 89]. This research work presents an innovative design in the domain by realising a quadruple cation organic-inorganic mixed lead halide perovskite. The exact chemical composition of the thin film active layer and single crystal is $(GA_{0.015},Cs_{0.046},MA_{0.152},FA_{0.787})Pb(I_{0.815}Br_{0.185})$. The aim of this work is to characterize the innovative quadruple cations lead halide perovskites in order to integrate it in solar cells. Novel analysis of the carrier kinetics ranging from femto- to microseconds are applied on the quadruple cation mixed lead halide perovskites.

7.3.2 Chemical composition approach

The chemical composition has been studied to address the stability problem of perovskite lead halides and each of the A-cations covers a functional role in the active layer. The choice of X-site halogens is also extremely important and delicate. We choose a ratio of 81.5% of bromide Br^- and 18.5% of iodide I^- in order to optimize the optical band gap while preserving the cubic structure. Indeed, the relative concentration of A-site cation and X-site halogen anions plays a primary role on the crystal structure, on the solar cell endurance and performance. Therefore, the quadruple cation perovskite was designed to achieve the highest possible structural stability with an effective Goldschmidt tolerance factor t_{eff} = 0.968.

The stoichiometry was verified after synthesis by performing ^{1}H nuclear magnetic resonance (NMR) spectroscopy. Fig. 7.7.(a) shows unambiguously identified FA^+, MA^+ and GA^+ cations through the chemical shift of protons. The quantification of the individual components by peak integration indicated an excellent matching with the intended composition.

The phase purity as well as the crystallinity was also ivestigated, using X-ray diffractometry (XRD). Single crystal were first characterized (Fig. 7.7.(b)). The single crystal powder signal was compatible with a $Pm\bar{3}m$ cubic structure with a lattice parameter a=6.22 Angström. No signature of the underisable δ-phase was observed. XRD was then performed on the polycrystalline (4cat)Pb(I,Br)$_3$ thin films (Fig. 7.7.(c)). The signal is nearly identical to the one observed in single crystal powder with the only notable difference being an extra diffraction peak around 12.65° ascribed to excess PbI_2 inclusion excess. According to litterature, enrichment with PbI_2 could hinder the accumulation of organic species at the grain boundaries, favor an optimal

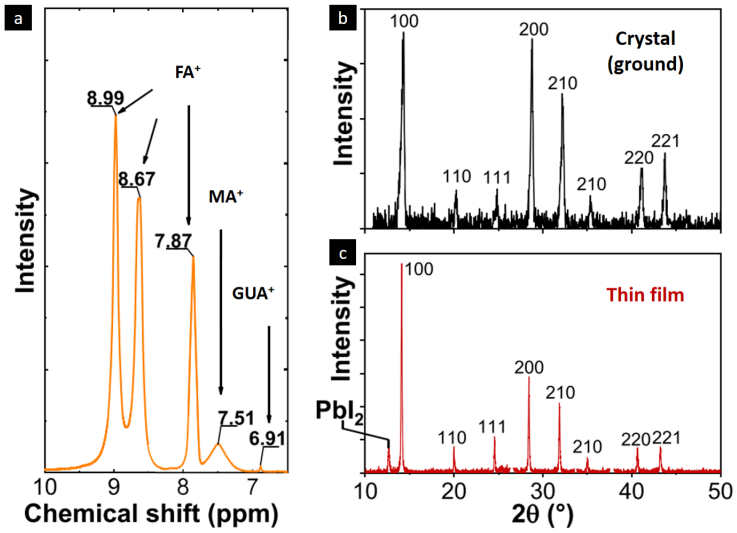

Figure 7.7: (a) Proton nuclear magnetic resonance (^{1}H NMR) spectra of single crystals dissolved in DMSO-d_6 showing chemical shifts of the hydrogen signal characteristic for each of the organic cations. (b) Powder X-ray diffraction pattern (PXRD) of $(GA_{0.015},Cs_{0.046},MA_{0.152},FA_{0.787})Pb(I_{0.815}Br_{0.185})$ ground single crystals. (c) XRD of the $(GA_{0.015},Cs_{0.046},MA_{0.152},FA_{0.787})Pb(I_{0.815}Br_{0.185})$ thin film. The extra Bragg peak visible around 12.65° is due to excess PbI_2 (5%).

embedding of the grains and improve charge carriers transport [255].

7.3.3 Solar cell device characterization

A mesoporous n-i-p single junction solar cell device was made using the quadruple cation lead halide perovskite as absorber material. The cross-sectional SEM of the mesoporous n-i-p device is shown on Fig. 7.8.a. The compact TiO_2 layer was prepared using aerosol spray pyrolysis on a fluorine doped tin oxide (FTO= substrate. The mesporous TiO_2 layer has been deposited by spin coating and treated with Li-TSFI, according to Saliba and Giordano et al. method [94, 256], in order to modulate the electronic conductivity and reduce the nonradiative recombination centers related to oxygen vacancies [257]. The (4cat)$Pb(I,Br)_3$ perovskite thin film was deposited on the mesoporous TiO_2. Finally, the perovskite thin film was capped by spiro-OMeTAD layer and a thermally evaporated gold cathode. In this n-i-p device, TiO_2 acts as the electron-selective transport layer (ETM) while the spiro-OMeTAD acts like an hole transport layer (HTM), meaning it extracts and transports the holes toward the gold contact. The compacity, the homogeneous filling and the good contact quality observed on the cross sectional SEM are indications of the high quality of the film.

J-V measurement was later performed on the (4cat)$Pb(I,Br)_3$ n-i-p architecture. The J-V curve

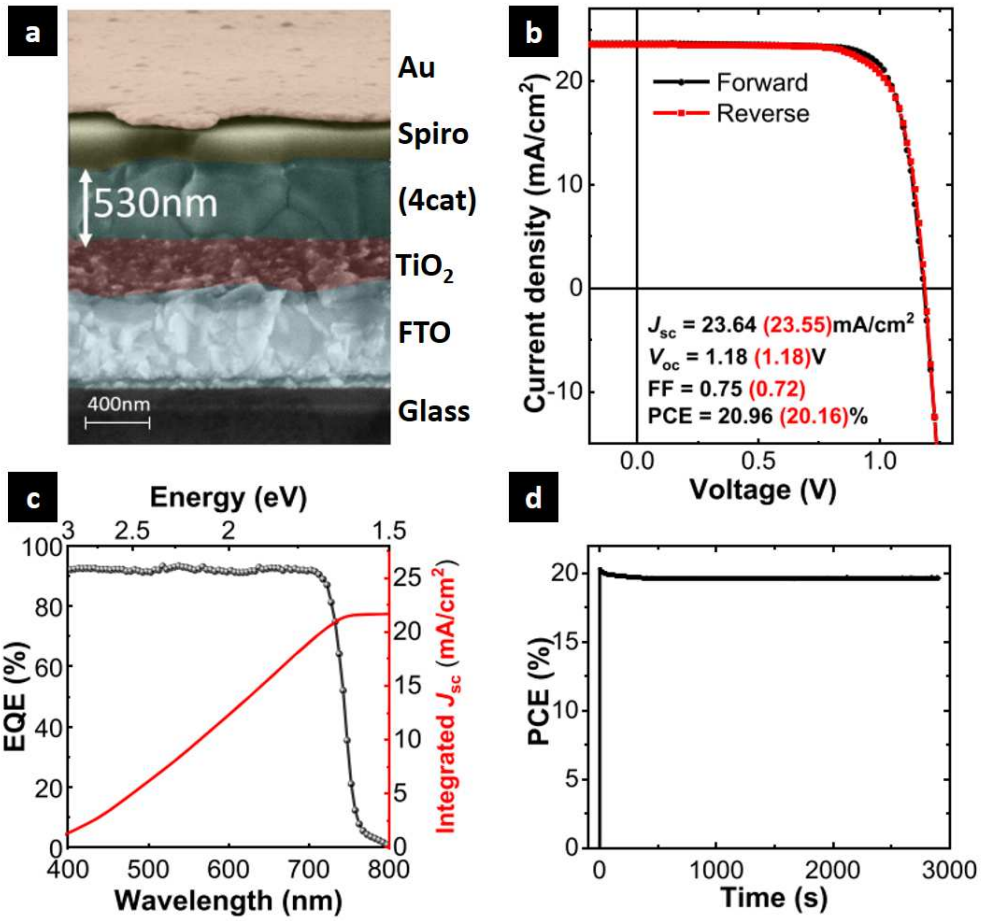

Figure 7.8: (a) Cross sectional SEM image of a photovoltaic n-i-p device with 500 nm of transparent electrode FTO, 400 nm of electron transport layer $Li(TFSI)_2$ mp-TiO_2 + perovskite, 530 nm of active perovskite layer $(GA_{0.015},Cs_{0.046},MA_{0.152},FA_{0.787})Pb(I_{0.815}Br_{0.185})$, and 280 nm of the hole transport layer Spiro-OMeTAD. (b) JV curve of the device showing short circuit current density of 23.6 mA/cm^2, open circuit voltage of 1.18 V, and an average power conversion efficiency (PCE) of 20.5%. (c) External quantum efficiency (EQE) as a function of the incident photon energy. (d) Maximum power point (MPP) tracking during the first hour under illumination AM1.5G 100 mW/cm^2.

shown on Fig. 7.8.b enabled to extract the power conversion efficiency (PCE) of the solar cell, which was 20.96% in the forward direction and 20.12% in the reverse direction. J-V hysterisis is remarkably low compared to other solar cells fabricated with the same transport layers [258] or closed chemical composition of the absorber [259, 87, 260]. This may be due to several factors: (i) guanidinium enhances grain size and passivates under-coordinated iodide species between adjacent crystalline grains thanks to its hydrogen bonding; (ii) guanidinium and the excess PbI_2 tend to minimize the halide ions migration at the interface with other layers [86]; Lithium incorpoation in the mesoporous TiO_2 reduces oxygen vacancies. Furthermore,

smooth roughness of the thin film observed with AFM measurements and presented in the Supplementary Information of the paper [245] probably enable good charge extraction.

External quantum efficiency (EQE) measurement was performed in order to know the ratio of the number of electronic charges collected to the number of photons incident on the photoreactive solar cell (Fig. 7.8.c). The EQE of the device is larger than 80% of the entire range covered by visible light spectrum. This confirms that most of the photogenerated charge carriers can be collected before recombination despite the relatively high thickness of the perovskite active layer (≈ 1 μm). This can be explained by good carrier transport properties and was confirmed by a diffusion coefficient of 0.05 cm^2s-1 of the thin film, measured via noninvasive transient grating method (Supplementary Information of [245]).

Finally, the power density output of the device has been characterized (Fig. 7.8.d). An illumination of 1 sun was employed for the characterization on a 0.16 cm^2 device. A stable power output of 19.5 mW/cm^2 (equivalent to a PCE of 20.5 %) was observed. This photocurrent power output stabilized within few seconds and remained constant throughout the entire duration of the measurement and the stability is comparable to the best current single junction perovskite solar cells.

These device characterization showed that, by optimizing the charge extraction at the electron-selective interface, a photoconversion efficiency above 20% and negligible hysteresis could be achieved. Due to the optimal mixing of different cations, the photovoltaic cells displayed a good operational stability.

7.3.4 Low degree of disorder and efficient passivation through optical characterization

This subsection focus on several optical characterizations on the quadruple cation lead halide perovskite thin film only (not related to the n-i-p device anymore). The film was first characterized using photothermal deflection spectroscopy (PDS). As shown by the PDS spectrum on Fig. 7.9.a, a sharp increase of the band gap coefficient at the bandgap value E_g = 1.62 eV in close agreement with former studies [259, 87]. By fitting the exponential rise of the absorption coefficient observed near the bandgap we obtain an Urbach energy ΔE_u = 18.5 meV. In typical and single cation $MAPbI_3$ perovskite, the Urbach energy value is usually around 13-15 meV [105], indicating an increased degree of disorder in our quadruple cation lead halide perovskite sample.

Steady-state photoluminescence (PL) was also performed and the PL peak is shown on Fig. 7.9.b. A sharp emission peak line is observed at the bandgap energy E_g = 1.62 eV. The PL peak shape indicates a low rate of non-radiative carrier recombination, which is of considerable interest for photovoltaic applications.

Fig. 7.9.b shows the temporal evolution of the photoluminescence intensity, also called time-resolved photoluminescence (TR-PL), and measured at the bandgap value after the photoex-

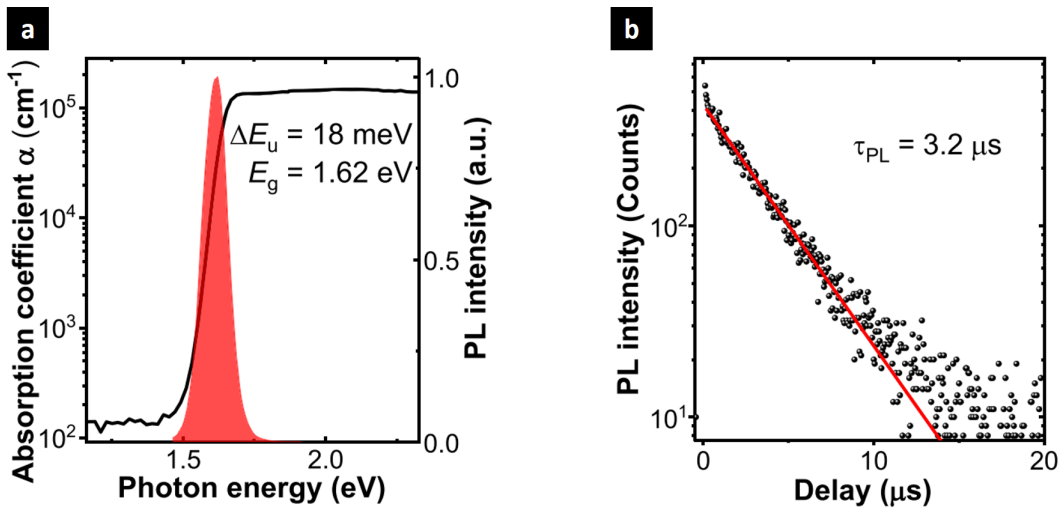

Figure 7.9: (a) Photothermal deflection spectroscopy (PDS) measurement (black line) of the absorption coefficient as a function of the incident photon energy. The spectrum indicates a gap energy E_g = 1.62 eV and an Urbach energy ΔE_u = 18 meV. The red area represents the photoluminescence intensity measured at room temperature as a function of emitted photon energy. (b) Time-resolved photoluminescence, acquired at a photon energy 1.62 eV and at room temperature as a function of delay time from the photoexcitation.

citation pulse with a density of 10^{12}-10^{13} cm^{-2}. The curve was fitted using a step function multiplied with a single exponential decay function, with a decay time of τ_{PL} = 3.2 µs. This lifetime is comparable to the relaxation time previously reported for halide thin films incorporating Guanidinium in the A-site cation [243]. Nonetheless, it is one order of magnitude higher than the one observed in lead halide perovskite with no Guanidinium. The remarkable increase of τ_{PL} by using Guanidinium confirms the efficient passivation of the non radiative recombination centers at the grain boundaries of our the quadruple cation mixed halide perovskite.

The suitable bandgap value of E_g = 1.62 eV, the high absorption coefficient α, the relatively low Urbach energy ΔE_u and the long τ_{PL} are favorable parameters in order to provide efficient harvesting of the solar energy.

7.3.5 Ultrafast dynamics in (4cat)$PbBr_3$ perovskites

This subsection focuses on the ultrafast dynamics in quadruple cations mixed halide perovskites. Initial dynamics of charge carriers after ultrafast photoexcitation has been characterized by two pump-probe experiments: two-photon photoemission (2PPE) and time-resolved transient absorption (TR-TA).

2PPE has been performed in order to observe the temporal evolution of the electronic excited state in terms of kinetic energy E_k. For this aims, quadruple cations mixed halide perovskite

single crystals were cleaved and measured in ultravacuum. Experiment have been performed at 180K to avoid any alteration of the surface composition by possible sublimation of halide or organic cations. The freshly cleaved cyrstal surface was then photoexcited with a pump (fluence of 8 $\mu J/cm^2$) centered at 3 eV. The population of photoelectrons was probed with a subsequent probe pulse centered at 4.5 eV. Pump-on minus pump-off photoelectron intensity as a function of kinetic energy and pump-probe delay is represented on Fig. 7.10.a. The kinetic energy E_k is referred to (4cat)Pb(I,Br)$_3$ surface's vacuum level but should be increased by 0.4 eV if referred to the spectrometer vacuum level. At zero delay t = 0 ps, primary electrons absorbing the pump photons are excited from the valence band to the conduction band. Then, their excess energy relaxes until reaching the conduction band minimum (CBM), located at E_k = 0.8 eV. The characteristic time scale of the electronic cooling is 0.25 ps, which matches the formerly measured value in $MAPbI_3$ [252]. Such fast relaxation of the photoexcited electrons is ascribed to highly dissipative collisions between electrons with large excess energy and the group of organic cations (such as -NH_2, -CH, -NH_3^+, -CH_3). The latter are much lighter than the inorganic cage vibrate with very high frequency after being impacted by photoelectron and can easily dissipate the excess energy of electrons. The efficient carrier cooling as well as the negligible effect that any phonon bottleneck has at low fluence hinder any viable application of this kind of halide perovskite for the realization of hot carrier solar cells [II]. Besides the primary photoelectrons visible when $E_k > 0.8$ eV, an additional signal is detected at 0 eV < E_k < 0.8 eV. This signal originates from secondary electron replica (SER) to photoelectrons facing inelastic scattering events while propagating from the sample out in the vacuum regions. SER can be considered as a measurement artifact and brings no information about energy of excited states in perovskites.

Ultrafast electron relaxation was then characterized using TR-TA at room temperature on thin films. The latter have been pumped by a femtosecond pulse centered at 2.5 eV and probed using a white light continuum. Fig. 7.10.b shows that slightly after time zero, photoinduced band filling (PBF) reduces the absorption around 1.68 eV due to Pauli blocking [52], which prevents fermions, and thus electrons, to simultaneously be in the same quantum state. In addition to this observed bleaching effect, a transient increase of the optical absorption occurs at 1.62 eV at early delay time. The dynamical screening of electron-electron interaction in the photoexcited state of the conduction band lead to this band gap renormalization (BGR). The evidence that BGR dynamics of Fig. 7.10.b and the electronic cooling on Fig. 7.10.a match particularly well is a signature that BGR takes place while electrons and holes are in a highly nonthermal state, which is somehow expected. Indeed, because it is drived by changes in dielectric function, BGR is largest when the nonequilibrium electronic distribution opens a large amount of intraband scattering channels. This condition is no longer verifier after 0.5 ps as the carriers have already fully thermalized.

[II] Electron–hole pairs generated in solar cells lose energy by cooling down from their initial energetic (so called "hot") position to the band edges by optical phonon emission. Hot carrier solar cells aim to minimize this loss by extracting carriers at elevated energies in a narrow time range, which requires a substantial delay in carrier cooling in the absorber material [261].

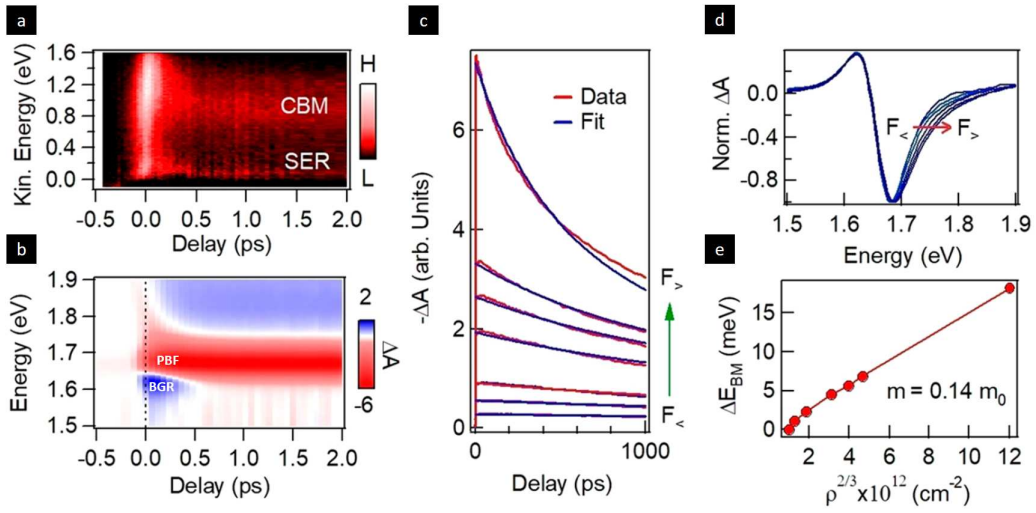

Figure 7.10: (a) Two photon photoemission spectroscopy (2PPE) measured on a quadruple cation mixed halide perovskite single crystal. The pump-on minus pump-off signals of primary electrons in the conduction band minimum (CBM) and secondary electrons replica (SER) are marked. (b) Differential absorption of a supercontinuum spectrum (TR-PL) measured on a quadruple cation mixed halide perovskite thin film as a function of pumpprobe delay. . (c) Differential absorption decay extracted at 1.68 eV after a pump pulse centered at 2.5 eV and with different fluence values. The traces have been acquired for an excitation density spanning from 3.7×10^{16} to 7.5×10^{17} cm^3. Red curves are the experimental data and blue curves are fits obtained via a recombination model. (d) Renormalized traces of the time-resolved transient absorption spectra acquired at a pump probe delay of 0.1 ps, for increasing photoexcitation density, marked with red arrow. (e) Broadening of transient absorption peak (red dots) is plotted against the photoexcitation density $\rho^{2/3}$.

On the longer time scale (i.e after 0.5 ps), electronic dynamics are ruled by a reduction of PBF because of carrier recombination. Fig. 7.10.c represents the decay of PBF for different excitation density F in the range of 3.7x10^{16} cm^{-3} ≤ F ≤ 7.5x10^{17} cm^{-3}. The entire fluence data set can be fit using the standard rate equation:

$$-\frac{dN}{dt} = aN + bN^2 \tag{7.1}$$

with the trap recombination rate a = 3x10^5 s^{-1} and the radiative coefficient b = 1.2x10^{-9} cm^3.s^{-1}, the later being not corrected for photon recycling process [262]. This radiative recomination rate a is slightly higher than the one obtained in other halide perovskite [263]. Recombination rate is 5 orders of magnitude lower than the one predicted by Langevin model [III] [53]. Some authors ascribed the high efficiency of these solar cells to a slightly indirect band

[III] Model describing how a system evolves when subjected to a combination of deterministic and fluctuating forces.

gap originating from dynamical effect [139]. Due to the presence of heavy atoms of Lead and thermal fluctuation, organic cation rotation might indeed induce a momentum mismatch between the band edges, called Rashba splitting [187, 264]. Nevertheless, recent calculations suggest that the indirect nature of the band gap only decrease radiative recombination rate a by less than a factor of 2 [265]. It is important to highlight that the radiative coefficient found in quadruple cation mixed halide perovskite is as high as the traditional semiconductor with direct band gap GaAs [266]. Moreover, the long carrier lifetime observed in Fig. 7.9.b as well as the high EQE show that radiative recombination has no impact on the overall performance of the solar cell device.

The normalized transient absorption measured just after photoexcitation at different pump fluences are represented on Fig. 7.10.d. When the photoexcitation density increases, a blue shift and broadening of the PBF peak is observed. This dynamical Burstein-Moss effect [52] is a consequence of the excited distribution of electrons in the conduction band and holes in the valence band. As represented on Fig. 2.2, Burstein-Moss effect can be described by an effective filling level leading to Pauli blocking of the optical transitions in the energy interval ΔE_{BM} from the band value, with:

$$\Delta E_{BM} = \frac{h^2}{2m^*_{eh}}(3\pi^2 N)^{2/3} \tag{7.2}$$

where m^*_{eh} is the reduced effective mass and N is the photoexcitation density.

Finally, Fig. 7.10.e shows the experimental broadening of PBF as function of the excitation density to the power of 2/3. In the low fluence regime, the curve is non linear and correlated to trap filling mechanism. At elevated fluence, the curve trend is linear and is ascribed to dominant radiative recombination. This linear dependence observed in a wide fluence range is highly consistent with Burstein-Moss model. Reduced effective mass m^*_{eh} = 0.14 m_0 is extracted from the linear slope. m_0 is the bare mass of the electron. The value of reduced effective mass is consistent with the one reported in $MAPbI_3$ (0.1 m_0 - 0.3 m_0) and other perovskite. This relatively small value of reduced effective mass in addition to long carrier lifetime and modest diffusion rate are in agreement with calculations suggesting a moderate dressing of carrier by lattice polarization [153, 136].

In conclusion, we showed that both hot carrier cooling and bandgap renormalization (i.e optical gap reduction induced by photocarriers) occur on the subpicosecond time scale. The radiative recombination in $(4cat)Pb(I,Br)_3$ is higher than the one measured in classical $MAPbI_3$ but has no role on solar cell performance because of good carrier transport properties. Using Guanidinium in A-site cation enables to passivate the recombination centers at the grain boundaries and increase charge carriers lifetime drastically up to the microsecond timescale.

7.4 Summary and discussion

This chapter has allowed us to demonstrate the effectiveness of time-resolved photoemission for the evaluation of the physical properties of hybrid perovskites. In a first time, 2PPE was employed to show that the temperature dependent crystallographic structure affects the polarizabilty of the organic A-site cation MA^+ since they can have the possibility to easily change orientation (tetragonal phase) or could be completely freezed (orthorhombic phase). The study of the accumulation of electrons on the surface of a $MAPI_3$ single crystal has shown that organic cations are responsible for a static screening of charges, inducing defect tolerance in this material.

Then, the observation of the conduction band of the 2D (BA)-$MAPI_3$ using tr-ARPES showed that this first proof of concept could later lead to the direct observation or not of a Rashba splitting.

Finally, time-resolved photoemission coupled with optoelectronic characterization and device design has allowed us to understand the important benefits of using the A-site cation Guanidinium in quadruple cation lead halide perovskites and to observe the band gap renormalization as well as the Burstein Moss filling in this extremely promising material for photovoltaic application.

8 Conclusion and perspectives

LHPs ultrafast dynamics have been characterized through different time-resolved techniques in order to understand the influence of A-site cation as well as lead-halide sublattice dynamics on the general charge carriers properties. The research I have conducted made use of time-resolved Kerr spectroscopy (OKE and TKE), as well as time and angle-resolved two-photon photoemission spectroscopy (2PPE and tr-ARPES), to investigate the ultrafast dynamics of lattice modes and electrons.

8.1 Optical and THz-induced Kerr effect spectroscopy

Time-resolved nonlinear Kerr effect was implemented with different excitation wavelengths. First, optical Kerr effect (OKE) applied on $MAPbBr_3$ and $CsPbBr_3$ perovskites outlined the importance to consider instantaneous electronic polarization response in the propagation of light field, in contrast to earlier interpretation. Experimental observation mixed with a four-wave mixing model proved that OKE signal observed were most likely not due to coherent phonons, liquid-like reorientation or polaron formation as claimed by previous work. Nevertheless, it highlighted the importance of distinguish the often-neglected anisotropic light propagation from underlying coherent quasiparticles responses (such as coherent phonons).

Thz-induced Kerr spectroscopy (TKE) was then applied to conventional A-site lead bromide perovskite $APbBr_3$ and to complex quadruple A-site cation lead bromide material. The intense THz field enabled the excitation of coherent optical phonons in the LHPs inorganic sublattice Pb-Br and probe the ultrafast lattice response via transient birefringence fluctuation. In agreement with previous optical Kerr effect studies, four-wave mixing simulation proved how crucial it is to account for dispersion and optical anisotropy to interpret time-resolved signals in these materials. At room temperature, TKE response was dominated by instantaneous electronic polarizability. On the contrary, lattice polarizibility governed by coherent phonon was predominant at nitrogen temperature (< 80K). The dominating polarizable Raman-active phonon mode was observed at 1.1 THz in $MAPbBr_3$ and at 0.9 THz and 1.3 THz in $CsPbBr_3$. These modes are suitable candidates for explaining dynamical screening, wich has been

suggested as a charge carrier protection mechanism in LHPs. Indeed, they govern the dynamic lattice response to a sub-picosecond transient electric, which can be regard as an intermediate between local electron-hole fields during electron-hole separation and localization. The THz strong field experiments demonstrate the potential to obtain direct coherent phonon control over LHPs properties via nonlinear excitation of highly polarizable modes, which were also found to be strongly coupled to the electronic bandgap. The same experimental TKE spectroscopy was applied to complex quadruple A-site cation lead bromide material, with A=($GA_{0.015}$,$Cs_{0.046}$,$MA_{0.152}$,$FA_{0.787}$). Interestingly, the highest polarizable mode in this complex A-site cation has the same frequency as the one in $MAPbBr_3$ (1.1 THz). This is not trivial, since the quadruple A-site cation blend contains mostly Formamidinium, which is known to lack Raman-active phonon mode that are highly polarizable. Besides, phonon lifetimes were even higher in the four cations compound than in $MAPbBr_3$. Further investigations of the Urbach energies as well as Raman spectroscopy are planned to understand the whole picture of the our experimental observation, , which may be required to decode the (4cat)$PbBr_3$ perovskites extended functionalities.

8.2 Time and angle-resolved two photon photoemission spectroscopy

Time- as well as angle-resolved spectroscopy was used to understand the role of A-site cations in electron cooling in the conduction band as well as surface ionic terminations. Two-photon photoemission was first used to characterize the transition across tetragonal to orthorhombic phase of the $MAPbI_3$ single crystal surface. The observed band offset and drift of the excited electrons highlighted the important role of organic cation MA^+ on the static screening of local electrostatic fields. These important results explain the modest impact that defects and grain boundaries have on solar cell performance. They highlight the existence of a slow static screening, which is complementary to the dynamics screening of the polaron picture studied with TKE.

Angle-resolved two-photoemission was then performed in order to experimentally investigate the presence of Rashba spin-orbit splitting in 2D-LHPs. The previous experimental and theoretical works of the community have not yet allowed to decide on the presence or not of this phenomenon. An experimental test on 2D perovskites, which are more likely to show this phenomenon due to their inversion symmetry breaking, has allowed to observe for the first time the conduction band dispersion of a 2D perovskites. A proof of concept of the observation of the conduction band in 2D perovskites is an important result for the community. It is also a preliminary starting point to study the time-resolved variation of the charge carriers in the conduction band and to quantify Rashba splitting. The peculiar interplay of spin and orbital degrees of freedom in LHPs seems promising for spintronic applications [267, 268].

Finally, femto- to microsecond dynamics of excited electrons were characterized in quadruple A-site LHPs using two-photon photoemission. The relatively small value of the reduced mass obtained, the long carrier lifetime and modest diffusion rate were in good agreement with

ab initio calculations [152], suggesting a moderate dressing of charge carriers in quadruple A-site cation perovskite, originating from Pb-X lattice polarization. A mesoscopic n-i-p single junction solar cell was created by collaborators from Cologne University by making use of the quadruple cations perovskite as absorber material and proved high efficiency (>20%) as well as excellent operational stability. These interesting results were attributed to the addition of Guanidinium cations which helps to passivate recombination centers at the grain boundaries and increases charge carriers lifetime from nanosecond up to microsecond timescale.

8.3 Towards a clearer understanding of charge screening in LHPs and next investigations

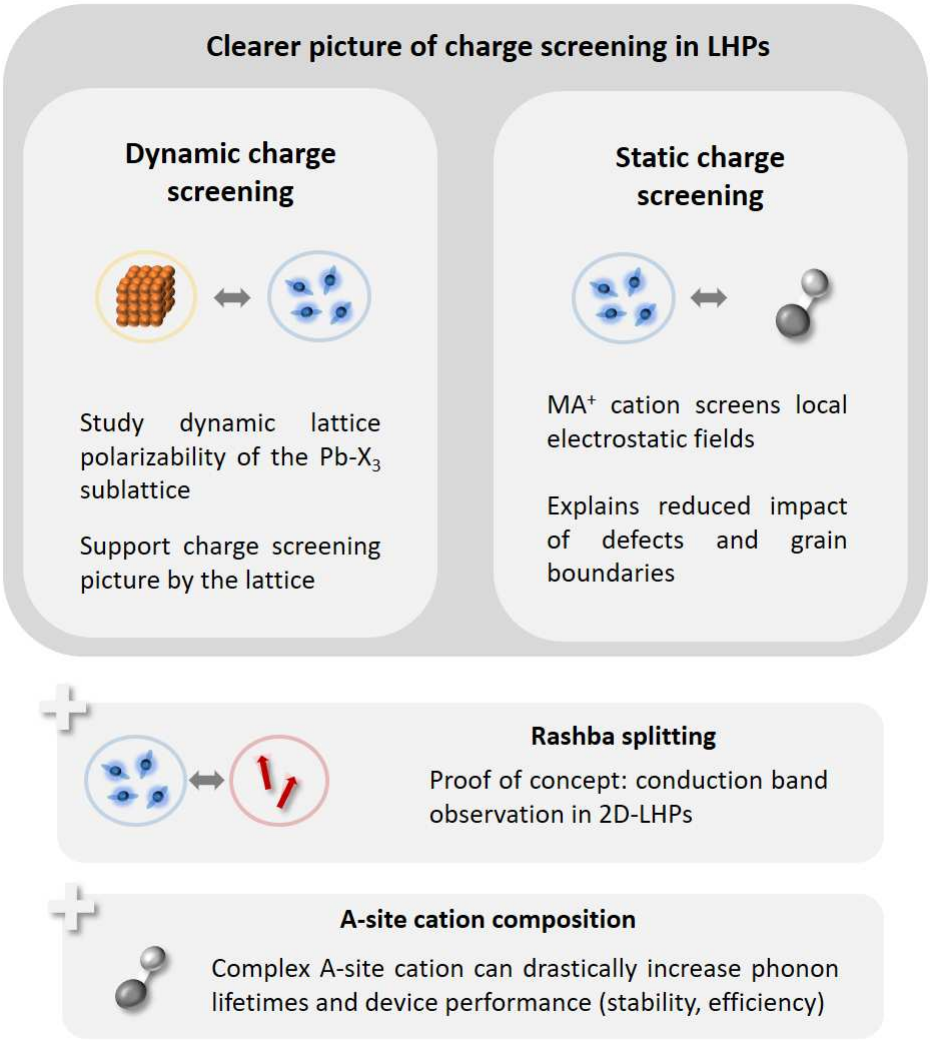

Figure 8.1: Global overview of the studied systems and dynamics.

Two photon photoemission spectroscopy as well as Kerr experiments indicate that the excep-

tional properties of LHPs are linked to the incorporation of highly polarizable organic cations with highly inorganic structure. The lead-halide sublattice hosts slightly heavier carriers (in case of polarons) and it generates a dynamic charge carrier screening via the formation of polaron-like particle, while A-site cation gives rise to static screening which favor mobility by reducing the defect-related trapping rate. The broad overview of ultrafast dynamics in this work can be also extented to the study of 2D-LHPs.

Bibliography

[1] Donella H Meadows et al. “The limits to growth-club of rome”. In: (1972).

[2] M Mesarovic and E Pestel. “Strategy for Tomorrow”. In: *Second Report of the Club of Rome* (1974).

[3] Lenny Bernstein et al. *IPCC 2007 climate change synthesis report*. 2008.

[4] Hans-Otto Pörtner et al. “Climate change 2022: Impacts, adaptation and vulnerability”. In: *IPCC Sixth Assessment Report* (2022).

[5] Robbert Biesbroek et al. “Policy attention to climate change impacts, adaptation and vulnerability: a global assessment of National Communications (1994–2019)”. In: *Climate Policy* 22.1 (2022), pp. 97–111.

[6] Céline Bellard et al. “Impacts of climate change on the future of biodiversity”. In: *Ecology letters* 15.4 (2012), pp. 365–377.

[7] “First Assessement Report: Working Group I: Scientific Assessment of Climate Change”. In: *IPCC* (1990).

[8] Lorenz T Keyßer and Manfred Lenzen. “1.5 C degrowth scenarios suggest the need for new mitigation pathways”. In: *Nature communications* 12.1 (2021), pp. 1–16.

[9] Smil Vaclav. “Energy transitions: global and national perspectives”. In: *BP Statistical Review of World Energy* (2017).

[10] M Mercedes Maroto-Valer, Chunshan Song, and Yee Soong. *Environmental challenges and greenhouse gas control for fossil fuel utilization in the 21st century*. Springer Science & Business Media, 2002.

[11] Ministère de la Transition Ecologique. “Le photovoltaïque : choix technologiques, enjeux matières et opportunités industrielles”. In: (2020). URL: https://www.ecologie.gouv.fr/sites/default/files/Plan\%20ressources\%20Photovoltaique.pdf.

[12] Yan Xu et al. “Global status of recycling waste solar panels: A review”. In: *Waste Management* 75 (2018), pp. 450–458.

[13] Md Shahariar Chowdhury et al. “An overview of solar photovoltaic panels’ end-of-life material recycling”. In: *Energy Strategy Reviews* 27 (2020), p. 100431.

[14] Morgan Bazilian et al. *Model and manage the changing geopolitics of energy*. 2019.

[15] Goksin Kavlak, James McNerney, and Jessika E Trancik. “Evaluating the causes of cost reduction in photovoltaic modules”. In: *Energy policy* 123 (2018), pp. 700–710.

[16] Laura Scherer and Stephan Pfister. “Hydropower’s biogenic carbon footprint”. In: *PloS one* 11.9 (2016), e0161947.

[17] Richard Perez and Marc Perez. “A fundamental look at supply side energy reserves for the planet”. In: *Int. Energy Agency SHC Program. Sol. Updat* 62 (2015), pp. 4–6.

[18] Jenny A Nelson. *The physics of solar cells*. World Scientific Publishing Company, 2003.

[19] Jarvist Moore Frost. “Calculating polaron mobility in halide perovskites”. In: *Physical Review B* 96.19 (2017), p. 195202.

[20] Zhaoning Song et al. “Pathways toward high-performance perovskite solar cells: review of recent advances in organo-metal halide perovskites for photovoltaic applications”. In: *Journal of photonics for energy* 6.2 (2016), p. 022001.

[21] Radha Krishnan Kothandaraman. “Development of four-terminal devices utilising thin-film solar cells”. In: (2018).

[22] Akihiro Kojima et al. “Organometal halide perovskites as visible-light sensitizers for photovoltaic cells”. In: *Journal of the american chemical society* 131.17 (2009), pp. 6050–6051.

[23] Ajay Kumar Jena, Ashish Kulkarni, and Tsutomu Miyasaka. “Halide perovskite photovoltaics: background, status, and future prospects”. In: *Chemical reviews* 119.5 (2019), pp. 3036–3103.

[24] NREL. “Best Research-Cell Efficiency Chart”. In: (2022).

[25] Silvia Binet. “Effects of compositional variation on structural and optical properties in hybrid perovskites”. In: (2017).

[26] Patrick M Woodward. “Octahedral tilting in perovskites. I. Geometrical considerations”. In: *Acta Crystallographica Section B: Structural Science* 53.1 (1997), pp. 32–43.

[27] Ruo Xi Yang et al. “Assessment of dynamic structural instabilities across 24 cubic inorganic halide perovskites”. In: *The Journal of chemical physics* 152.2 (2020), p. 024703.

[28] Jianfeng Yang et al. “Acoustic-optical phonon up-conversion and hot-phonon bottleneck in lead-halide perovskites”. In: *Nature Communications* 8 (Jan. 2017), p. 14120. ISSN: 2041-1723. DOI: 10.1038/ncomms14120. URL: /brokenurl#http:https://dx.doi.org/10.1038/ncomms14120.

[29] Santosh Kumar Radha, Churna Bhandari, and Walter RL Lambrecht. “Distortion modes in halide perovskites: To twist or to stretch, a matter of tolerance and lone pairs”. In: *Physical Review Materials* 2.6 (2018), p. 063605.

[30] Xu Huang et al. “Understanding Electron–Phonon Interactions in 3D Lead Halide Perovskites from the Stereochemical Expression of 6s2 Lone Pairs”. In: *Journal of the American Chemical Society* (2022).

[31] David P McMeekin et al. “A mixed-cation lead mixed-halide perovskite absorber for tandem solar cells”. In: *Science* 351.6269 (2016), pp. 151–155.

[32] Taketo Handa et al. “Phonon, thermal, and thermo-optical properties of halide perovskites”. In: *Physical Chemistry Chemical Physics (Incorporating Faraday Transactions)* 22.45 (Nov. 2020), pp. 26069–26087. DOI: 10.1039/D0CP04426A.

[33] Joanna M Urban. “Optical and vibrational properties”. PhD thesis. Université Paul Sabatier-Toulouse III, 2019.

[34] Claudine Katan, Nicolas Mercier, and Jacky Even. “Quantum and dielectric confinement effects in lower-dimensional hybrid perovskite semiconductors”. In: *Chemical reviews* 119.5 (2019), pp. 3140–3192.

[35] Samuel D Stranks et al. “Electron-hole diffusion lengths exceeding 1 micrometer in an organometal trihalide perovskite absorber”. In: *Science* 342.6156 (2013), pp. 341–344.

[36] Yu Bi et al. “Charge carrier lifetimes exceeding 15 μs in methylammonium lead iodide single crystals”. In: *The journal of physical chemistry letters* 7.5 (2016), pp. 923–928.

[37] David Cahen, Leeor Kronik, and Gary Hodes. “Are Defects in Lead-Halide Perovskites Healed, Tolerated, or Both?” In: *ACS energy letters* 6.11 (2021), pp. 4108–4114.

[38] Albrecht Poglitsch and Daniel Weber. “Dynamic disorder in methylammoniumtrihalogenoplumbates (II) observed by millimeter-wave spectroscopy”. In: *The Journal of chemical physics* 87.11 (1987), pp. 6373–6378.

[39] Omer Yaffe et al. “Local polar fluctuations in lead halide perovskite crystals”. In: *Physical review letters* 118.13 (2017), p. 136001.

[40] Alexander N Beecher et al. “Direct observation of dynamic symmetry breaking above room temperature in methylammonium lead iodide perovskite”. In: *ACS energy Letters* 1.4 (2016), pp. 880–887.

[41] Jacky Even et al. “Electronic model for self-assembled hybrid organic/perovskite semiconductors: Reverse band edge electronic states ordering and spin-orbit coupling”. In: *Physical Review B* 86.20 (2012), p. 205301.

[42] Jacky Even et al. “Importance of spin–orbit coupling in hybrid organic/inorganic perovskites for photovoltaic applications”. In: *The Journal of Physical Chemistry Letters* 4.17 (2013), pp. 2999–3005.

[43] Ling-yi Huang and Walter RL Lambrecht. “Electronic band structure trends of perovskite halides: Beyond Pb and Sn to Ge and Si”. In: *Physical Review B* 93.19 (2016), p. 195211.

[44] Laura M Herz et al. “Charge-carrier dynamics in organic-inorganic metal halide perovskites”. In: *Annu. Rev. Phys. Chem* 67.1 (2016), pp. 65–89.

[45] Jagdeep Shah. *Ultrafast spectroscopy of semiconductors and semiconductor nanostructures*. Vol. 115. Springer Science & Business Media, 2013.

[46] D Von der Linde and R Lambrich. “Direct measurement of hot-electron relaxation by picosecond spectroscopy”. In: *Physical Review Letters* 42.16 (1979), p. 1090.

[47] V Klimov, P Haring Bolivar, and H Kurz. “Hot-phonon effects in femtosecond luminescence spectra of electron-hole plasmas in CdS”. In: *Physical Review B* 52.7 (1995), p. 4728.

[48] Chaw Keong Yong et al. “Direct Observation of Charge-Carrier Heating at WZ–ZB InP Nanowire Heterojunctions”. In: *Nano letters* 13.9 (2013), pp. 4280–4287.

[49] Claus F Klingshirn. *Semiconductor optics*. Springer Science & Business Media, 2012.

[50] Elias Burstein. “Anomalous optical absorption limit in InSb”. In: *Physical review* 93.3 (1954), p. 632.

[51] TS1954 Moss. “The interpretation of the properties of indium antimonide”. In: *Proceedings of the Physical Society. Section B* 67.10 (1954), p. 775.

[52] Joseph S Manser and Prashant V Kamat. “Band filling with free charge carriers in organometal halide perovskites”. In: *Nature Photonics* 8.9 (2014), pp. 737–743.

[53] Christian Wehrenfennig et al. “Charge carrier recombination channels in the low-temperature phase of organic-inorganic lead halide perovskite thin films”. In: *Apl Materials* 2.8 (2014), p. 081513.

[54] Riley E Brandt et al. “Searching for “defect-tolerant” photovoltaic materials: combined theoretical and experimental screening”. In: *Chemistry of Materials* 29.11 (2017), pp. 4667–4674.

[55] Dong-Nyuk Jeong, June-Mo Yang, and Nam-Gyu Park. “Roadmap on halide perovskite and related devices”. In: *Nanotechnology* 31.15 (2020), p. 152001.

[56] Jozef T Devreese. “Optical properties of few and many Fröhlich polarons from 3D to 0D”. In: *Polarons in Advanced Materials*. Springer, 2007, pp. 3–61.

[57] Jozef T Devreese. “Polarons”. In: *Encyclopedia of applied physics: vol. 14*. 1996, p. 383.

[58] Kiyoshi Miyata et al. “Large polarons in lead halide perovskites”. In: *Science advances* 3.8 (2017), e1701217.

[59] EI Rashba and VI Sheka. *Fiz. Tverd. Tela*. 1960.

[60] Yua A Bychkov and É I Rashba. “Properties of a 2D electron gas with lifted spectral degeneracy”. In: *JETP lett* 39.2 (1984), p. 78.

[61] Gustav Bihlmayer, O Rader, and Roland Winkler. “Focus on the Rashba effect”. In: *New journal of physics* 17.5 (2015), p. 050202.

[62] Xiuwen Zhang et al. “Hidden spin polarization in inversion-symmetric bulk crystals”. In: *Nature Physics* 10.5 (2014), pp. 387–393.

[63] John P Perdew and Alex Zunger. “Self-interaction correction to density-functional approximations for many-electron systems”. In: *Physical Review B* 23.10 (1981), p. 5048.

[64] Igor Žutić, Jaroslav Fabian, and S Das Sarma. "Spintronics: Fundamentals and applications". In: *Reviews of modern physics* 76.2 (2004), p. 323.

[65] Jaroslav Fabian et al. "Semiconductor spintronics". In: *arXiv preprint arXiv:0711.1461* (2007).

[66] Carlo Motta et al. "Revealing the role of organic cations in hybrid halide perovskite CH3NH3PbI3". In: *Nature communications* 6.1 (2015), pp. 1–7.

[67] Thibaud Etienne, Edoardo Mosconi, and Filippo De Angelis. "Dynamical Rashba band splitting in hybrid perovskites modeled by local electric fields". In: *The Journal of Physical Chemistry C* 122.1 (2018), pp. 124–132.

[68] Thibaud Etienne, Edoardo Mosconi, and Filippo De Angelis. "Dynamical origin of the Rashba effect in organohalide lead perovskites: A key to suppressed carrier recombination in perovskite solar cells?" In: *The journal of physical chemistry letters* 7.9 (2016), pp. 1638–1645.

[69] P. A. Franken et al. "Generation of Optical Harmonics". In: *Phys. Rev. Lett.* 7 (4 1961), pp. 118–119. DOI: 10.1103/PhysRevLett.7.118. URL: https://link.aps.org/doi/10.1103/PhysRevLett.7.118.

[70] Manuel Joffre. "Optique non-linéaire en régimes continu et femtoseconde". Master. Lecture. Ce cours a été enseigné au master Concepts fondamentaux de la Physique (ENS - Ecole Polytechnique - Paris VI - Paris XI) entre 2000 et 2012, 2010. URL: https://cel.archives-ouvertes.fr/cel-00092964.

[71] Robert W. Boyd. *Nonlinear Optics, Third Edition*. 3rd. USA: Academic Press, Inc., 2008. ISBN: 0123694701.

[72] Rüdiger Paschotta. "Phase matching". In: ().

[73] F. Vidal and A. Tadjeddine. "Sum-frequency generation spectroscopy of interfaces". In: *Reports on Progress in Physics* 68 (2005), pp. 1095–1127. DOI: 10.1088/0034-4885/68/5/R03. URL: https://hal.archives-ouvertes.fr/hal-00008952.

[74] Yuen Ron Shen and Victor Ostroverkhov. "Sum-frequency vibrational spectroscopy on water interfaces: polar orientation of water molecules at interfaces". In: *Chemical reviews* 106.4 (2006), pp. 1140–1154.

[75] Sebastian F Mährlein. "Nonlinear terahertz phononics: A novel route to controlling matter". PhD thesis. 2017.

[76] Mildred S Dresselhaus, Gene Dresselhaus, and Ado Jorio. *Group theory: application to the physics of condensed matter*. Springer Science & Business Media, 2007.

[77] Matthias C Hoffmann et al. "Terahertz kerr effect". In: *Applied Physics Letters* 95.23 (2009), p. 231105.

[78] Dominik M Juraschek and Sebastian F Maehrlein. "Sum-frequency ionic Raman scattering". In: *Physical Review B* 97.17 (2018), p. 174302.

[79] Sebastian Maehrlein et al. “Terahertz sum-frequency excitation of a Raman-active phonon”. In: *Physical review letters* 119.12 (2017), p. 127402.

[80] Michael Först et al. “Nonlinear phononics as an ultrafast route to lattice control”. In: *Nature Physics* 7.11 (2011), pp. 854–856.

[81] Alaska Subedi, Andrea Cavalleri, and Antoine Georges. “Theory of nonlinear phononics for coherent light control of solids”. In: *Physical Review B* 89.22 (2014), p. 220301.

[82] Somayeh Gholipour and Michael Saliba. “Bandgap tuning and compositional exchange for lead halide perovskite materials”. In: *Characterization Techniques for Perovskite Solar Cell Materials*. Elsevier, 2020, pp. 1–22.

[83] Tomas Leijtens et al. “Towards enabling stable lead halide perovskite solar cells; interplay between structural, environmental, and thermal stability”. In: *Journal of Materials Chemistry A* 5.23 (2017), pp. 11483–11500.

[84] Feng Xu et al. “Mixed cation hybrid lead halide perovskites with enhanced performance and stability”. In: *Journal of Materials Chemistry A* 5.23 (2017), pp. 11450–11461.

[85] Feray Ünlü et al. “Chemical Processing of Mixed-Cation Hybrid Perovskites: Stabilizing Effects of Configurational Entropy”. In: *Perovskite Solar Cells: Materials, Processes, and Devices* (2021), pp. 1–31.

[86] Nicholas De Marco et al. “Guanidinium: a route to enhanced carrier lifetime and open-circuit voltage in hybrid perovskite solar cells”. In: *Nano letters* 16.2 (2016), pp. 1009–1016.

[87] Weihai Zhang et al. “Guanidinium induced phase separated perovskite layer for efficient and highly stable solar cells”. In: *Journal of Materials Chemistry A* 7.16 (2019), pp. 9486–9496.

[88] Jiaxu Yao et al. “Trap passivation and efficiency improvement of perovskite solar cells by a guanidinium additive”. In: *Materials Chemistry Frontiers* 3.7 (2019), pp. 1357–1364.

[89] Ngoc Duy Pham et al. “Tailoring crystal structure of FA0. 83Cs0. 17PbI3 perovskite through guanidinium doping for enhanced performance and tunable hysteresis of planar perovskite solar cells”. In: *Advanced Functional Materials* 29.1 (2019), p. 1806479.

[90] Xiaomeng Hou et al. “Effect of guanidinium on mesoscopic perovskite solar cells”. In: *Journal of Materials Chemistry A* 5.1 (2017), pp. 73–78.

[91] Qifeng Han et al. “Single crystal formamidinium lead iodide (FAPbI3): insight into the structural, optical, and electrical properties”. In: *Advanced Materials* 28.11 (2016), pp. 2253–2258.

[92] Giles E Eperon et al. “Formamidinium lead trihalide: a broadly tunable perovskite for efficient planar heterojunction solar cells”. In: *Energy & Environmental Science* 7.3 (2014), pp. 982–988.

[93] Anna Amat et al. “Cation-induced band-gap tuning in organohalide perovskites: interplay of spin–orbit coupling and octahedra tilting”. In: *Nano letters* 14.6 (2014), pp. 3608–3616.

[94] Michael Saliba et al. “Cesium-containing triple cation perovskite solar cells: improved stability, reproducibility and high efficiency”. In: *Energy & environmental science* 9.6 (2016), pp. 1989–1997.

[95] Alexander D Jodlowski et al. “Large guanidinium cation mixed with methylammonium in lead iodide perovskites for 19% efficient solar cells”. In: *Nature Energy* 2.12 (2017), pp. 972–979.

[96] Matěj Velickỳ and Peter S Toth. “From two-dimensional materials to their heterostructures: An electrochemist’s perspective”. In: *Applied Materials Today* 8 (2017), pp. 68–103.

[97] Tian Tian et al. “Electronic polarizability as the fundamental variable in the dielectric properties of two-dimensional materials”. In: *Nano letters* 20.2 (2019), pp. 841–851.

[98] J-C Blancon et al. “Scaling law for excitons in 2D perovskite quantum wells”. In: *Nature communications* 9.1 (2018), pp. 1–10.

[99] Matthew D Smith et al. “Structural origins of broadband emission from layered Pb–Br hybrid perovskites”. In: *Chemical science* 8.6 (2017), pp. 4497–4504.

[100] Félix Thouin et al. “Stable biexcitons in two-dimensional metal-halide perovskites with strong dynamic lattice disorder”. In: *Physical Review Materials* 2.3 (2018), p. 034001.

[101] Félix Thouin et al. “Enhanced screening and spectral diversity in many-body elastic scattering of excitons in two-dimensional hybrid metal-halide perovskites”. In: *Physical Review Research* 1.3 (2019), p. 032032.

[102] Stefanie Neutzner et al. “Exciton-polaron spectral structures in two-dimensional hybrid lead-halide perovskites”. In: *Physical Review Materials* 2.6 (2018), p. 064605.

[103] Hak-Beom Kim et al. “Mixed solvents for the optimization of morphology in solution-processed, inverted-type perovskite/fullerene hybrid solar cells”. In: *Nanoscale* 6.12 (2014), pp. 6679–6683.

[104] Wan-Jian Yin, Tingting Shi, and Yanfa Yan. “Unusual defect physics in CH3NH3PbI3 perovskite solar cell absorber”. In: *Applied Physics Letters* 104.6 (2014), p. 063903.

[105] S De Wolf et al. “per, B. Niesen, M. Ledinsky, FJ. Haug, JH. Yum, and C. Ballif,“Organometallic halide perovskites: sharp optical absorption edge and its relation to photovoltaic performance,”” in: *J. Phys. Chem. Lett* 5.6 (2014), pp. 1035–1039.

[106] Rebecca L. Milot et al. “Full Paper”. Undetermined. In: *Advanced Functional Materials* 25.39 (Oct. 2015), pp. 6218 –6227. DOI: 10.1002/adfm.201502340.

[107] Seth Hubbard. “Recombination”. In: *Photovoltaic Solar Energy: From Fundamentals to Applications* (2016), pp. 39–46.

[108] Mark T. Weller et al. “Complete structure and cation orientation in the perovskite photovoltaic methylammonium lead iodide between 100 and 352 K”. English. In: *Chemical communications (Cambridge, England)* 51.20 (Feb. 2015), pp. 4180–4183. ISSN: 1359-7345. DOI: 10.1039/C4CC09944C.

[109] Sudeep Maheshwari et al. “The Relation between Rotational Dynamics of the Organic Cation and Phase Transitions in Hybrid Halide Perovskites”. English. In: *The Journal of Physical Chemistry C* 123.23 (2019), pp. 14652–14661. ISSN: 1932-7455. DOI: 10.1021/acs.jpcc.9b02736.

[110] Irina Anusca et al. “Dielectric Response: Answer to Many Questions in the Methylammonium Lead Halide Solar Cell Absorbers”. In: *Advanced Energy Materials* 7.19 (Oct. 2017). DOI: 10.1002/aenm.201700600. URL: https://hal.archives-ouvertes.fr/hal-01781461.

[111] Jarvist M. Frost and Aron Walsh. “What Is Moving in Hybrid Halide Perovskite Solar Cells?” In: *Accounts of Chemical Research* 49.3 (2016), pp. 528–535. DOI: 10.1021/acs.accounts.5b00431. URL: https://doi.org/10.1021%2Facs.accounts.5b00431.

[112] Paolo Umari, Edoardo Mosconi, and Filippo De Angelis. “Infrared Dielectric Screening Determines the Low Exciton Binding Energy of Metal-Halide Perovskites”. In: *The Journal of Physical Chemistry Letters* 0.0 (2018). PMID: 29336156, pp. 620–627. DOI: 10.1021/acs.jpclett.7b03286. eprint: http://dx.doi.org/10.1021/acs.jpclett.7b03286. URL: http://dx.doi.org/10.1021/acs.jpclett.7b03286.

[113] Aurélien M. A. Leguy et al. “The dynamics of methylammonium ions in hybrid organic–inorganic perovskite solar cells”. In: *Nature Communications* 6 (2015).

[114] Xiaoxi Wu et al. “Trap states in lead iodide perovskites.” In: *Journal of the American Chemical Society* 137 5 (2015), pp. 2089–96.

[115] Limin She, Meizhuang Liu, and Dingyong Zhong. “Atomic structures of CH3NH3PbI3 (001) surfaces”. In: *ACS nano* 10.1 (2016), pp. 1126–1131.

[116] Azimatu Seidu et al. “Surface reconstruction of tetragonal methylammonium lead triiodide”. In: *APL Materials* 9.11 (2021), p. 111102.

[117] Claudia Caddeo, Alessio Filippetti, and Alessandro Mattoni. “The dominant role of surfaces in the hysteretic behavior of hybrid perovskites”. In: *Nano Energy* 67 (2020), p. 104162.

[118] Laura M Herz. “Charge-carrier mobilities in metal halide perovskites: fundamental mechanisms and limits”. In: *ACS Energy Letters* 2.7 (2017), pp. 1539–1548.

[119] Samuel Poncé, Martin Schlipf, and Feliciano Giustino. “Origin of low carrier mobilities in halide perovskites”. In: *ACS Energy Letters* 4.2 (2019), pp. 456–463.

[120] Cesare Franchini et al. “Polarons in materials”. In: *Nature Reviews Materials* 6.7 (2021), pp. 560–586.

[121] Yasuhiro Yamada and Yoshihiko Kanemitsu. “Electron-phonon interactions in halide perovskites”. In: *NPG Asia Materials* 14.1 (2022), pp. 1–15.

[122] LD Landau and SI Pekar. “Effective mass of a polaron”. In: *Zh. Eksp. Teor. Fiz* 18.5 (1948), pp. 419–423.

[123] Michael Sendner et al. “Optical phonons in methylammonium lead halide perovskites and implications for charge transport”. In: *Materials Horizons* 3.6 (2016), pp. 613–620.

[124] Mischa Bonn et al. “Role of dielectric drag in polaron mobility in lead halide perovskites”. In: *ACS Energy Letters* 2.11 (2017), pp. 2555–2562.

[125] Fan Zheng and Lin-wang Wang. “Large polaron formation and its effect on electron transport in hybrid perovskites”. In: *Energy & Environmental Science* 12.4 (2019), pp. 1219–1230.

[126] X-Y Zhu and V Podzorov. *Charge carriers in hybrid organic–inorganic lead halide perovskites might be protected as large polarons*. 2015.

[127] M Sotoodeh, AH Khalid, and AA Rezazadeh. “Empirical low-field mobility model for III–V compounds applicable in device simulation codes”. In: *Journal of applied physics* 87.6 (2000), pp. 2890–2900.

[128] Kyle Frohna et al. “Inversion symmetry and bulk Rashba effect in methylammonium lead iodide perovskite single crystals”. In: *Nature communications* 9.1 (2018), pp. 1–9.

[129] Fan Zhang et al. “Comparative studies of optoelectrical properties of prominent PV materials: Halide perovskite, CdTe, and GaAs”. In: *Materials Today* 36 (2020), pp. 18–29.

[130] Dong Shi et al. “Low trap-state density and long carrier diffusion in organolead trihalide perovskite single crystals”. In: *Science* 347.6221 (2015), pp. 519–522.

[131] Qingfeng Dong et al. “Electron-hole diffusion lengths> 175 μm in solution-grown CH3NH3PbI3 single crystals”. In: *Science* 347.6225 (2015), pp. 967–970.

[132] AC Ferreira et al. “Direct evidence of weakly dispersed and strongly anharmonic optical phonons in hybrid perovskites”. In: *Communications Physics* 3.1 (2020), pp. 1–10.

[133] Sebastian F. Maehrlein et al. “Decoding ultrafast polarization responses in lead halide perovskites by the two-dimensional optical Kerr effect”. In: *Proceedings of the National Academy of Sciences* 118.7 (2021). DOI: 10.1073/pnas.2022268118. URL: https://doi.org/10.1073%2Fpnas.2022268118.

[134] Yinsheng Guo et al. “Dynamic emission Stokes shift and liquid-like dielectric solvation of band edge carriers in lead-halide perovskites”. In: *Nature communications* 10.1 (2019), pp. 1–8.

[135] Peijun Guo et al. “Polar fluctuations in metal halide perovskites uncovered by acoustic phonon anomalies”. In: *ACS Energy Letters* 2.10 (2017), pp. 2463–2469.

[136] Feifan Wang et al. “Optical anisotropy and phase transitions in lead halide perovskites”. In: *The Journal of Physical Chemistry Letters* 12.20 (2021), pp. 5016–5022.

[137] Alessandro Stroppa et al. “Ferroelectric polarization of CH3NH3PbI3: a detailed study based on density functional theory and symmetry mode analysis”. In: *The journal of physical chemistry letters* 6.12 (2015), pp. 2223–2231.

[138] Jarvist M Frost et al. “Atomistic origins of high-performance in hybrid halide perovskite solar cells”. In: *Nano letters* 14.5 (2014), pp. 2584–2590.

[139] Shi Liu et al. “Ferroelectric domain wall induced band gap reduction and charge separation in organometal halide perovskites”. In: *The journal of physical chemistry letters* 6.4 (2015), pp. 693–699.

[140] Arthur Marronnier et al. “Structural instabilities related to highly anharmonic phonons in halide perovskites”. In: *The journal of physical chemistry letters* 8.12 (2017), pp. 2659–2665.

[141] Claudine Katan, Aditya D Mohite, and Jacky Even. “Entropy in halide perovskites”. In: *Nature materials* 17.5 (2018), pp. 377–379.

[142] Francesco Ambrosio et al. “Charge localization, stabilization, and hopping in lead halide perovskites: competition between polaron stabilization and cation disorder”. In: *ACS Energy Letters* 4.8 (2019), pp. 2013–2020.

[143] Yin Chen et al. “Extended carrier lifetimes and diffusion in hybrid perovskites revealed by Hall effect and photoconductivity measurements”. In: *Nature communications* 7.1 (2016), pp. 1–9.

[144] Mark E Ziffer et al. “Charge carrier coupling to the soft phonon mode in a ferroelectric semiconductor”. In: *arXiv preprint arXiv:2205.10960* (2022).

[145] Artem A Bakulin et al. “Real-time observation of organic cation reorientation in methylammonium lead iodide perovskites”. In: *The journal of physical chemistry letters* 6.18 (2015), pp. 3663–3669.

[146] Tobias Glaser et al. “Infrared spectroscopic study of vibrational modes in methylammonium lead halide perovskites”. In: *The journal of physical chemistry letters* 6.15 (2015), pp. 2913–2918.

[147] Christian Müller et al. “Water infiltration in methylammonium lead iodide perovskite: Fast and inconspicuous”. In: (2015).

[148] Chan La-o Vorakiat et al. “Phonon mode transformation across the orthohombic–tetragonal phase transition in a lead iodide perovskite CH3NH3PbI3: a terahertz time-domain spectroscopy approach”. In: *The journal of physical chemistry letters* 7.1 (2016), pp. 1–6.

[149] N. Onoda-Yamamuro. “Dielectric study of CH3NH3PbX3 (X = Cl, Br, I)”. In: *Journal of Physics and Chemistry of Solids* 53.7 (July 1992), pp. 935–939. DOI: 10.1016/0022-3697(92)90121-S.

[150] Laura M Herz. “How lattice dynamics moderate the electronic properties of metal-halide perovskites”. In: *The journal of physical chemistry letters* 9.23 (2018), pp. 6853–6863.

[151] Martin Schlipf, Samuel Poncé, and Feliciano Giustino. “Carrier lifetimes and polaronic mass enhancement in the hybrid halide perovskite CH 3 NH 3 PbI 3 from multiphonon Fröhlich coupling”. In: *Physical Review Letters* 121.8 (2018), p. 086402.

[152] Chelsea Q Xia et al. “Ultrafast photo-induced phonon hardening due to Pauli blocking in MAPbI3 single-crystal and polycrystalline perovskites”. In: *Journal of Physics: Materials* 4.4 (2021), p. 044017.

[153] Myeongkee Park et al. “Excited-state vibrational dynamics toward the polaron in methylammonium lead iodide perovskite”. In: *Nature communications* 9.1 (2018), pp. 1–9.

[154] Federico Brivio et al. “Lattice dynamics and vibrational spectra of the orthorhombic, tetragonal, and cubic phases of methylammonium lead iodide”. In: *Physical Review B* 92.14 (2015), p. 144308.

[155] EL Unger et al. “Roadmap and roadblocks for the band gap tunability of metal halide perovskites”. In: *Journal of Materials Chemistry A* 5.23 (2017), pp. 11401–11409.

[156] Lukas Schmidt-Mende et al. “Roadmap on organic–inorganic hybrid perovskite semiconductors and devices”. In: *APL Materials* 9.10 (2021), p. 109202.

[157] T Umebayashi et al. “Electronic structures of lead iodide based low-dimensional crystals”. In: *Physical Review B* 67.15 (2003), p. 155405.

[158] Heejae Kim et al. “Direct observation of mode-specific phonon-band gap coupling in methylammonium lead halide perovskites”. In: *Nature communications* 8.1 (2017), pp. 1–9.

[159] Peijun Guo et al. “Direct observation of bandgap oscillations induced by optical phonons in hybrid lead iodide perovskites”. In: *Advanced Functional Materials* 30.22 (2020), p. 1907982.

[160] Simon A Bretschneider et al. “Quantifying polaron formation and charge carrier cooling in lead-iodide perovskites”. In: *Advanced Materials* 30.29 (2018), p. 1707312.

[161] Stephen Palese et al. “Femtosecond optical Kerr effect studies of water”. In: *The Journal of Physical Chemistry* 98.25 (1994), pp. 6308–6316.

[162] Roberto Righini. “Ultrafast optical Kerr effect in liquids and solids”. In: *Science* 262.5138 (1993), pp. 1386–1390.

[163] Andrew P Schlaus et al. “How lasing happens in CsPbBr3 perovskite nanowires”. In: *Nature communications* 10.1 (2019), pp. 1–8.

[164] Rui Su et al. “Observation of exciton polariton condensation in a perovskite lattice at room temperature”. In: *Nature Physics* 16.3 (2020), pp. 301–306.

[165] Luis M Pazos-Outón et al. “Photon recycling in lead iodide perovskite solar cells”. In: *Science* 351.6280 (2016), pp. 1430–1433.

[166] Brandon R Sutherland and Edward H Sargent. “Perovskite photonic sources”. In: *Nature Photonics* 10.5 (2016), pp. 295–302.

[167] Jacky Even et al. “Solid-state physics perspective on hybrid perovskite semiconductors”. In: *The Journal of Physical Chemistry C* 119.19 (2015), pp. 10161–10177.

[168] Silvia Picozzi. “Ferroelectric Rashba semiconductors as a novel class of multifunctional materials”. In: *Frontiers in Physics* 2 (2014), p. 10.

[169] Kenichiro Tanaka et al. “Comparative study on the excitons in lead-halide-based perovskite-type crystals CH3NH3PbBr3 CH3NH3PbI3”. In: *Solid state communications* 127.9-10 (2003), pp. 619–623.

[170] Kai Leng et al. “Ferroelectricity and Rashba effect in 2D organic–inorganic hybrid perovskites”. In: *Trends in Chemistry* 3.9 (2021), pp. 716–732.

[171] Christian Wehrenfennig et al. “High charge carrier mobilities and lifetimes in organolead trihalide perovskites”. In: *Advanced materials* 26.10 (2014), pp. 1584–1589.

[172] Chao Zheng, Shidong Yu, and Oleg Rubel. “Structural dynamics in hybrid halide perovskites: Bulk Rashba splitting, spin texture, and carrier localization”. In: *Physical Review Materials* 2.11 (2018), p. 114604.

[173] Zhi-Gang Yu. “Estimation of the Rashba strength from second harmonic generation in 2D and 3D hybrid organic–inorganic perovskites”. In: *The Journal of Physical Chemistry C* 122.51 (2018), pp. 29607–29612.

[174] Edoardo Mosconi, Thibaud Etienne, and Filippo De Angelis. “Rashba band splitting in organohalide lead perovskites: bulk and surface effects”. In: *The Journal of Physical Chemistry Letters* 8.10 (2017), pp. 2247–2252.

[175] Eline M Hutter et al. “Direct–indirect character of the bandgap in methylammonium lead iodide perovskite”. In: *Nature materials* 16.1 (2017), pp. 115–120.

[176] Pooya Azarhoosh et al. “Research Update: Relativistic origin of slow electron-hole recombination in hybrid halide perovskite solar cells”. In: *Apl Materials* 4.9 (2016), p. 091501.

[177] Federico Brivio, Alison B Walker, and Aron Walsh. “Structural and electronic properties of hybrid perovskites for high-efficiency thin-film photovoltaics from first-principles”. In: *Apl Materials* 1.4 (2013), p. 042111.

[178] Marina R Filip and Feliciano Giustino. “Computational screening of homovalent lead substitution in organic–inorganic halide perovskites”. In: *The Journal of Physical Chemistry C* 120.1 (2016), pp. 166–173.

[179] Jun Yin et al. “Layer-dependent Rashba band splitting in 2D hybrid perovskites”. In: *Chemistry of Materials* 30.23 (2018), pp. 8538–8545.

[180] Chang Woo Myung et al. “Rashba–Dresselhaus effect in inorganic/organic lead iodide perovskite interfaces”. In: *ACS Energy Letters* 3.6 (2018), pp. 1294–1300.

[181] Shidong Yu et al. “Rashba band splitting in two-dimensional Ruddlesden–Popper halide perovskites”. In: *Journal of Applied Physics* 128.17 (2020), p. 175101.

[182] Tanja Schmitt et al. “Control of crystal symmetry breaking with halogen-substituted benzylammonium in layered hybrid metal-halide perovskites”. In: *Journal of the American Chemical Society* 142.11 (2020), pp. 5060–5067.

[183] Seth B Todd et al. “Detection of Rashba spin splitting in 2D organic-inorganic perovskite via precessional carrier spin relaxation”. In: *APL Materials* 7.8 (2019), p. 081116.

[184] Yaxin Zhai et al. “Giant Rashba splitting in 2D organic-inorganic halide perovskites measured by transient spectroscopies”. In: *Science advances* 3.7 (2017), e1700704.

[185] Constantinos C Stoumpos, Christos D Malliakas, and Mercouri G Kanatzidis. “Semiconducting tin and lead iodide perovskites with organic cations: phase transitions, high mobilities, and near-infrared photoluminescent properties”. In: *Inorganic chemistry* 52.15 (2013), pp. 9019–9038.

[186] J Beilsten-Edmands et al. “Non-ferroelectric nature of the conductance hysteresis in CH3NH3PbI3 perovskite-based photovoltaic devices”. In: *Applied Physics Letters* 106.17 (2015), p. 173502.

[187] Fan Zheng et al. “Rashba spin–orbit coupling enhanced carrier lifetime in CH3NH3PbI3”. In: *Nano letters* 15.12 (2015), pp. 7794–7800.

[188] Yuri D Glinka et al. “Distinguishing between dynamical and static Rashba effects in hybrid perovskite nanocrystals using transient absorption spectroscopy”. In: *arXiv preprint arXiv:1909.03605* (2019).

[189] Martin Schlipf and Feliciano Giustino. “Dynamic rashba-dresselhaus effect”. In: *Physical Review Letters* 127.23 (2021), p. 237601.

[190] John Kerr. “XL. A new relation between electricity and light: Dielectrified media birefringent”. In: *The London, Edinburgh, and Dublin Philosophical Magazine and Journal of Science* 50.332 (1875), pp. 337–348.

[191] P Weinberger. “John Kerr and his effects found in 1877 and 1878”. In: *Philosophical Magazine Letters* 88.12 (2008), pp. 897–907.

[192] Masayoshi Tonouchi. “Cutting-edge terahertz technology”. In: *Nature photonics* 1.2 (2007), pp. 97–105.

[193] Jamal Uddin. *Terahertz Spectroscopy: A Cutting Edge Technology*. BoD–Books on Demand, 2017.

[194] Neil W Ashcroft and N David Mermin. “Solid state physics (brooks cole, 1976)”. In: *Cited on* 26 (1993).

[195] Dixit N Sathyanarayana. *Vibrational spectroscopy: theory and applications*. New Age International, 2015.

[196] Matteo Rini et al. “Control of the electronic phase of a manganite by mode-selective vibrational excitation”. In: *Nature* 449.7158 (2007), pp. 72–74.

[197] Daniele Fausti et al. “Light-induced superconductivity in a stripe-ordered cuprate”. In: *science* 331.6014 (2011), pp. 189–191.

[198] Hui-Seon Kim et al. “Lead iodide perovskite sensitized all-solid-state submicron thin film mesoscopic solar cell with efficiency exceeding 9%”. In: *Scientific reports* 2.1 (2012), pp. 1–7.

[199] Mengkun Liu et al. “Terahertz-field-induced insulator-to-metal transition in vanadium dioxide metamaterial”. In: *Nature* 487.7407 (2012), pp. 345–348.

[200] Eugenio Cinquanta et al. “Ultrafast THz probe of photoinduced polarons in lead-halide perovskites”. In: *Physical review letters* 122.16 (2019), p. 166601.

[201] Daming Zhao et al. “Monitoring electron–phonon interactions in lead halide perovskites using time-resolved THz spectroscopy”. In: *ACS nano* 13.8 (2019), pp. 8826–8835.

[202] Daming Zhao and Elbert EM Chia. “Free carrier, exciton, and phonon dynamics in lead-halide perovskites studied with ultrafast terahertz spectroscopy”. In: *Advanced Optical Materials* 8.3 (2020), p. 1900783.

[203] H Hirori et al. “Single-cycle terahertz pulses with amplitudes exceeding 1 MV/cm generated by optical rectification in LiNbO 3”. In: *Applied Physics Letters* 98.9 (2011), p. 091106.

[204] J Hebling et al. “Tunable THz pulse generation by optical rectification of ultrashort laser pulses with tilted pulse fronts”. In: *Applied Physics B* 78.5 (2004), pp. 593–599.

[205] Julius JF Heitz et al. “Optically Gated Terahertz-Field-Driven Switching of Antiferromagnetic Cu Mn As”. In: *Physical Review Applied* 16.6 (2021), p. 064047.

[206] Mohsen Sajadi, Martin Wolf, and Tobias Kampfrath. “Terahertz-field-induced optical birefringence in common window and substrate materials”. In: *Optics express* 23.22 (2015), pp. 28985–28992.

[207] Mohsen Sajadi, Martin Wolf, and Tobias Kampfrath. “Transient birefringence of liquids induced by terahertz electric-field torque on permanent molecular dipoles”. In: *Nature communications* 8.1 (2017), pp. 1–9.

[208] H. Hertz. “Ueber einen Einfluss des ultravioletten Lichtes auf die electrische Entladung”. In: *Annalen der Physik* 267.8 (Jan. 1887), pp. 983–1000. DOI: 10.1002/andp.18872670827.

[209] A. Einstein. “Uber einen die Erzeugung und Verwandlung des Lichtes betreffenden heuristischen Gesichtspunkt”. In: *Annalen der Physik* 17 (1905), pp. 132–148. DOI: 10.1002/andp.19053220607.

[210] W. E. Spicer and C. N. Berglund. “*d* Band of Copper”. In: *Phys. Rev. Lett.* 12 (1 1964), pp. 9–11. DOI: 10.1103/PhysRevLett.12.9. URL: https://link.aps.org/doi/10.1103/PhysRevLett.12.9.

[211] Andrea Damascelli. “Probing the electronic structure of complex systems by ARPES”. In: *Physica Scripta* 2004.T109 (2004), p. 61.

[212] Mahdi Hajlaoui. “Between metal and insulator: ultrafast dynamics in the topological insulator Bi2Te3and microscopic domains at the Mott transition in V2O3”. PhD thesis. Université Paris Sud-Paris XI, 2013.

[213] Antonio Tejeda. *Photoémission dans les solides*. EDP Sciences, 2016.

[214] Niloufar Nilforoushan. “Out-of-equilibrium electron dynamics of Dirac semimetals and strongly correlated materials”. PhD thesis. Université Paris-Saclay (ComUE), 2018.

[215] M Pl Seah and WA Dench. “Quantitative electron spectroscopy of surfaces: A standard data base for electron inelastic mean free paths in solids”. In: *Surface and interface analysis* 1.1 (1979), pp. 2–11.

[216] Jérôme Faure et al. “Full characterization and optimization of a femtosecond ultraviolet laser source for time and angle-resolved photoemission on solid surfaces”. In: *Review of Scientific Instruments* 83.4 (2012), p. 043109.

[217] Z Yang et al. “Two-Inch-Sized Perovskite 474 CH3NH3PbX3 (X= Cl, Br, I) Crystals: Growth and Characterization. 475”. In: *Adv. Mater* 27 (2015), pp. 5176–5183.

[218] Lucas Huber et al. “The ultrafast Kerr effect in anisotropic and dispersive media”. In: *The Journal of Chemical Physics* 154.9 (2021), p. 094202.

[219] Dennis S. Kim et al. “Temperature-dependent phonon lifetimes and thermal conductivity of silicon by inelastic neutron scattering and ab initio calculations”. In: *Physical Review B* 102.17 (Nov. 2020). DOI: 10.1103/physrevb.102.174311.

[220] Suruchi Anand et al. “Temperature dependence of optical phonon lifetimes in ZnSe”. In: *Physica B-condensed Matter* 226 (1996), pp. 331–337.

[221] Lucy D Whalley et al. “Perspective: Theory and simulation of hybrid halide perovskites”. In: *The Journal of chemical physics* 146.22 (2017), p. 220901.

[222] H Mashiyama, Y Kawamura, E Magome, et al. “Displacive Character of the Cubic-Tetragonal Transition in CH _3 NH _3 PbX _3”. In: *Journal of the Korean Physical Society* 42.9 (2003), pp. 1026–1029.

[223] PS Whitfield et al. “Structures, phase transitions and tricritical behavior of the hybrid perovskite methyl ammonium lead iodide”. In: *Scientific reports* 6.1 (2016), pp. 1–16.

[224] Mirosław Mączka and Maciej Ptak. “Temperature-Dependent Raman Studies of FAPbBr3 and MAPbBr3 Perovskites: Effect of Phase Transitions on Molecular Dynamics and Lattice Distortion”. In: *Solids* 3.1 (2022), pp. 111–121.

[225] Mirosław Maczka, Jan A Zienkiewicz, and Maciej Ptak. “Comparative Studies of Phonon Properties of Three-Dimensional Hybrid Organic–Inorganic Perovskites Comprising Methylhydrazinium, Methylammonium, and Formamidinium Cations”. In: *The Journal of Physical Chemistry C* 126.8 (2022), pp. 4048–4056.

[226] Claudiu M Iaru et al. “Fröhlich interaction dominated by a single phonon mode in CsPbBr3”. In: *Nature communications* 12.1 (2021), pp. 1–8.

[227] Johan Klarbring and Sergei I Simak. “Nature of the octahedral tilting phase transitions in perovskites: A case study of CaMnO 3”. In: *Physical Review B* 97.2 (2018), p. 024108.

[228] Lisheng Chi et al. “The ordered phase of methylammonium lead chloride CH3ND3PbCl3”. In: *Journal of Solid State Chemistry* 178.5 (2005), pp. 1376–1385.

[229] IP Swainson et al. “Phase transitions in the perovskite methylammonium lead bromide, CH3ND3PbBr3”. In: *Journal of Solid State Chemistry* 176.1 (2003), pp. 97–104.

[230] IP Swainson et al. “From soft harmonic phonons to fast relaxational dynamics in CH 3 NH 3 PbBr 3”. In: *Physical Review B* 92.10 (2015), p. 100303.

[231] Adi Cohen et al. “Diverging Expressions of Anharmonicity in Halide Perovskites”. In: *Advanced Materials* 34.14 (2022), p. 2107932.

[232] Feng Jin et al. “Characterization of structural transitions and lattice dynamics of hybrid organic–inorganic perovskite CH3NH3PbI3”. In: *Chinese Physics B* 28.7 (2019), p. 076102.

[233] JF Scott. “Soft-mode spectroscopy: Experimental studies of structural phase transitions”. In: *Reviews of Modern Physics* 46.1 (1974), p. 83.

[234] Rohit Prasanna et al. “Band gap tuning via lattice contraction and octahedral tilting in perovskite materials for photovoltaics”. In: *Journal of the American Chemical Society* 139.32 (2017), pp. 11117–11124.

[235] Binbin Luo, Sara Bonabi Naghadeh, and Jin Z Zhang. “Lead halide perovskite nanocrystals: Stability, surface passivation, and structural control”. In: *ChemNanoMat* 3.7 (2017), pp. 456–465.

[236] Kang Wang et al. “All-inorganic cesium lead iodide perovskite solar cells with stabilized efficiency beyond 15%”. In: *Nature communications* 9.1 (2018), pp. 1–8.

[237] Jino Im et al. “Antagonism between spin–orbit coupling and steric effects causes anomalous band gap evolution in the perovskite photovoltaic materials CH3NH3Sn1–x Pb x I3”. In: *The journal of physical chemistry letters* 6.17 (2015), pp. 3503–3509.

[238] Pradeep R Varadwaj et al. “Significance of hydrogen bonding and other noncovalent interactions in determining octahedral tilting in the CH3NH3PbI3 hybrid organic-inorganic halide perovskite solar cell semiconductor”. In: *Scientific reports* 9.1 (2019), pp. 1–29.

[239] Jung-Hoon Lee et al. “Resolving the physical origin of octahedral tilting in halide perovskites”. In: *Chemistry of Materials* 28.12 (2016), pp. 4259–4266.

[240] Maximiliano Senno and Silvia Tinte. “Mixed formamidinium–methylammonium lead iodide perovskite from first-principles: hydrogen-bonding impact on the electronic properties”. In: *Physical Chemistry Chemical Physics* 23.12 (2021), pp. 7376–7385.

[241] Fabian Ruf et al. “Temperature-dependent studies of exciton binding energy and phase-transition suppression in (Cs, FA, MA) Pb (I, Br) 3 perovskites”. In: *Apl Materials* 7.3 (2019), p. 031113.

[242] Krzysztof Gałkowski et al. “Determination of the exciton binding energy and effective masses for the methylammonium and formamidinium lead tri-halide perovskite family”. In: *Energy Environ. Sci.* 9 (Nov. 2015). DOI: 10.1039/C5EE03435C.

[243] Dominik J Kubicki et al. “Cation dynamics in mixed-cation (MA) x (FA) 1–x PbI3 hybrid perovskites from solid-state NMR”. In: *Journal of the American Chemical Society* 139.29 (2017), pp. 10055–10061.

[244] Marcelo A Carignano et al. “Critical fluctuations and anharmonicity in lead iodide perovskites from molecular dynamics supercell simulations”. In: *The Journal of Physical Chemistry C* 121.38 (2017), pp. 20729–20738.

[245] Eunhwan Jung et al. “Femto-to microsecond dynamics of excited electrons in a quadruple cation perovskite”. In: *ACS Energy Letters* 5.3 (2020), pp. 785–792.

[246] AC Ferreira et al. “Elastic softness of hybrid lead halide perovskites”. In: *Physical Review Letters* 121.8 (2018), p. 085502.

[247] Stefan Zeiske et al. “Static Disorder in Lead Halide Perovskites”. In: *The journal of physical chemistry letters* 13.31 (2022), pp. 7280–7285.

[248] K Xerxes Steirer et al. “Defect tolerance in methylammonium lead triiodide perovskite”. In: *ACS Energy Letters* 1.2 (2016), pp. 360–366.

[249] Jinsong Huang et al. “Understanding the physical properties of hybrid perovskites for photovoltaic applications”. In: *Nature Reviews Materials* 2.7 (2017), pp. 1–19.

[250] Alexander J Knight et al. “Trap states, electric fields, and phase segregation in mixed-halide perovskite photovoltaic devices”. In: *Advanced Energy Materials* 10.9 (2020), p. 1903488.

[251] Hairen Tan et al. “Dipolar cations confer defect tolerance in wide-bandgap metal halide perovskites”. In: *Nature communications* 9.1 (2018), pp. 1–10.

[252] Zhesheng Chen et al. “Time-resolved photoemission spectroscopy of electronic cooling and localization in CH_3 NH_3 PbI_3 crystals”. In: *Physical Review Materials* 1.4 (2017), p. 045402. DOI: 10.1103/PhysRevMaterials.1.045402. URL: https://hal.archives-ouvertes.fr/hal-03268867.

[253] Zafer Hawash et al. “Interfacial Modification of Perovskite Solar Cells Using an Ultrathin MAI Layer Leads to Enhanced Energy Level Alignment, Efficiencies, and Reproducibility”. In: *Journal of Physical Chemistry Letters* 8.17 (2017), pp. 3947–3953. DOI: 10.1021/acs.jpclett.7b01508.

[254] Jennifer Emara et al. “Impact of Film Stoichiometry on the Ionization Energy and Electronic Structure of CH3NH3PbI3 Perovskites”. In: *Adv. Mater.* 28.3 (2016), S. 553–561. URL: https://kups.ub.uni-koeln.de/28711/.

[255] T Jesper Jacobsson et al. “Unreacted PbI2 as a double-edged sword for enhancing the performance of perovskite solar cells”. In: *Journal of the American Chemical Society* 138.32 (2016), pp. 10331–10343.

[256] Fabrizio Giordano et al. “Enhanced electronic properties in mesoporous TiO2 via lithium doping for high-efficiency perovskite solar cells”. In: *Nature communications* 7.1 (2016), pp. 1–6.

[257] Trilok Singh et al. “Sulfate-assisted interfacial engineering for high yield and efficiency of triple cation perovskite solar cells with alkali-doped TiO2 electron-transporting layers”. In: *Advanced Functional Materials* 28.14 (2018), p. 1706287.

[258] Martin Thomas Neukom et al. “Why perovskite solar cells with high efficiency show small IV-curve hysteresis”. In: *Solar Energy Materials and Solar Cells* 169 (2017), pp. 159–166.

[259] Shengfan Wu et al. “Efficient large guanidinium mixed perovskite solar cells with enhanced photovoltage and low energy losses”. In: *Chemical Communications* 55.30 (2019), pp. 4315–4318.

[260] Zhenxuan Zhao et al. “Probing the photovoltage and photocurrent in perovskite solar cells with nanoscale resolution”. In: *Advanced Functional Materials* 26.18 (2016), pp. 3048–3058.

[261] Dirk König et al. “Hot carrier solar cells: Principles, materials and design”. In: *Physica E: Low-dimensional Systems and Nanostructures* 42.10 (2010), pp. 2862–2866.

[262] Timothy W Crothers et al. “Photon reabsorption masks intrinsic bimolecular charge-carrier recombination in CH3NH3PbI3 perovskite”. In: *Nano letters* 17.9 (2017), pp. 5782–5789.

[263] Thomas Kirchartz. “High open-circuit voltages in lead-halide perovskite solar cells: experiment, theory and open questions”. In: *Philosophical Transactions of the Royal Society A* 377.2152 (2019), p. 20180286.

[264] Daniel Niesner et al. “Giant Rashba splitting in CH 3 NH 3 PbBr 3 organic-inorganic perovskite”. In: *Physical review letters* 117.12 (2016), p. 126401.

[265] Xie Zhang et al. “First-principles analysis of radiative recombination in lead-halide perovskites”. In: *ACS Energy Letters* 3.10 (2018), pp. 2329–2334.

[266] GW T Hooft. “The radiative recombination coefficient of GaAs from laser delay measurements and effective nonradiative carrier lifetimes”. In: *Applied Physics Letters* 39.5 (1981), pp. 389–390.

[267] David Giovanni et al. “Highly spin-polarized carrier dynamics and ultralarge photoinduced magnetization in CH3NH3PbI3 perovskite thin films”. In: *Nano letters* 15.3 (2015), pp. 1553–1558.

[268] Yu-Che Hsiao et al. “Magneto-optical studies on spin-dependent charge recombination and dissociation in perovskite solar cells”. In: *Advanced Materials* 27.18 (2015), pp. 2899–2906.

[269] Zhiyuan Zuo et al. “Enhanced optoelectronic performance on the (110) lattice plane of an MAPbBr3 single crystal”. In: *The Journal of Physical Chemistry Letters* 8.3 (2017), pp. 684–689.

[270] Wenxin Mao et al. “Controlled Growth of Monocrystalline Organo-Lead Halide Perovskite and Its Application in Photonic Devices”. In: *Angewandte Chemie* 129.41 (2017), pp. 12660–12665.

[271] Chol-Jun Yu. "Advances in modelling and simulation of halide perovskites for solar cell applications". In: *Journal of Physics: Energy* 1.2 (2019), p. 022001.

[272] Rui Wang et al. "A review of perovskites solar cell stability". In: *Advanced Functional Materials* 29.47 (2019), p. 1808843.

[273] Qingdong Lin et al. "Phase-Control of Single-Crystalline Inorganic Halide Perovskites via Molecular Coordination Engineering". In: *Advanced Functional Materials* 32.16 (2022), p. 2109442.

[274] Jijun Qiu, Lance L McDowell, and Zhisheng Shi. "Room-temperature cubic perovskite thin films by three-step all-vapor conversion from PbSe to MAPbI3". In: *Crystal Growth & Design* 19.3 (2019), pp. 2001–2009.

[275] Francisco Palazon et al. "Room-temperature cubic phase crystallization and high stability of vacuum-deposited methylammonium lead triiodide thin films for high-efficiency solar cells". In: *Advanced Materials* 31.39 (2019), p. 1902692.

[276] Wissam A Saidi and Joshua J Choi. "Nature of the cubic to tetragonal phase transition in methylammonium lead iodide perovskite". In: *The Journal of chemical physics* 145.14 (2016), p. 144702.

[277] Riccardo Comin et al. "Lattice dynamics and the nature of structural transitions in organolead halide perovskites". In: *Physical Review B* 94.9 (2016), p. 094301.

[278] Ling-yi Huang and Walter RL Lambrecht. "Lattice dynamics in perovskite halides CsSn X 3 with X= I, Br, Cl". In: *Physical Review B* 90.19 (2014), p. 195201.

[279] Cheng Chen et al. "Elucidating the phase transitions and temperature-dependent photoluminescence of MAPbBr3 single crystal". In: *Journal of Physics D: Applied Physics* 51.4 (2018), p. 045105.

[280] Hanadi Mehdi et al. "MAPbBr 3 perovskite solar cells via a two-step deposition process". In: *RSC advances* 9.23 (2019), pp. 12906–12912.

[281] Ravi K Misra et al. "Temperature-and component-dependent degradation of perovskite photovoltaic materials under concentrated sunlight". In: *The journal of physical chemistry letters* 6.3 (2015), pp. 326–330.

[282] Patrycja Makuła, Michał Pacia, and Wojciech Macyk. *How to correctly determine the band gap energy of modified semiconductor photocatalysts based on UV–Vis spectra*. 2018.

[283] Sung Hun Kim, Kyoung-Duck Park, and Hong Seok Lee. "Growth kinetics and optical properties of CsPbBr3 perovskite nanocrystals". In: *Energies* 14.2 (2021), p. 275.

[284] Tom PA van der Pol et al. "The Intrinsic Photoluminescence Spectrum of Perovskite Films". In: *Advanced Optical Materials* 10.8 (2022), p. 2102557.

[285] Anand S Subbiah et al. "Stable p–i–n FAPbBr3 devices with improved efficiency using sputtered ZnO as electron transport layer". In: *Advanced Materials Interfaces* 4.8 (2017), p. 1601143.

[286] Rocío García-Aboal et al. “Single crystal growth of hybrid lead bromide perovskites using a spin-coating method”. In: *ACS omega* 3.5 (2018), pp. 5229–5236.

[287] J.-P. Rueff et al. “The GALAXIES beamline at the SOLEIL synchrotron: inelastic X-ray scattering and photoelectron spectroscopy in the hard X-ray range”. In: *Journal of Synchrotron Radiation* 22.1 (2015), pp. 175–179. DOI: 10.1107/s160057751402102x. URL: https://doi.org/10.1107%2Fs160057751402102x.

[288] Senol Öz. *Process-, Solvent and Chemical Engineering for Solution Processed Organic-Inorganic Lead Halide Perovskite Solar Cells*. München: Hut, 2018.

A Appendix

A.1 Supplementary measurements on (4cat)$PbBr_3$

This part includes additional results related to Section.6.3 about (4cat)$PbBr_3$ studies with THz-induced Kerr effect. The measurements were performed by Niusha Heshmati from University of Cologne and the interpretation were done by both of us.

A.1.1 Crystallographic analysis with X-Ray diffraction (XRD)

Thinfilms at room temperature

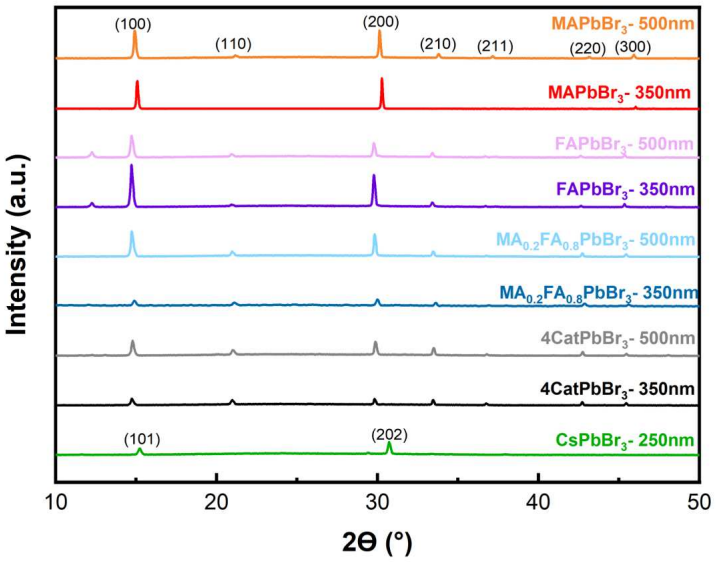

Figure A.1: Room temperature XRD pattern for each different thin films.

The crystallographic structure of both thin films and single crystals were analyzed using X-Ray

diffraction (XRD), in order to know precisely the structure and the phase of each sample, at ambient temperature but also at lower temperature for the (4cat)$PbBr_3$ (Fig.A.1). This technique is particularly interesting to know the purity of the phase. The XRD pattern of the 350nm thick $MAPbBr_3$ sample demonstrates pure perovskite cubic crystal with a characteristic cubic structure finger print $Pm3\bar{m}$, and sharp high intensity peaks in planes (100) at almost 2Θ=15° and (200) at 2Θ=30° [269]. Therefore, the (h00) peaks dominate the final diffraction pattern of the $MAPbBr_3$ thin films which is compatible with the SEM results that monocrystalline microplates cover surface [270]. $FAPbBr_3$ samples also show cubic perovskite peaks, but there is a new peak at 2θ = 12.3° in both thickness results. Regarding the calculated tolerence factor (1.01), we can consider this peak is ascribed to hexagonal non-perovskite structures when the Goldschmidt tolerance factor $t > 1$ [271]. The $CsPbBr_3$ sample shows different diffraction pattern with preferred orientation of (101) at 2Θ=15.2° and (202) at 2Θ=30.7° representing 3D $CsPbBr_3$ structure, suggesting the formation of a crystalline perovskite phase and consistent with reported values [272][273]. (MA,FA)$PbBr_3$ keeps the cubic structure and, such as the $MAPbBr_3$ sample, microcubes appear with high intensity peaks. In the case of (4cat)$PbBr_3$ samples, we could not detect peaks of the δ-phase compounds (explained in Subsection.3.1.2). The quadruple cation structure has less crystallinity in comparison to single cation ones, as shown by the lower peak intensity.

Temperature-dependence XRD measurements on single crystal

We then evaluated the fundamental properties of (4cat)$PbBr_3$ single crystal by utilizing temperature-dependent XRD from 80K to 300K, as shown on Fig. A.2. A clear intense orange, splinter of a cube-like single crystal with approximate dimensions 0.060 mm x 0.100 mm x 0.190 mm, was used for the XRD crystallographic analysis.

a

Temperature (K)	Crystalline phase
300 (full measurement)	Cubic
230	Tetragonal P (still 50% cubic)
165	Tetragonal P (still 50% cubic)
155	Tetragonal P (still 40% cubic)
135	Tetragonal P(still 40% cubic)
110	Orthorhombic P (still 40% cubic)
80 (full measurement)	Orthorhombic P (still 34% cubic)

b

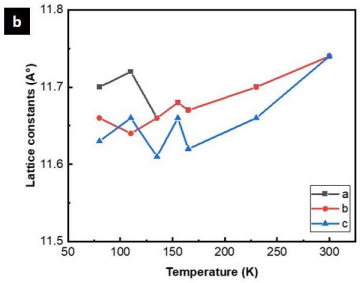

Figure A.2: (a) Crystalline phase as function of the temperature of the (4cat)$PbBr_3$ single crystal. (b) Temperature-dependence of the lattice constants a, b and c.

Photoactive perovskite cubic phase is needed for high efficiency and stability of hybrid (i.e organic and inorganic) halide-based optoelectric perovskite devices [274]. Indeed, achieving the highly symmetric cubic phase for perovskites at room temperatures or lower can reduce the costs of energy for making a device which needs heating in order to cross the tetragonal to cubic phase transition [275]. The results at 300K is compatible with a $P-43m$ cubic structure

and lattice parameter a = 11.72 Å and Volume = 1612.5 Å^3. At 230K tetragonal ($C2mm$) unit cell with cell constants of a = 11.7008(5) Å, c = 11.6583(6) Å, volume = 1596.1(2) Å^3 was detected. Cubic-to-tetragonal structural phase transition which lowers the lattice symmetry have been highly studied, as discussed in Section. 3.4.3. Phonons are the most important factor for stabilizing the cubic phase at higher temperatures, and tetragonal to cubic phase transition is driven by low-energy phonon modes related to the inorganic lattice [276]. The phase transition could be displacive type including the softening of a zone-center or zone-edge mode and it will be followed by distortion of the lattice condensation in the lower symmetry tetragonal phase. At the wave vector that the phonon softening happens a superlattice Bragg reflection will appear in reciprocal space and it would be a sign of symmetry change in the crystal [277][278]. At 300K, $a = b = c$ and the software considers the cubic structure as cubic. By cooling down we can see a slight change of a, b and c which is less than 0.1 Å. The software considers any $a = b \neq c$ as tetragonal, but because of too small difference the phase can still have a probability to be cubic. This means that although precise phase determination is tetragonal, but because of too small changes in lattice constant, there is still 50% of probability for this structure to be considered as cubic. Indeed, by cooling down the sample, tetragonal structure remains and the probability of having a cubic structure reduces. At 80K orthorhombic ($Pmmm$) unit cell with constants of a = 11.6519(13) Å, b = 11.6744(14) Å, c = 11.6091(13) Å, are achieved. As shown in Fig.A.2.b, lattice constants changed less than 0.1Å during the whole measurement, leading to conclude that lattice constant was the same and that only a small shrinking happened by reducing the temperature. Furthermore, there is still 34% of probability being in the cubic structure at 80K according to the simulation (Fig.A.2.a). As a conclusion, the total phase change is compatible with reported measurements for fully bromide perovskites [252][279], but interestingly the cubic phase of the quadruple cation lead bromide perovskite was almost preserved until 80K.

A.1.2 Optoelectronic characteristics

To investigate the effect of A-site cation engineering on absorption and radiative recombination of charge carriers' behavior, UV-VIS absorption spectra and PL emission of the samples were measured. Fig.A.3 depicts the static absorptance spectrums at room temperature and the corresponding Tauc plots for certain samples in Fig.A.4. As shown in Fig.A.3, all the layers exhibit a characteristic absorption edge around 530 nm, with a broad absorption of light which infers the formation of perovskite layer on the substrate [280]. According to the results highest absorbance belongs to $MAPbBr_3$ with 350nm thickness with considerable difference in comparison to other samples. We can attribute these results to crystallinity of the layer that has direct influence on absorbance of the layer[280][281]. $MAPbBr_3$ sample is the only one that had high intensity peaks attributed to cubic structure of perovskite and XRD results similar to single crystal sample, therefore it has high absorbance and the remaining layers also are compatible with XRD results and with improved the crystallinity of the layer the absorbance improved too. Also, the optical bandgap of the samples were calculated from Tauc plots. The Tauc method is based on assumption that the energy-dependent absorption

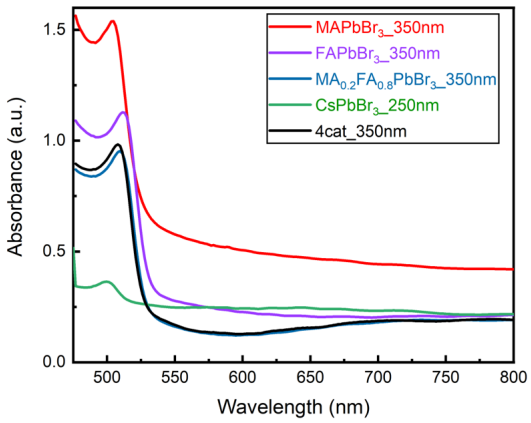

Figure A.3: Aborption spectra of several thin films.

coefficient (α), which is proportional to the incident photon energy ($h\nu$) and optical density, can be determined by the following equation.

$$(\alpha \cdot h\nu)^{\frac{1}{\gamma}} = B(h\nu - E_g) \tag{A.1}$$

In this equation ν is the photon's frequency, h is the Planck constant, B is a constant, and E_g is the band gap energy. The factor γ is related to the nature of the material and electronic transition is equal to 1/2 or 2 for the direct and indirect transition band gaps, respectively [282]. Therefore, extrapolating a straight-line portion of the plot of the quantity $(\alpha \cdot h\nu)^{\frac{1}{\gamma}}$ versus photon energy bring to the optical bandgap E_g [283]. The obtained values for the optical band gap E_g are in agreement with the maximum absorption, shown in Fig. A.6. $FAPbBr_3$ have the lowest E_g while $MAPbBr_3$ with the shortest wavelength have the highest E_g. Furthermore, the tolerance factor t of $MAPbBr_3$ is 0.92 while the rest of analyzed perovskite samples is close to 1, indicating a higher symmetry of the crystal structure, as well as less tilted $PbBr_6$ octahedral cage, leading to a lower band gap E_g. This confirms previous results demonstrate that there is a opposite relation between t and band gap E_g of the LHPs, as well as higher tolerance factor (ranging t=0.8–1.0) leads to lower bandgap [85].

Photoluminescence

Photoluminescence (PL) results can shed a light on important properties such as materials quality, impurity, and defect detection [284]. Furthermore, bandgap measurement and explanation of recombination process is possible according to PL results. The energetic values of photoluminescence photons in a semiconductor are usually somewhat smaller than the actual band gap of the material. Indeed, once excited into the conduction band, electrons can

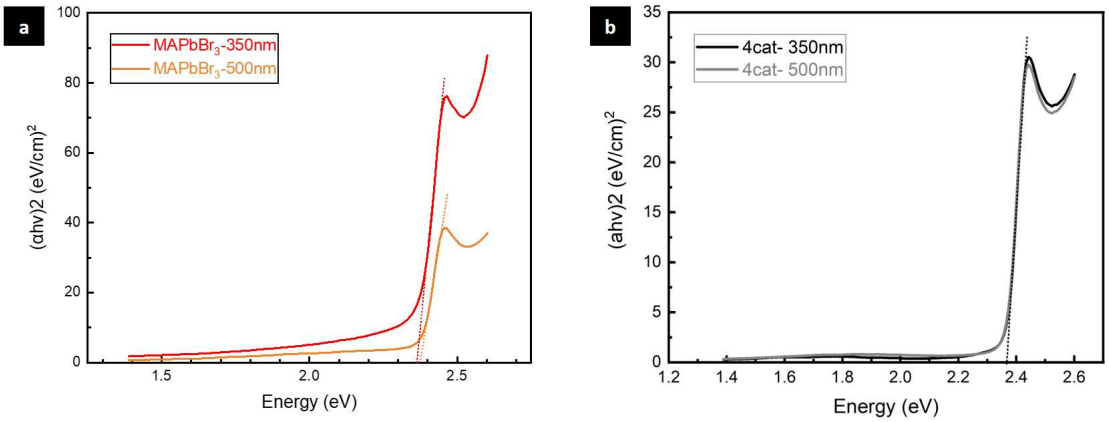

Figure A.4: Absorption measurements and Tauc parameter extraction (dashed line) in different thickness thinfilm of (a) $MAPbBr_3$ and (b) (4cat)$PbBr_3$.

relax into shallow defect states right below the conduction band and from there recombine with holes in the valence band, emitting photons with a smaller energy than the bandgap.

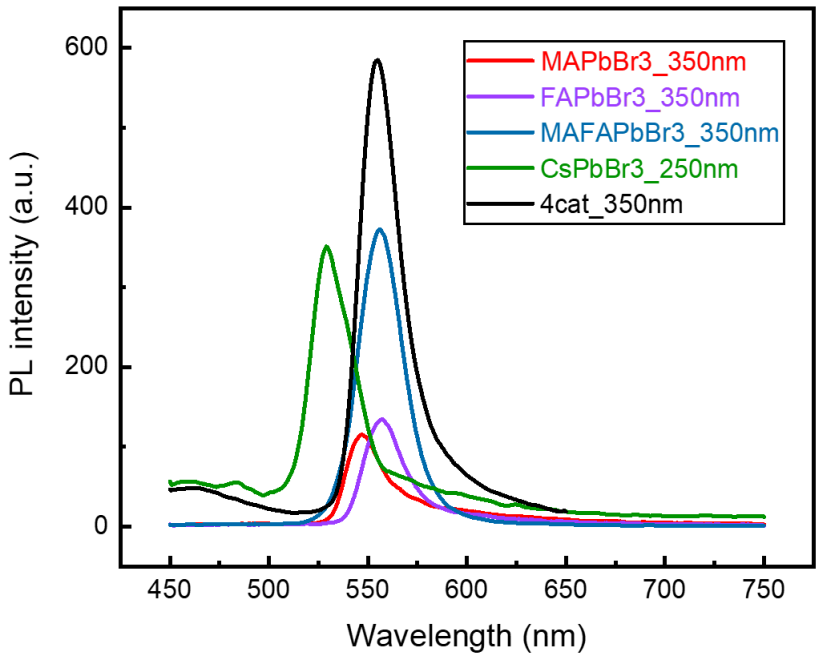

Figure A.5: Photoluminescence measurements at room temperature for different thinfilms.

Photoluminescence spectra are shown in Fig. A.5. With mixed cation structure the intensity of all PL peaks increased considerably, and the highest possible amount was achieved with 350nm thick (4cat)$PbBr_3$ sample. Intensified PL peak for (4cat)$PbBr_3$ sample can be explained

by suppression of the non-radiative recombination an reduction the density of traping this perovskite layer.

Sample properties		UV-Vis results			PL results	
Perovskite	Thickness [nm]	λ_{max} [nm]	Abs onset [nm]	E_g [eV]	λ_{max} [nm]	E_g [eV]
$MAPbBr_3$	350	505	531	2.38	547	2.27
$MAPbBr_3$	500	505	539	2.38	547.5	2.26
$FAPbBr_3$	350	511	538	2.35	557.5	2.22
$FAPbBr_3$	500	513	536	2.35	554	2.24
$MA_{0.2}FA_{0.8}PbBr_3$	350	510	535	2.36	556	2.23
$MA_{0.2}FA_{0.8}PbBr_3$	500	510	535	2.36	556.5	2.23
4-cat$PbBr_3$	350	508	530	2.37	555	2.23
4-cat$PbBr_3$	500	508	530	2.37	553	2.24

Figure A.6: Summary of the optoelectronic properties obtain for different thin films at room temperature.

Scanning electron microscopy (SEM)

Earlier studies have shown the importance of the film morphology and surface coverage of perovskite absorbing layer in order to get better performance [285]. To investigate the surface structure, thin films with 350 nm and 500 nm thick photoactive layer were analyzed through scanning electron microscopy (SEM). Fig.A.7 shows the fabricated samples under different magnification. Both (4cat)$PbBr_3$ samples show a uniform and relatively smooth surface with a grain size of approximately 200 nm without major defects. The surface of 350 nm thick $MAPbBr_3$ shows the presence of monocrystaline microplates between 5 – 10 μm with a cubic structure. Microplates structures are interesting for evaluating the crystal properties as photonic microcavities. It has been demonstrated that oriented grains of perovskite layer in photovoltaic devices can increase the photocurrent and final device performance [286]. Observing the contrast within the SEM pictures indicates a rough surface with potential defects between the grains. In the case of 500 nm thick $MAPbBr_3$, a smooth and uniform structure with small grains appeared but still similar to the 350 nm one. Besides, presence of bumps are clear. This size reduction infers that the nucleation density is high and leads to formation of a large number of small crystals. $CsPbBr_3$ shows rather a poor surface coverage, in agreement with reported results [272].

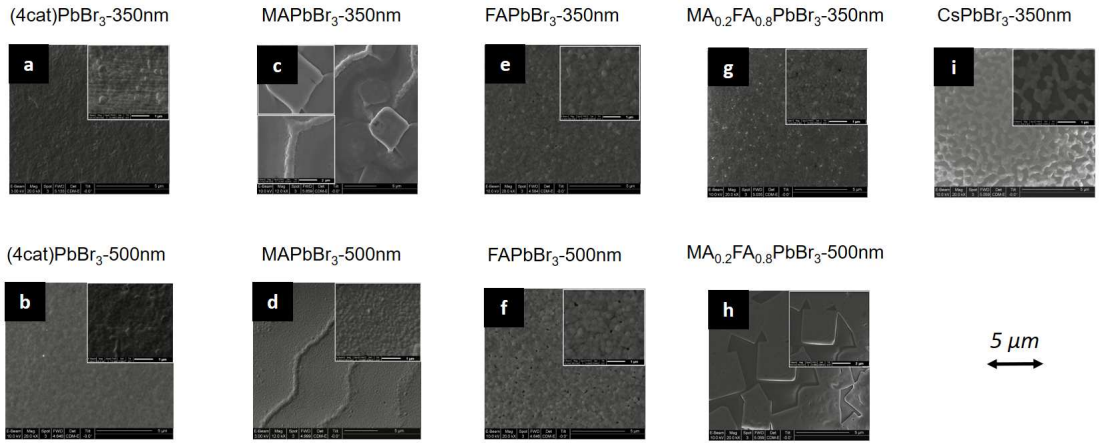

Figure A.7: Scanning electron microscopy of the different thinfilms used in TKE experiments.

A.2 Supplementary experimental techniques

This section describes the experimental information concerning the secondary characterization techniques used to obtain certain experimental results and performed by collaborators.

A.2.1 Hard X-ray photoelectron spectroscopy (HAXPES)

Hard X-ray photoelectron spectroscopy (HAXPES) has been performed at the GALAXIES beamline of SOLEIL synchrotron [287]. HAXPES is a powerful technique to characterize the electronic properties of materials. The beamline is optimized to operate in the 2.3 - 12 keV energy range with high resolution and micro beam. The resolution is ΔE from 100 meV to 1 eV at 8 keV. The spot size is 20 (V) x 80 (H) μm^2 in standard mode and the flux is 1.5x10^{1}2 ph/s in the standard focalisation. The HAXPES techniques used a high resolution electron analyzer of 30 meV at 12 keV.

X-ray photoelectron spectroscopy (XPS) is a surface-sensitive quantitative spectroscopic technique based on the photoelectric effect. It allows to identify the elements existing within a material or covering its surface, as well as their chemical state, the electronic structure and density of the electronic states in the material. XPS is a powerful measurement technique because it not only shows what elements are present, but also what other elements they are bonded to. The advantage of using hard X-ray is that deeper core level can be excited compared to soft x-ray, due to the high incident energy of hard x-ray. Using the emitted electrons' kinetic energies measured by the detector and knowing the X-ray energy, the electron binding energy of the emitted electrons are determined with the photoelectric effect equation. It is then possible to reconstruct the valence band and the core levels of the studied sample.

A.2.2 2D-OKE spectroscopy

A Fourier-transform-based laser spectroscopy technique, two-dimensional optical Kerr effect (2D-OKE) spectroscopy has been developped to investigate the light propagation and nonlinear polarization responses with a femtosecond timescale. One of the most interesting features of this experiment is that it allows to energetically dissect broadband light propagation and thus to obtain a superior excitation energy resolution. To implement the 2D-OKE, a phase-stable co-propagating double pump-pulse sequence was setup. The Fourier transform with respect to τ provides a precise and unprecedented pump-energy resolution of few millielectronvolt. This is particularly interesting for our experiments near electronic resonances, where highly dispersive linear and nonlinear optical responses are expected.

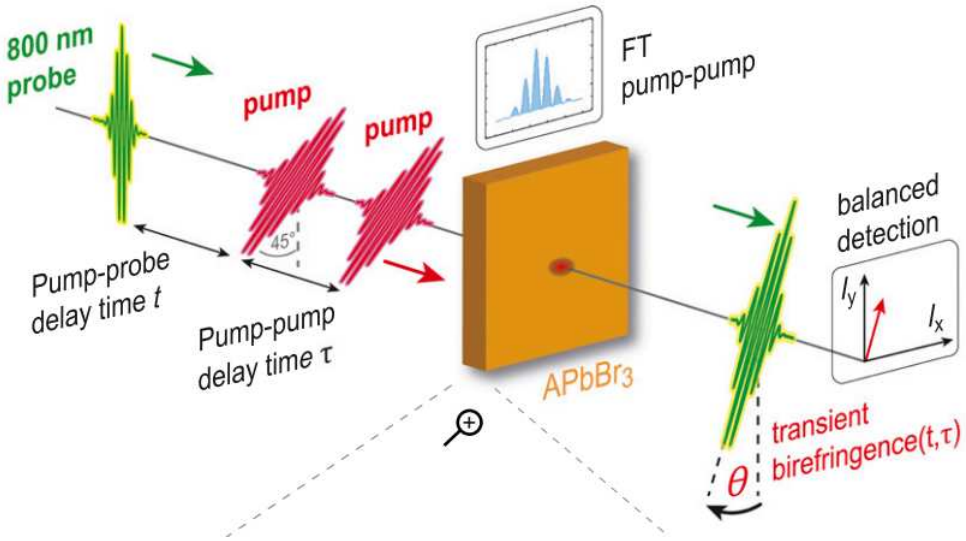

Figure A.8: Experimental scheme of 2D-OKE spectroscopy. Two phase-controlled and co-propagating pump pulses induce a nonlinear polarization response in the lead halide perovskite sample, while interacting with a time-delayed probe pulse. Nonlinear polarization response is traced via transient birefringence S(t, τ) as a function of pump-pump delay τ and prump-probe delay t. S(t,τ) monitors anisotropy and dispersion of light propagation, which is dominated by nonlinear $\chi^{(3)}$.

.

The figure Fig. A.8 illustrates time-resolved probing allowed by optical Kerr effect spectroscopy. This technique probes light propagation through dispersive crystal with birefringence characterized by an anisotropic refractive index Δn0(ν), as in the case in the orthorhombic phase of $MAPbBr_3$ and $CsPbBr_3$. The pump pulse navigates through the crystal and, in the case of an anisotropic material, decomposes into two orthogonal fields : a fast and a slow one, with different propagation velocities. The two orthogonal pump polarizations and the time-delayed probe pulse nonlinearly mix to produce a third-order nonlinear polarization. This contribution, obtained by a four-wave mixing process, is the origin of the observe OKE dynamics. The high dispersion near the bandgap is reflected in the pump-probe walk-off due to

velocity mismatching and in the temporal spread of the pump pulses due to the group velocity dispersion (GVD).

A.2.3 X-Ray Diffraction XRD on thinfilms

Measurements were performed by Niusha Heshmati with other collaborators from the University of Cologne.

Thin films

The polycrystal structure analysis was investigated by X-ray diffractometer, which monitor the crystallinity, crystal structure, phase purity and the preferred crystal growth orientation. The XRD measurements in the Institute of Inorganic Chemistry at University of Cologne were done in a STOE-STADI MP diffractometer from STOE with Cu Kα (λ = 1.5406 Å) operated at 40 kV and 40 mA in reflection mode for thin films.

(4cat)$PbBr_3$ single crystal

Single crystal XRD was done in the Institute of Inorganic Chemistry at University of Cologne in a SC XRD Bruker D8 Venture with Mo radiation (λ = 0.71073 Å).

A.2.4 Scanning Electron Microscopy (SEM)

Surface morphology and quality was evaluated with scanning electron microscope, which scans the materials surface with high energetic incident electron beam in an evacuated chamber. SEM images have been acquired with a Strata DualBeam 235 from FEI, using a 50 pA aperture during milling.

A.2.5 Time-resolved transient absorption (TR-TA)

Time-resolved transient absorption spectroscopy (TR-TA) is also based on the principle of pump–probe measurements. In our experiment, the sample is excited with a 2.5 eV pump pulse, followed by a white light continuum probe pulse with a variable time delay [26]. The dependence of the measured absorbance gives information on the temporal evolution of the system after excitation, such as excited-state populations evolution. For example, a change of the absorption could be explained by band gap renormalization.

A.2.6 Scannning electron microscopy (SEM)

Surface morphological studies were operated with a scanning electron microscopy (SEM). By focusing a beam of electrons on the sample surface, the electrons interact with the atoms of

the material leading to the emission of both secondary electrons and backscattered electrons. The first ones are emitted by atoms excited by the beam of electrons and give information about the surface topography by detecting their intensity in function of their position. The second ones gives information about the chemical composition of the sample.

A.2.7 Photothermal deflection spectroscopy

Photothermal deflection spectroscopy (PDS) is a highly sensitive technique for measuring the optical absorption characteristics of thin film samples by monitoring the change of the refractive index due to heating of a medium by a pump light source. The photothermal deflection measured is proportional to the absorption coefficient of a given material. A curve representing the normalized absorbance in function of the photon energy (eV) is then plotted. An exponential drop is normally observed at the energy band gap value. The fit of the linear part of the slope, called Urbach tail, allows to obtain the so-called Urbach energy E_u, indicating the degree of electronic disorder in the material. The smaller Eu is, the lower electronic disorder there is [288].

A.2.8 Current-voltage measurements (J-V)

Current-voltage (J-V) measurements under simulated sunlight condition allow the experimental evaluation of the solar cell parameters. J-V curves are measured by applying a forward- or reverse bias and by measuring the current response of the solar cell. In our experiments, current has been measured at different external voltage and at a temperature of 25 °C.

Plotting of the J-V curve lead to find the open-circuit voltage V_{OC} and the short-circuit current J_{SC}. The curve also allow to obtain the filling factor (FF) value, which is the area spanned by the products $J_{MP}.V_{MP}$ divided by the product $J_{SC}.V_{OC}$, with J_{MP} the maximum power current point and V_{MP} the maximum power voltage point. Knowing the incident solar power P_{IN}, the efficiency of the solar cell, also called power conversion efficiency (PCE), is obtained. The PCE is defined in percentage.

A.2.9 External quantum efficiency (EQE)

The spectral response of a solar cell device is measured by recording the wavelength dependent current response, the external quantum efficiency (EQE). The EQE is defined as the ratio of generated and collected charge carriers to the incident photons on the solar cell device emitted by the light source. The higher EQE percentage is and the most photons are converted into charge. Indeed, efficient solar cells always have high EQE value.

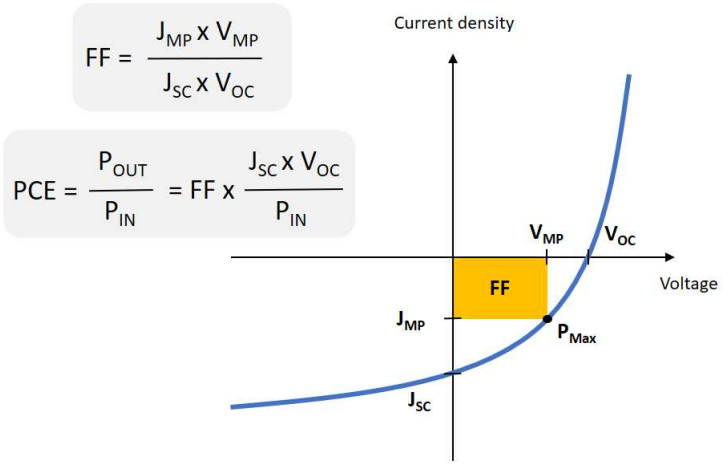

Figure A.9: J-V curve sketch, including fill factor (FF) and power conversion efficiency (PCE).

A.3 Supplementary TKE simulations

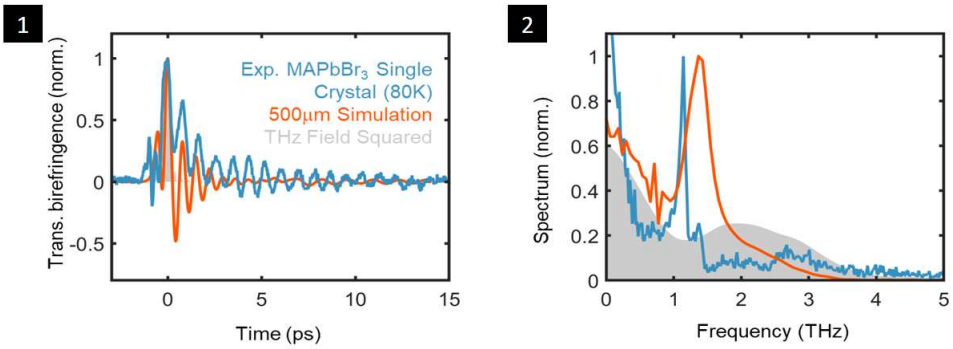

Figure A.10: Four-wave-mixing simulation for orthorhombic LHPs phase, assuming an instantaneous electronic hyperpolarizability response only. For 0 degree azimuthal angle and for all thicknesses larger than 200 µm, we can see the appearance of a short-lived oscillatory signal of around 1.4 THz in (1,2). These oscillations arise due to static birefringence, but are too short-lived to explain our experimental observation at 80K.

Publications and Awards

A.3.1 Scientific publications in peer-reviewed Journals

In preparation

CHERASSE, M.*, HESHMATI, N.*, ÜNLÜ, F., WAGNER, J., PERFETTI, L, MATHUR, S., ., MAEHRLEIN, S., "Lattice Polarization Influence on Charge Screening in Four Cations Lead Halide Perovskites", *in preparation*

FRENZEL, M.*, CHERASSE, M.*, WANG, F., XIANG, B., URBAN, J., NEST, L., HUBER, L., WOLF, M., KAMPFRATH, T., ZHU, X.-Y., MAEHRLEIN, S., "Nonlinear THz Control of the Highly Polarizable Lead Halide Perovskite Lattice", *in preparation*

Published

CHERASSE, M., DONG, J., ALLARD-TRIPPE, G., DELEPORTE, E., GARROT, D., MAEHRLEIN, S. F., WOLF, M., CHEN, Z., PAPALAZAROU, E., MARSI, M., RUEFF, J.-P., TALEB, A., PERFETTI, L., "Electrons dynamics in hybrid perovskites reveal the role of organics cations on the screening of local charges", Nano Lett., 22, 5, 2065–2069 (2022)

MAEHRLEIN, S., JOSHI, P. P., HUBER, L., WANG, F. CHERASSE, M., LIU, Y., JURASCHEK, D. M., MOSCONI, E., MEGGIOLARO, D., DE ANGELIS, F., ZHU, X.-Y., "Decoding ultrafast polarization responses in lead halide perovskites by the two-dimensional optical Kerr effect", *PNAS*, 118, 7 (2021)

JUNG, S., BUDZINAUSKAS, K., ÖZ, S., ÜNLÜ, F., KUHN, H., WAGNER, J., GRABOWSKI, D., KLINGEBIEL, B., CHERASSE, M., DONG, J., AVERSA, P., VIVO, P., KIRCHARTZ, T., MIYAZAKA, T., VAN LOOSDRECHT, P. H. M., PERFETTI, L., MATHUR, S., "Femto- to microsecond dynamics of excited electrons in a quadruple cation perovskite", *ACS Energy Letter*, 5, 3, 785–792, (2020)

A.3.2 Conferences and poster session

CHERASSE, M., " Towards an understanding of the dynamic lattice polarization of lead halide perovskites", *CNRS workshop Peroquium*, talk (2022)

CHERASSE, M., "Disentangling electronic and lattice polarization in lead halide perovskites using Kerr effects", *GDR HPero summer school*, poster (2021)

A.3.3 Scientific outreach

2022 - Scientific outreach with high school students at Conservatoire des Arts et Metiers, in partnership with L'Oréal-UNESCO.
2022 - Online scientific outreach with high school students via Declics events.
2021 - Scientific outreach in the street with Soapbox Science Berlin.

A.3.4 Fellowship and awards

2022 - L'Oréal-UNESCO Young talent for Women in Science Award.

2020 - DAAD Fellowship for PhD student in french-german scientific collaboration.

INSTITUT POLYTECHNIQUE DE PARIS

Titre : Dynamiques ultrarapides dans les pérovskites hybrides

Mots clés : Physique de la matière condensée, Spectroscopie THz, Photoémission résolue en temps, Dynamique de réseau, Pérovskites

Résumé : Les pérovskites hybrides aux halogénures de plomb (ABX_3) sont une classe de semiconducteurs présentant d'excellentes propriétés optoélectroniques et particulièrement prometteuses pour les applications photovoltaïques. Une compréhension fondamentale des dynamiques ultrarapides de ces matériaux est nécessaire. Ces travaux traitent deux thématiques principales : (1) L'étude de la relaxation des électrons dans la bande de conduction à l'aide de la photoémission résolue en temps et en angle. Cette technique a permis d'étudier l'influence de l'orientation des cations A et de la structure cristallographique sur l'écrantage des charges et ainsi d'expliquer la grande tolérance au piégeage des électrons sur la surface des cristaux de $MAPbI_3$. (2) Comprendre le rôle des phonons et leur influence sur les électrons à l'aide de l'effet Kerr excité au THz. Le mode de phonon Raman le plus polarisable lié au sous-réseau Pb-Br a été dévoilé dans les pérovskites à cation A unique et complexe. Cette découverte met en évidence le rôle du réseau inorganique le mécanisme d'écrantage des porteurs de charges.

Title : Ultrafast dynamics in hybrid perovskites

Keywords : Condensed matter physics, THz spectroscopy, Photoemission, Lattice dynamics, Lead halide perovskites

Abstract : Hybrid lead halide perovskites are an intriguing class of semiconductors with excellent optoelectronic properties and promising for photovoltaic applications. A fundamental understanding of the ultrafast dynamics in these materials is required. This work deals with two main topics: (1) The study of electron relaxation in the conduction band using time-resolved photoemission (2PPE) and angle-resolved photoemission (tr-ARPES). Here, the influence of the orientation of A-site cations and crystallographic structure on charge screening have been studied, explaining the high tolerance to electron trapping on the surface in $MAPbI_3$ crystals. (2) Understanding the dynamic role of phonons and their influence on electrons using the THz-induced Kerr effect. We obtained coherent control over a Raman-active Pb-Br sublattice mode, which was found to dominate the ultrafast lattice polarizability in both single and complex A-site cation perovskites. This finding highlights the potential of the inorganic lattice for dynamic carrier screening and the related mechanism of charge carrier protection.

Institut Polytechnique de Paris
91120 Palaiseau, France